課程博士（地球環境科学専攻のみ）

Age of ore-related intrusions and formation conditions of ore-bearing veins at Cerro Colorado porphyry copper mine, northern Chile

(チリ北部に位置するセロコロラド銅鉱山における鉱床形成に関連する貫入岩体の年代決定及び鉱石を含む鉱物脈の形成条件)

TSANG, Pui Wai Debbie

（曾　珮蔚)

A dissertation for the degree of Doctor of Science

Department of Earth and Environmental Sciences,

Graduate School of Environmental Studies, Nagoya University

（名古屋大学大学院環境学研究科地球環境科学専攻学位論文　博士（理学)）

2018

Table of Contents

Part I Thesis overview 1

Supplementary materials

Supplementary research paper

List of Figures

Part I

Part II

Part III

List of Tables

Part I

Part II

Supplementary materials

Part II

Supplementary sheets 1 Summary of published ages in N. Chile

Supplementary sheets 2 Major element data for representative samples from CEF, PTO1 (porphyritic quartz monzonite of this study) and PQZ (leucocratic quartz porphyry of this study) provided by CMCC

Supplementary sheets 3 Full raw dataset for LA-ICP-MS U–Pb age dating and weighted mean plots of each rock types

Part III

Supplementary sheet 4 Calculation of few scenarios of removed loads since 50 Ma

Part I

Thesis Overview

1. Introduction

This thesis reports the results of zircon U–Pb dating and fluid inclusion studies in an active porphyry copper mine in northern Chile, the Cerro Colorado mine (in Spanish: Compañía Minera Cerro Colorado or CMCC). The mine site is located 120 km to the northeast of Iquique and is one example of a series of Eocene to Oligocene porphyry copper deposits (Cornejo et al., 1997; Camus, 2005; Charrier et al., 2007; Mpodozis & Cornejo, 2012) developed along the S. America convergent margin. Selection of the samples used in these studies was guided by extensive field work including observation of a total of about 5200 m core preserved in the mine site and bulk rock geochemical analyses. The mine core samples offer an unprecedented opportunity to examine the porphyry intrusions, the original volcanic basement and the mineralised zones in the Cerro Colorado area but have not previously been available for academic research.

In this overview, I first present a review of the general understanding of how copper porphyry deposits form, some of the contentious issues that remain to be resolved and summarise how the results of this thesis have contributed to furthering our understanding of the Cerro Colorado mine site deposit and copper porphyry deposits in general. The following Parts II and III focus on the geochronology and fluid inclusions studies respectively. These are intended as largely independent pieces of work that can stand by themselves and inevitably some of the introductory material is repeated in the different sections.

2. General understanding of porphyry copper deposits

Porphyry ore deposits host up to 70 % of the world's total copper production and are a main source for molybdenum and gold (e.g. Seedorff et al. 2005; Cooke et al., 2005; Sillitoe, 2010, 2012). Almost 40 % of the entire world production of Cu is mined in Northern Chile, where porphyry copper is the dominant style of mineralisation (Maksaev et al., 2007). These commercially important Cu mineral deposits associated with porphyritic intrusions are known as Porphyry Copper Deposits or PCDs and characteristically form in convergent plate margins with South America being the best-known example (e.g. Richards, 2011a, 2013; Cooke et al., 2005; Sillitoe, 1973, 2010, 2012) (Fig. 1).

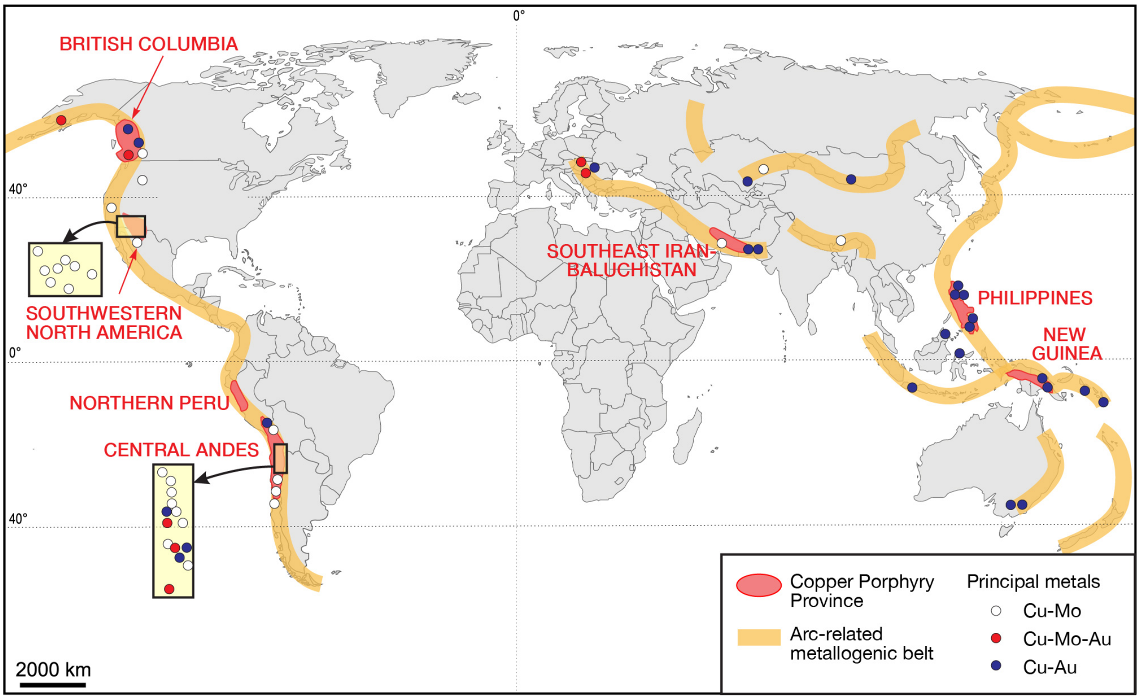

Fig. 1 World distribution of porphyry copper deposits and metallogenic belts coinciding with arc and paleo-arc settings (Modified after Sillitoe, 2010, 2012; Richards, 2013).

In addition to the association of PCDs with convergent tectonic settings, the clear alignment of metallogenic belts parallel to the convergent plate margins suggests that PCDs form under specific tectonic conditions. In addition, the clustering of igneous stocks associated with concentrations of mineralisation is commonly considered to be the result of interaction between tectonically controlled structures and magmatic processes (Tosdal & Richards, 2001; Richards, 2005, 2013; Cooke et al., 2005; Sillitoe, 2010, 2012). Changes in the angle and direction of subduction can induce an inversion of the stress field (e.g. James & Sacks 1999; Haschke et al., 2002a) and it has been suggested that such events exert a fundamental control on the timing and locations of porphyry emplacement (e.g. Kay & Mpodozis, 2001; Sillitoe, 2012). Many workers also emphasise the importance of pre-existing faults or folds. The pre-existence of these structures is thought to help open up pathways for magma to ascend, for instance, in pull-apart extensional domains (e.g. Richards, 2003, 2005; Sapiie & Cloos, 2004). A recent geochemical simulation of melt compositions relevant to PCD formation suggests known compositions are compatible with magmatism during both compressional and near neutral to slightly extensional stress states (Chiaradia & Caricchi, 2017). Changes in the regional stress field due to events such as subduction reversal have also been proposed (e.g. Solomon, 1990; Rohrlach & Loucks, 2005).

The average grade of copper in a typical subsurface hydrothermal (hypogene) PCD environment is estimated to be 0.5–1.5 wt % (Sillitoe, 2010), and is about 200 times enriched compared to average crustal concentrations (Ulrich et al., 1999). The most widely accepted model for the copper source is the orthomagmatic model (e.g. Gustafson & Hunt, 1975, Dilles, 1987; Candela, 1989; Cline & Bodnar, 1991), which proposes that the metals are derived from fluids exsolved from a magma source. These exsolved magmatic aqueous fluids typically contain 10–30 wt % NaCl (e.g. Bodnar et al., 1985; Wilkinson, 2001) and are referred to as brines. Brine fluids have the interesting property that at pressures less than about 210 MPa they can separate into two coexisting immiscible fluids: a high-density hypersaline brine and a low-density relatively low-salinity vapour (e.g. Sourirajan & Kennedy, 1962; Bodnar et al., 1985; Driesner, 2007; Driesner & Heinrich, 2007). Due to the high affinity of Cu for the Cl^- ligand, and the higher concentration of Cl^- in the fluid phases compared to the original magma, both the brine and vapour saline fluids have the high potential to extract and carry significant quantities of Cu and other metal ions away from the magma source (e.g. Candela, 1989; Cline & Bodnar, 1991; Cline 1995).

Mass balance calculations show brine fluids derived from relative small magma bodies with sizes of 13–17 km^3 can extract sufficient Cu required to form typical PCDs (Cline, 1995). PCDs are cored by sub-volcanic intrusions and these intrusive bodies are assumed to be the source of the metals in the deposit.

The Cu and Mo in PCDs form as sulphides such as chalcopyrite and molybdenite although these are commonly altered to sulphates and hydroxides at shallow levels due to the interaction with meteoric water (the supergene domain). The initial mineralisation requires interaction with sulphur and the origin of this element is an important part of understanding PCD formation. Magmas in convergent arc settings are typically oxidised, and the dominant S species is typically SO_2 (e.g. Lerchbaumer & Audètat, 2012; Humpreys et al., 2015). It is suggested that the presence of oxidised S species promotes higher solubility of Cu in brine-rich ore fluids (Zajacz et al., 2011; Audètat & Simon, 2012), thus allowing higher concentrations of Cu to be transported. In this case, the precipitation in the form of sulphides requires a change in the redox state to supply reduced sulphur in the form of S^{2-} and HS^-. The disproportionation reaction of SO_2 is commonly proposed as an important source for H_2S that can react to form metal sulphide:

$$4SO_2 + 4H_2O = 3H_2SO_4 + H_2S$$

This reaction occurs at temperatures below 400 °C (e.g. Holland, 1965; Landtwing et al., 2005; Kouzmanov & Pokrovski, 2012) and is one of the reasons that PCD metal formation is commonly thought to occur at temperatures significantly lower than magma crystallisation.

Alteration of country rocks by interaction with hydrothermal fluids is an important part of PCD development (e.g. Sillitoe, 2010, Richards, 2011a). Alteration zones can be defined based on the type of secondary mineralisation with which they are associated. Alteration zones commonly documented in PCDs are, in general order of decreasing temperature: potassic, sericite-chlorite-clay (SCC), phyllic (sericitic) and propylitic (Meyer & Hemley, 1967; Lowell & Guilbert, 1970; Rose & Burt, 1979; Sillitoe, 2010). A less well defined argillic alteration zone is also described in some areas (Cooke et al., 1998). The normal configuration of alteration zoning pattern around a PCD stock involves a deeper potassic alteration zone closest to and surrounding the intrusive body. Moving to upper (closer to surface) and outer (further away from intrusion) regions of the profile, alteration zones typically change to SCC, then phyllic and finally argillic zones, corresponding to a decreasing temperature. SCC and phyllic alteration zones commonly host hypogene Cu mineralisation (e.g. Sillitoe, 2010). The clayish advanced argillic zone developed in the lithocap and may not be preserved if the shallow supergene enrichment (due to interaction with meteoric water) has overprinted the hypogene alteration (Sillitoe, 2010). Propylitic alteration is pervasive, affecting all the surrounding rocks, mainly due to circulation of heated groundwater (Richards, 2011a).

Metal ions are transported by magmatic-hydrothermal fluids into the wall rocks surrounding the porphyritic intrusions to form PCDs. High-permeability domains can provide pathways more favourable for concentrating fluid flow and thus enhancing higher concentration of ore metal deposition (Sillitoe, 2012). Highly permeable rocks include material such as magmatic-hydrothermal breccias (Sillitoe, 2012, and examples within). Dissolution processes also enhance the permeability. At relatively shallow depths, the solubility of SiO_2 in H_2O shows a local maximum at moderate temperatures. This results in a period of enhanced solution during cooling and can contribute to a local increase in permeability. Acidic alteration and dissolution of the host rock that commonly accompanies PCD formation (Sillitoe, 2010; Richards, 2011a) also increases permeability. Acidic alteration is generally thought to be triggered by the disproportionation of SO_2 gas into H_2S and H_2SO_4 (sulphuric acid). However, gas–brine reactions during deposition of chalcopyrite is a potentially important source for HCl (hydrochloric acid), which will also contribute to acidic alteration (Blundy et al., 2015).

3. Link between porphyry copper formation and active volcanism

Although there is a clear general link between the volcanic arc and PCD formation, many workers have proposed that the conditions needed for PCD formation are characteristic of times when volcanism was suppressed or absent (e.g. Cloos, 2001; Cooke et al., 2005; Sillitoe, 2010). A catastrophic voluminous eruption, such as one that forms large volumes of pyroclastic lava or ignimbrite, would likely empty most of the materials within a magma chamber, resulting in the release of the metal into the volcanic lava and ash and gas, leaving insufficient quantities to form economically viable deposits (e.g. Richards, 2005; Sillitoe, 2010). Kay et al. (1999) and Kay and Mpodozis (2001) propose that the termination of a period of metallogenesis in northern Chile coincided with major late Miocene eruptions forming large ignimbrite sheets. Age dating suggests that as this phase of eruption occurred in the north, the locus of copper mineralisation migrated towards the south.

Less explosive volcanic processes such as degassing are also generally considered to result in release of Cu and depletion in the remaining magma. Cu and other metal ions involved in PCD formation are thought by many workers to be mainly transported in the vapour phase (e.g. Williams-Jones & Heinrich, 2005; Simon et al., 2006; Audètat et al., 2008; Landtwing et al., 2010; Seo et al., 2012; Vigneresse et al., 2014). These ideas are largely based on the empirical observations that the presence of reduced sulphur species, in particular HS^-, results in the formation of metal ligands and the preferential fractionation of Cu into the vapour phase rather than the coexisting brine (Drummond & Ohmoto, 1985). In the case that HS^- is present in the ore-forming fluid, metal ions would be selectively partitioned into the gaseous phase of the fluid forming stable Cu–S complexes. Possibilities such as $[Cu(HS)]+$, $[Cu(HS)_2]^0$, $[Cu(HS)]^0$, $[Cu(HS)_2]^-$, $[Cu_2S(HS)_2]^{2-}$, $[Cu(HS)(H_2S)]^0$ have been reported by different authors (Heinrich et al., 1999; Mountain & Seward, 1999, 2003; Al-Farawati & van den Berg, 1999; Etschmann et al., 2010; Simon et al., 2006). In these situations, the release of volcanic gases into the atmosphere would result in the loss of most of the Cu-bearing phase from the rock system (e.g. Williams-Jones & Heinrich, 2005; Audètat et al., 2008).

In order to prevent the release of the Cu-bearing vapour, many models of PCD formation require the presence of an impermeable cupola within the shallow crust above an intrusion front. This impermeable cupola traps the metal-bearing brine and gas that have been exsolved from the magma and facilitates interaction with the wall rock. The presence of a steep thermal gradient is important in concentrating the copper mineralisation (e.g. Tosdal & Richards, 2001; Richards, 2005; Wilkinson, 2013). In this scenario, arc volcanism including degassing is suppressed during PCD formation (e.g. Cloos, 2001; Cooke et al., 2005). Alternative genetic models for PCDs propose brine fluids are the main medium for Cu transport (Cline & Bodnar, 1991; Hedenquist & Lowenstern, 1994; Shinohara, 1994; Leuchbaumer & Audètat, 2012; Blundy et al., 2015). In such cases, volcanic degassing would not necessarily hinder PCD development and the two may be closely related.

In contrast to the above arguments, some workers consider there is a link between active volcanism and PCD formation. One school of thought suggests that PCD formation coincides with either the waning stages of arc magmatism, or the final magmatic ascent in the arc prior to arc migration. These changes commonly coincide with stages of major tectonic transition for instance where neutral or extensional horizontal stresses change to compressive stresses and crustal thickening (e.g. Kay et al., 1999; Kay & Mpodozis, 2001; Sillitoe, 2010) or to an initial relaxation after a period of crustal compression (e.g. Tosdal & Richards, 2001; Richard, 2003, 2005). Studies of sulphur isotopes of melt inclusions and sulphide minerals from PCDs, and volcanic vapour chemistry (Hedenquist et al., 1998; Hattori & Keith, 2001; Nadeau et al., 2010, 2016) have been used to suggest a direct link between active volcanism and PCD formation.

Reflecting the uncertainties in PCD models, many well-cited studies of PCD formation models remain agnostic about the role of active volcanism and how this may relate to subvolcanic intrusion and mineralisation (e.g. Shinohara et al., 1995; Shinohara & Hedenquist, 1997; Tosdal & Richards, 2001; Kay et al., 1999; Kay & Mpodozis 2001; Wilkinson, 2013; Zellmer et al., 2015), and many do not address the question of how to explain the potential problem of losing Cu during active volcanism due to volatile loss.

In terms of future prospecting, the role of active volcanism in the formation of PCDs is a critical question to address: for instance, are there at present active Cu-PCDs forming under arc volcanoes of Japan? Potential links between PCD formation and active volcanism are also important to investigate to help determine if the vapour or brine phases are the main Cu carrier. Better understanding of this part of the Cu-mineralisation process would help expand the exploration potential of copper minerals in volcanic arc regimes. Despite this importance, there is no consensus about the role of active volcanism in PCD formation.

4. Origin of Sulphur

Under normal magmatic arc conditions, partial melting and dehydration of the subducting slab and transfer of oxidised fluids to the mantle generate relatively oxidised arc magmas (e.g. Mungall, 2002; Wilkinson, 2013). The concentrations of metal in PCDs can be readily explained by extraction from medium-sized felsic intrusions. It is more difficult to account for the amount and oxidation state of the sulphur required to form the main metal sulphide deposits.

Experimental work done by Matjuschkin et al. (2016) shows that at middle crustal depths (ca. 15 km) under normal magmatic arc oxidation conditions, a S-rich primary magma would undergo early sulphide saturation, which would sequester and disseminate Cu in deeper crustal rocks leaving a Cu-depleted melt, which could not then continue to form PCDs at shallower levels. In order to maintain the Cu concentrations needed for PCD formation in shallow relatively oxidised melts, many workers suggest that there is a late stage of sulphur addition that is introduced as a secondary phase during the mineralisation process: Cu (and other metal ions) and S are not derived from the same parental oxidised magma (e.g. Hattori & Keith, 2001; Collins et al., 2012; Vigneresse et al., 2014; Henley et al., 2015; Blundy et al., 2015). Mafic magmas can contain much larger amounts of sulphur than felsic magmas and some authors (e.g. Wilkinson, 2013; Steinberger et al., 2013) suggest mafic underplating and magma mixing is an integral part of supplying sulphur, and copper mineralisation occurs during this phase. Others suggest a secondary sulphur phase is introduced by degassing (e.g. Collins et al., 2012; Henley et al., 2015; Blundy et al., 2015) or directly associated with mafic magma eruption (e.g. Hattori & Keith, 2001, Nadeau et al., 2016).

If an external source of sulphur is considered, this alleviates many of the problems associated with trying to account for the transport and precipitation of Cu and other metals by the action of a single fluid. The supply of sulphur from a separate source also has implications for the effects of degassing on PCD formation. Matjuschkin et al. (2016) suggest an early phase of volatile release removing dissolved S from PCD parental magma during early magmatic segregation may be a way to retain the Cu in the then S-poor magma. This would imply that gas release during volcanic activity should have no direct influence in suppressing PCD formation. In the absence of reduced S in the system, both the introduction of copper into shallow crustal level by brine fluids, and the mineralisation of copper (determined by the time at which sulphur is introduced by a liquid or gas phase), can occur at the same time as active volcanism.

In addition to volatile release from a deep-seated magma, S^{2-} gas emitted from a volcanic system can also be the product of hydrothermal reaction between SO_2 and oxidised ground water at relatively low temperatures (ca. 300–400 °C). Under these conditions a disproportionation reaction occurs to give H_2S (e.g. Holland, 1965; Landtwing et al., 2005; Kouzmanov & Pokrovski, 2012), which can react with metal ligands in brine to form metal sulphides. This reaction can be expressed as follows:

$$11H_2S\text{ (gas)} + SO_2\text{ (gas)} + 6CuCl^{2-}\text{ (brine)} + 6FeCl_2\text{ (brine)} =$$
$$6CuFeS_2\text{ (chalcopyrite)} + 6Cl^{-}\text{ (brine)} + 18HCl\text{ (gas)} + 2H_2O\text{ (gas)}$$

(e.g. Landtwing et al., 2005; Blundy et al., 2015):

This reaction (and similar reactions with other metal ions) has the potential to trigger extensive Ccp deposition at hydrothermal temperatures. The release of large amounts of acidic gas as a result of this reaction will contribute to the alteration fronts associated with PCD formation and the accompanying volume increase may lead to brecciation of rock. The resulting dissolution and fracture permeability may influence the path of subsequent mineralising fluids.

5. The significance of geochronology in PCD formation studies in particular in northern Chile

The ages of formation of PCDs are key in understanding the processes that cause them to be formed. This includes relating the PCD formation to tectonic events such as changes in plate convergence vectors and magmatic events reflected in volcanic and other magmatic activity. Geochronology also helps place constraints on the timeframe for magmatic-hydrothermal activity and duration of mineralisation, both key aspects of understanding the main processes underlying PCD formation.

This thesis examines an area of northern Chile. Geochronological studies of metallogenic provinces in northern Chile have been used to define six metallogenic belts: Late Paleozoic–Triassic (298–230 Ma), Early Cretaceous (132–97 Ma), Paleocene–Early Eocene (60–50 Ma), Late Eocene–Early Oligocene (43–31 Ma), Early Oligocene–Middle Miocene (23–12 Ma) and Late Miocene–Pliocene (12–4.3 Ma) (Sillitoe, 1974, 1988; Camus, 2005; Maksaev et al., 2007). A summary of the published data for the Andean PCDs of northern Chile (Fig. 2 and supplementary sheet 1) is in good general agreement with the proposed division, but there are many intermediate ages and some of the belts are only defined on the basis of a few ages. At least part of the spread in ages may be due to the method used. Many of the ages that have been reported in porphyry deposit districts are based on the K–Ar decay system. These ages generally reflect the timing of cooling and cannot be directly related to the timing of the porphyritic intrusions and associated mineralisation. In addition, there are potentially significant problems with extraneous Ar in K-bearing minerals.

U–Pb dating of zircon from igneous rocks at the core of PCDs and Re–Os dating of molybdenite from the main ore bodies have been used by many workers to estimate the ages of igneous intrusion and metallogenesis, respectively (e.g. Maksaev et al., 2004; Rosera et al., 2013;

Barra et al., 2013; Simmons et al., 2013). However, in northern Chile only a few Re–Os dates have been reported and the limited number of zircon U–Pb ages are generally restricted to rocks of Jurassic age or older. The limited number of U–Pb ages are generally restricted to mine reports and have not been fully published in the public domain. Obtaining a greater number of high-resolution zircon U–Pb dates is a high priority.

6. PCD formation temperature and depth

There is good general agreement that PCD formation occurs at submagmatic temperatures with most of the activity occurring around 300–400 ˚C. There are three main reasons for this. The first two are chemical and to some degree model dependent, the third is based on direct observation of formation conditions.

1. Sulphide for metal sulphide formation and acid for alteration is generally thought to be provided as a result of the disproportionation reaction of SO_2 with hydrothermal fluid forming H_2S and H_2SO_4:

   $$4SO_2 + 4H_2O = H_2S + 3H_2SO_4$$

   (e.g. Holland, 1965; Landtwing et al, 2005; Kouzmanov & Pokrovski, 2012). This reaction occurs at temperatures ≤ 400 ˚C.

2. The solubility of copper-chloride species in hydrothermal ore fluid drops drastically in this temperature range (e.g., Crerer & Barnes, 1976; Hemley & Hunt, 1992; Hezarkhani et al., 1999; Brugger et al., 2007), supplying excess metal ions required for the ore formation.

3. The copper and iron sulphides ore minerals are commonly crystallised as an important constituent of dominantly quartz veins. Quartz is transparent and stable over a wide range of temperatures. This means that any fluids trapped during its growth as fluid inclusions can be observed in situ over a wide range of temperatures and the

information used to estimate the conditions at which fluid became trapped. Analyses of quartz fluid inclusions in vein material associated with PCD formation generally show trapping temperatures of 300–400 ˚C (e.g. Ulrich et al., 2002; Landtwing et al., 2005; Rusk et al 2008).

Despite this good general agreement between the theoretical considerations and observations of natural systems suggesting PCD formation around 300–400°C, there is also a significant body of data suggesting that chalcopyrite-bearing veins from PCDs can form at significantly higher temperatures reaching magmatic temperatures. The high temperature data, i.e. 650–725 ˚C, up to 800 ˚C, tend to be reported in the older literature (e.g. Roedder 1971, 1972; Sheppard et al., 1971; Hedenquist & Lowenstern, 1994) although the results are also reproduced in some recent studies (e.g. Landtwing et al., 2010; Kouzmanov & Pokrovski, 2012).

In addition to fluid inclusions studies, Sheppard et al. (1971) used hydrogen and oxygen isotope ratios of minerals to suggest that in a few studied PCDs hydrothermal alteration temperatures related to the formation of a quartz-biotite-K-feldspar-chalcopyrite assemblage achieved temperatures of at least 650 ˚C. The same two authors also present fluid inclusion data locally indicating homogeniation temperatures in PCDs higher than 600 ˚C and even, rarely, up to 800 ˚C. However, it is unclear how these high temperature fluids relate to the distribution of copper in the mineraliation veins. If some of the copper mineraliation did indeed take place at close to magmatic temperatures, this would imply that the origin of sulphur and the chemistry of sulphide formation need to be reconsidered.

The general consensus is that PCDs form at shallow crustal levels around 1–5 km with an average of around 2 km (e.g. Sheppard et al., 1971; Fournier, 1999; Cloos, 2001; Singer et al., 2008; Richards, 2011a) and the main associated magma body lies at deeper levels of around 4–10 km (e.g. Cline, 1995; Shinohara & Hedenquist, 1997; Audètat & Simon, 2012; Wilkinson, 2013; Blundy et al., 2015; Chiaradia & Caricchi, 2017). Singer et al. (2008) suggests that Cu-dominated PCDs form at relatively shallow levels of around 1.5–2.5 km, whereas Cu–Mo PCDs in general form at slightly deeper levels of up to 4 km. The majority of such estimates are based on temperatures recorded by fluid inclusions comparing with the temperature and depth of brittle-plastic deformation boundary in the upper crust in a subvolcanic environment (e.g. Fournier 1999; Landtwing et al., 2005). In most fluid inclusion studies in PCDs, the ranges of trapping temperatures are < 400 ˚C, and are at or below the brittle-plastic boundary. Fluid pressure in shallow brittle fault zones is likely to be close to hydrostatic and hydrostatic pressure gradients are commonly assumed when estimating the depths at which the lower temperature group of inclusions formed. In contrast, lithostatic pressure gradients are commonly assumed when estimating the depths at which the higher temperature group of inclusions formed (e.g. Cline & Bodnar, 1994; Hedenquist et al., 1998; Landtwing et al., 2005, 2010).

Another method used to estimate depth is by fission track analysis to reveal the thermal history, which can be combined with assumptions about the thermal gradient to derive an exhumation history. McInnes et al. (2005) used this approach to estimate emplacement depth of 3 mine sites. Two of these gave estimated emplacement depths of 2.8–2.9 km, agreeing with the general consensus. However, their results also indicate the formation depth of a PCD can be as shallow as 800 m. The authors further suggest the associated porphyritic unit was directly intruded within a volcanic edifice.

7. Project objectives

In this study, I report the results of geochronology and fluid inclusion studies with the aim of examining the various models for PCD formation. In particular, I focused on how these data can help reveal the relationships between active volcanism and PCD formation and the *P–T* conditions of PCD formation. In addition to the overview, Part I, this thesis is divided into two main parts covering the results from the two main types of investigation.

Part II of this study focuses on zircon U–Pb geochronology analyses for each of the rock units exposed in CMCC. The subvolcanic magmatic bodies lie in the core of the ore body and are taken to be the source for the Cu. Determining the ages of the ore-forming subvolcanic intrusive units reveals the timeframe when Cu was available in the system. Comparing the ages of the andesitic to dacitic host rocks and locally exposed units with the main intrusive bodies can provide a better understanding of the evolution of the arc volcanic-plutonic system. I chose the U–Pb zircon dating because diffusion rates for both parent and daughter nuclides are slow resulting in a high closure temperature. In addition, zircon is generally thought to be chemically resistant to alteration even at high temperatures meaning the ages can be interpreted as representing formation ages of magmatic rocks.

Part III of this study focuses on fluid inclusion analyses from mineralised quartz veins samples in CMCC. Obtaining the trapping temperature and pressure of the fluid inclusions reveals the formation pressure-temperature condition when the ores were deposited. Attention is paid in particular to the relationship between high temperature fluid and sulphide minerals. The trapping conditions are then used to infer plausible formation pressures and related processes.

8. Main Findings of Thesis

Part II: Zircon U–Pb Geochronology

1. The main host for the ore of the Cerro Colorado mine is the regionally developed volcanic Cretaceous Cerro Empexa Formation. The new ages obtained for this Formation generally fall in the range of 80–70 Ma in agreement with previous studies. A new finding of this study is a minor younger phase of volcanic activity associated with formation of a breccia unit with an age of 57 Ma.
2. The subvolcanic intrusive bodies at the core of the mine site have been separated into three distinct bodies by mine geologists. However, field observations suggest two of these may in fact represent different degrees of alteration of the same body. The inferences from field observations are supported by the geochronological studies, which suggest the main subvolcanic units can be divided into a porphyritic tonalite and a porphyritic quartz monzonite that formed at ca. 53.5 and ca. 50 Ma, respectively. The monzonite is locally highly sericitised with a considerable degree of silicification.
3. Zircon age populations of the intrusive rocks suggest the presence of a third early intrusion with an age of ca. 60 Ma. This corresponds well with the age of the breccia unit. Intrusive bodies with a similar age are found surrounding the Cerro Colorado area, but a corresponding intrusive body was not recognised in the mine site.
4. Reported molybdenite Re–Os ages suggest a mineralisation phase in Cerro Colorado mine at ca. 56–54 Ma (Cotton, 2003; CMCC, 2014), which is compatible with, i.e. slightly younger than the ages of the ca. 57 Ma breccia unit and the ca. 60 Ma phase of magmatic activity.
5. The older tonalitic intrusive body is strongly altered and mineralised. In contrast, the youngest recognised intrusive body, a small porphyritic granodioritic dyke, is lightly mineralised. The

difference in age is around 3–4 m.y. and represents the approximate time scale for mineralisation in the Cerro Colorado area.

6. The close temporal relationship between the early magmatic phase, the recorded early mineralisation phase, the breccia unit, and the younger ore-related subvolcanic units, suggest PCD formation occurs closely associated with volcanic activity.
7. The age of the youngest intrusion corresponds closely with a major change in plate convergence direction at around 49 Ma (Pardo-Casas & Molnar, 1987), which also coincides with the onset of a change in stress state from extensional or neutral to compressive in the Chilean Andes region (James & Sacks, 1999; Haschke et al., 2002a; O'Driscoll et al., 2012). This suggests that the Cerro Colorado PCD formation may have formed when the magmatism was waning and eruption was becoming less dominant.

Part III: *P–T* Formation Conditions and Microtextural Studies of Ore-bearing Quartz Veins

1. Observations using CL, SEM, reflected and transmitted light polarizing microscopes show ore-bearing quartz veins can be separated into four microtextural domains. In order of older to younger these are: fine-grained massive, idiomorphic, infilling, and late-stage dissolution-reprecipitation features including splatter- and cobweb-like features. Copper mineralisation is mainly associated with the third and fourth stage quartz growth, but is also locally seen associated with the second stage.
2. Both coexisting hypersaline brine and low salinity vapour primary inclusions are commonly observed suggesting formation of quartz at below the immiscibility curve for brines.
3. Halite dissolution temperatures for salt crystals in the fluid inclusions suggest salinities of 30–45 wt % NaCl.

4. Homogenization temperatures for brine inclusions fall into two main groups: 240–390°C and 390–420 ˚C. The gap between the two groups is best explained as due to the presence of the local peak in SiO_2 solubility in this temperature range rather than reflecting two different stages or processes of vein formation.
5. A significant number of high homogenization temperatures up to 700°C are recognised in the stage 3 infilling quartz grains. These quartz grains are commonly associated with large grains of Cu and Mo sulphide minerals suggesting the main ore mineralisation in these veins occurred at close to magmatic temperatures.
6. The fluid inclusions record a wide range of pressures with a higher group around four times greater than the lowest group. An estimate for the depth of formation of the Cerro Colorado PCD can be made using regional erosion rates and results in an estimated depth of around 2–3 km. This is in good agreement with other studies of similar deposits. The recorded pressure variation exceeds possible variations between purely lithostatic and purely hydrostatic. The most likely explanation is formation of the mineralised veins during fracturing caused by overpressurised fluid in excess of lithostatic conditions. The rupture would cause a large and rapid drop of pressure to below hydrostatic conditions. Fluid flow would be enhanced along the space created by rupture.

9. Implications for PCD Formation

In addition to the important results for understanding the evolution of the Cerro Colorado PCD in northern Chile, this study also provides information that has significant implications for the formation of PCDs in general. The three main points are summarized below.

The U–Pb ages for the Cerro Colorado mine site show that multiple pulses of magmatic activity related to the PCD formation took place between ca. 60–50 Ma. The detailed geochronological study covering all the main units of the mine site allows a close comparison to be made with regional plate tectonic reconstructions for southern America. This shows that Cerro Colorado PCD formed during a period of rapid change in plate motion vector that is commonly related to the onset of shallow slab subduction and a shift from extensional or neutral stress states to compressive. This correlation between the tectonic events in the southern American realm and PCD formation lends support to the idea that periods of change in the tectonic stresses, in particular from extensional or neutral to compressive favour the formation of PCDs.

Geochronology shows that the main phase of mineralisation is bracketed by the two intrusions forming porphyritic tonalite at ca. 53.5 Ma and porphyritic quartz monzonite at ca. 50 Ma. The age range derived for the local breccia unit overlaps with the tonalite, which implies active volcanism within the timeframe of PCD formation. The fluid inclusion studies indicate explosive release of fluid pressure due to hydrofracturing with a range of recorded pressures from supra lithostatic to sub hydrostatic. These results imply powerful degassing occurred at the same time veins were forming that are one of the main hosts for Cu mineralisation. These results indicate that active volcanism including explosive degassing is closely related to a major part of the PCD mineralisation. The implied link between active volcanism and PCD formation is important when deciding where to search for new ore bodies.

In addition, the evidence for explosive gas release at the time of PCDs, implies that contrary to the suggestions of many studies, the gas phase is unlikely to be the main Cu carrier and liquid brines are of prime importance when considering transport and deposition of sulphide minerals.

Microthermometry studies of Cu-ore-bearing quartz veins revealed a wide range of trapping conditions. In many of the well-formed quartz crystals, fluids were trapped at 300–400°C. This is the range commonly reported in other studies of PCDs and is thought by many to correspond to the main phase of ore mineralisation. However, this study also revealed the presence of fluids trapped at temperatures 500–700°C. Microtextural studies showed a close link between the quartz containing these originally high T fluids and large grains of ore minerals. This implies that a significant part of the ore mineral deposition occurred at temperatures close to the solidus temperatures for dacitic rocks. This is above the temperature at which disproportionation of SO_2 occurs through the reaction with H_2O, implying that alternative mechanisms have to be considered to supply the sulphur at suitable redox conditions to form the sulphide ore minerals. This is good observational evidence in favour of the suggestion that the sulphur is introduced external to the main observed rock units (e.g. Hattori & Keith, 2001; Collins et al., 2012; Vigneresse et al., 2014; Henley et al., 2015; Blundy et al., 2015).

Part II

Magmatic evolution of the Cerro Colorado Porphyry Copper Deposit, northern Chile: a combined study using geochronology, geochemistry and field observations

1. Introduction

One of the geological characteristics of the South America convergent margin is the presence of multiple belts of Cu mineralisation related to porphyritic intrusions known as Porphyry Copper Deposits or PCDs. The coincidence of the ages of these metallogenic belt ages with those of four subparallel eastward-younging magmatic arcs suggests that PCD mineralisation and volcanic arc activity are genetically related (Richards, 2003, 2013; Camus, 2005; Maksaev et al., 2007; Sillitoe, 2010, 2012). The north Chilean PCDs form in restricted time intervals suggesting that special conditions are required for their formation that may include both tectonic (e.g. Skewes & Stern, 1994; Maksaev & Zentilli, 1999; Rosenbaum et al., 2005; Proffett, 2009; Bertrand et al., 2014) and magmatic processes (e.g. Cline & Bodnar, 1991; Hedenquist & Lowenstern, 1994; Halter et al., 2005; Richards & Kerrich, 2007; Wilkinson, 2013; Blundy et al., 2015) or a combination of both (e.g. Solomon, 1990; Kay et al., 1999; Kay & Mpodozis 2001; Mungall, 2002; Cooke et al., 2005; Richards, 2005, 2011a; Mpodozis & Cornejo, 2012; Sillitoe, 2010, 2012). Despite the clear general link between subduction-related magmatism and PCD formation, many workers have proposed that the conditions needed for PCD formation occur at separate times from active volcanism (e.g. Cloos, 2001; Cooke et al., 2005; Sillitoe, 2010).

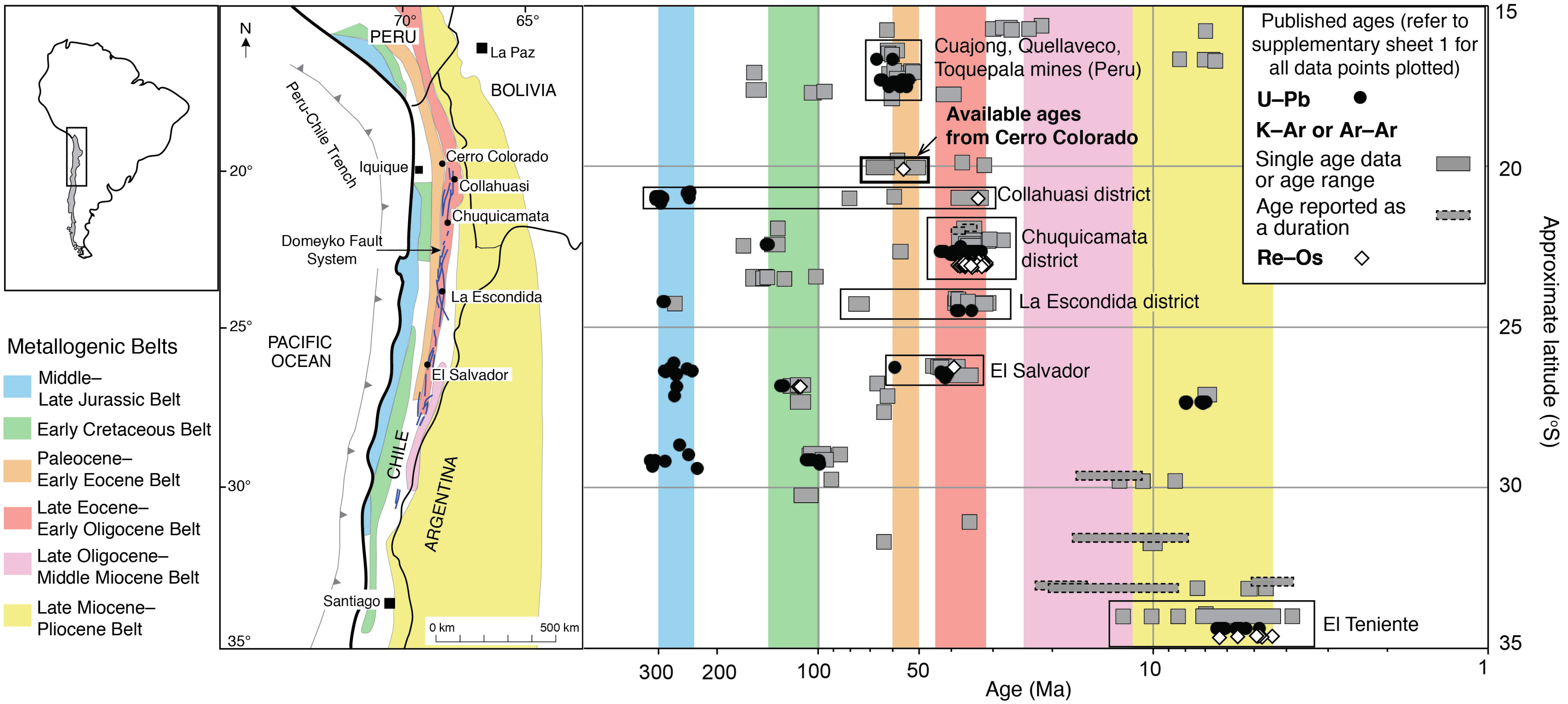

Fig. 2 Summary of published U–Pb, Ar–Ar and Re–Os ages in metallogenic provinces plotted against latitude in northern Chile (Map modified after Sillitoe, 2010 & 2012). Error bars are generally smaller than the size of the symbols and are not shown on the plot. All data points and corresponding references are provided in supplementary sheet 1.

Changes in stress state related to changes in plate motion vectors may also influence PCD formation. The kinematic framework for studying this aspect of the evolution of the Chilean convergent margin is provided by plate tectonic reconstructions in the South American and Pacific realm (Pardo-Casas & Molnar, 1987). A large increase in convergence rate occurs at around 49 Ma and is generally correlated with the onset of the main Incaic phase of crustal shortening (Coira et al., 1982; Pardo-Casas & Molnar, 1987; Charrier et al., 2007). It has also been proposed that the transition towards compressional crustal deformation may be related to an initiation phase of flat slab subduction (Isacks, 1988; James & Sacks, 1999; Haschke et al., 2002a; O'Driscoll et al., 2012). Obtaining reliable data for the ages of PCD-related intrusions is essential to test the feasibility of the connections between tectonic, magmatic and mineralisation events.

Geochronological studies of metallogenic provinces in northern Chile have been used to define six metallogenic belts: Late Paleozoic–Triassic (298–230 Ma), Early Cretaceous (132–97 Ma), Paleocene–Early Eocene (60–50 Ma), Late Eocene–Early Oligocene (43–31 Ma), Early Oligocene–Middle Miocene (23–12 Ma) and Late Miocene–Pliocene (12–4.3 Ma) (Sillitoe, 1974, 1988; Camus, 2005; Maksaev et al., 2007). Numerous studies have documented the geological, geochemical and geochronological characteristics of these PCDs (e.g., Clark et al., 1990, 1998; Cornejo et al., 1997; Maksaev et al., 2004, 2010; Sillitoe & Perelló, 2005; summary of Camus & Dilles, 2001). A summary of the published geochronological data for the Andean PCDs of northern Chile (Fig. 2 and supplementary sheet 1) is in good general agreement with the proposed division. However, there are also many intermediate ages and some of the belts are only defined on the basis of a few ages. At least part of the spread in ages may be due to the method used. Many of the ages that have been reported in porphyry deposit districts are based on the K–Ar decay system using K-bearing alteration minerals associated with ore formation. These ages generally reflect the timing of cooling and cannot be directly related to the timing of the porphyritic intrusions and associated mineralisation. In addition, there are potentially significant problems with extraneous Ar being introduced into the system due to initial trapping from magma and the action of hydrothermal fluids (e.g., Chiaradia et al., 2013). U–Pb dating of zircon from igneous rocks at the core of PCDs and Re–Os dating of molybdenite from the main ore bodies have been used by many workers to estimate the ages of igneous intrusion and metallogenesis, respectively. However, in northern Chile only a few Re–Os dates have been reported. In addition, U–Pb dating from the younger and better-preserved PCD belts of South America has only been reported in a limited number of academic publications, and most attention has been focused on supergiant PCDs (e.g., Richards et al., 1999; Ballard et al., 2001; Maksaev et al., 2004; Munizaga et al., 2008) (see also supplementary sheet 1).

To improve the understanding of the Cenozoic PCD formation in northern Chile, there is a great need to expand the data sets for U–Pb geochronology. This contribution focuses on the Cerro Colorado Mine (in Spanish: Compañía Minera Cerro Colorado or CMCC) site located 120 km to the northeast of Iquique (Fig. 3). This is the most northerly active PCD mine currently being exploited in Chile and is located at the northern end of the Domeyko Fault System, which hosts several important Eocene to Oligocene porphyry copper deposits (Fig. 2) (Cornejo et al., 1997; Camus, 2005; Charrier et al., 2007; Mpodozis & Cornejo, 2012).

To facilitate a geological interpretation of the U–Pb ages determined in this study, I first present field relationships preserved in cores from the mine site and combine these with geochemical analyses to document a relative sequence of geological events associated with mineralisation. I then present LA-ICP-MS and SHRIMP U–Pb zircon ages of the main intrusive bodies. These zircon ages provide i) better time constraints on the age of PCD formation, which can be compared to documented changes in plate motion vectors and regional volcanic activity, and ii) constraints on time scales for the magmatic activity that led to

PCD formation. The few available dates for igneous rock around the CMCC region are mainly based on Ar dating techniques (Fig. 2). Zircon U–Pb dating of the mine site has not previously been reported in peer-reviewed literature although some age data are given in mine reports.

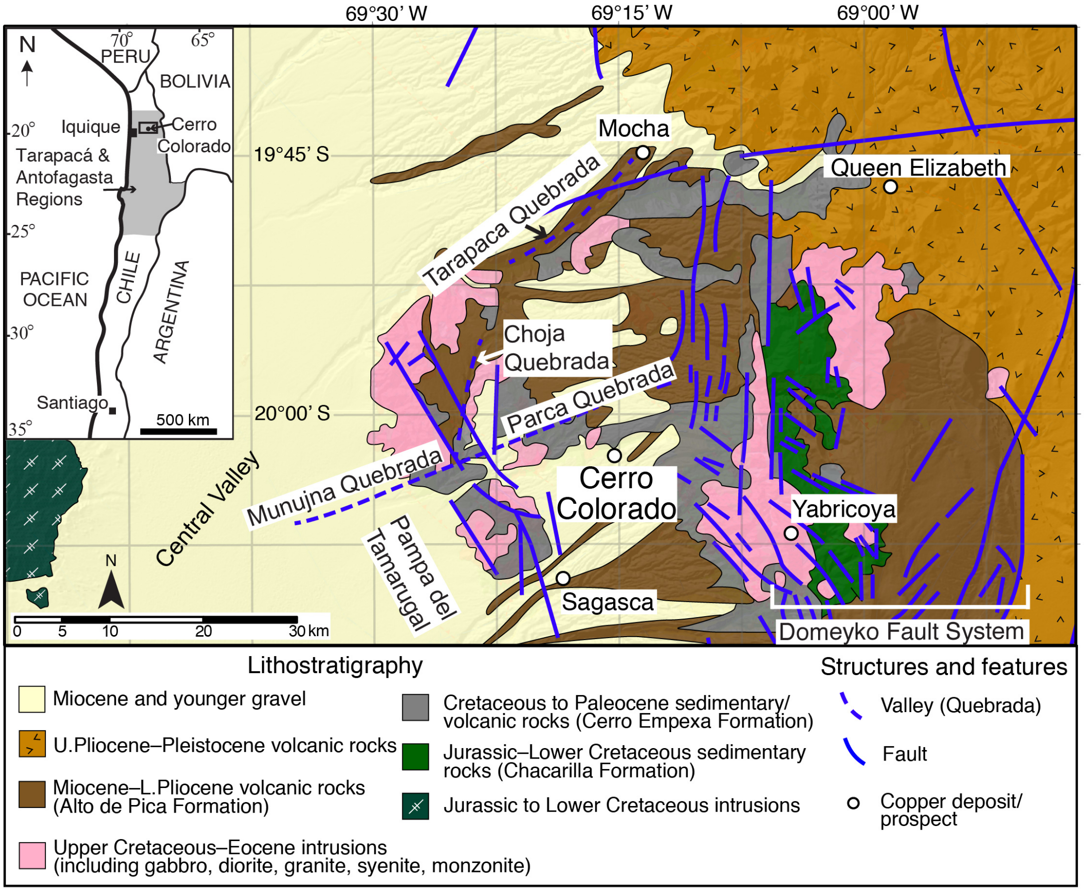

Fig. 3 Geologic map of the Cerro Colorado area (area shown in the rectangle in small map) showing major structures and lithostratigraphical units (after Bouzari & Clark, 2006).

2. Geological Background

2.1 Geological Overview of the Cerro Colorado Area

The Cerro Colorado porphyry copper mine is a BHP Billiton property located in the Tarapacá Region, northern Chile (Fig. 2). The mine site is located on the upper flank of the Pampa de Tamarugul, a blanket of tertiary sediments and lava flows (Mortimer et al., 1974), which slopes gradually from the Precordillera at 2600 m a.s.l. to the Central Valley (Fig. 3) at about 1000 m a.s.l.

The Cerro Empexa Formation (CEF) dominates the geology of the CMCC area and is the principal host for Cu mineralisation of this area. The CEF is a thick regionally developed volcanic succession composed of mainly andesitic volcanic and minor continental siliciclastic sedimentary rock units and is present in large parts of the Precordillera of the Tarapacá and Antofagasta Regions of northern Chile (Tomlinson et al., 2001; Bouzari & Clark, 2002, 2006; Charrier et al., 2007). Previous workers have divided the CEF into two subgroups: (1) an earlier subgroup composed mainly of andesitic lavas and breccias, lahars, a few local layers of ignimbrite, and some sedimentary rocks; and (2) a later subgroup composed of andesitic lava and breccia with more minor dacitic tuff (Tomlinson et al. 2001). Geochronological studies using U–Pb and K–Ar dating methods (Tomlinson et al., 2001) indicate the lower part of the CEF is latest Cretaceous (69–65 Ma), in agreement with earlier suggestions based on lithostratigraphy (Galli, 1968). A younger age for parts of the CEF is suggested by a proposed correlation between the CEF and voluminous andesitic and rhyolitic–dacitic volcanic rocks associated with the formation of calderas including the Hornitos Formation (Charrier et al. 2007), which is thought to be Paleocene to Eocene in age (Segerstrom, 1959; Muñoz, 1975; Lortie & Clark, 1987). However, the details of the geochronology remain poorly defined.

In general, the CEF unconformably overlies volcanogenic and marine sedimentary rocks of the Jurassic to Early Cretaceous Chacarilla Formation (Galli, 1968; Bouzari and Clark, 2006; Charrier et al., 2007). In northern Chile, the pre-CEF basement also locally consists of the Late Paleozoic to Triassic Choiyoi Granite-Rhyolite Province (Kay et al., 1989; Munizaga et al., 2008; Maksaev et al., 2014). This province can be correlated with the Permo–Triassic Mitu Pluton Group exposed to the north in Southern Peru (Carlier et al., 1982; Charrier et al., 2007; Maksaev et al., 2014).

Numerous small Late Cretaceous to Paleocene calc-alkaline to alkaline plutons and subvolcanic stocks were emplaced in the CEF (Agemar et al., 1999; Haschke et al., 2002b; Bouzari & Clark, 2002, 2006). Previous K–Ar and Ar–Ar dating yielded ages of 68–62 Ma for several intrusive bodies in the border area of CMCC, none of which is associated with mineralisation (Huete et. al., 1977; Maksaev, 1990; Agemar et al., 1999). Economically viable PCD mineralisation forms locally associated with intrusions, such as the porphyritic stocks associated with Cerro Colorado copper mineralisation (Bouzari & Clark, 2002, 2006). The whole sequence, consisting of the CEF and intrusions, is unconformably overlain by the Miocene Altos de Pica Formation—a thick sequence of ignimbrites and tuffs intercalated with two gravel units (Bouzari & Clark, 2002, 2006).

The dominant structural architecture in northern Chile—including the main faults and folds—has probably existed at least since Late Cretaceous (Mpodozis et al., 2005; Amilibia et al., 2008; Mpodozis & Cornejo, 2012), and the location of many PCDs seems to have been influenced by the presence of these structures. Several major faults are recognised in the area immediately surrounding the mine site. These are reflected in the development of deep gulleys or Quebradas, such as the 300 m deep ENE–WSW trending Parca-Quipisca Quebrada that joins the NE–SW trending Munujna Quebrada and the N–S trending Choja Quebrada (Fig. 3). These faults around the CMCC area and the overall NW–SE trending structures in the mine site belong to the regional Domeyko Fault Zone associated with mineralisation (Scheuber & Reutter, 1992; Cornejo et al., 1997; Mpodozis & Cornejo, 2012).

Previous geological studies of the mine site show it dominantly consists of the CEF, which overlies older granitic and metamorphic basement and is intruded by subvolcanic felsic units (Bouzari & Clark, 2002, 2006)(Fig. 4). Unpublished U–Pb zircon dating reported by the mine site (CMCC, 2014) gives an age for the CEF of 73.2 ± 0.3 Ma (unless otherwise specified, all errors for age dating are reported at the 2σ level or with 95% confidence level for means), agreeing with previously suggested Cretaceous ages. Similar zircon U–Pb dating of the granitic basement to the CEF yields an age of 317 ± 11 Ma consistent with the presence of late Paleozoic to Triassic granitic rocks underpinning the area rather than the Jurassic to Early Cretaceous Chacarilla sedimentary strata seen elsewhere.

The subvolcanic intrusions in the CMCC area are generally divided into two distinct types: a quartz porphyry and a biotite-quartz-plagioclase porphyry (Bouzari & Clark, 2006). Nomenclature developed for use by mine geologists refers to the former as PQZ and divides the latter into a porphyritic quartz monzonite (PTO 1) and a porphyritic tonalite (PTO 2). Here I use a similar terminology but more closely related to the lithological names: PTN for the porphyritic tonalite, PMN for the porphyritic monzonite and LQP for the leucocratic quartz porphyry. Table 1 lists the correlation between the nomenclature referred by the mine, Bouzari & Clark (2006) and this study. Compared to PMN, PTN shows a less distinct porphyritic texture with a relatively coarse groundmass, lacks alkali-feldspars and is strongly altered and mineralised. In contrast, PMN is only weakly altered and mineralised (Fig. 5 a, b). These observations imply that PTN was emplaced either before or during PCD mineralisation. The three different porphyry types are thought to be independent intrusive bodies. All rocks in CMCC are hydrothermally altered to varying degrees. The most widely recognised alteration grades are potassic, sericite-chlorite-clay (SCC) and phyllic.

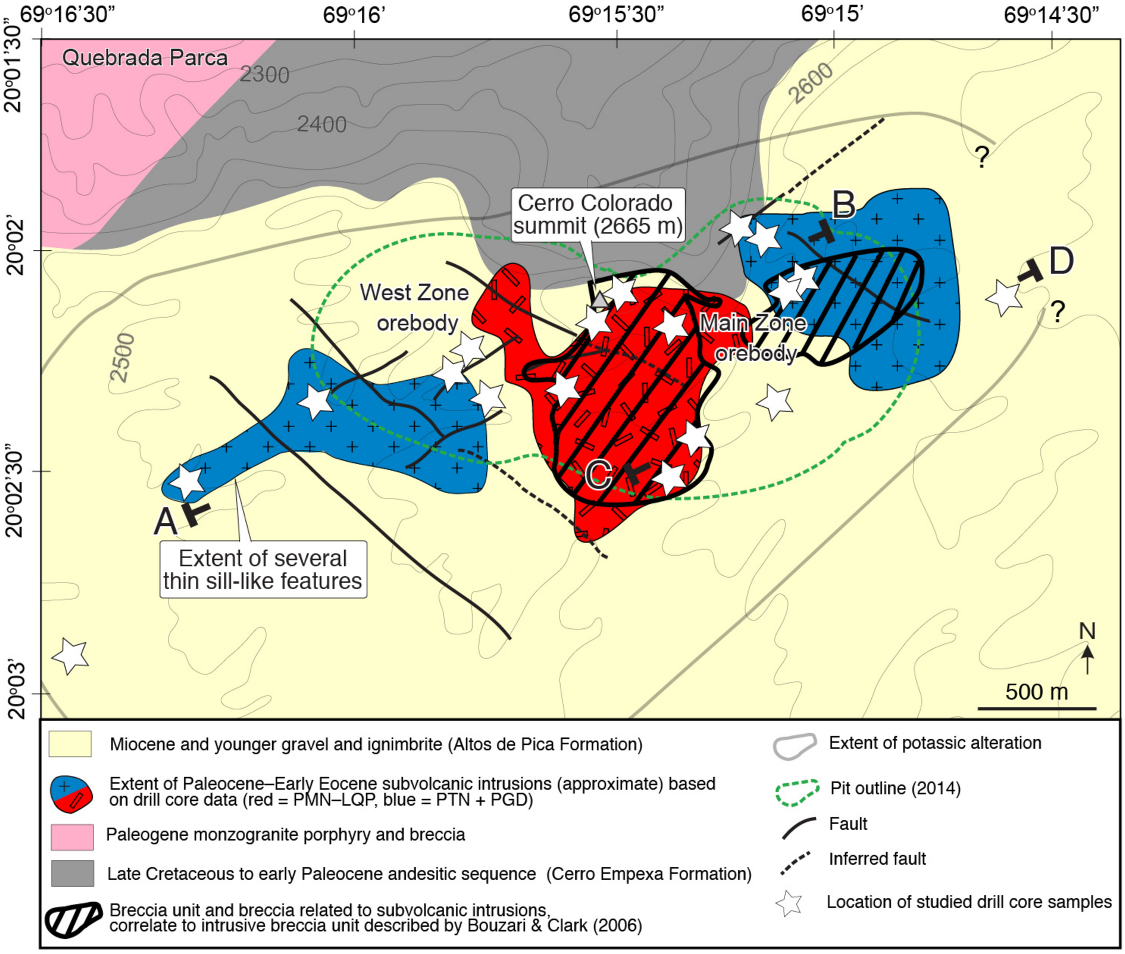

Fig. 4 Local geological map of Cerro Colorado Mine pit area with locations of the inspected drill cores (modified after Bouzari & Clark, 2006).

The ages of the subvolcanic intrusions, PTN, PMN and LQP are not well known. K–Ar dating of plutonic rocks located outside CMCC mine yields latest Cretaceous to Paleogene ages of 68–62 Ma (Huete et al., 1977; Maksaev, 1990; Agemar et al., 1999). In contrast, unpublished U–Pb age dating by the mine yields ages for PMN and PTN of 54.4 ± 0.1 Ma and 52.8 ± 0.1 Ma, respectively (CMCC, 2014). For LQP, the same mine report gives ages of 51.7 ± 0.2 Ma and as old as 63.5 ± 0.1 Ma (CMCC, 2014). Mine geologists have treated the 63.5 Ma Paleocene age of the LQP as anomalous, and suggest PMN was the first intrusion followed by PTN and finally LQP. A geological history culminating in a phase of intrusion around 52 Ma is compatible with the slightly younger 52–50 Ma age range reported for Ar–Ar dating of minerals developed during hydrothermal alteration (Bouzari & Clark 2002, 2006; Cotton, 2003, CMCC, 2014).

Re–Os dating of molybdenite from brecciated LQP suggests metal mineralisation at 55.5 ± 0.3 Ma (Cotton, 2003) and 53.8 ± 0.3 Ma (CMCC, 2014). These ages are significantly older than the Ar–Ar ages of alteration and difficult to reconcile with the known U–Pb ages given for the porphyritic intrusions in the mine site: these intrusions should predate mineralisation but in fact appear to be mostly younger. The Re–Os mineralisation ages are compatible with the older magmatic activity recognised in plutonic rocks in the vicinity of CMCC mine.

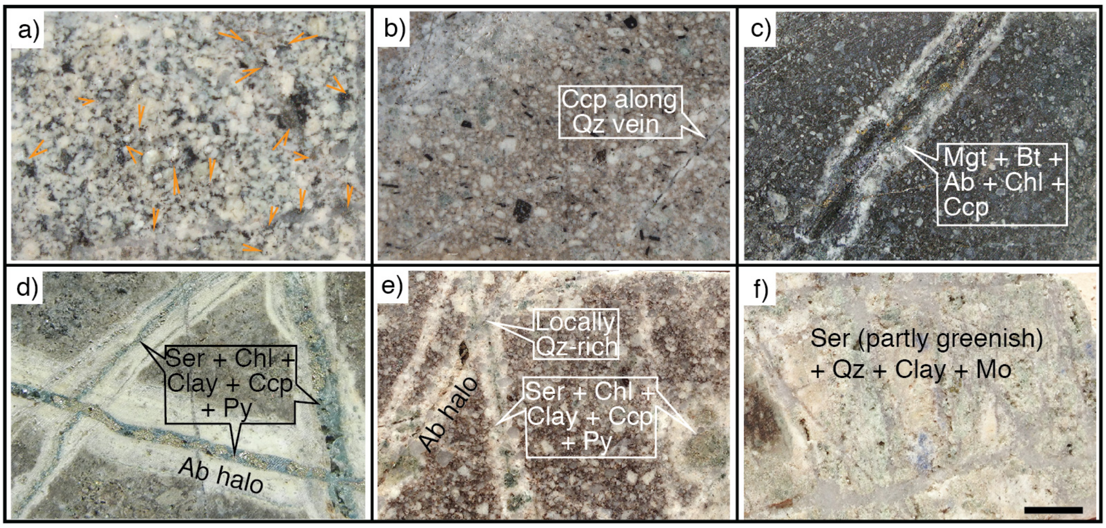

Fig. 5 Various styles of alteration and mineralisation (scale bar is 1cm, all photos are at the same scale). a)–b) Comparison of mineralisation intensity in the groundmass from a less stockwork veins affected domain of PTN and PMN. **a)** PTN, the orange arrows point at disseminated sulphides; **b)** PMN weakly mineralised, sulphide concentrate along veins. c)–f) Representative veins with typical mineral assemblages of each of the hydrothermal alteration zones. **c)** A typical biotite, albite, magnetite vein that represents potassic alteration and bears chalcopyrite. **d)** Sericite, chlorite and clay veins with thick albite halos. This type of vein is typical in the SCC alteration zone, and generally hosts high-grade chalcopyrite. **e)** An example of quartz-rich SCC veins cutting PMN. Albite halos are also observed around the veins. **f)** Phyllic alteration veins are typically quartz veins associated with sericite, with or without clay. In this example, some sericite has a greenish colour, the veins are molybdenite-bearing but chalcopyrite is not observed.

In summary, the limited available age data in and around the CMCC mine area suggest igneous intrusion, mineralisation and hydrothermal alteration occurred in the time interval ca. 65–50 Ma, but the data show considerable scatter and lack internal consistency.

2.2 CMCC Lithology and Petrology

A total of 17 cores ranging in length from about 300 m to 1000 m each, were studied at the mine site. Most of the recovered core consists of the CEF and the subvolcanic intrusive bodies. Locally the underlying basement can also be observed. The cores were grouped into a NW set of 13 cores that provide a good coverage along an SW–NE transect through the mine, including the main centres of Cu and Mo mineralisation (Fig. 6a), and a second set of four cores that provide information on a subsidiary section parallel to the first but located approximately 500 m to the SE (Fig. 6b). In these studies of the cores, I recorded both different lithologies—with particular emphasis on the intrusive units—and the type of veining and alteration. I used these observations as the basis for selecting samples for geochronological studies. The details of each logged cores including lithology, alteration grade, percentage of vein types and sample locations, are attached in session 2.4.

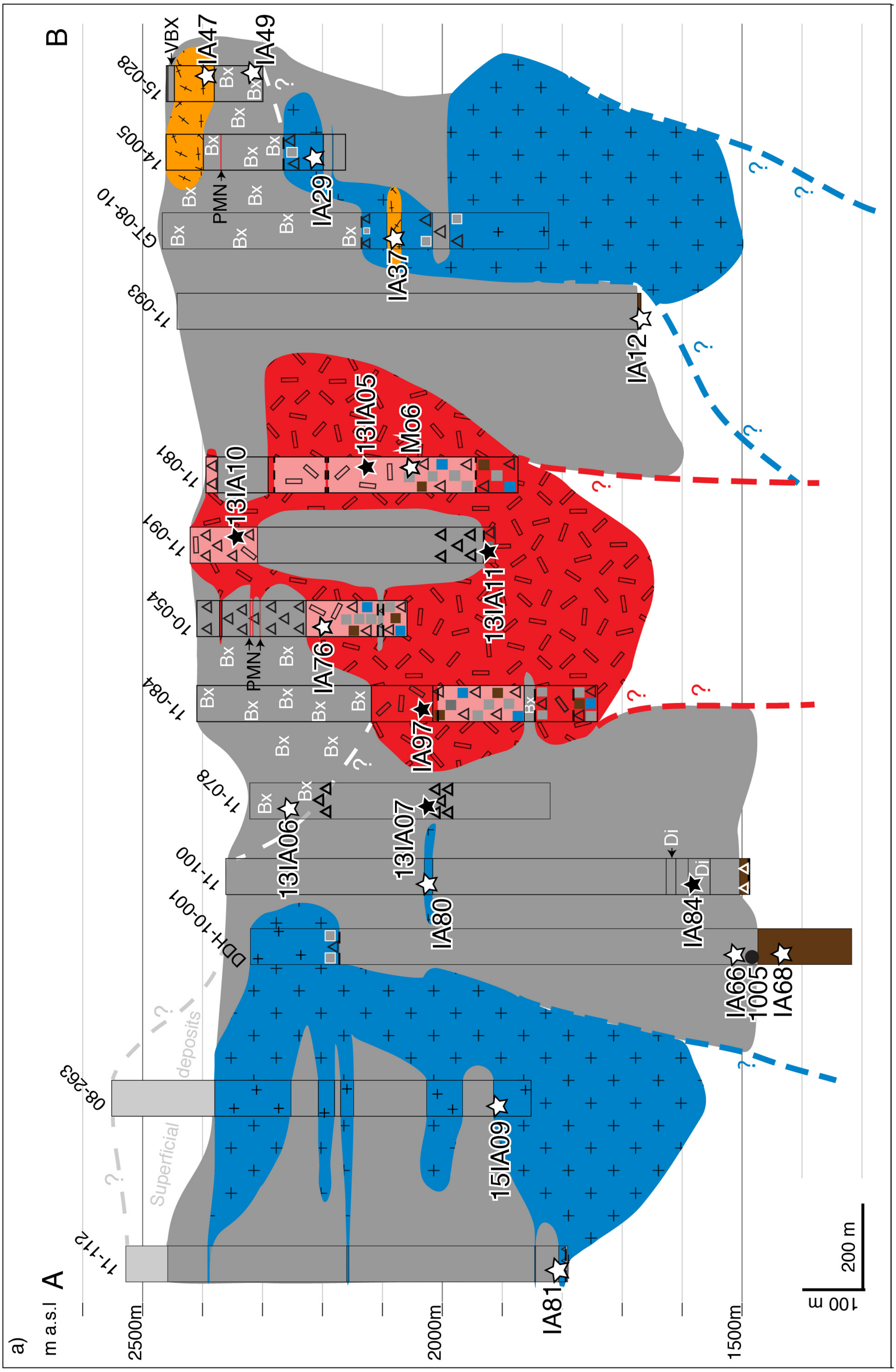
a)
m a.s.l
2500m
2000m
1500m
A
B
11-112
08-263
DDH-10-001
11-100
11-078
11-084
10-054
11-091
11-081
11-093
GT-08-10
14-005
15-028
IA81
15IA09
Superficial deposits
?
IA66
1005
IA68
IA80
IA84
Di
13IA06
13IA07
IA97
IA76
PMN
13IA11
13IA10
13IA05
Mo6
IA12
IA37
IA29
IA47
IA49
VBX
Bx
100 m
200 m

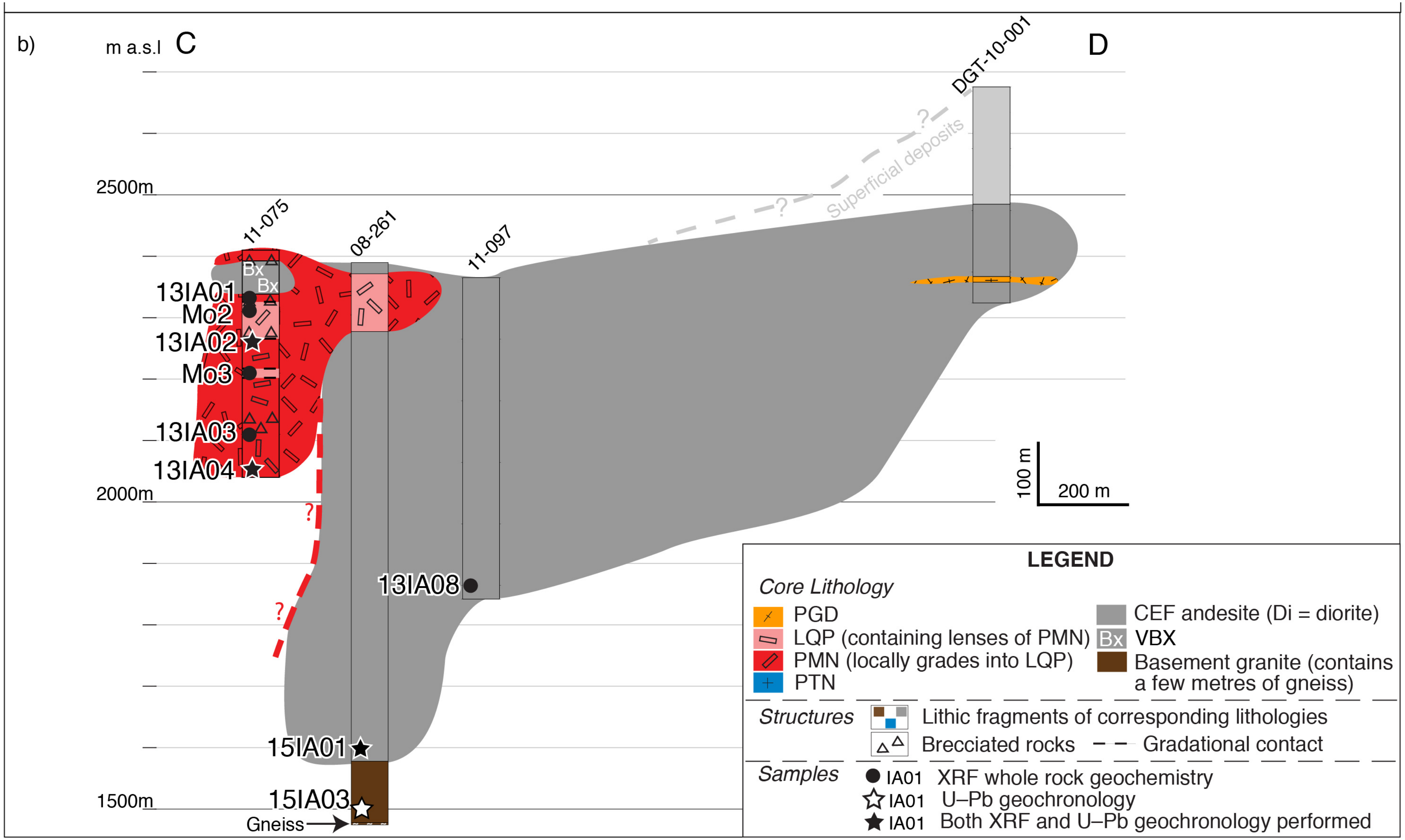

Fig. 6 Cross-sections derived from projecting information from core logs onto two subparallel roughly E–W sections across the mine pit. **a)** North section (A–B in Fig. 4), **b)** South section (C–D in Fig. 4).

2.2.1 Rock units and petrographical descriptions

1) Basement units

Four of the deepest cores expose coarse-grained basement granite (Fig. 7b) at around 800 m below surface. In one core, 2 m of mafic gneiss (Fig. 7a) is also exposed beneath the granite. The granite is composed of 1–2 cm equigranular K-feldspar, plagioclase and quartz with rare biotite. Graphic texture is locally developed. Some samples show alteration of feldspars into epidote and illite. Tourmaline is observed in zones that are highly epidotized, suggesting the tourmaline is of hydrothermal origin. The basement granite hosts small amounts of disseminated chalcopyrite (ca. 1 %) and molybdenite, and sulphide-bearing quartz veins cut the granite.

2) Dominant host rock–The Cerro Empexa Formation (CEF)

The CEF has a maximum observed thickness of 800 m and consists of andesitic to dacitic volcanic rocks. The dominant rock type is porphyritic andesite (Fig. 7c), comprising phenocrysts of 1–3 mm plagioclase and quartz set in a dark fine-grained matrix. The proportion of phenocrysts varies greatly, comprising 5–25 volume %, with intervals where the andesite is largely aphanitic. Lithic fragments up to 5 cm are locally present. Basement granite clasts are common in the basal 20 m of the formation with a clear unconformable relationship with the granite.

The CEF is pervasively affected by a wide range of hydrothermal alteration grades and is the major host rock for the copper mineralisation. Point counting of 3 samples from the homogeneous domain of this andesite shows presence of ca. 1.5–3.5 volume % chalcopyrite (see Table 2), locally highly rich in stockwork veins. In addition to a wide range of alteration-associated minerals in the matrix, the CEF is cut by stockwork veins that are closely associated with chalcopyrite and molybdenite mineralisation.

These aspects and their relationships to alteration grade are discussed in more detail in the section "Alteration and veining".

3) Breccia unit (VBX)

A distinct breccia unit (Fig. 7d) is identified in the upper parts of many of the cores and is mainly exposed in the central and eastern parts of the mine site (Fig. 5). This unit has a thickness of up to 300 m, it contains on average 15 volume %, locally up to 40 volume % of 5–30 mm sub-angular to sub-rounded clasts with irregular shapes, including altered volcanic lithic fragments together with quartz grains and minor identifiable CEF clasts (Fig. 8 a & b) enclosed in a fine-grained light-coloured, locally porous matrix consisting of quartz, muscovite, sericite, clay minerals with minor calcite. The VBX shows pervasive phyllic (sericitic) alteration. Disseminated chalcopyrite, bornite, chalcocite (together these make up ca. 1–1.5 volume %) and pyrite are present in the matrix and fine-grained molybdenite is locally abundant. This unit corresponds to the bodies described by Bouzari and Clark (2006) as intrusive breccias and proposed to be associated with the porphyritic intrusive units.

The VBX contains clasts of CEF and cross-cuts these volcanic units (Bouzari & Clark, 2006) showing that it is relatively young. VBX matrix is composed of mainly 100–400 µm quartz, muscovite and even finer clay-altered material, a porous texture and a high proportion of sub-rounded clasts, indicating fluidisation and an intense abrasive action. These features point to the presence of a large amount of gas occurring as a fluid phase during brecciation. However, there is also limited evidence for crystallisation of new magmatic material (see section on dating). These features suggest that VBX is best described as magmatic-hydrothermal breccia (e.g., Sillitoe 1985), which is normally considered an intrusive type. However, the large amount of gas involved suggests volcanic activity at relatively shallow levels. In the following I refer to this breccia as volcanic, but leave open the question of whether or not the brecciation associated with volatile release reached the surface.

4) Intrusive units

i) PTN (Porphyritic tonalite)

PTN (Fig. 7e) is exposed in the eastern and western region of CMCC and shows thin sill features (Fig. 6a) intruding the CEF. The porphyritic unit contains plagioclase and biotite phenocrysts (1–4 mm) making up to 40–50 volume % of the rock set in a quartz, plagioclase and biotite groundmass (300–500 μm) and can be classified as a tonalite. The matrix of PTN is commonly silicified and sericitised, giving the rock a general greyish white colour. Pseudomorphs of biotite and chlorite after hornblende are commonly observed. Biotite is commonly replaced by chlorite with rutile needles. Plagioclase crystals generally show multiple lamellae twining, and partial replacement by sericite, phengite and illite is common. Zircon is a common accessory mineral.

Disseminated chalcopyrite is observed in the matrix (on average 2–2.5 volume % in altered domain, locally rich in stockwork veins) but molybdenite is scarce. PTN is commonly cut by SCC or phyllic stockwork veins, which contain chalcopyrite associated with chlorite and sericite alteration (discussed in more detail below in alteration and veining). The intensity of hydrothermal alteration is greater in PTN than in the other porphyritic units. A localised 14–30 m wide brecciation zone is observed between the tonalite and CEF in the eastern zone.

ii) PMN (Porphyritic quartz monzonite)

PMN (Fig. 7f) is exposed in the central region of CMCC. It is characterised by a porphyritic texture with 1–5 mm phenocrysts of euhedral to subhedral K-feldspar, plagioclase and biotite making up to ca. 30 volume % of the rock. Similar-sized but rarer quartz phenocrysts are also present. These phenocrysts are uniformly distributed in an aphanitic

(< 20 μm) matrix and can be classified as a porphyritic quartz monzonite. In hand specimen, the matrix of PMN shows a range of colours from creamy grey to light brown, suggesting the rock has undergone various degrees of alteration. Sericitisation is pervasive and replacement of plagioclase and K-feldspar by sericite, phengite and illite is common. Similar to PMN, biotite pseudomorphs after hornblende are locally present (Fig. 9c). Rutile needles are also commonly observed where chlorite replaces biotite (Fig. 9d). Lamellae twins and oscillatory zones are observed in plagioclase, and simple twinning is observed in orthoclase. Zircon is a common accessory mineral.

Although less pervasive than in the CEF, PMN is also cut by quartz-rich SCC and phyllic veins, which commonly contain chalcopyrite (± molybdenite) and are surrounded by albite-rich halos (Fig. 5e). Sparse chalcopyrite is also found disseminated in the matrix, in average ca. 0.5–1.5 volume % chalcopyrite.

Brecciation features can be observed throughout most of the PMN body. Angular clasts, mainly composed of PMN and LQP (leucocratic quartz porphyry) units, and also locally xenoliths of PTN, CEF and basement units, are cemented by weathered clay or quartz fill (Fig. 8 c–f). Chalcopyrite and molybdenite mineralisation is commonly found along the clast boundaries and in the breccia matrix. Lesser amounts are disseminated in the clasts, and as part of quartz veins that cut the PMN-associated breccia.

iii) LQP (Leucocratic Quartz Porphyry)

LQP (Fig. 7g) is exposed in close association with PMN. It is characterized by having more than 5% volume of rounded to irregular, partially embayed quartz "eyes" (1–5 mm diameter) and 10–30 volume % of similar-sized plagioclase phenocrysts and aggregates comprised of K-rich phyllosilicates and clay, which are interpreted as altered products of K-feldspar. These phenocrysts are distributed within a leucocratic aphanitic groundmass and the rock can be classified as a leucocratic quartz porphyry. Both the phenocrysts and matrix are highly altered into quartz, sericite, phengite, illite and other clay minerals. This unit essentially lacks biotite, but biotite and also chlorite are locally observed.

Some of the quartz eyes in strongly altered domains have unusual lath shapes. The presence of clay mineral aggregates in the cores of some these grains and presence of grains with outlines similar to K-feldspar with Carlsbad twining suggests that at least some of the quartz eyes are secondary and pseudomorphing pre-existing K-feldspar grains as a result of hydrothermal alteration (Fig. 9 f–i). Similar processes have been reported in other studies of hydrothermal alteration systems (e.g., Kerr et al. 1950; Brauhart et al. 2001).

LQP commonly contains disseminated pyrite in the matrix. Copper is mainly present in the form of chalcocite and covellite. These minerals probably represent secondary sulphides after chalcopyrite (e.g., Sillitoe & Clark, 1969; Buckley & Woods, 1984), and make up < 1 volume %. Both molybdenite and chalcopyrite are rare as matrix minerals, but commonly occur in quartz veins that cut LQP. Brecciation features similar to PMN are also observed in LQP (Fig. 8 c–d).

iv) PGD (Porphyritic granodiorite)

In a confined region in the NE part of the mine site, some porphyritic granodioritic rocks intrude PTN and VBX. These younger rocks show considerable variations in texture and abundance of quartz in groundmass, which may be an effect of alteration, but since the occurrence is small and localised, here I treat them as one unit. PGD (Fig. 7h) is characterised by ca. 20–30 volume % of 1–3 mm phenocrysts of mainly plagioclase and biotite, with minor quartz in a dark fine-grained to aphanitic, locally chloritised or phyllic altered groundmass. The plagioclase is partly replaced by sericite, but to a much lesser extent than the other intrusive units. Previously the mine site geologists suggested this unit was essentially post mineralisation and intruded at a late stage. However, the occurrences of rare chalcopyrite-bearing SCC and phyllic veins cutting PGD were observed in the core samples. The matrix of PGD also contains disseminated chalcopyrite suggesting this rock type was intruded before Cu mineralisation was complete.

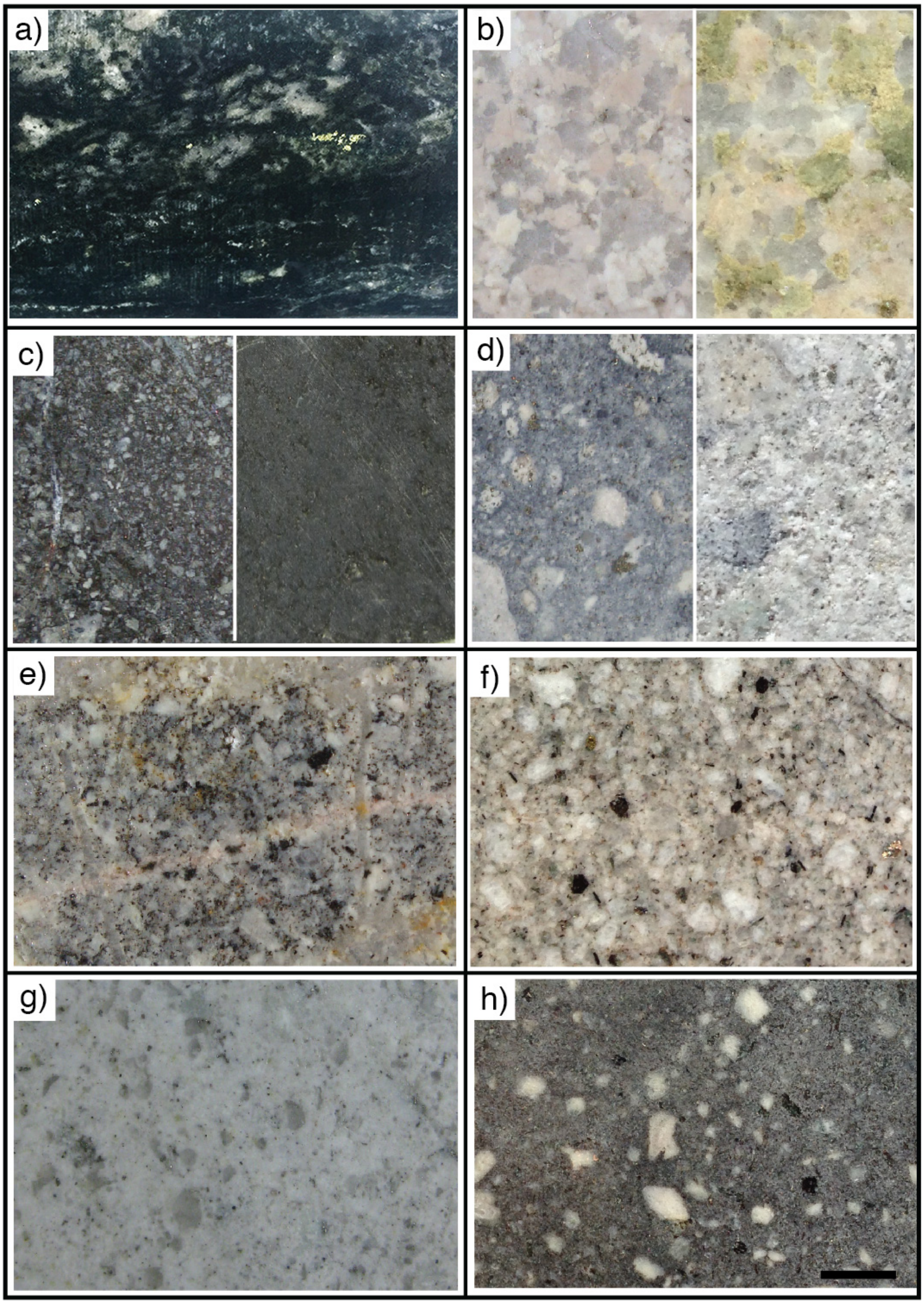

(Refer to next page for figure captions)

Fig. 7 Different rock types exposed in drill cores (scale bar is 1cm, all photos are at the same scale). **a)** Mafic gneiss underlying granite. **b)** Basement granite, locally epidotized (left: fresh; right: epidotized). **c)** Cerro Empexa Formation (CEF) andesite with common plagioclase phenocrysts and lithic fragments. Aphanitic layers are also present, in contrast to the porphyritic CEF (left: with phenocrysts and clasts; right: aphanitic). **d)** Volcanic breccia unit (VBX). Locally abundant disseminated molybdenite gives the rock a bluish grey tint, in contrast to the light-coloured matrix VBX (left: disseminated molybdenite in matrix; right: mainly matrix clayish). **e)** Porphyritic tonalite (PTN) containing biotite and plagioclase phenocrysts in a matrix of grain size 300–500 µm. **(f)** Porphyritic quartz monzonite (PMN) containing biotite, two feldspars and quartz phenocrysts in an aphanitic matrix. **g)** Leucocratic quartz porphyry (LQP) containing phenocrysts of both plagioclase and K-feldspar and significant amount of subrounded quartz "eyes" in a matrix of quartz and feldspars. **h)** Porphyritic granodiorite (PGD), with two feldspar and biotite phenocrysts in an intermediate matrix.

(Fig. 8 on next page)

Fig. 8 Features observed in hand specimens of VBX, breccia unit related to PMN–LQP emplacement, and the PMN–LQP stock itself. Size of bar is 1 cm.

(a, b) VBX consists of fine-grained textured clasts suggesting a volcanic origin. The clasts are commonly highly altered and silicified and the matrix is locally rich in disseminated molybdenite (a).

(c, d) Brecciated LQP within the subvolcanic stock. All fragments are derived from the PMN–LQP unit. The fine-grained, clayish matrix in between the fragments is commonly mineralised.

(e, f) Xenoliths (PTN and CEF) incorporated in PMN–LQP. Enclaves of PTN (e) seen in breccia formed related to LQP emplacement suggest PMN–LQP postdate PTN.

(g–i) A series of observations suggesting PMN and LQP represent different alteration grades of the same rock type.

g) Sample of LQP. Rare biotite occurs in this sample. Chlorite is formed as an alteration product. These observations suggest the leucocratic LQP has a more mafic precursor.

h) Examples of PMN–LQP transitions with 1–2 cm boundary zones, showing the contacts are gradual.

i) Different degrees of alteration in PMN–LQP. The altered parts of the rock have turned into a quartz eye-bearing leucocratic rock, but do not show a clear contact with PMN.

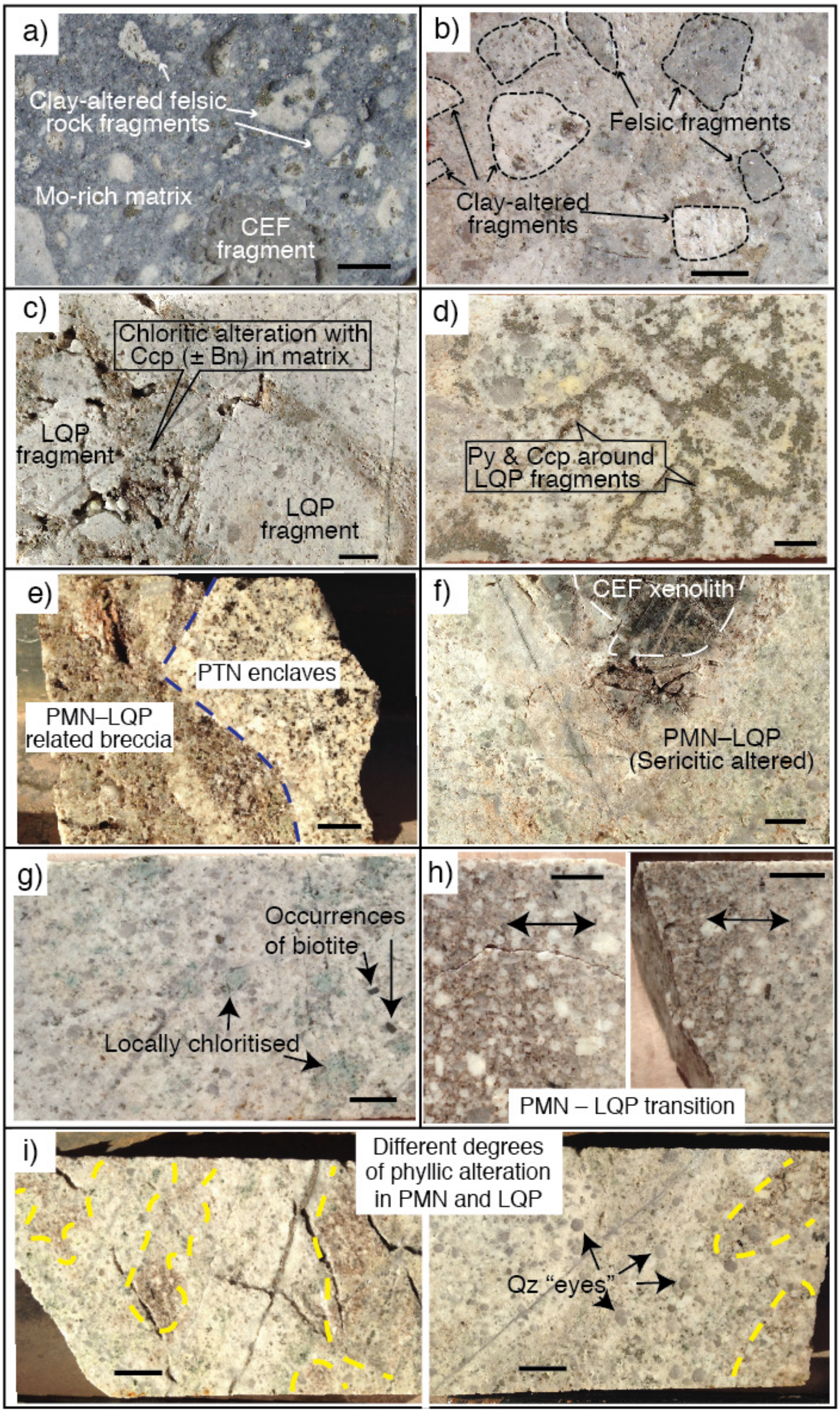
a)
Clay-altered felsic rock fragments
Mo-rich matrix
CEF fragment
b)
Felsic fragments
Clay-altered fragments
c)
Chloritic alteration with Ccp (± Bn) in matrix
LQP fragment
LQP fragment
d)
Py & Ccp around LQP fragments
e)
PTN enclaves
PMN–LQP related breccia
f)
CEF xenolith
PMN–LQP (Sericitic altered)
g)
Occurrences of biotite
Locally chloritised
h)
PMN – LQP transition
i)
Different degrees of phyllic alteration in PMN and LQP
Qz "eyes"

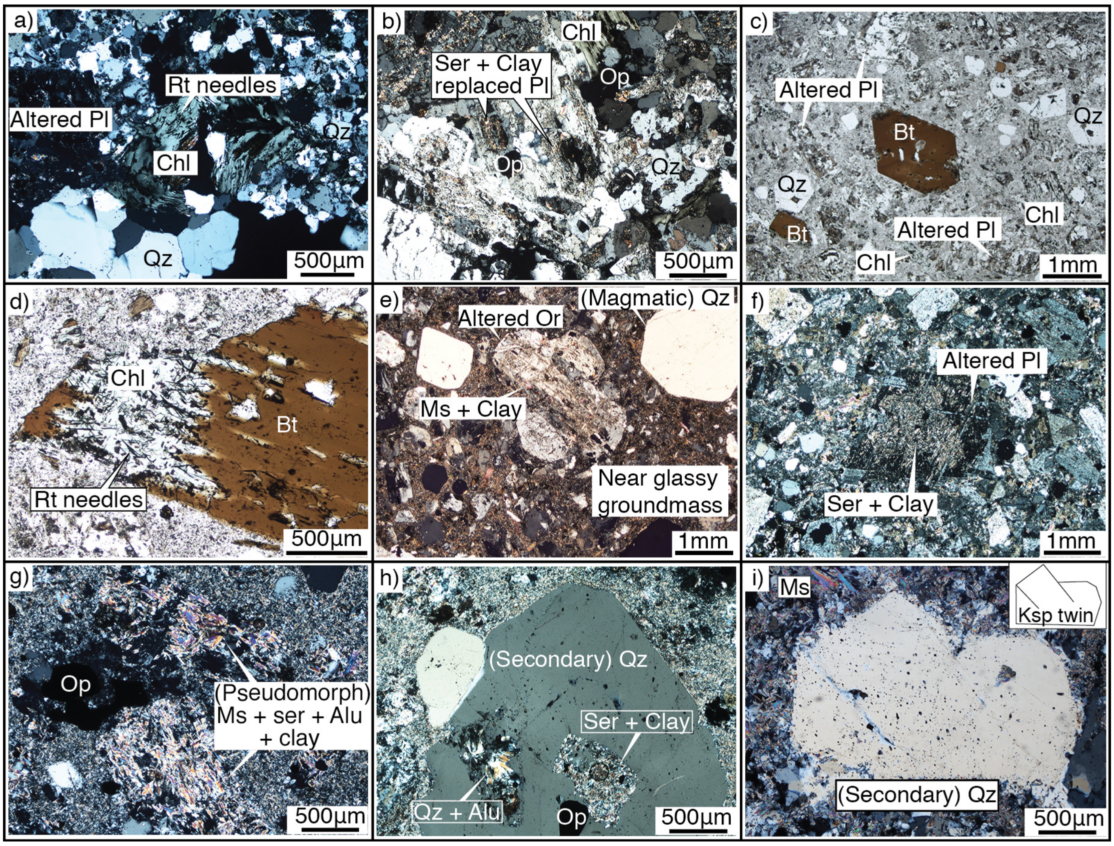

Fig. 9. Photomicrographs of examples of hydrothermal alterations in PTN, PMN and LQP (c and d are taken under open nicol; others are crossed nicols).

a) Rutile needles coexisting with chlorite replacing biotite in PTN.

b) Plagioclase altered into a mixture of sericite and clay in PTN.

c) Pseudomorph of biotite after hornblende in PMN.

d) Chlorite partially replacing biotite and coexisting with rutile needles in PMN.

e) Quartz and altered feldspar phenocrysts sitting in an ultrafine-grained matrix in PMN. Carlsbad twinning is clearly observed in one orthoclase crystal.

f)– i) Examples of LQP showing different levels of feldspar alteration and subsequent replacement by quartz, forming secondary quartz “eyes” in LQP.

f) Feldspar alteration to form sericite and clay minerals such as illite and smectite.

g) Feldspar completely replaced by sericite, phengite and clay minerals.

h) Incomplete replacement of illite and clay mineral pseudomorphs by quartz.

i) Good candidate for a quartz grain completely pseudomorphing a lath-shaped feldspar with an outline resembling Carlsbad twinning. The straight sides of the quartz grain make an apparent angle of 145°, which corresponds closely to the expected angle of ~147.5° between the (100) and the inverse twin face (001) of orthoclase (e.g., Lewis, 1899)

2.2.2 Field observations and relative age relationships

In the field studies, I paid particular attention to contact areas between the different lithologies. LQP and PTN are generally distributed in distinct parts of the mine. Although no direct intrusive contacts were observed between them, enclaves that closely resemble PTN are commonly observed included in the LQP unit (Fig. 8e) suggesting LQP is younger. In contrast, although LQP and PMN occur in similar parts of the mine site, similar enclave relationships were not observed. In addition, all observed contacts between LQP and PMN show gradual transitions (Fig. 8h & i). This could be explained as the result of assimilation by the later intrusion or that the two units are in fact different aspects of the same intrusion. No contacts were observed between PMN and PTN, either as enclaves or larger units. Therefore, the relative ages of PTN and PMN, and hence also PMN and LQP, remain elusive. Sharp contacts can be observed between the PGD and PTN, and the former displays a chilled margin, clearly indicating the PGD is younger than PTN. However, no direct crosscutting relationships were observed between the PGD and either PMN or LQP. Further information concerning the relative ages of the intrusions comes from geochemistry and geochronology.

2.3 CMCC alteration and veining

Hypogene alteration zones are distinctive features associated with porphyry copper deposits. Alteration mineral assemblages that are commonly documented in most porphyry copper deposits are potassic alteration, phyllic (sericitic) alteration and propylitic alteration (Meyer & Hemley, 1967; Lowell & Guilbert, 1970; Rose & Burt, 1979). The alteration mineral assemblages in argillic zones show greater variation (Cooke et al., 1998). Here, I adopt the scheme proposed by Sillitoe (2010), and the alteration zones have been divided into the following types in order of decreasing temperature: potassic, sericite-chlorite-clay (SCC), phyllic (or sericitic) and advanced argillic alteration (AAA). Propylitic alteration is not recognised at the CMCC (Bouzari & Clark, 2006). All of the inspected holes are drilled within the inferred subsurface extent of potassic alteration (Fig. 4).

The typical mineral assemblage for each alteration zone can be represented by the types of corresponding stockwork veins associated with early- to main-stage mineralisation. Crosscutting of different types of hydrothermal veins in the same location is common and this complicates the definition of a unique alteration grade. Here, I define the alteration grades of the drill core rocks based on a combination of the dominant hydrothermal alteration mineralogy of the host rocks together with the stockwork vein types. Stockwork vein alteration commonly overprints pre-existing hydrothermal alteration in the host rocks or cuts earlier sets of veins, thus the two indicators of alteration grade are not necessarily consistent. In cases where the vein overprinting is dominant and pervasive such that the original alteration grade is less distinct, the overprinting grade is recorded. In cases where the stockwork veins are less intense and the original alteration grade is still dominant, this grade is recorded. Combining the results of logging drill core from the present study with information provided by the mine geologists, two alteration profiles were constructed along the same cross sections used to display the lithologies (Fig. 10a & b). The main features of the different alteration zones are summarized below.

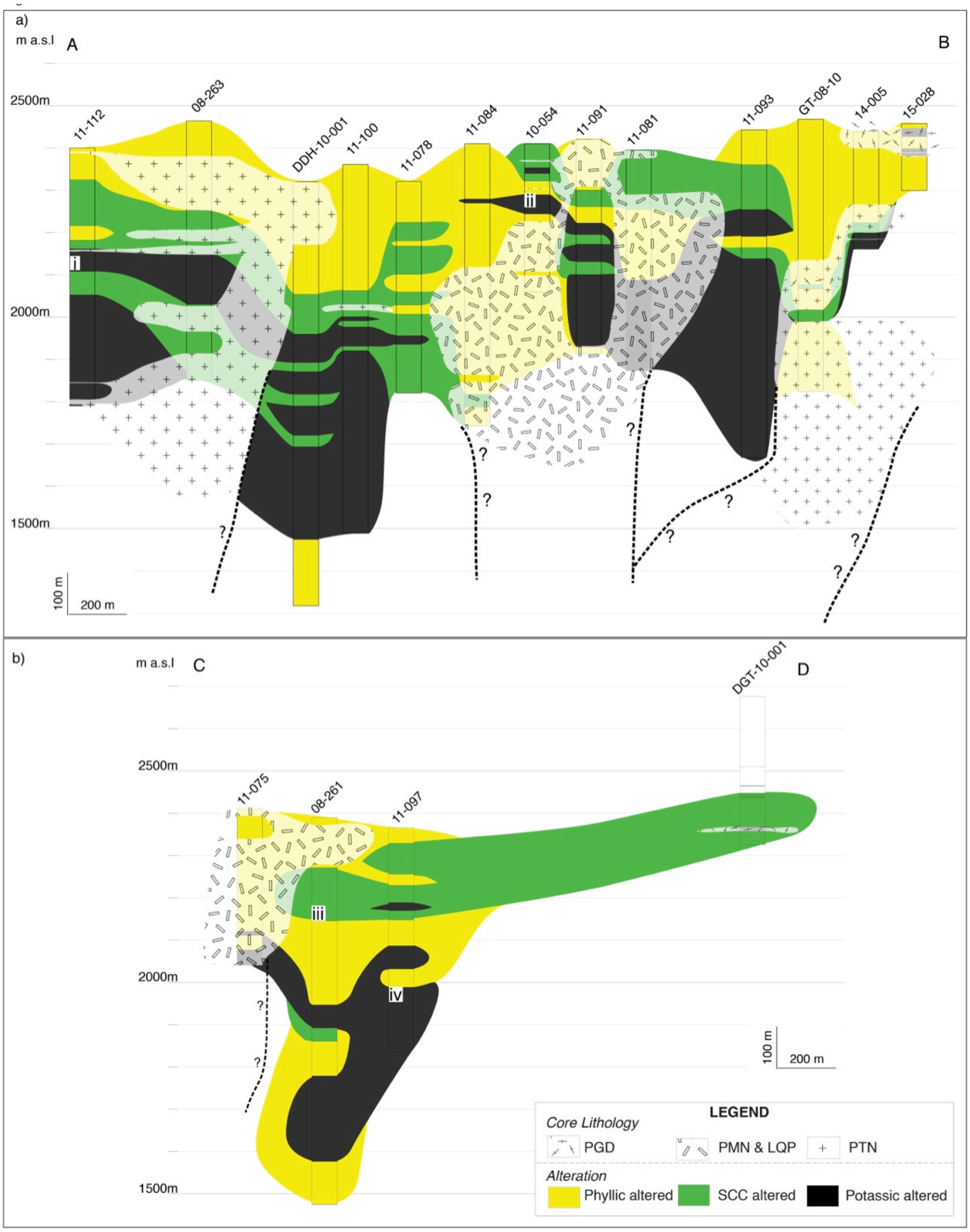

Fig. 10 Distribution of alteration zones shown on the two lithological cross-sections through the mine site. For locations of the cross-sections see Fig. 6. a) North section. b) South section. Refer to Fig. 10c for the explanation of the roman numerals (i)–(iv).

2.3.1 Alteration zones

1) Potassic zone

The potassic alteration zone is recognised by the appearance of hydrothermal biotite, albite, magnetite, with or without chlorite and quartz. The associated veins in this zone are mainly biotite and albite veins (Fig. 5c). Locally there are also magnetite-rich veins some of which also contain chalcopyrite. Potassic alteration is associated with high-temperature fluid and in general it is thought that this zone forms deep in the PCD in areas adjacent to the intrusive stock (e.g. Gustafson & Hunt, 1975; Frank & Vaccaro, 2012). In CMCC, potassic alteration zones do occur most commonly close to intrusive bodies, but there are also significant areas of potassic alteration at high levels (up to 150 m below the present surface). The inflow of high-temperature K-rich fluid to high levels which locally crosscuts earlier lower grade alteration suggesting there are at least two discrete hydrothermal events.

2) Sericite-Chlorite-Clay (SCC) alteration

SCC alteration imparts a greenish colour to the rock due to the pervasive development of chlorite and greenish sericite. Together with clay minerals such as illite and smectite, these minerals replace both mafic minerals and feldspars. The SCC veins are commonly associated with milky albite halos (Fig. 5d). At depths of about 300–500 m in the cores, the SCC zone can commonly be observed overprinting the potassic zone. At higher levels SCC alteration also occurs intermingling with phyllic to argillic alteration. This is especially clear in the central region of the mine site where SCC alteration overprints phyllic alteration up to current mine surface. The distribution of the SCC zones is particularly important because this is the main host domain for the hypogene copper mineralisation. Chalcopyrite and pyrite are formed in veins as well as being disseminated in the matrix, where they are intergrown with chlorite, sericite and clay. Molybdenite is uncommon in the SCC zone, but when present, it is developed within veins.

3) Phyllic (Sericitic) alteration (sericite-quartz with or without clay)

The phyllic alteration zone is characterized by the replacement of feldspar and mafic minerals by sericite and quartz. This alteration gives a light grey to creamy colour to the rock. In the CEF andesite, chlorite is locally abundant. This zone overprints the higher temperature zones and forms pervasively at the higher levels (from the present surface to an average depth of about 300 m) of the CMCC. The related stockwork veins are mainly quartz veins associated with both sericite and clay minerals (Fig. 5f), which could, therefore, be defined as argillic alteration. The quartz veins commonly bear pyrite, and lesser amounts of chalcopyrite. Disseminated pyrite and chalcopyrite also occur in the matrix of the host rocks. At the upper level (above 200 m depth) of the deposit, chalcocite and covellite are commonly found, which are likely formed as secondary sulphides after chalcopyrite (e.g. Sillitoe & Clark, 1969; Buckley & Woods, 1984). Molybdenite is locally abundant and is strongly associated with quartz veins. The volcanic breccia forming the top unit of CEF is dominantly phyllic altered, with sericite, phengite, clay minerals and calcite as the main alteration minerals in the matrix. Locally where the clay minerals have been washed out, this clastic unit develops high porosity. The whole unit is commonly silicified, and rich in disseminated molybdenite.

4) Advanced argillic alteration (AAA)

Bouzari and Clark (2006) describe the presence of an AAA subfacies in the CMCC but also note that this is masked by supergene alteration. Most of the drill cores inspected were drilled from below or the bottom level of the supergene zone in the currently operating mine. Thus, the AAA zone has not been recorded in this study.

2.3.2 Features observed from the alteration profile

The distribution of the different alteration zones shows a good general correlation with the distribution of the intrusive bodies: there is a general increase in grade of alteration from shallow levels to deep structural levels close to the intrusions. However, clearly distinct stages of SCC and potassic alteration zones also occur at relatively high levels in the alteration profile and higher temperature hydrothermal alteration veins locally cutting lower temperature veins have been observed (Fig. 10c), compatible with the idea that this shallow hydrothermal alteration profile is caused by multiple fluid events.

Retrograde alteration zones are recognised within the PMN and LQP units where early-stage higher-temperature alteration zones are overprinted by later-stage alteration zones (e.g. phyllic alteration cutting into SCC alteration in hole 11-091 and into K alteration in hole 11-081). Such down-cutting features are described as telescoping features (Sillitoe, 1994) and are commonly formed due to the contraction of hydrothermal systems during cooling (Pohl, 2001), or due to a change in the fluid flow pattern, which can be caused by rapid exhumation, or a sector (or caldera) collapse of a related volcano (Sillitoe, 1994).

2.4 Details of drill core logging

The detailed information of the 17 studied drill cores (Figs. 11–27) are compiled in the following log sheets. Each sheet displays the downhole lithology of a single core, alongside with the alteration grade and if available, the average proportion of different types of veins in the rocks. The information is a compilation of the information provided by CMCC combined with my own observations. Locations of samples collected are shown on the corresponding cores, and analyses that have been carried out in this study are indicated. These log sheets aim to document the extent of my present study and to organize the available information to in a manner suitable for potential future research.

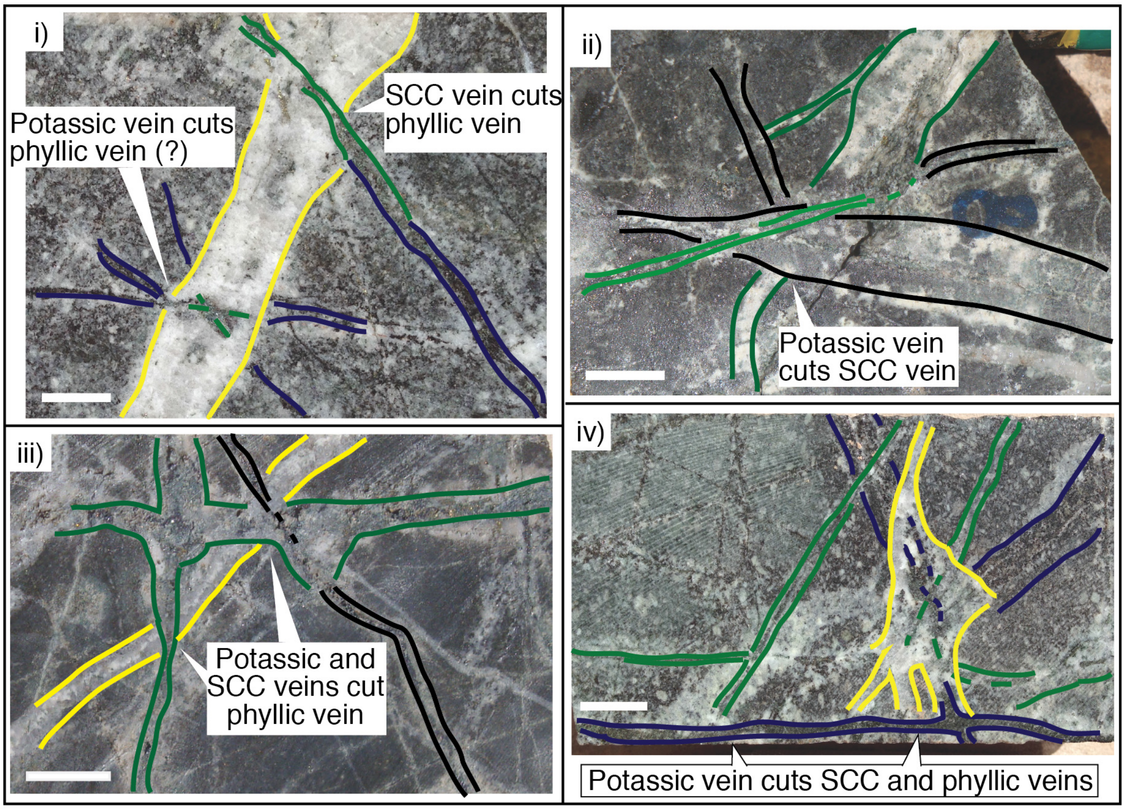

Fig. 10 c) Four examples of reversed sequence of cross-cutting relationships, where high-temperature hydrothermal veins cut lower-temperature veins. i) – iv) Examples observed at the locations marked with the same letters in the drill core sections on the alteration profiles Fig. 10a and 10b.

Fig. 11 Log for 08-261

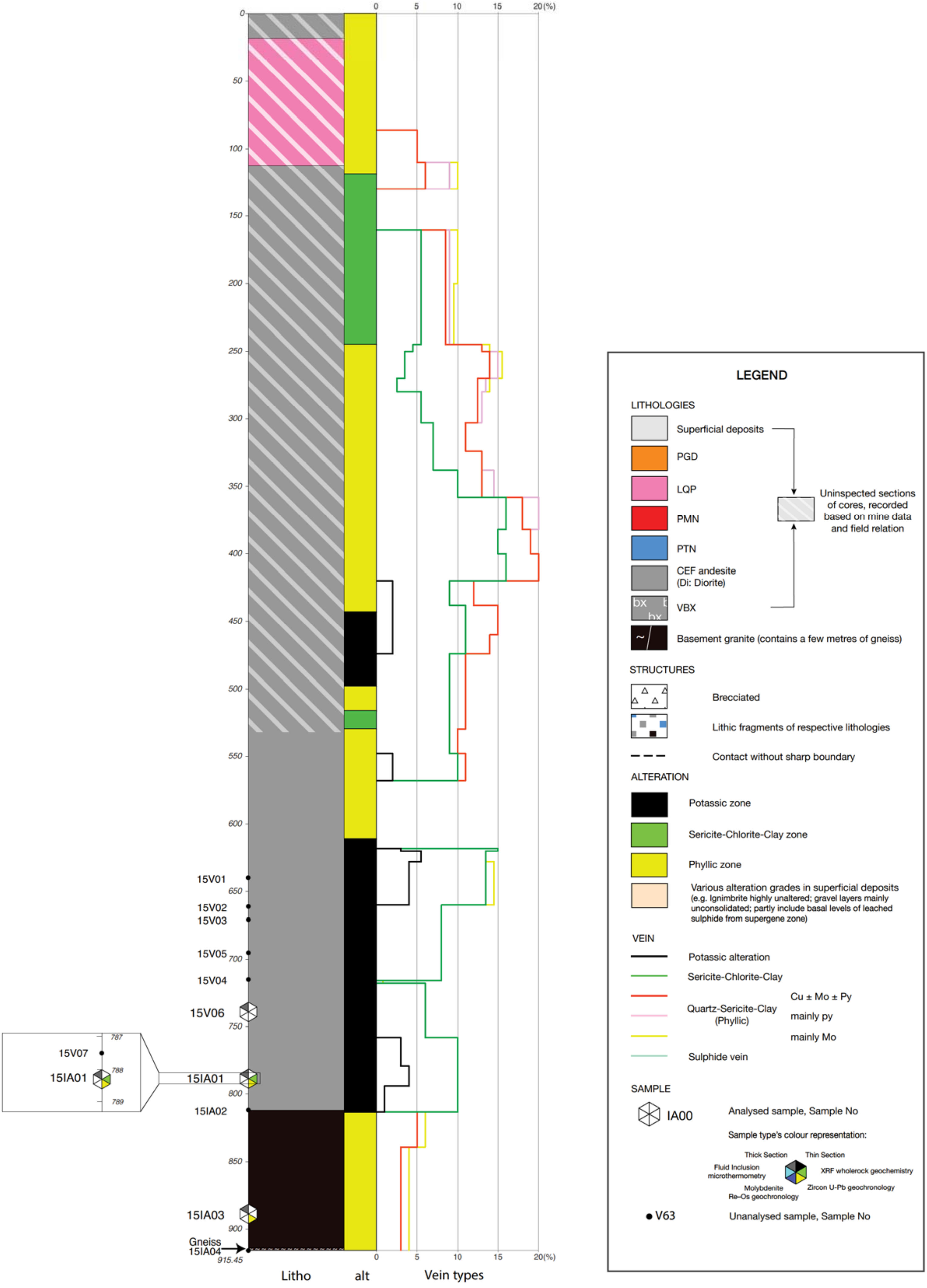

Fig. 12 Log for 08-263

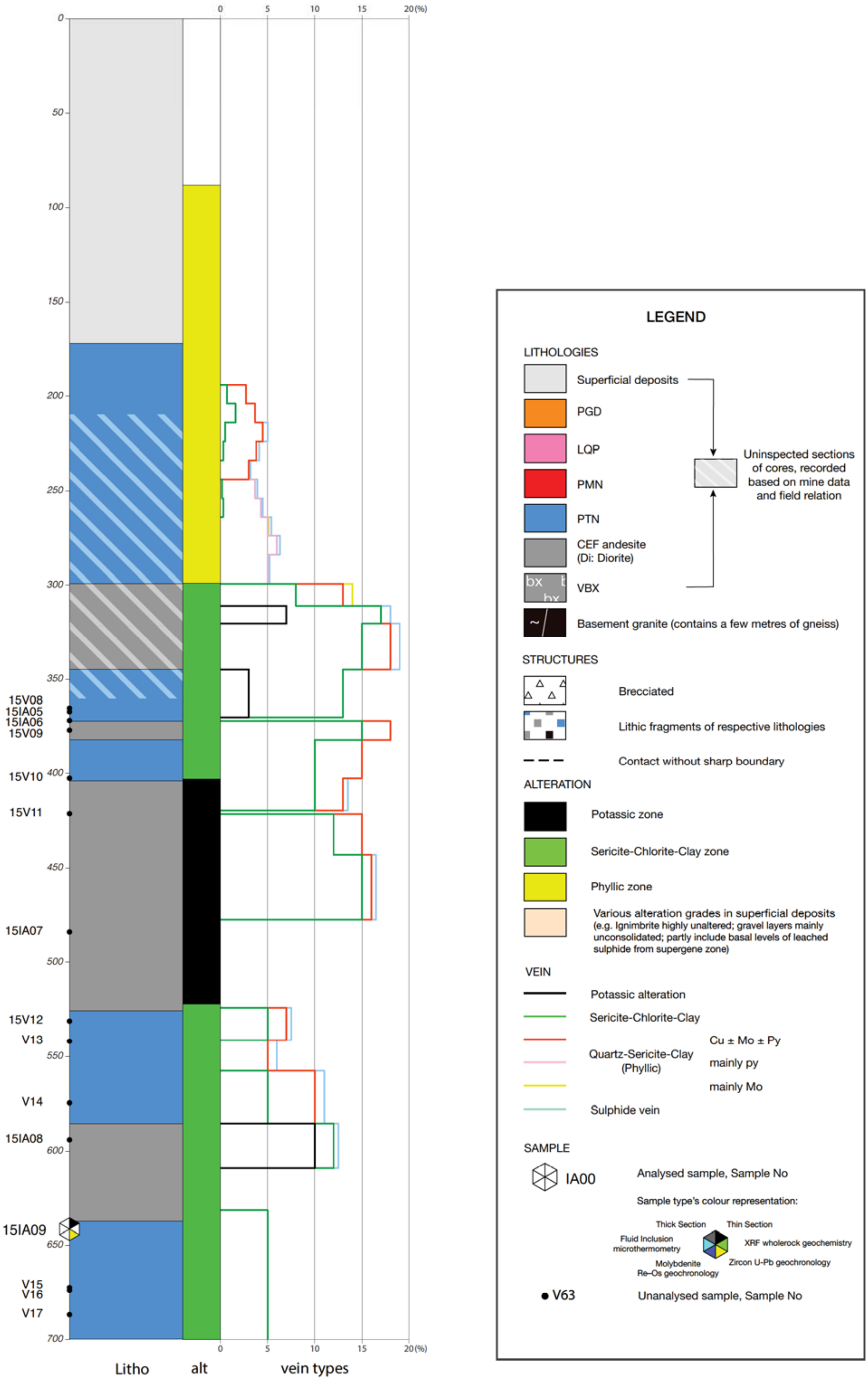

Fig. 13 Log for GT-08-10

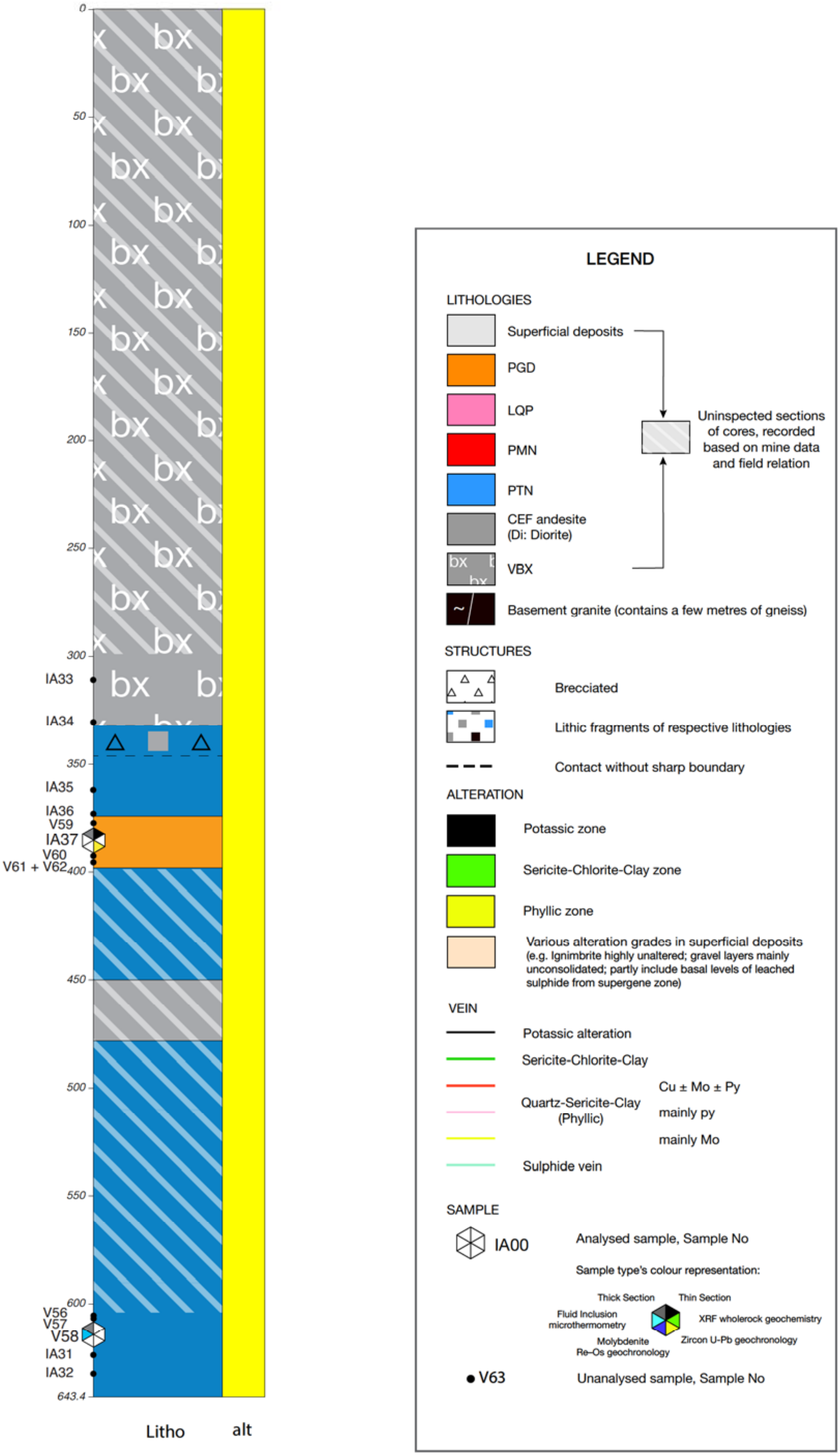

Fig. 14 Log for 10-054

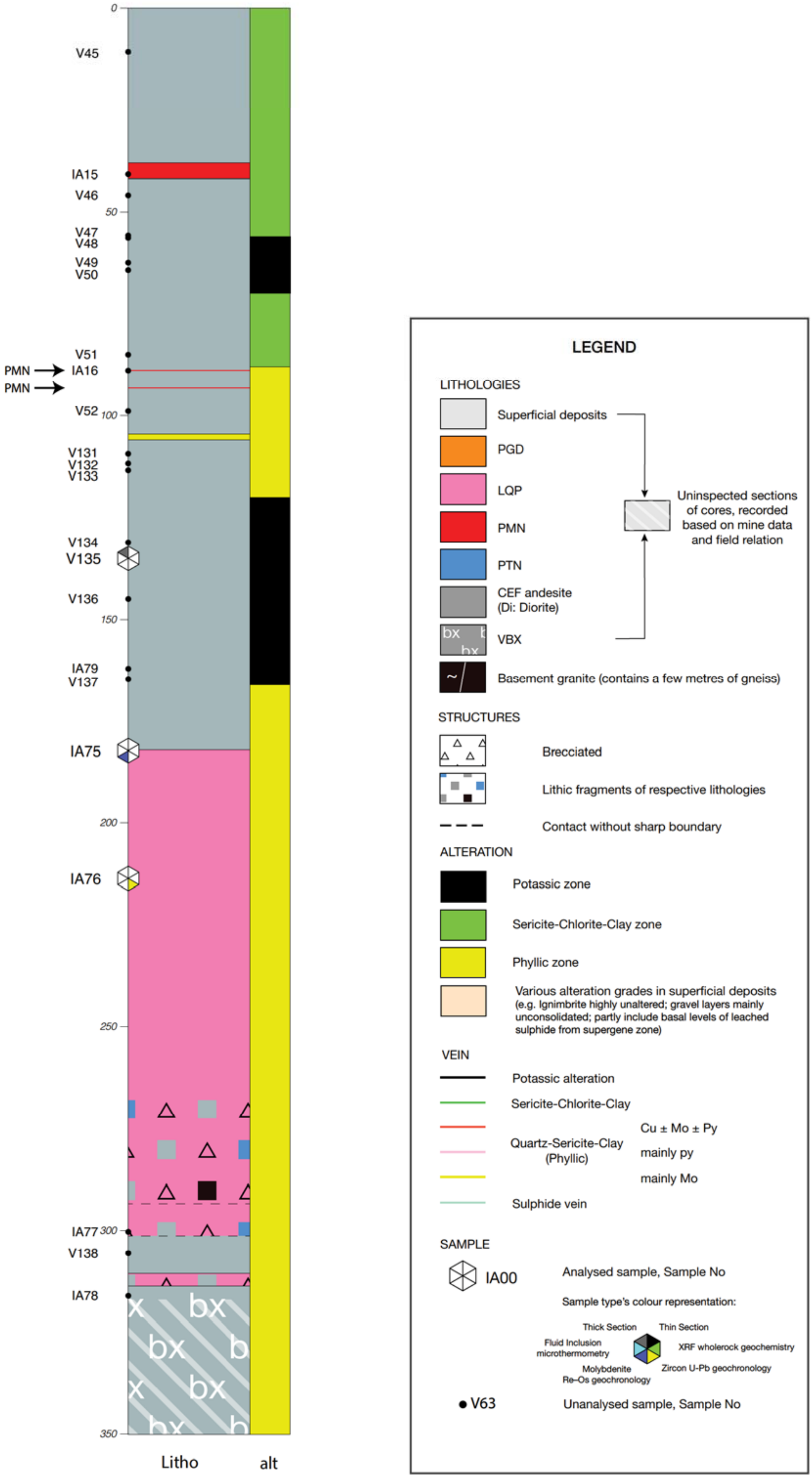

Fig. 15 Log for DDH-10-001

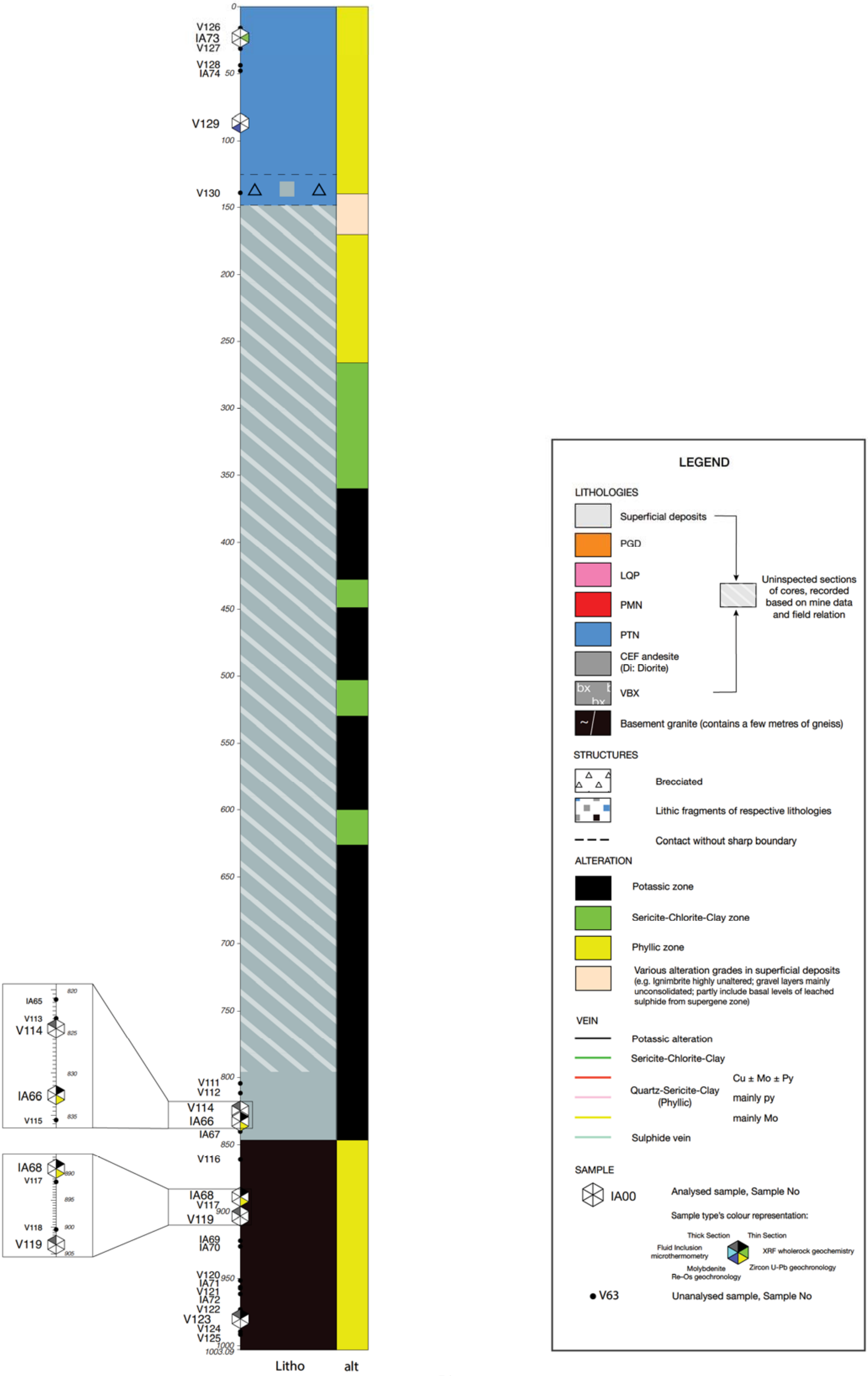

Fig. 16 Log for DGT-10-001

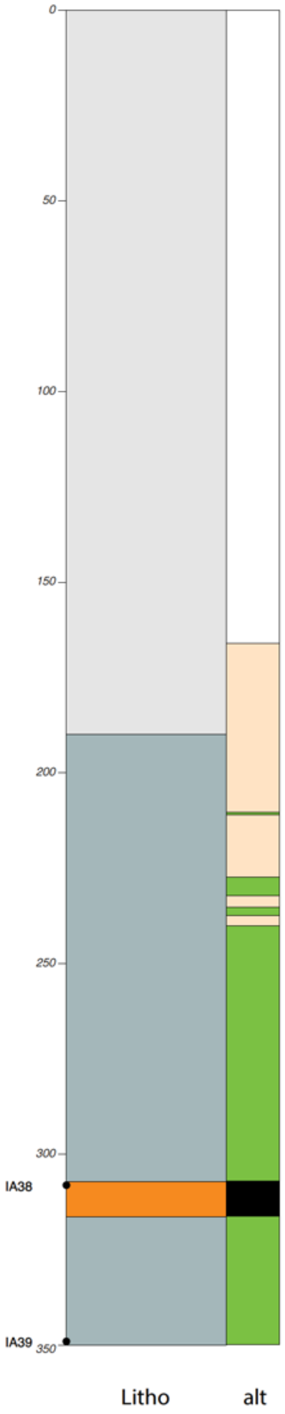

LEGEND

LITHOLOGIES

- ⬜ Superficial deposits
- 🟧 PGD
- 🟪 LQP
- 🟥 PMN
- 🟦 PTN
- ⬛ CEF andesite (Di: Diorite)
- ▨ VBX
- ⬛ Basement granite (contains a few metres of gneiss)

▨ Uninspected sections of cores, recorded based on mine data and field relation

STRUCTURES

- △ Brecciated
- ▪ Lithic fragments of respective lithologies
- – – – Contact without sharp boundary

ALTERATION

- ⬛ Potassic zone
- 🟩 Sericite-Chlorite-Clay zone
- 🟨 Phyllic zone
- 🟧 Various alteration grades in superficial deposits (e.g. Ignimbrite highly unaltered; gravel layers mainly unconsolidated; partly include basal levels of leached sulphide from supergene zone)

VEIN

- — Potassic alteration
- — Sericite-Chlorite-Clay
- — Quartz-Sericite-Clay (Phyllic) — Cu ± Mo ± Py
- — Quartz-Sericite-Clay (Phyllic) — mainly py
- — Quartz-Sericite-Clay (Phyllic) — mainly Mo
- — Sulphide vein

SAMPLE

IA00 Analysed sample, Sample No

Sample type's colour representation:

Thick Section
Thin Section
Fluid Inclusion microthermometry
XRF wholerock geochemistry
Molybdenite Re-Os geochronology
Zircon U-Pb geochronology

● V63 Unanalysed sample, Sample No

Fig. 17 Log for 11-075

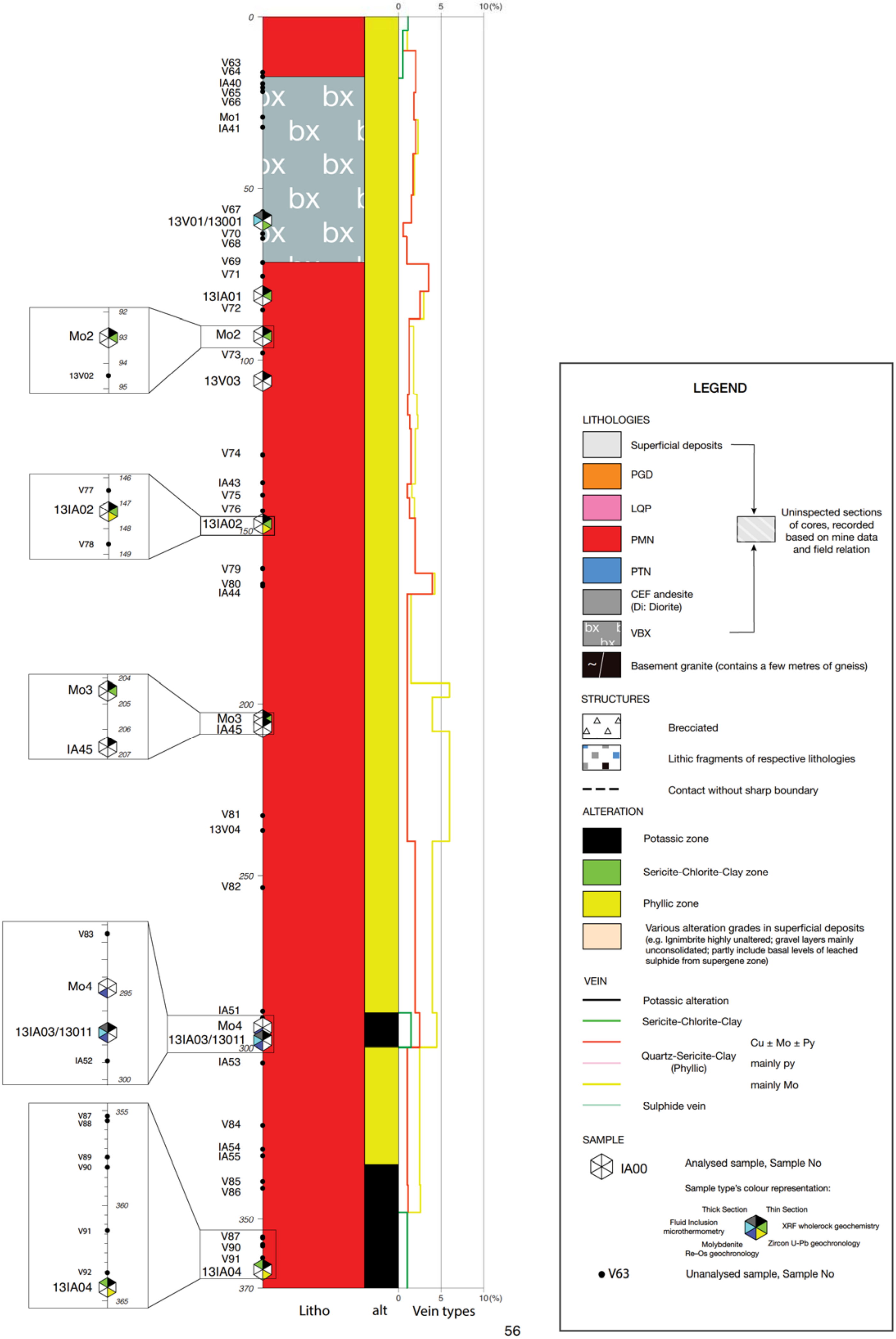

Fig. 18 Log for 11-078

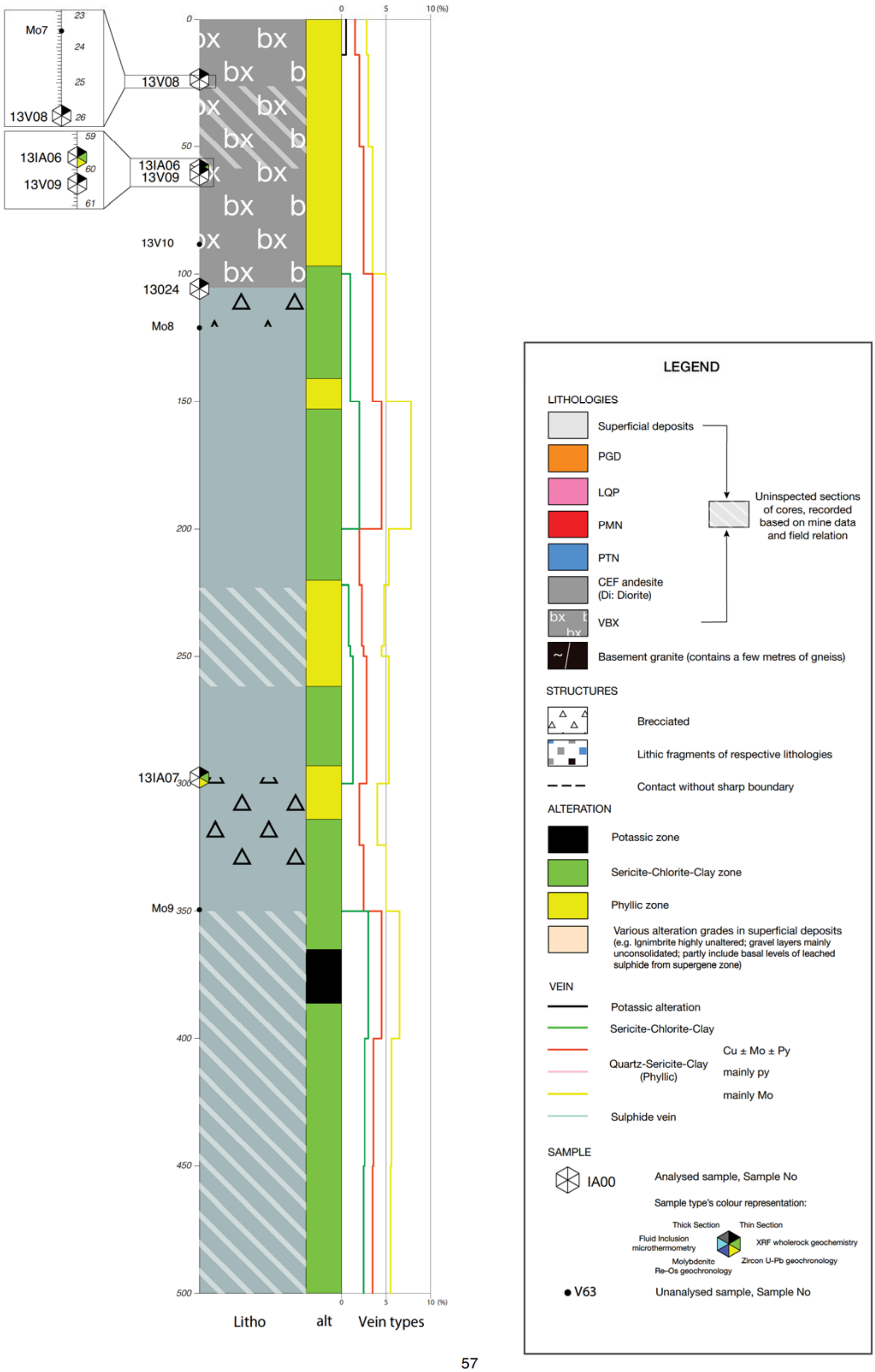

Fig. 19 Log for 11-081

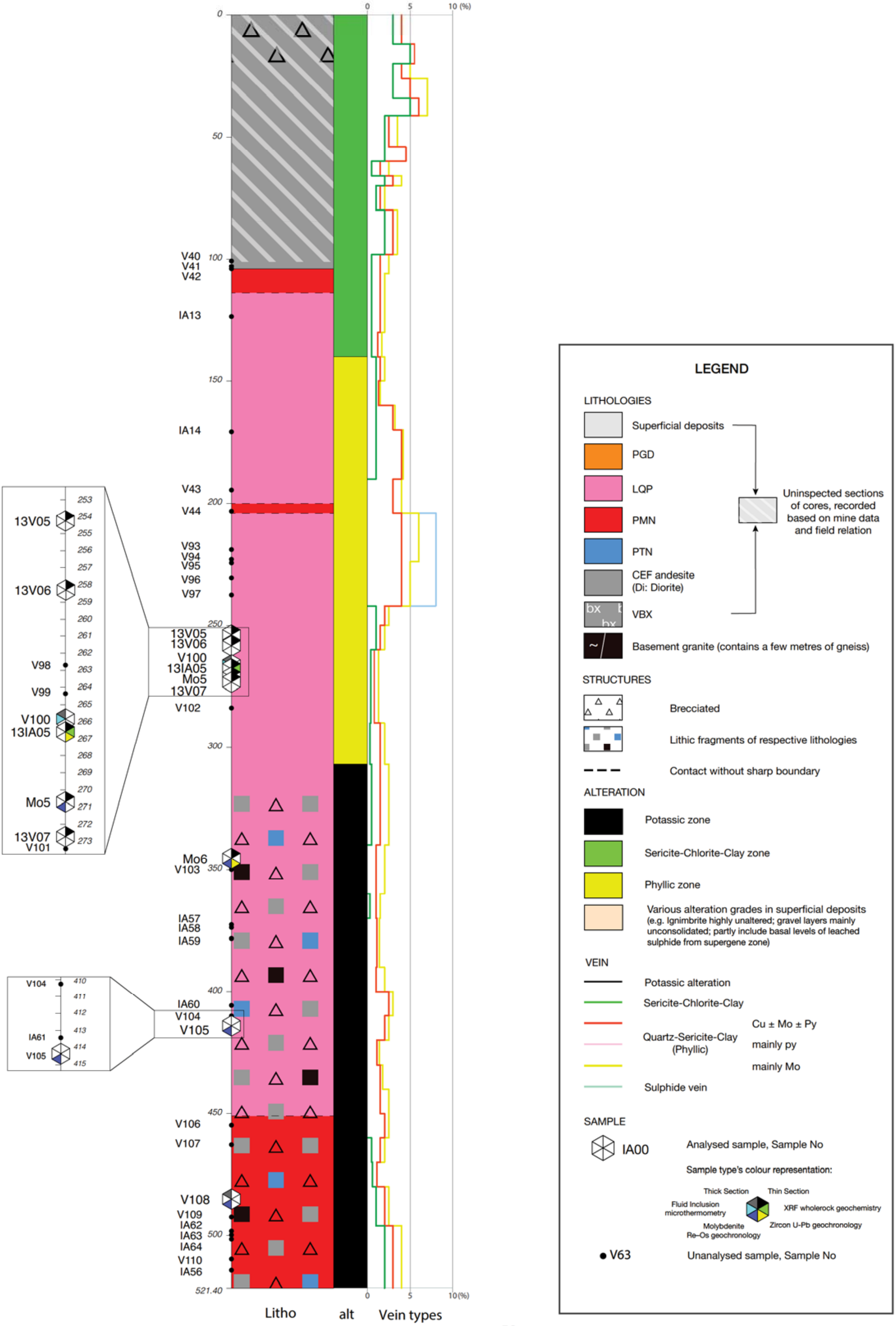

Fig. 20 Log for 11-084

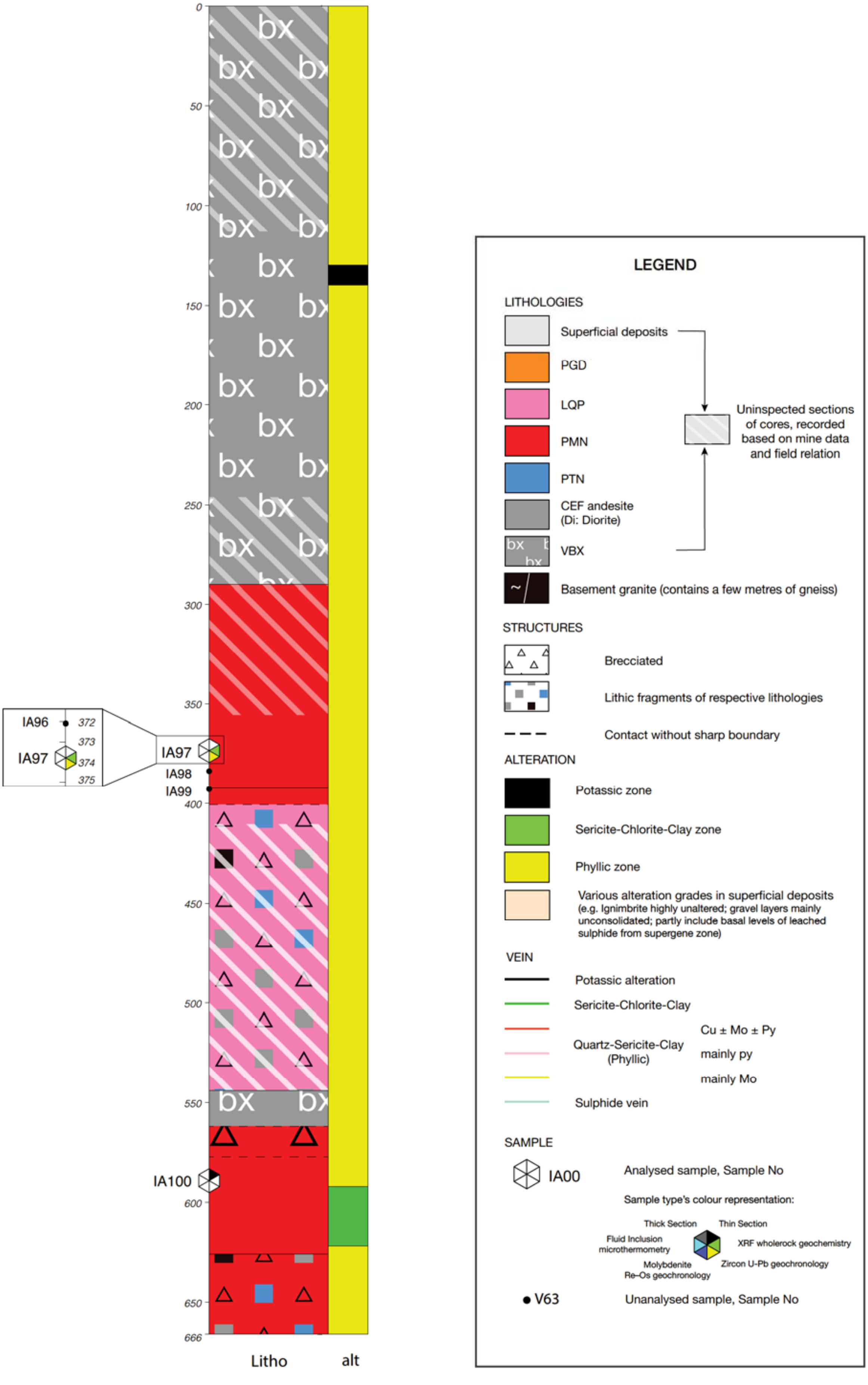

Fig. 21 Log for 11-091

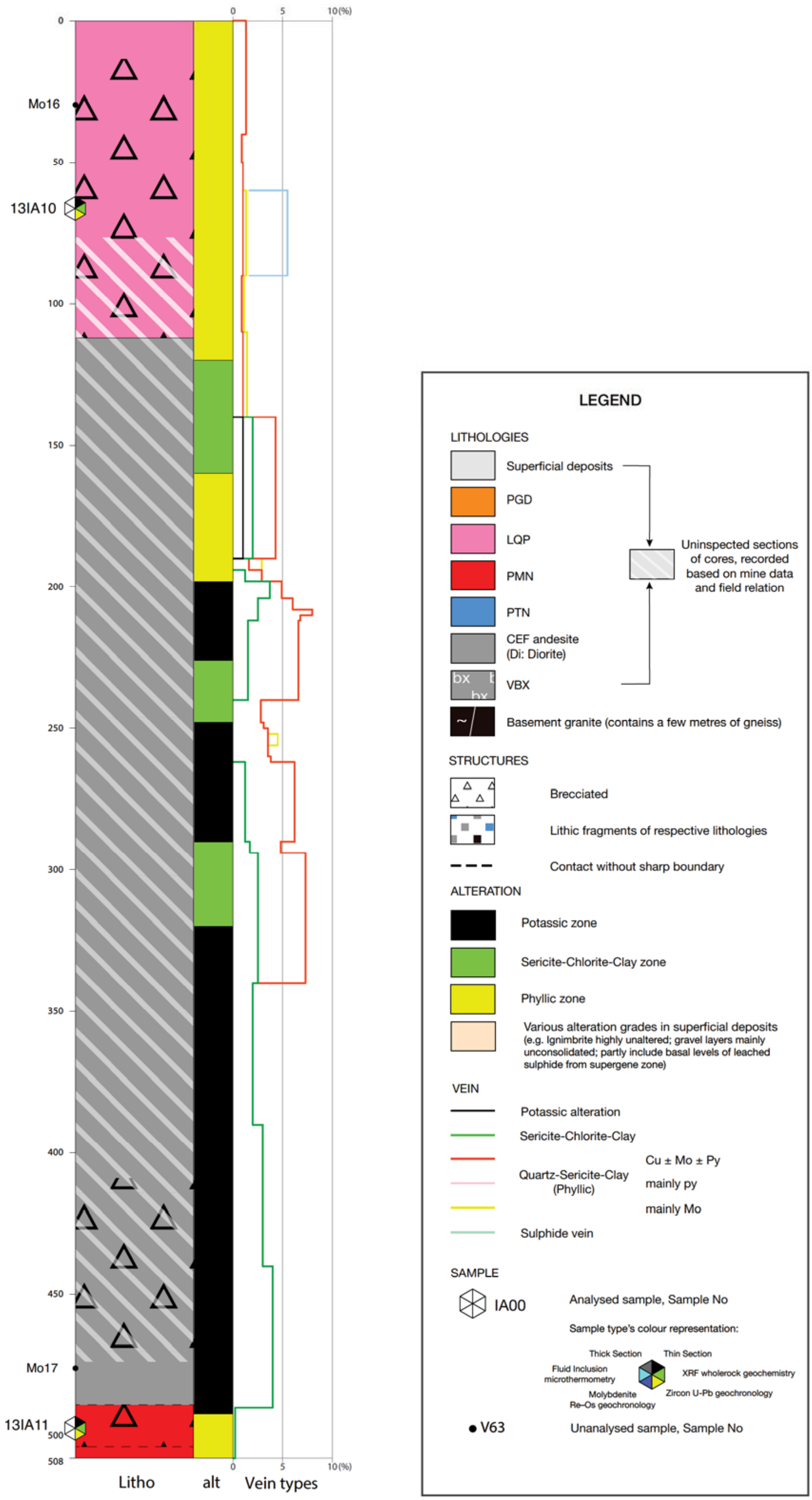

Fig. 22 Log for 11-093

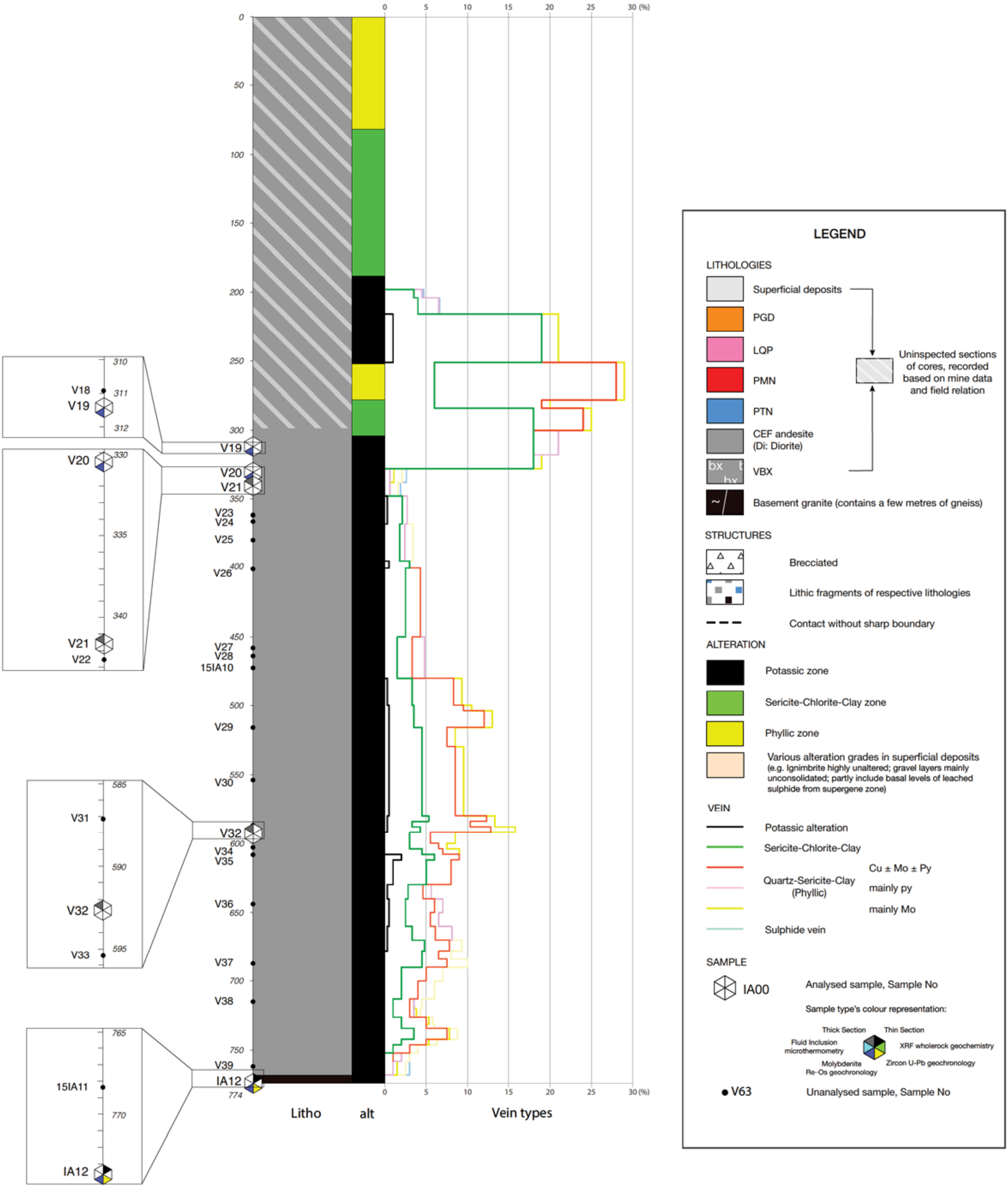

Fig. 23 Log for 11-097

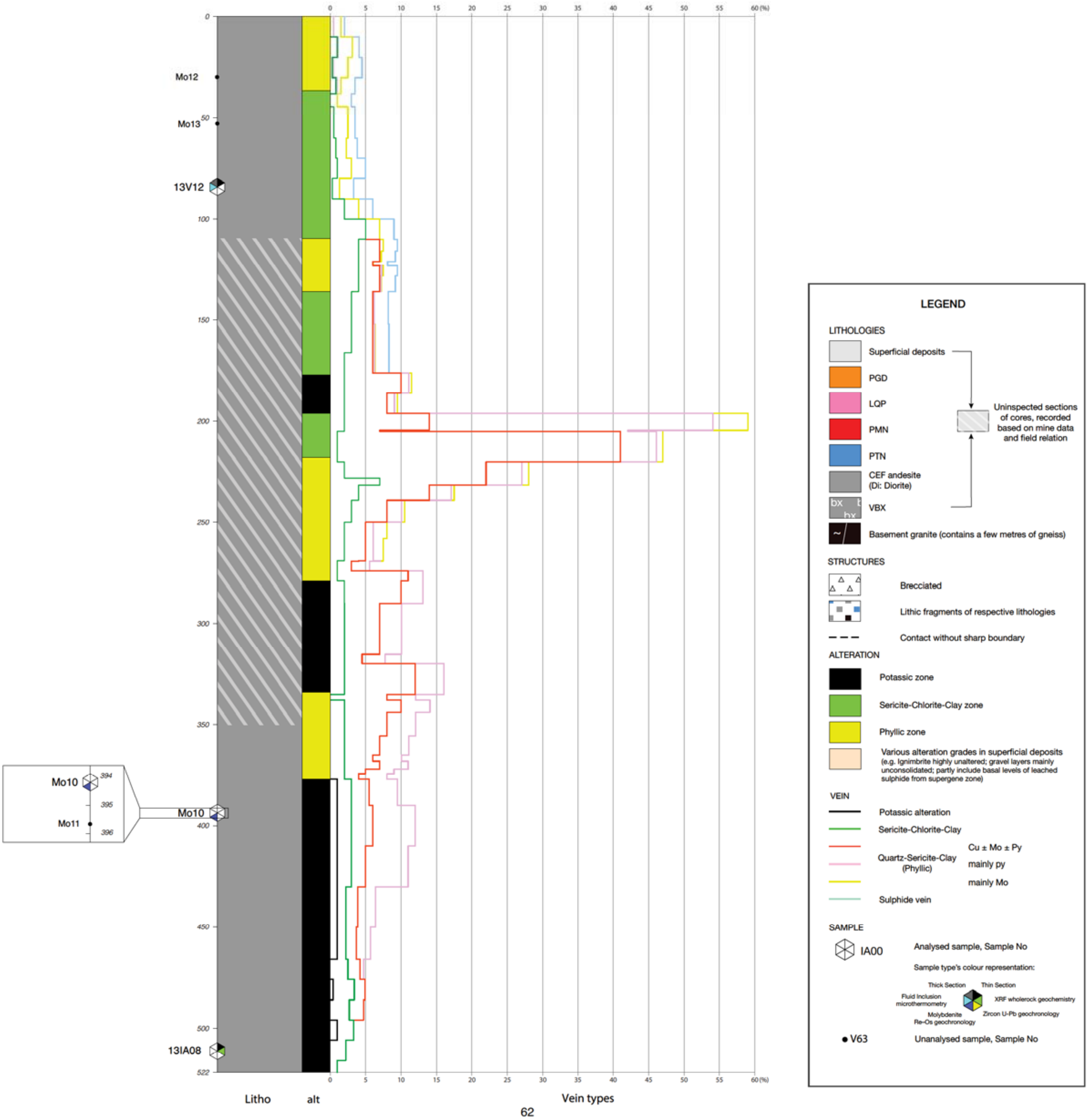

Fig. 24 Log for 11-100

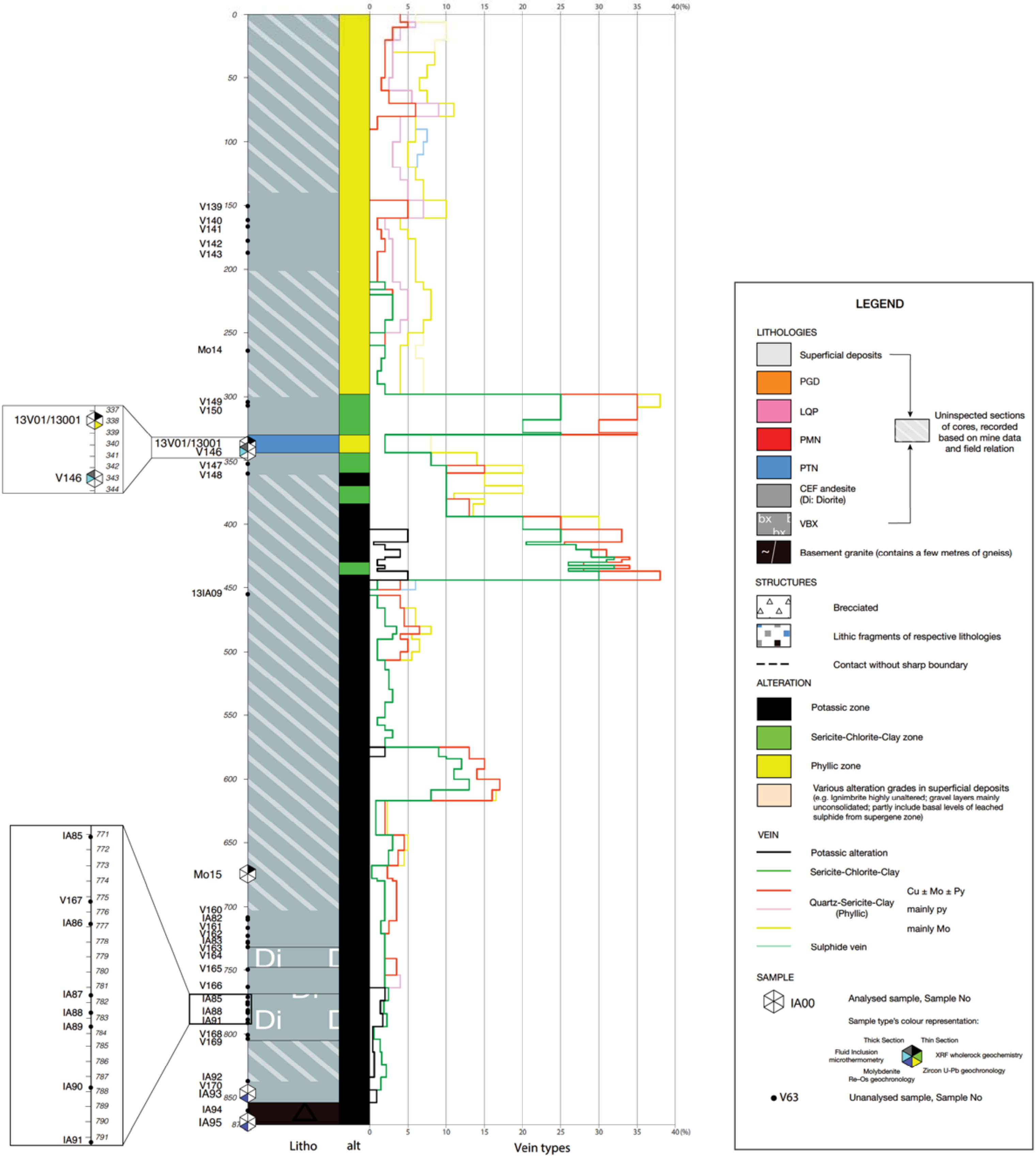

Fig. 25 Log for 11-112

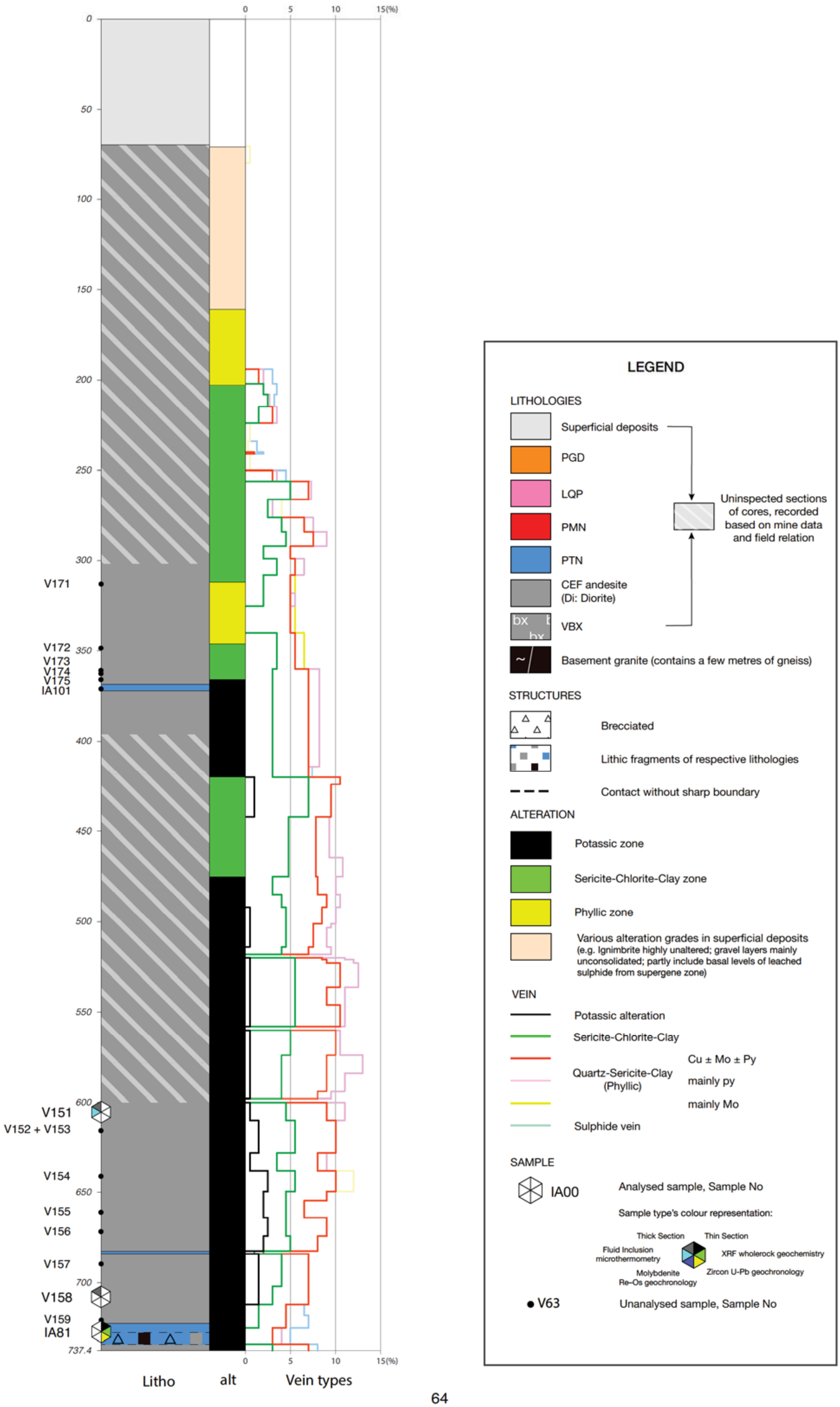

Fig. 26 Log for 14-005

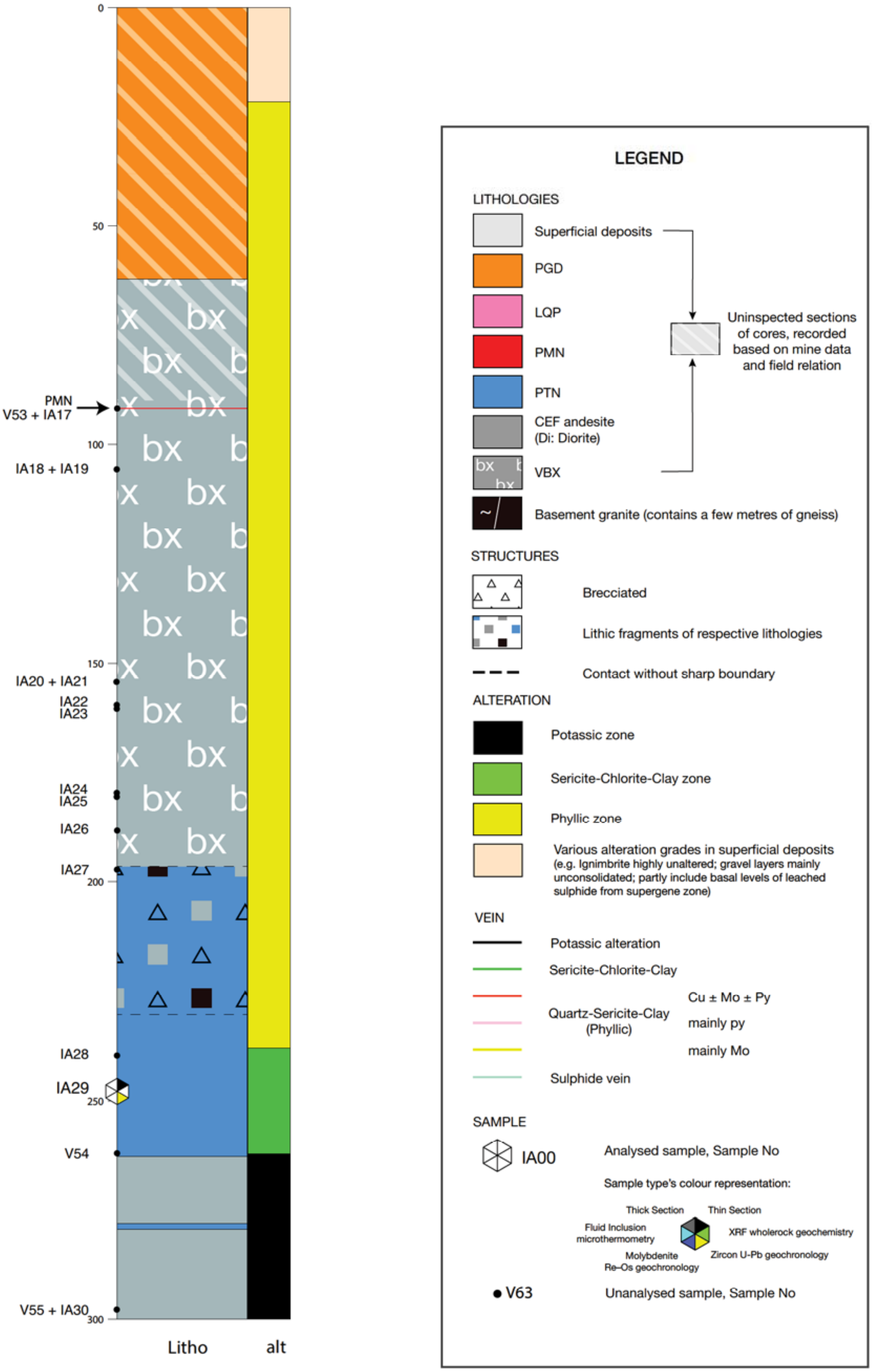

Fig. 27 Log for 15-028

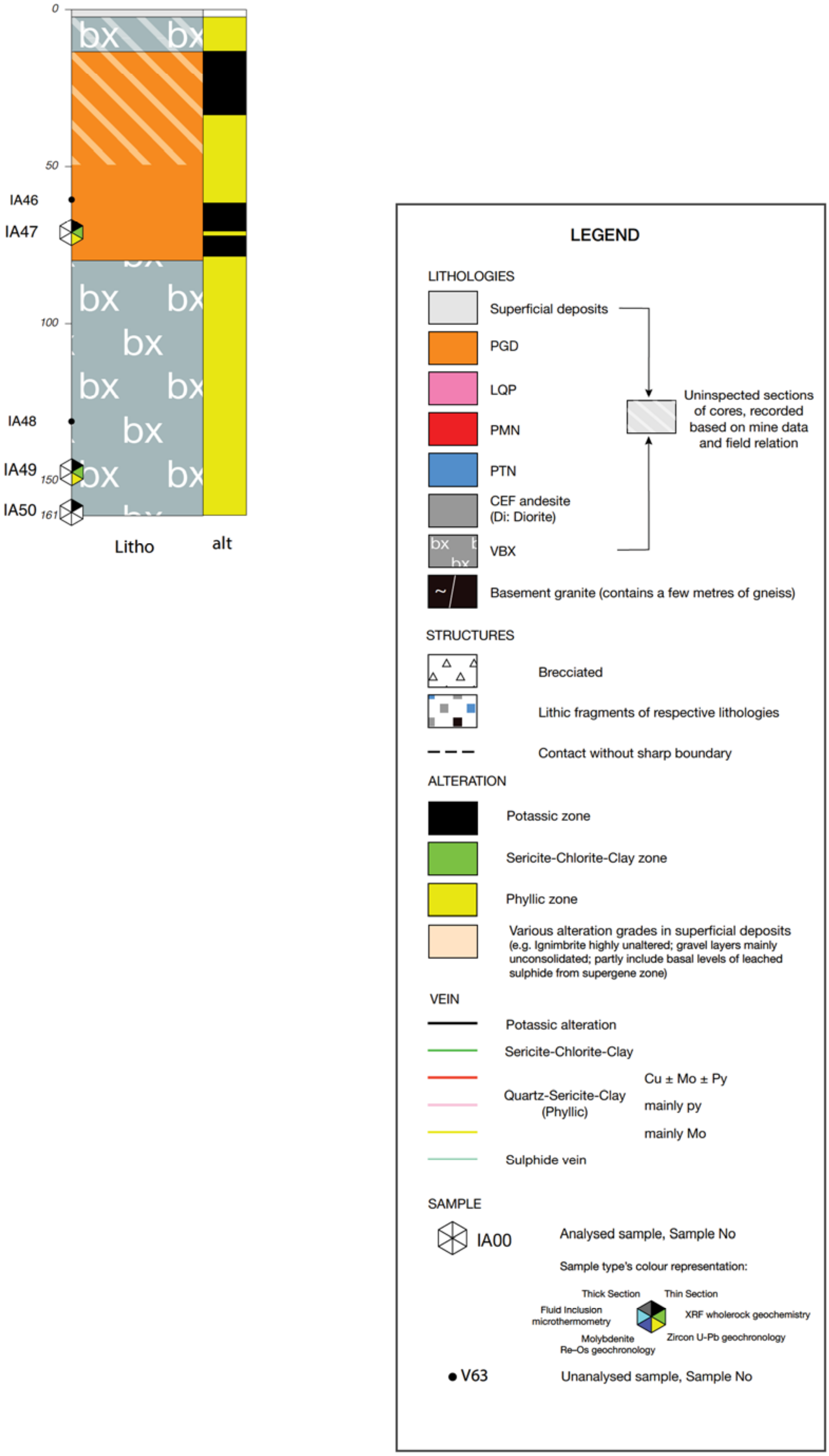

3. Whole-rock geochemistry

3.1 Analytical procedures

A total of 28 samples were selected from CEF, VBX and the main intrusive units for bulk rock geochemical analysis. When preparing the samples, care was taken to avoid the areas affected by veins and halos. Samples were crushed by hand and then powdered using an agate ball mill. Mixtures of 0.5 g of each sample and 5.0 g of lithium tetraborate for major element analyses, or 1.5 g of sample and 6.0 g of lithium tetraborate for trace element analyses, were fused into glass beads for XRF analysis, which was carried out at Nagoya University using a Rigaku ZSX Primus II instrument equipped with a Rh tube (50 kv, 60 mA). Major element calculations used 20 igneous and sedimentary rocks issued by the Geological Survey of Japan as reference materials. For trace element calculations, 15 synthetic samples analysed by Yamamoto & Morishita (1997) were used as reference materials. The wholerock geochemistry data is given in Table 3. In addition, geochemical data for CEF and the intrusive units contained in mine reports were also compiled in supplementary sheets 2.

3.2 Results

All samples of CEF and the subvolcanic intrusions are peraluminous and subalkaline. Total alkali versus silica (TAS) plots (Fig. 28a) give a good general indication of the types of igneous lithologies. Samples of the CEF show considerable geochemical variation. The K-altered CEF and units identified as diorite in the field plot in the andesite to trachy-andesite fields. SCC-altered samples generally lie in the dacite field. VBX samples show very high SiO_2 contents, one of my two samples lies in the rhyolite field and one has an SiO_2 content exceeding 77%, the maximum value of the plot range for TAS diagram. The subvolcanic units show evolved compositions across the dacite, trachydacite, and rhyolite fields. PMN compositions are the most alkali-rich, and PTN is dominantly dacite. LQP is the most silicic of the three units and lies in the dacite to rhyolite fields. The andesitic porphyry is more mafic and lies in trachy-andesite field.

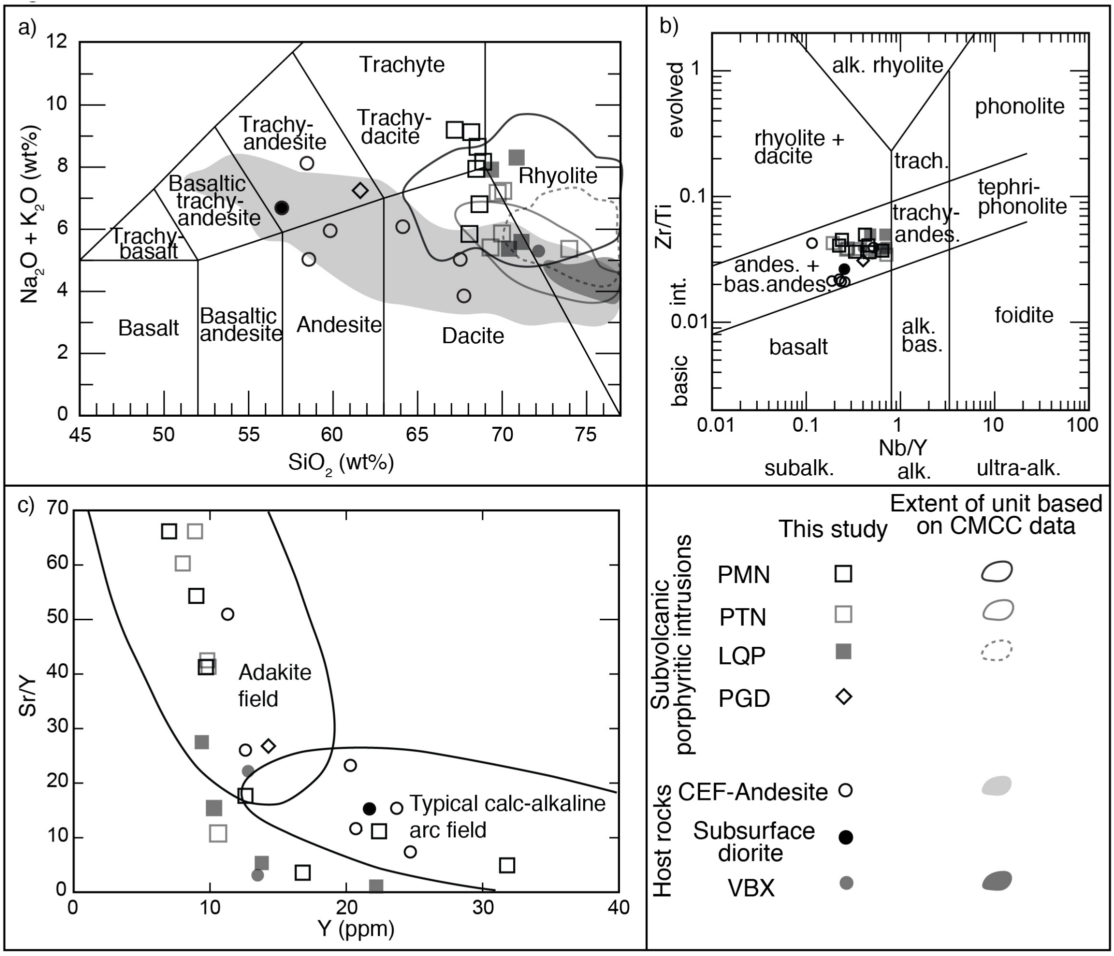

Fig. 28 Whole-rock geochemistry.

a) Na_2O+K_2O vs SiO_2 (TAS) diagram of Le Maitre et al. (1989). Analyses recalculated to 100% on an H_2O- and CO_2- free basis.

b) Zr/TiO_2 vs Nb/Y diagram of Pearce (1996) (after Winchester & Floyd, 1977).

c) Sr/Y vs Y discrimination diagram for adakite rocks (fields after Defant & Drummond, 1990)

There has clearly been hydrothermal alteration of many of the rocks and alkalis are particularly susceptible to transport. This implies that the TAS plots may not be good representations of the original compositions of the intrusive bodies. An alternative approach based on elements generally considered to less mobile in hydrothermal systems uses Zr/TiO_2 and Nb/Y ratios. Plots of Zr/TiO_2 versus Nb/Y (Fig. 28b) suggest less evolved and less alkaline original magma compositions than the TAS plots and the results are much less dispersed. Using these indications, all of the CEF and subvolcanic intrusions plot in the andesite to basaltic andesite fields.

The contrast between rock names using the two types of classification diagrams suggests that hydrothermal alteration in this area has resulted in a relative increase in Si and alkalis. This type of alteration is typical for PCD environments (Gifkins & Allen, 2001; Ulrich & Henrich, 2001; Derakhshani & Abdolzadeh, 2009). However, xenocrystic and xenolithic material in the analysed samples may influence both the TAS and Zr/TiO_2 vs Nb/Y plots. In view of these uncertainties, in this study, I adopt the rock names based on their petrography, as discussed in section 2.2.1.

High Sr/Y ratio reflects crustal assimilation or slab melting processes, both are suggested to be associated with PCDs formation (e.g. Richards & Kerrich, 2007; Richards, 2011b). Recent studies on PCDs suggest that the Sr/Y ratio can be used to estimate the potential of a magma to carry economically significant amounts of metal ions (Richards & Kerrich, 2007; Richards, 2011b; Chiaradia et al., 2012; Williamson et al., 2016). For most PMN and PTN samples the Sr/Y ratios (Fig. 28c) are high (> 40) and comparable to values seen in adakite (Gill, 2010). In contrast, LQP samples show relatively low Sr/Y ratios (1.1–27.5). These results suggest that the magma responsible for both PMN and PTN had a high metal-carrying potential.

3.3 Alteration geochemistry implying PMN–LQP relationship

To examine the idea that LQP may be a more strongly altered equivalent of PMN, I analysed bulk rock geochemistry of samples from the CEF that had undergone different degrees and grades of alteration. I then compared these alteration vectors with the range in composition shown by the intrusive bodies.

Harker diagrams emphasize several major element variation features of the three main types of intrusive rocks (Fig. 29). To examine the effects of hydrothermal alteration on major element chemistry, samples of CEF from different alteration grades are also plotted on the same composition diagrams. Compared to relatively less altered CEF andesite, the SCC and phyllic altered rock shows general increases in SiO_2 and K_2O content, and decreases in CaO and Na_2O. These changes suggest silicification and feldspar destruction, and formation of sericite—features that can also be observed in thin section. Similarly, when samples of phyllic altered PTN and less altered PTN are compared, phyllic alteration is associated with a clear decrease in CaO and Na_2O contents, suggesting feldspar alteration. The increase in K_2O content is reflected in the pervasive occurrence of secondary sericite and illite. PMN and LQP crop out in the same region in the mine site and with increasing alteration PMN seems to grade into material that looks very similar to LQP. When the compositions of these rock types are plotted together there is a clear spectrum of transitional compositions defining the two units; this is likely due to increased alteration pushing LQP samples to have higher SiO_2 and K_2O contents, and lower CaO and Na_2O contents than PMN. These geochemical characteristics reflect the field observations that no clear boundaries or crosscutting relationships could be observed between these two rock types.

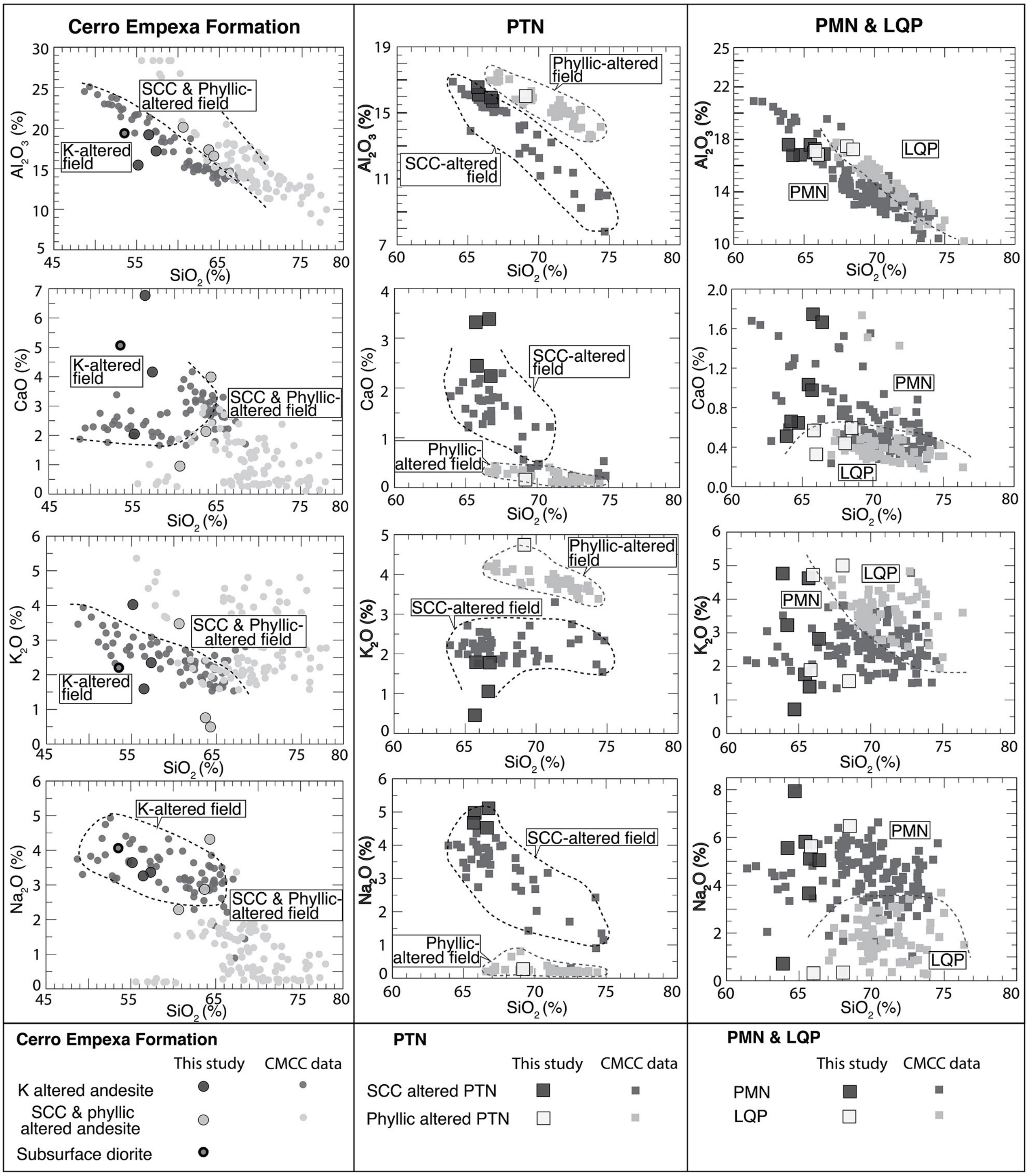

Fig. 29 Harker diagrams showing Al_2O_3, CaO, K_2O and Na_2O compositions plotted against SiO_2 emphasizing hydrothermal alteration signatures of various rock types. All geochemical data are provided in Table 3.

3.4 Molar element ratio plot

It has been suggested that in regimes that have undergone hydrothermal alteration, direct chemical composition comparisons between altered and relatively fresh rocks is not representative (e.g. Gresens, 1967; Grant, 1986; Warren et al., 2007). In order to evaluate relative gain and loss of elements between the altered and equivalent relative unaltered rocks, it is a common approach to assume one or more of the elements in the rocks are immobile during alteration (Warren et al., 2007). Here I follow the approach proposed by Warren et al. (2007) that uses molar ratio to evaluate relative mass transfer in hydrothermally altered rocks. These plots can help evaluate the appropriateness of the alteration vectors indicated from the Harker plots.

Warren et al. (2007) molar ratio plot:

Using a graphical illustration of (2Ca + Na + K)/Al versus K/Al molar ratio plot, the intensity of K metasomatism, Ca metasomatism and K, Ca, Na depletion can be accessed (Madeisky, 1996, cited in Warren et al., 2007). A unity value for (2Ca + Na + K)/Al represents fresh plagioclase and having both (2Ca + Na + K)/Al and K/Al values at 1 represents biotite and/or K-feldspar. Thus, fresh intermediate to felsic rocks should be plotted around along the $x = 1$ line; K metasomatism brings the K/Al value higher whereas formation of clay minerals will cause a decrease in the (2Ca + Na + K)/Al value. Sericite is formed as a major alteration product in the phyllic alteration zone as a result of K metasomatism. Therefore, a good proxy for sericitisation is the molar ratio of muscovite. Figure 30 shows the molar ratio plot of CEF of various alteration grades, together with PMN and LQP, using the same geochemical dataset for plotting Fig. 29. The mass transfer vector indicates a general decrease in (2Ca + Na + K)/Al and increase in K/Al from less altered rock to more altered rock, justifying the suggestions of sericitisation and feldspar destruction processes based on the Harker plots. This result is consistent with the suggestion that LQP is a more altered equivalent of PMN.

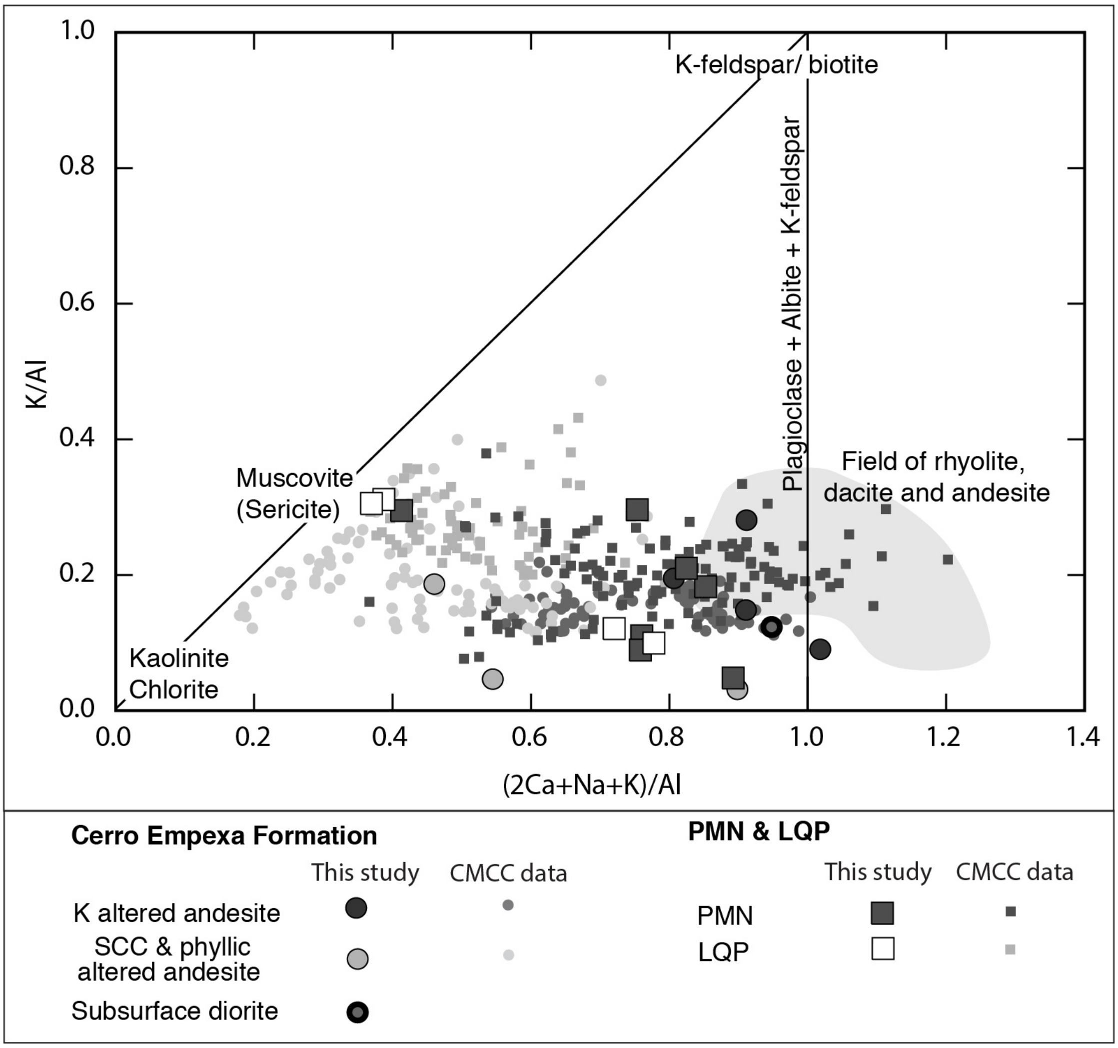

Fig. 30 Molar ratio plot of K/Al vs. (2Ca + Na + K)/Al for K altered to SCC and phyllic altered CEF, in comparison with PMN and LQP. The metasomatism vector indicates LQP has undergone significant Ca and Na loss, suggesting feldspar destruction, and a considerable K gain. The K-gain is compatible with the high abundance of sericite. Muscovite is plotted as a proxy for sericitisation.

4. Zircon Geochronology

The above information provides a geological framework to discuss the temporal evolution of the CMCC porphyry copper deposit. In this section, I present the results of zircon U–Th–Pb dating that help define ages for igneous activity in the CMCC area including the basement, Cerro Empexa host unit and the multiple subvolcanic intrusions.

A total of 24 samples were selected for zircon separation. The main focus was on the intrusive units but samples were also taken from the CEF and basement. Sample locations are shown in Fig. 5. Each sample of about 1–2 kg was first crushed by hand to < 840 μm, and then further reduced to a grain size of 105–177 μm by milling and wet sieving. This range corresponds to the average size of zircon grains observed in thin sections. Heavy liquid, diiodomethane (CH_2I_2), was used to separate the heavy mineral portions from the felsic fraction. Zircon crystals were then hand-picked, mounted and polished. CL images of zircon grains were taken using a SEM-CL unit at the Department of Earth and Environmental Sciences, Nagoya University to characterize zircon zonation patterns and help reveal the presence of distinct growth domains. Representative zircon CL images are presented in Fig. 31.

4.1 CL Imaging

The majority of the CL images of zircon grains from the subvolcanic bodies, PMN, PTN and LQP show sector and oscillatory zoning textures and can be divided into 2 main types. The first type lacks distinct cores and rims and commonly shows continuous concentric oscillatory zoning. The second type is composed of distinctive cores, which are darker and irregular in shape, and overgrown by zoned rims.

In order to obtain ages that are representative of the final emplacement age of the rocks, I used laser ablation that allows specific domains within individual zircon grains to be measured. The resulting precision is lower than isotope dilution thermal ionization mass spectrometry (ID-TIMS) but does provide good spatial resolution and allows a link to be made with microtextural observations. Where they were present, cores of zircon grains were analysed, but most analyses were carried out on the outer most rim of zircon grains. CL images were used to select ablation spots that did not overlap boundaries between cores and rims. Care was also taken to avoid cracks and inclusions in the zircon grains.

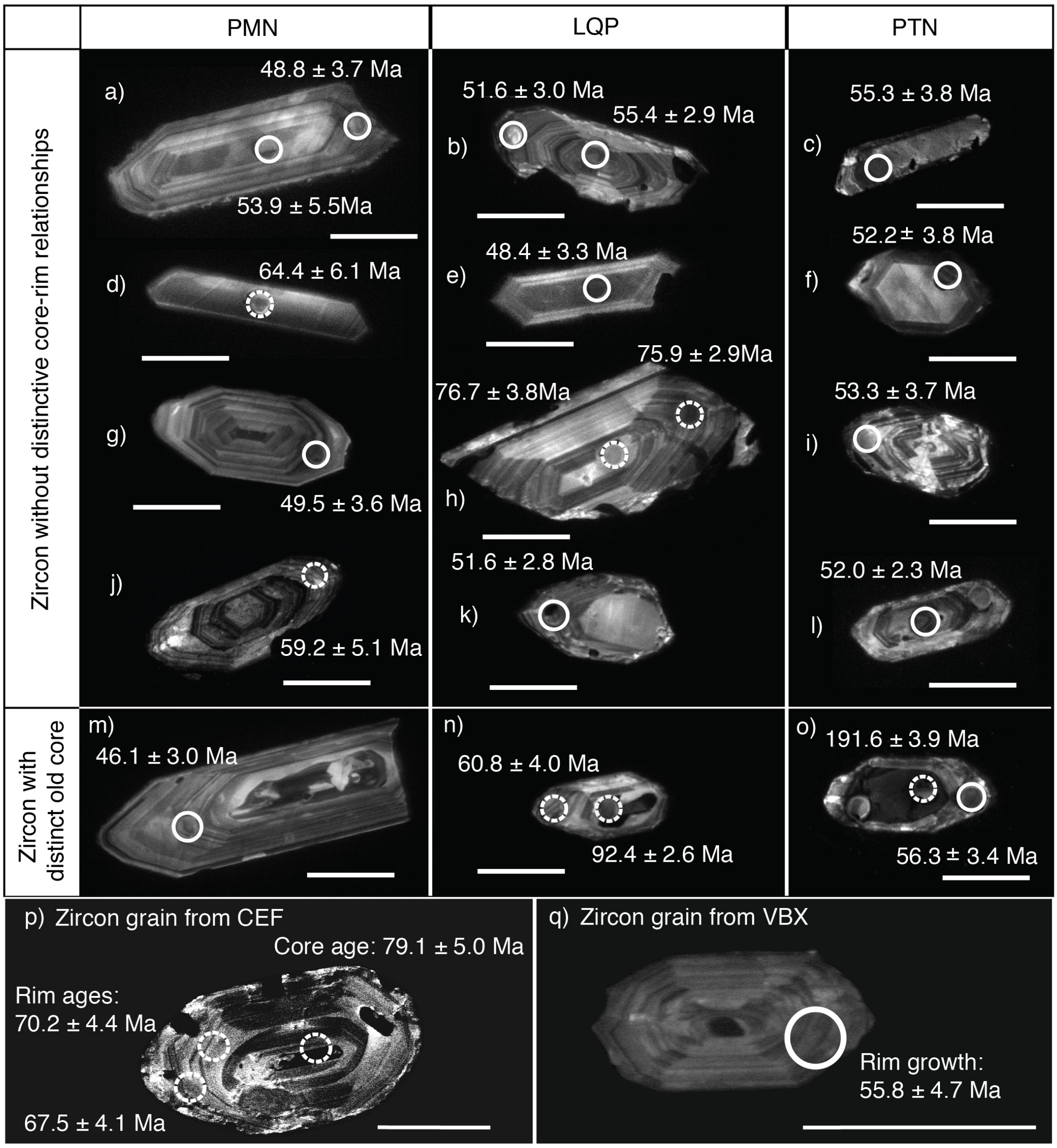

(Refer to next page for figure captions)

Fig. 31 Examples of CL images of zircon from the three main intrusive units (PMN, PTN and LQP). Size of bar is 100 µm. The circles show locations of laser ablation spots. Symbols with solid lines show ages of intrusive units, whereas symbols with dashed lines indicate ages of host rock units. Zircon with different microtextures can be seen. The zircon type on top does not show distinctive core-rim relationships, and commonly shows clear sector and concentric oscillatory zoning from interior to rim. Both core and rim domains of zircon grains show a spread of ages with Cretaceous, Paleocene and Eocene ages. The zircon type at the bottom shows a distinct old core overgrown by zoned rims. Late Paleozoic to Mesozoic and also Cretaceous cores are observed, suggesting the presence of zircon grains inherited from both basement units and the host rock CEF or VBX sequence.

4.2 Isotope Analyses

Zircon U–Pb analysis was carried out at the Graduate School of Environmental Studies, Nagoya University using a NWR213 (Electro Scientific Industries, Inc., USA) laser ablation system coupled with a Agilent 7700x (Agilent Technologies, USA) inductively coupled-plasma mass spectrometer (ICP-MS) with Nd-YAG laser source of $\lambda = 213$ nm. The analyses were carried out with a laser energy of 11.7 J/cm^2, a repetition rate of 10 Hz, a pre-ablation time of 8 seconds, an integration time of 10 seconds and with a laser spot size of 25 µm for all analyses.

For all analyses NIST SRM610 glass (Horn and von Blanckenburg, 2007), 91500 zircon (238U–206Pb age = 1062.4 ± 0.4 Ma; Wiedenbeck et al., 1995) and OD-3 zircon (238U–206Pb age = 33.0 ± 0.1 Ma; Iwano et al., 2012) were used as standard samples. The analytical procedures follow Orihashi et al. (2008) and Kouchi et al. (2015).

Altogether 15–50 spots were analysed for each of the 24 samples (Table 4, Supplementary sheet 3). U–Pb ages were calculated using Isoplot version 4.15 (Ludwig, 2012). Using the probability of concordance as an approach to filter U–Pb data (Ludwig, 1998), only data with probabilities of concordance ≥ 0.1 (e.g., Rossignol et al., 2016) were used for interpretation for the three main intrusive units (PTN, PMN and LQP) and the small PGD unit. For the basement granite, CEF and VBX, data with probabilities of concordance > 0.01 (e.g., Matthews & Guest, 2016) were used. An additional filter was applied to exclude data with high uncertainties. Individual analyses with 2σ error < 10.0% for the subvolcanic intrusive units, or < 10% for the basement and host rocks units, were used for the calculation (e.g., Gehrels et al., 2011; Zimmerer & McIntosh, 2013).

4.3 Results

4.3.1 Approach to age interpretations

The age results show multiple peaks indicating that inherited zircon is common in all rock units. In order to estimate representative ages of formation, age distribution histograms are used to identify distinct age groups present in each rock unit (Fig. 32). A single result that gives the youngest age places an older limit on the age of formation. When multiple results concentrate around the same young age showing a single peak, a weighted mean age of the young peak can be calculated to represent the age of crystallisation. An unmixing multicomponents algorithm method (Sambridge & Compston, 1994) is used if multiple peaks are recognised in the age distribution. I use the mean squared weighted deviation (MSWD) values to help determine if the calculated ages are statistically representative of single crystallisation events (Wendt & Carl, 1991). For the units in which multicomponents are recognised, weighted mean ages are recalculated using the constituent fractions of the youngest peaks given by the unmixing multicomponent model to achieve suitable MSWD values (e.g., Bolhar et al., 2010; Murray et al., 2013).

4.3.2 Data description and interpretation

The data set for the concordant U–Pb ages used for calculation is provided in Table 4, and the plots described in the text below are shown in Fig. 32. The complete set of U–Pb data and the plots for weighted mean age calculations are provided in supplementary sheet 3.

1) Basement granite

Three samples from the basement granite unit, IA12, 15IA03 and IA68, yielded two age groups (Fig. 32a). Sample IA12 yielded a wide spread of ages 340–232 Ma while samples 15IA03 and IA68 yielded an age distribution of 347–300 Ma. The scattering of age data suggests inherited zircon grains are common, and thus it is difficult to determine a precise emplacement age for the basement granite. However, episodic magmatism during the Gondwanan tectonic cycle from late Devonian to Permian ages has been reported (e.g. Mpodozis & Ramos, 1989; Mpodozis & Kay, 1990). My Carboniferous–Permian granite ages agree with the late Paleozoic–Triassic magmatism reported in Collahuasi district—the northernmost exposure of Choiyoi Magmatic Province (Munizaga et al., 2008; Maksaev et al., 2014). The results suggest the granite basement of the CMCC area formed during the Gondwanan to early pre-Andean tectonic cycles.

2) Cerro Empexa Formation

Four samples were selected from different levels of the CEF with the aim of obtaining dates over the full range of the CEF sequence in this area.

Data for two andesite samples, 15IA01 and IA66, are plotted together on Fig. 32b. These two samples, collected at about 800 m below the surface, close to the contact with the granite basement, yielded a complex age spectrum with a young peak showing a range of 83–76 Ma and a weighted mean of 79.1 ± 2.6 Ma (Fig. 10b). Inherited zircon is also common. Zircon grains yielding ages as old as 600 Ma can be correlated with the Pampean orogenic cycle of northern Chile.

13IA07 is an andesite collected from 300 m below the surface, and is located near the middle of the volcanic succession. Most analyses yield old ages up to 1 Ga. These are clearly inherited zircon grains, with ages correlating to the Grenville Orogeny are not uncommon in the Central Andes (Chew et al., 2007). The remaining two Cretaceous dates of this sample are 75.1 ± 5.5 Ma and 68.8 ± 4.6 Ma indicating that the middle level of CEF in CMCC mine is late Cretaceous in age.

The diorite sample, IA84, was derived from 700 m below surface and is part of a minor body seen in a single drill core that was intruded into the andesitic lava sequences of the CEF. This unit yielded a spread of ages mainly falling in the range 78–67 Ma with a weighted mean of 72.5 ± 1.4 Ma (Fig. 32c). Some older ages from inherited grains were also recorded. These results show the presence of magmatic intrusions occurring at the same time as the CEF volcanism. Differences in ages of cores and rims of zircon grains suggest zircon growth over a period of several millions of years possibly related to recycling and autocrystic zircon crystallisation during diorite emplacement (e.g., Fig. 31p).

3) Breccia Unit

The data for two VBX samples, 13IA06 and IA49, are plotted together on Fig. 32d. VBX overlies the late Cretaceous CEF and yielded a unimodal spread in ages 68–54 Ma with a weighted mean age of 57.2 ± 1.4 Ma. These data show the presence of volcanic activity after the development of the CEF, which ended about 70 Ma. Ages older than 70 Ma show the presence of inherited grains, implying the brecciation event had induced mixing of older, inherited zircon, and crystallisation of new zircon occurred at ca. 57 Ma. The VBX represents a distinct phase of magmatic activity at CMCC with a restricted areal distribution.

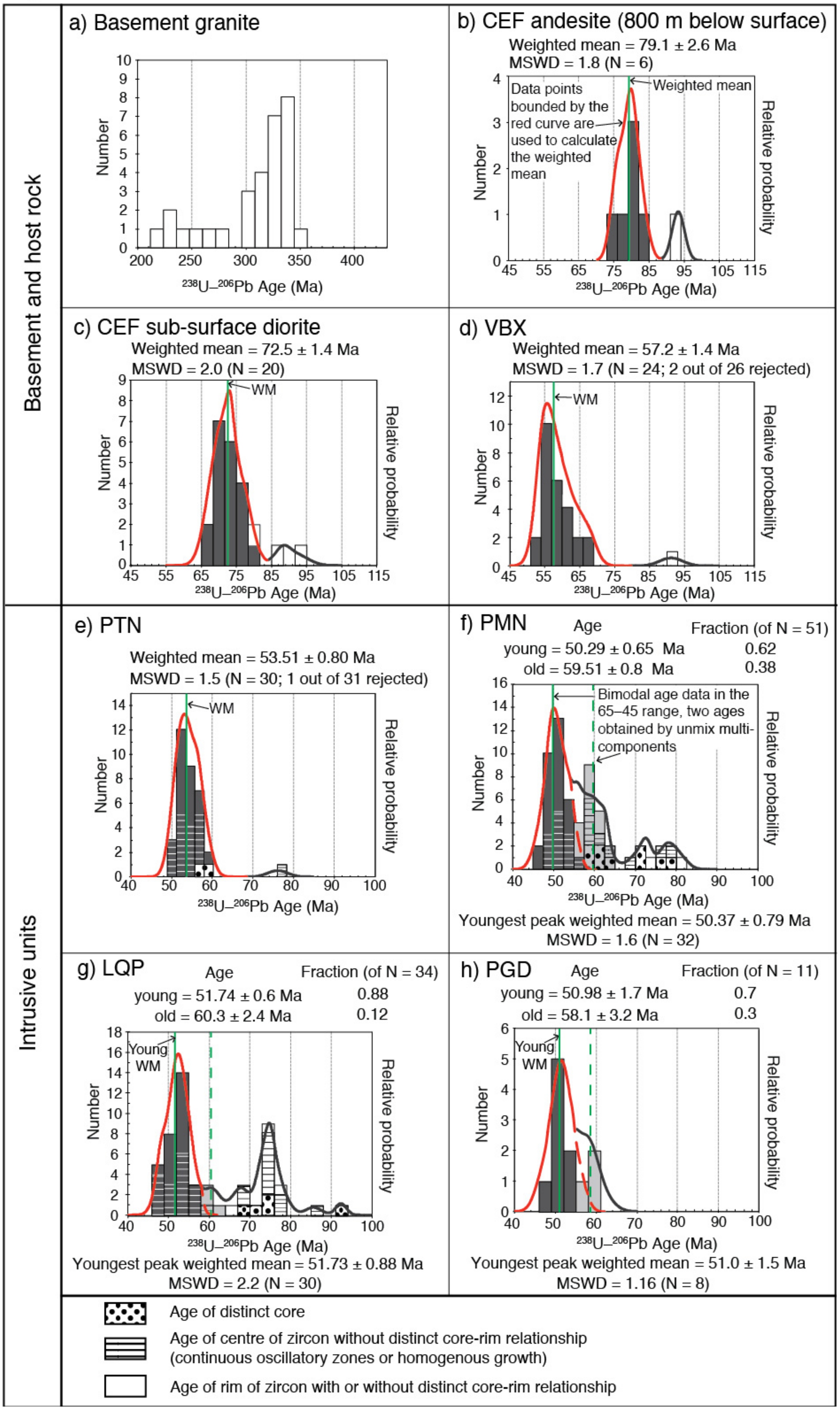

(Refer to next page for figure captions)

Fig. 32 Age population histograms for all measured rock units. Weighted mean ages calculated using Isoplot 4.15 (Ludwig, 2012) are plotted. Data points that are statistically rejected from weighted mean calculation are marked on Table 4 and shown on plots in supplementary sheet 3. For PMN, LQP and the PGD, the dotted red lines represent the projection of the population belonging to the spread of the first Gaussian peaks. Ages are calculated using bars shown with dark grey shades only. The light grey bars showing subordinate peaks at ca. 60 Ma are included in the unmixing multicomponents calculation (see text). For the intrusive units, data points collected from distinct cores, centres and rims of zircon grains are represented by different symbols. The widespread of ages from Cretaceous to Eocene suggests xenocrysts and antecrysts are common in the system.

4) Porphyritic tonalite

Almost all PTN zircon ages collected from 5 samples, 15IA09, IA29, IA80, IA81 and 1006, fall in the range 59–50 Ma. The age distribution histogram (Fig. 32e) shows a single peak with a weighted mean age of 53.51 ± 0.80 Ma.

Zircon grains for which both rims and cores were analysed commonly show concordant early Eocene core ages and discordant rim analyses. One explanation for the rim results is addition of extraneous Pb during hydrothermal interaction of zircon with metal-rich brines (e.g., Sinha et al., 1992; Mattinson et al., 1996). The discordant results were not included in the final age interpretation.

5) Porphyritic quartz monzonite

Four PMN samples, 13IA02, 13IA04, 13IA11 and IA97, yield a continuous spread of zircon grain ages 64–46 Ma. All ages older than 69 Ma are considered to be inherited zircon grains.

Within the 64–46 Ma range, the age distribution histogram (Fig. 32f) shows a clear bimodal distribution, with an obvious peak occurring at around 50 Ma and a subordinate peak at ca. 60 Ma. CL images of some well-formed relatively small single grains of zircon suggest a single continuous phase of growth and have rim ages of ca. 60 Ma (Fig. 31 j, n). This suggests the 60 Ma peak of the age distribution represents a discrete phase of zircon crystallisation. This zircon growth and implied magmatic activity occurred contemporaneously with the formation of VBX suggesting a significant phase of Paleocene volcanic activity.

Due to the bimodal age distribution of ages for this sample, I use the unmixing multicomponents by Gaussian deconvolution method (Sambridge & Compston, 1994) to separate the two peaks. Application of this algorithm results in two ages of 59.51 ± 0.8 Ma and 50.29 ± 0.65 Ma, which I interpret as both representing significant phases of zircon growth associated with magma crystallisation. The spread around the young age peak can be considered to be due to analytical errors associated with a single age of crystallisation, whereas the older ages lying outside the youngest Gaussian bell curve can be interpreted as xenocrysts or antecrysts that formed within the magma chamber prior to the emplacement of PMN (Bacon & Lowenstern, 2005; Charlier et al., 2005; Miller et al., 2007). Such antecrystic zircon grains are commonly identified in active magmatic systems and have been reported in PCDs (e.g. Miller et al., 2007; von Quadt et al., 2011; Simmons et al., 2013; Tapster et al., 2016). New zircon that grew during PMN emplacement can form individual grains, also known as autocrysts, or new rims on inherited zircon grains and antecrysts (Miller et al., 2007). In this case, recalculation of the young group of ages (N = 32), which represents the main PMN crystallisation event, gives a weighted mean of 50.37 ± 0.79 Ma with an MSWD of 1.6.

6) Leucocratic quartz porphyry

The results for 4 LQP samples, 13IA05, 13IA10, Mo6 and IA76, yield a very similar age population set to PMN with a continuous spread of zircon ages from 62–48 Ma with a peak at around 50 Ma and a less prominent shoulder at around 60 Ma (Fig. 32g). Ages older than 67 Ma are considered to be inherited zircon grains.

Applying unmixing multicomponents analysis to the data yields ages of 60.3 ± 2.4 Ma and 51.74 ± 0.6 Ma, very similar to the ages for the PMN. Recalculation of the young group of ages (N = 30) gives a weighted mean of 51.73 ± 0.88 Ma with an MSWD of 2.2. This MSWD value is somewhat greater than that expected for a single age population (Wendt & Carl, 1991), suggesting these age data include some unresolved component possibly related to the presence of zircon antecrysts.

7) Porphyritic granodiorite

Two samples of the porphyritic granodiorite, IA37 and IA47, yielded a range of ages of 61–47 Ma. The age distribution histogram (Fig. 32h) shows two peaks: a prominent peak at ca. 50 Ma and a smaller one at ca. 60 Ma, similar to the porphyritic quartz monzonite and the leucocratic quartz porphyry. The unmixing multicomponents analysis yields ages of 58.1 ± 3.2 Ma and 50.98 ± 1.7 Ma. Recalculation of the young group of ages (N = 8) gives a weighted mean of 51.0 ± 1.5 Ma with an MSWD of 1.2.

4.4 Zircon U–Pb SHRIMP analysis

To constrain the ages of the main intrusive porphyritic bodies in the CMCC mine site, I selected well-formed grains that were concordant, had simple continuous CL zoning and yielded the youngest peak LA-ICP-MS ages were selected to carry out Sensitive High Resolution Ion Microprobe (SHRIMP IIe) analysis at the National Institute of Polar Research, Japan.

SHRIMP has a higher spatial resolution than LA-ICP-MS and this allows several measurements to be made within a single CL band or within well-defined CL domains of single grains. For SHRIMP analyses, both the depth of the ablated pit and its mean diameter are considerably smaller than for LA-ICP-MS. Similar to the procedure for the LA-ICP-MS analyses, both backscattered electron images and CL images were used to select the sites for SHRIMP analyses. Concentric CL zones in minerals reflect contemporaneous growth surfaces and measurements and their distribution allows those parts of the crystal that grew at the same time to be identified. The results are summarised in Table 5.

4.4.1 Experimental procedures

The analyses were carried out with an O_2^- primary ion beam intensity of 1.1 nA and a spot size with mean diameter of approximately 14 μm. Analytical condition attained a mass resolution of 5100 (M/ΔM) and a sensitivity of 24 cps/^{206}Pb ppm/nA. To minimise possible contamination, the sample surface was first cleaned by rastering using a 90 μm beam for 2 minutes before actual measurement.

The standards THMORA2 (age = 416.8 ± 0.3 Ma; Black et al., 2004) and 91500 (Wiedenbeck et al., 1995) were used for U–Pb calibration and for determining U concentrations, respectively. The standard OD3 with reference value 32.853 ± 0.016 Ma (Lukàcs et al., 2015) was used as an external reference material. The sample preparation and experimental procedures of SHRIMP measurements follows Horie et al., (2013).

4.4.2 SHRIMP results of zircon grains from the three main porphyritic lithologies

A zircon grain was selected from the PTN sample 15IA09. Two spots from the same CL growth zone, and one from a similar domain were analysed. The probability of concordance of individual analysis was first calculated using Isoplot 4.15 (Ludwig, 2012) to check for data validity. All 3 spots attained values ≥ 0.94 and together they yield a weighted mean

^{206}Pb/ ^{238}U age of 53.5 ± 1.2 Ma (following normal practice errors for SHRIMP analyses are represented at the 1σ level) (Fig. 33a). The 53.5 Ma SHRIMP age for PTN is, within error, identical to the age derived from LA-ICP-MS analyses.

A zircon grain was selected from the PMN sample 13IA02. Six spots from the same CL growth zone were analysed. The probability of concordance for all 6 spots is ≥ 0.94 and together they yield a weighted mean ^{206}Pb/ ^{238}U age of 49.9 ± 0.64 Ma (Fig. 33b). This age is, within error, identical to the younger age derived from LA-ICP-MS analyses for PMN.

A zircon grain from the LQP sample 13IA10. Two spots from the same CL growth zone, and two others from a similar oscillatory zircon domain were analysed. The probability of concordance for all 4 spots is ≥ 0.94 and together they yield a weighted mean ^{206}Pb/ ^{238}U age of 49.4 ± 0.78 Ma (Fig. 33c). This result is slightly younger than the estimate from LA-ICP-MS analyses, but almost identical to the result for the PMN sample.

The weighted mean ages of the zircon from PMN and from LQP give results that are indistinguishable within error. The age dating shows that both the leucocratic silicified quartz-porphyry-like domain (LQP) and the monazite-porphyry domain (PMN) were crystallising at the same time around 50 Ma. The SHRIMP dating confirms the inference from LA-ICPMS age analyses and lends strong support to the idea that the two domains are in fact part of the same intrusive body with different degrees of alteration, and the PTN formed 3–4 million years earlier.

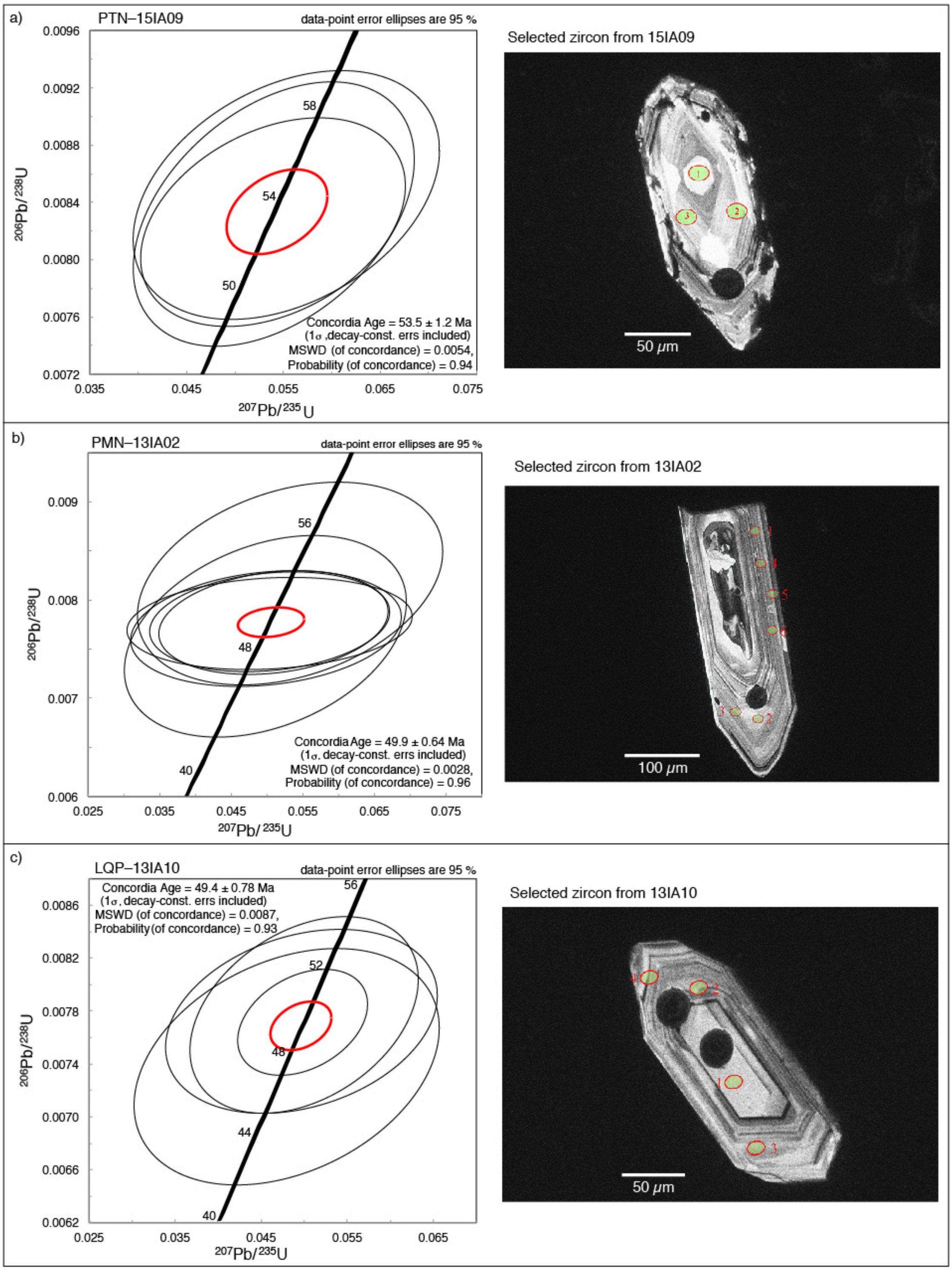

Fig. 33 Concordia ages calculated and plots generated using Isoplot 4.15 (Ludwig, 2012) for SHRIMP analyses of three individual zircon grains. a) Three spots analysed for the porphyritic tonalite (PTN) b) Six spots analysed for the porphyritic quartz monzonite (PMN); c) Four spots analysed for leucocratic quartz porphyry (LQP). The analysed spots are shown on zircon images. For the porphyritic tonalite and leucocratic quartz porphyry, concordia ages calculated excluding the spot ages obtained from the centre of the two zircon grains yield concordia ages of 53.5 ± 1.5 Ma and 49.3 ± 0.86 Ma. These are almost identical to the results calculated when the two spot ages are included (a and c).

5. Geochronology discussion

5.1 Zircon U–Pb dating results and tectonic implications

The presence of 350–230 Ma granitic basement in the CMCC area extends the known northern extent of the Late Paleozoic to Triassic Choiyoi magmatic province by about 100 km. In addition, the lack of the Jurassic–Early Cretaceous Chacarilla Formation in CMCC area suggests that this unit was eroded away prior to the deposition of CEF.

My new U–Pb dating shows the presence of large amounts of inherited zircon in the CEF, but the cluster of ages from 80 to 70 Ma agrees well with the proposed Upper Cretaceous age for this unit (Galli, 1968; Tomlinson et al. 2001; Charrier et al., 2007). Zircon grains from the bodies that intrude the CEF in the CMCC mine site show widespread evidence for crystallisation at ca. 60 Ma. This agrees with K–Ar and Ar–Ar ages reported in earlier studies for intrusive bodies of varying compositions that occur in the wider region and intrude the CEF (Huete et al., 1977; Maksaev, 1990; Agemar et al., 1999; Wörner et al., 2000). The VBX that cuts CEF shows evidence for crystallisation at ca. 57 Ma and is additional evidence for significant igneous activity around 60 Ma.

The age distributions for samples of PMN and LQP are very similar supporting the inference from field and geochemical evidence that LQP is simply a more altered equivalent of PMN. The 52.8 Ma age of PTN reported by mine site is within error agreeing with my new age of the same unit, but the 54.4 Ma for PMN and the 63.5 Ma for LQP are more likely to be inherited zircon grains recycled in the same magmatic system. An age of 51.7 Ma reported for LQP is almost identical to my weighted mean age for the same unit. However, new SHRIMP data suggest crystallisation of this unit continued until 49.4 ± 0.78 Ma (1σ error). The presence of numerous slightly older ages can be explained as due to the presence of zircon antecrysts formed in the active magmatic system prior to final emplacement.

The PMN–LQP body is likely to have been the main ore forming intrusion, and it is associated with an intrusion age of ca. 50 Ma, tightly constrained by SHRIMP analysis. This corresponds closely to the time when the regional tectonic setting entered a transition stage from extensional to compressional regime, possibly related to the initiation phase of a flat slab subduction environment (Isacks, 1988; James & Sacks, 1999; Haschke et al., 2002b; O'Driscoll et al., 2012). This adds circumstantial evidence to the idea that the tectonic stress regime is an important factor influencing where and when PCDs form as suggested by many previous workers (e.g. Solomon, 1990; Skewes & Stern, 1994; Kay et al., 1999; Kay & Mpodozis, 2001). The PTN body was intruded ca. 53.5 Ma and is slightly older than the PMN–LQP body. An early intrusion of PTN is consistent with its strong alteration compared to other intrusions. There is also clear evidence for magmatic activity at ca. 60 Ma, but a discrete intrusive body associated with this age was not recognised. To properly assess the regional significance of my new age dating, more integrated studies are required.

Figure 34 summarises all the ages from CEF, VBX and the younger sub-volcanic intrusions including the recycled zircon components up to 100 Ma. My study has shown a complex and prolonged history of zircon crystallisation, but the obtained ages clearly define the intrusion ages of the main porphyry bodies at around 53.5–50 Ma, suggest the copper mine was formed at the end of the late Cretaceous to early Eocene igneous activity of the Andean tectonic cycles (Maksaev & Zentilli, 1999; Charrier et al., 2007). The results also indicate that while the CEF andesitic sequence formed from 80 to 70 Ma, a younger, volcanic-related event locally occurring at CMCC formed the VBX breccia ca. 57 Ma. This younger event agrees well with the ages shown by minor peaks in the age distribution shown by PMN and LQP, suggesting the local volcanic unit belonged to the same magmatic system with the subvolcanic intrusions. This revised chronology of CMCC geology is significant because it implies the ore-related magmatic activity in CMCC occurred contemporaneously with a spatially related phase of volcanism.

5.2 Timeframe of intrusion, alteration and mineralisation

Available Ar–Ar ages of biotite and muscovite for the mine site are 50.18 ± 1.95 Ma and 51.8 ± 0.6 Ma, respectively (Bouzari & Clark, 2006). Unpublished mine data give a slightly older range of biotite ages 52.3 ± 1.0 Ma, which is interpreted as the age of potassic alteration, and sericite ages of 51.76 ± 0.58 – 50.23 ± 0.52 Ma which are interpreted as the age range for the main stage alteration (CMCC, 2014). Cotton (2003) obtained Ar–Ar ages for biotite and muscovite from a relatively unaltered porphyritic andesite of 51.8 ± 0.4 Ma and 51.5 ± 0.2 Ma, respectively. These are indistinguishable within error from the other existing data.

The new porphyritic intrusion ages reported here agree closely with the hydrothermal alteration ages, such that they bracket the alteration ages. The ca. 52 Ma potassic and main stage sericite alteration ages might be achieved by gradual cooling of the earlier PTN body to below the closure temperature (300 ˚C for biotite and 400 ˚C for muscovite) for free argon diffusion. The youngest sericite age and the reset biotite age (Bouzari & Clark, 2006) at ca. 50 Ma likely represent the alteration induced by the younger PMN–LQP intrusion. As seen from the alteration profile (Fig. 10), later phase potassic alteration overprinting earlier SCC and phyllic alteration is common and unevenly distributed. This can explain the difference in the obtained Ar–Ar ages of the potassic alteration age.

The only reported ages that can be directly related to sulphide formation are two molybdenite Re–Os ages: 55.5 ± 0.3 Ma (Cotton, 2003) and 53.8 Ma recorded in the mine site reports. These ages are older than the PMN–LQP intrusion. And although the younger of these two ages overlaps with the age of PTN, it is difficult to interpret them as dating a phase of molybdenite formation that developed as a result of the intrusions. Metal mineralisation events commonly occur up to several million years after the main phase of intrusion in an active magmatic system (e.g., Valencia et al., 2006; Barra et al., 2013). Magmatic events identified by the new U–Pb dating as occurring at 60–57 Ma and the similar K–Ar and Ar–Ar ages for surrounding plutonic rocks are, therefore, in good agreement with the reported Re–Os molybdenite ages. This early intrusion may have been the cause of an early phase of mineralisation in CMCC.

To summarise, at least 3 phases of events can be identified in CMCC. The onset of magmatic system at CMCC in the Paleocene at around 60 Ma following a lull in activity from the Cretaceous may have triggered a first phase of mineralisation at ca. 55.5 Ma. A second stage of intrusion and mineralisation occurred ca. 53.5 Ma related to PTN. Hydrothermal alteration ages can be easily reset at relatively low temperature, and the long-lived magmatic system would cause gradual cooling to below 300–400 ˚C. Thus Ar–Ar ages in the mine site would likely only record the younger phases of events clustered ca. 52–50 Ma. The third and final phase is associated with the intrusion of the PMN-LQP unit. Although no existing Re–Os age data is reported associating to the youngest intrusion, field observations show that copper and molybdenite mineralisation is clearly associated with the formation of this unit (see Table 1 and Figure 5) and mineralisation must have continued after 50 Ma.

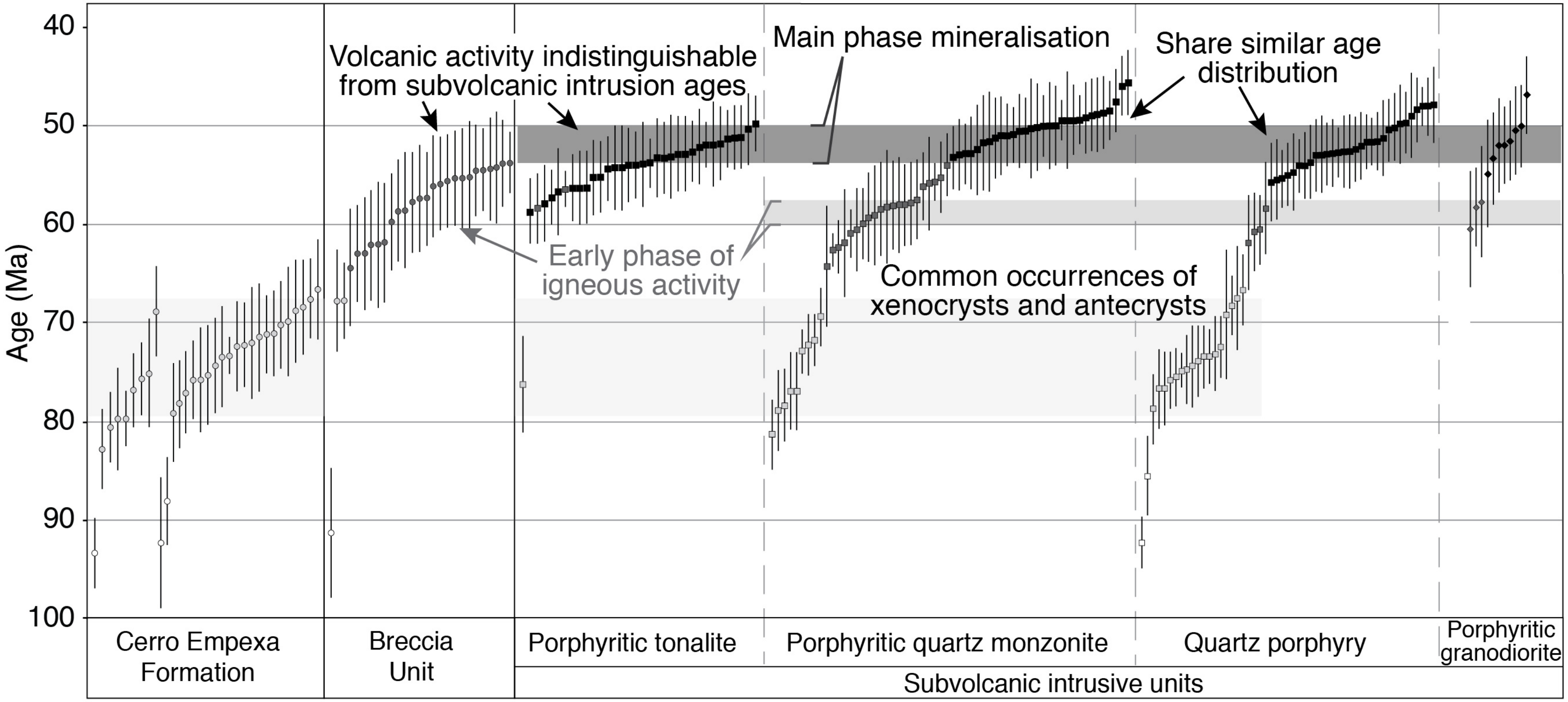

Fig. 34. Ages determined for samples of CEF, VBX and the intrusive units showing continuous igneous activities from Cretaceous to Eocene

5.3 Syn-mineralisation active volcanic activity associated with PCD formation

PTN exposed in the west of the mine site includes several thin sill structures (Fig. 6a). Such horizontal magma propagation commonly occurs at shallow crustal level where the rocks undergo elastic deformation (Vigneresse et al., 1999; Menand, 2001; Hansen, 2015). Despite the inferred relatively shallow intrusion depth, PTN shows a clearly crystalline matrix suggesting the country rock was warm enough to prevent sudden cooling. In contrast, PMN shows an aphanitic groundmass (Fig. 9e) implying rapid crystallisation. One way to explain rapid crystallisation is by rapid cooling. However, this is difficult to reconcile with the observed coarser grain size of the matrix of PTN that is exposed at similar structural levels. The average exhumation rate in northern Chile prior during the time of intrusion was about 50 m/10^6 yr (Maksaev & Zentilli, 1999). Thus, only small amounts of relative depth change are likely during the ca. 3 My gap between the emplacement of PTN and PMN–LQP. This implies the two intrusions were emplaced at similar shallow paleo-depths and, by implication, similar ambient temperatures. Furthermore, the lack of a chilled margin to the PMN–LQP stock implies that quenching implied by the fine grain size of PMN–LQP is not simply due to cooling.

An alternative explanation to rapid cooling which can account for the main features of PMN–LQP is rapid crystallisation due to rapid decompression. At isothermal conditions, rapid decompression would shift the melt to below solidus, creating an undercooling effect, which would cause crystallisation of phenocrysts and quenching of the groundmass (e.g. Cashman, 1992; Cashman & Blundy, 2000; Hammer & Rutherford, 2002). Decompression-induced crystallisation during magma ascent has been highlighted as a potentially important process associated with formation of porphyritic stocks in hydrothermal ore environments (Cashman, 2004). Rapid exsolution of a volatile phase during decompression is likely to cause fracturing and may be related to surface volcanism (e.g., Sillitoe, 1973, 1985). An observation in support of this hypothesis is that both LQP and the host rock surrounding the PMN–LQP stock is commonly strongly brecciated (Fig. 8c & d). This brecciation can be linked to decompression and exsolution of a gas phase related to surface volcanism. These observations suggest the formation of the PMN–LQP body is directly associated with active volcanism. The idea of magmatic-hydrothermal brecciation leading to fragmentation and possible eruption has been proposed in earlier studies (e.g. Sillitoe, 1973, 1985).

The recognition of the ca. 57 Ma VBX unit, slightly predating the porphyritic units suggests a magmatic event with intense volatile release had occurred within a close timeframe with the subvolcanic intrusions which are associated with mineralisation. A brecciated rock provides a higher permeability medium which is favourable for concentrating fluid flow, thus enhances ore deposition (Sillitoe, 2012), which explains the high concentration of disseminated molybdenite in the fine grain matrix of VBX.

An alternative explanation for intense brecciation in PCD deposits is that it results from a large volume of gas released during Cu-sulphide mineralisation reactions (e.g. Blundy et al., 2015). However, in CMCC, the main brecciated zone occurs around the PMN–LQP stock and is not present above the main host of hypogene copper mineralisation—the SCC-alteration zone around PTN intrusion. These observations suggest that the brecciation is caused by the PMN–LQP emplacement rather than sulphide mineralisation. All these physical features associated with PTN and PMN–LQP are summarized in Fig. 35.

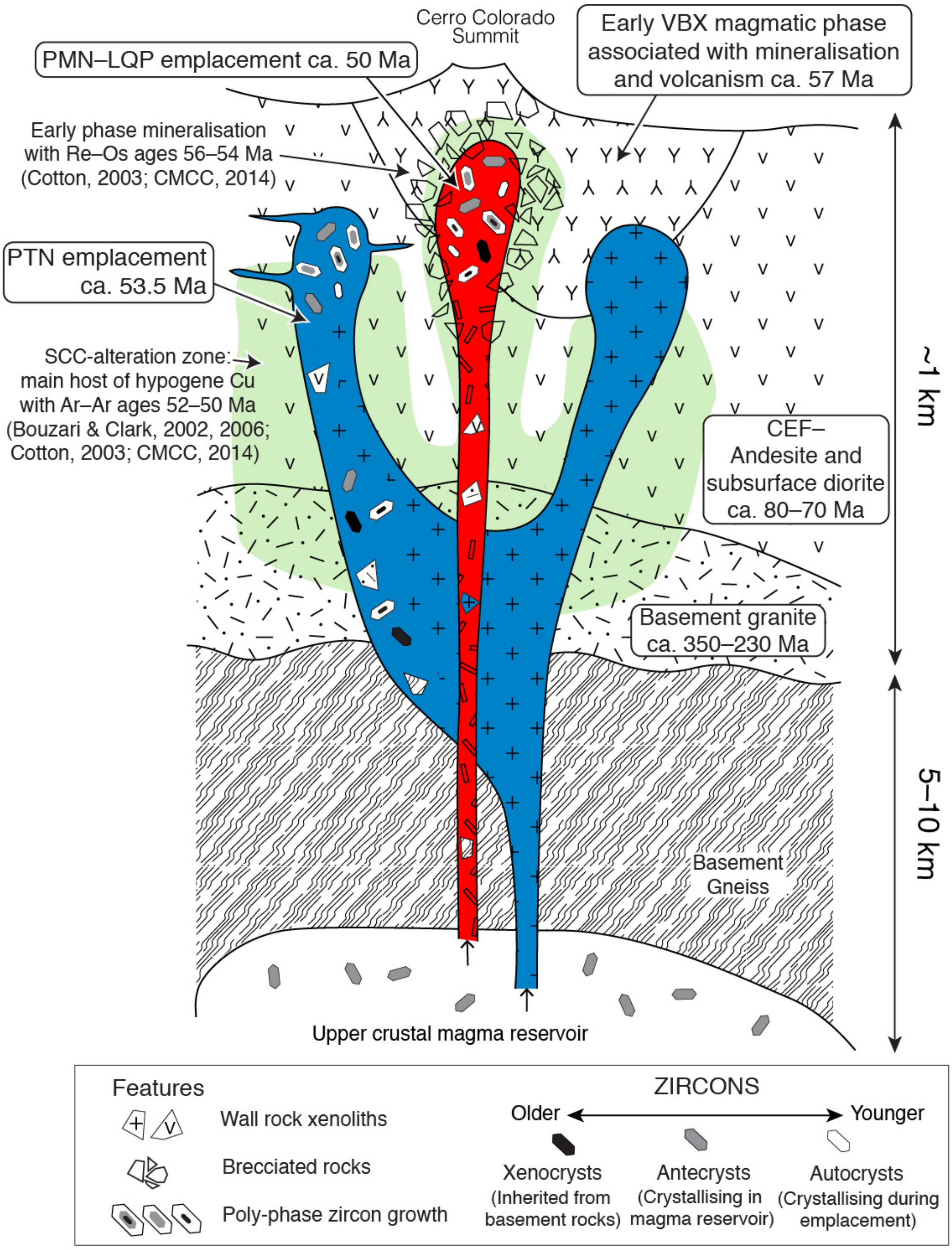

Fig. 35. Schematic geological evolution of Cerro Colorado area. Observed physical features related to the shallow PTN intrusion and the PMN–LQP volcanic pipe are illustrated. Xenoliths are broken off from the wall rocks, introducing zircon xenocrysts into the system. Antecrysts that begin to crystallise in the upper crustal magma chamber are incorporated into the ascending magma. Thus, the zircon collected from the shallow volcanic environment shows a wide range of ages, and polyphase zircon growth can be observed.

6. Conclusions

The main host rock of the mineralisation, the Cerro Empexa Formation, unconformably overlies Late Paleozoic–Triassic basement granite that can be correlated with the Choiyoi Magmatic Province. This extends the previously known distribution of this granite unit by about 100 km northward—the northernmost limit was previously thought to be at Collahuasi district.

U–Pb zircon dating confirms earlier studies that suggest the andesitic to dacitic Cerro Empexa Formation is mainly Cretaceous. In addition, field and geochronological data suggest that there is a volcanic-related breccia (VBX) that developed at around 57 Ma. The age of the breccia unit can be linked to an early magmatic phase mainly recognised in the broader Cerro Colorado area outside of the mine site that formed ca. 60 Ma and a phase of magmatism identified from zircon dating within the mine but not clearly associated with a distinct intrusive body. Magmatic activity at this time is compatible with reported evidence for an early phase of mineralisation at ca. 56 and 54 Ma. This age is significantly younger than previously recognised volcanic activity associated with Cerro Colorado and is within a close timeframe with the subvolcanic magma intrusions associated with Cu mineralisation. The earliest subvolcanic intrusion is a tonalite with an age of ca. 53.5. A younger monzonite-quartz porphyry unit was emplaced ca. 50 Ma. These results suggest a timescale for formation of the porphyry copper deposit of ca. 3–4 m.y.

The timing of the Cerro Colorado PCD suggests that the final stage of porphyry stock formation occurred at the same time or shortly before the regional tectonic stress field changed from horizontal extension to horizontal compression, which also marks the terminal stage for the Oligocene–Eocene metallogenic belt in N. Chile.

The overlapping ages derived for the volcanic-related breccia unit and the early magmatic phase, and the close formation timeframe with the porphyry intrusions, all of which associated with mineralisation, imply PCD formation was related to an active volcanic system. Further evidence for a direct relationship between volcanic activity and copper mineralisation is provided by the fine-grained matrix of the later monzonite unit and the associated locally intense brecciation, both of which are best explained as the result of pressure release due to rapid decompression due to volcanic eruption.

Table 1 Descriptions and comparison of nomenclatures of different rock types and their alteration styles at Cerro Colorado mine

Table 2 Summary of point counting of different minerals from each rock units. The samples were chosen from different depths from the drill cores in Cerro Colorado mine. The percentages of Cu bearing minerals are relatively small and vary among samples; for other major rock forming minerals, the normalized point counts (calculated at an increase of every 100 counts) achieved consistency toward higher number of total counts.

Table 3 Whole rock XRF geochemical data for representative samples from CEF, PMN and LQP

Table 4 LA-ICP-MA U–Pb geochronology data for zircons from host rocks and intrusive units in CMCC mine site

Table 5 SHRIMP U–Pb geochronology data for three single zircon grains selected from a porphyritic tonalite, a porphyritic quartz monzonite and a quartz porphyry sample

Table 1 Descriptions of rock types in different nomenclatures

	Bouzari & Clark, 2006	Mine Nomenclature	Rock type	Abbreviation used in figures and tables in this study
Host rock	Cerro Empexa Formation—andesite	PDI	Cerro Empexa Formation— andesite	CEF
	Intrusive hydrothermal breccia	BXIPQZ	Breccia unit	VBX
Intrusive / subvolcanic units	Quartz porphyry	PQZ	Leucocratic quartz porphyry	LQP
	Biotite-quartz-plagiocalse porphyry	PTO1	Porphyritic quartz monzonite	PMN
		PTO2	Porphyritic tonalite	PTN
	Hornblende-plagioclase porphyry dyke (outcrop)	Dyke	Porphyritic granodiorite (exposed in drilled core)	PGD

	Alteration types	Metallic minerals
Host rock	Almost all types are present: mainly sericite-chlorite-clay (SCC) alteration, biotite-quartz-magnetite alteration (potassic), and sericite-quartz-pyrite (± clay) (phyllic). Locally cut by quartz-albite veins (with big halos, with or without chlorite), which represents a transition from potassic to SCC (Bouzari & Clark, 2006)	Main host rock, closely associated with chalcopyrite and molybdenite mineralisation; depending on alteration types, locally associated with magnetite, bornite, pyrite, and copper oxide minerals.
	Pervasive phyllic with sericite, quartz, pyrite and clay minerals	Subsidiary host rock, contains disseminated chalcopyrite and bornite. Rich in fine-grained molybdenite. Disseminated pyrite occurs in matrix.
Intrusive / subvolcanic units	Transitional stage, phyllic alteration (quartz-sericite-pyrite)	
	Mainly phyllic alteration with quartz-sericite-pyrite and clay minerals. Cut by quartz-sericite-clay veins and less commonly quartz-sericite (± chlorite) veins	Disseminated pyrite is common in matrix; Cu-oxide minerals occur locally in matrix and veins. Molybdenite and chalcopyrite mainly associate with stockwork phyllic veins.
	Less altered compared to LQP and PTN. Biotite and chlorite replace pre-existing hornblende. Cut by quartz-sericite-clay veins, and less commonly by quartz-sericite (± chlorite) veins	Disseminated chalcopyrite sparsely found in matrix; chalcopyrite and molybdenite mineralisation mainly associated with stockwork phyllic veins. Cu-oxide minerals common in veins in upper parts of the unit.
	More intensely altered compared to PMN. SCC- and phyllic alteration common, local potassic alteration contains biotite–quartz-magnetite veins	Disseminated chalcopyrite common in the matrix, but molybdenite is scarce. Chalcopyrite closely associated with SCC- and phyllic stockwork veins. Locally contains magnetite.
	Intense phyllic alteration and pyrite veins	
	Essentially unaltered, locally displays low degree of phyllic–chloritic alteration	Largely unmineralised but local occurrence of disseminated chalcopyrite and rare SCC- and phyllic veins.

Table 2 Summary of point counting of different minerals from each of the rock units

Rock unit	Number of samples	Counts per sample	Cu minerals (sulphide and oxide) in matrix (%)	Quartz* (%)	Plagioclase (%)	K-Feldspar (%)	Biotite (%)	Chlorite, sericite, clay minerals (%)	Groundmass (%)
Granite	2	500	1–1.3	31.6–33.6	26.8–28.5	23.3–24.2	N.O.	11.4–15.3	N.O.
CEF (andesite)	2	1000	1.6–2.1	1.4–2	40.7–43.6	N.O.	14.7–15.2	21.5–27.4	10.3–18
CEF (diorite)	1	1000	3.7	13.3	25.2	N.O.	6.9	40.3	6.1
VBX	2	1000	0.6–1.3	22.6–24.1	6.3–7.4	N.O.	N.O.	44.6–48	14.7–19.2
PTN	3	1000	2–2.6	43.1–48.1	17.8–25.9	N.O.	1.2–4.4	20.5–31.8	N.O.
PMN	3	1000	0.6–1.3	9.3–17.1	15.3–24.5	11.9–21.9	10–29	7.8–16.1	27.6–35.5
LQP	3	1000	0.5–0.7	21.3–24.3	3.3–15.9	2.3–11.8	N.O.	21.1–61.4	4.7–17.2
PGD	1	1000	0.2	2.2	35.5	5.1	4.4	28.5	20.7

* Percentages of quartz include identifyable microcrystalline quartz, likely formed during quartz-phyllic alteration

N.O. = not observed

Table 3 Whole rock XRF geochemical data for representative samples of porphyritic quartz monzonite, leucocratic quartz porphyry and host rock andesite

Rock unit	sample name	SiO[2] mass%	TiO[2] mass%	Al[2]O[3] mass%	Fe[2]O[3] mass%	MnO mass%	MgO mass%	CaO mass%	Na[2]O mass%	K[2]O mass%	P[2]O[5] mass%	Cr ppm	Co ppm	Ni ppm
Subvolcanic intrusions														
Porphyritic quartz monzonite	13IA01	64.71	0.629	16.82	2.244	0.011	1.323	0.646	7.937	0.724	0.099	6.4	5.5	12.9
Porphyritic quartz monzonite	13IA02	65.44	0.682	17.58	1.601	0.009	1.718	1.034	5.823	1.768	0.078	6.1	6.2	11.5
Porphyritic quartz monzonite	13IA03	65.76	0.675	17.28	1.705	0.011	2.144	1.746	5.117	1.402	0.107	4.8	5.9	13.3
Porphyritic quartz monzonite	13IA04	66.41	0.563	16.88	1.582	0.026	1.440	1.665	5.053	2.826	0.132	12.0	7.1	10.2
Porphyritic quartz monzonite	13IA11	65.69	0.463	16.99	1.716	0.003	1.670	0.977	3.665	4.628	0.207	4.9	4.9	9.6
Porphyritic quartz monzonite	IA97	64.21	0.541	16.78	1.283	0.022	3.141	0.662	5.559	3.232	0.260	15.4	5.6	15.7
Porphyritic quartz monzonite	1001*	63.89	0.741	17.59	2.884	0.029	2.847	0.512	0.720	4.770	0.174	16.3	15.3	15.1
Leucocratic quartz porphyry	13IA05	68.04	0.520	17.48	3.161	-0.006	0.695	0.438	0.346	5.005	0.283	-2.5	7.8	5.8
Leucocratic quartz porphyry	13IA10	65.99	0.664	16.82	4.086	-0.006	1.056	0.327	0.314	4.724	0.165	11.1	24.5	7.5
Leucocratic quartz porphyry	Mo2	65.82	0.656	17.12	2.209	-0.003	1.084	0.568	5.630	1.890	0.170	0.0	12.4	9.2
Leucocratic quartz porphyry	Mo3	68.49	0.486	17.24	0.950	0.009	0.835	0.593	6.472	1.562	0.119	3.6	4.9	8.0
Cerro Empexa Formation														
Sericite-chlorite-clay altered	13IA07	60.75	0.975	20.12	3.211	0.014	3.039	0.947	2.292	3.469	0.244	7.7	9.4	10.6
Sericite-chlorite-clay altered	CCDH4*	63.85	0.759	17.33	4.790	0.018	1.997	2.134	2.879	0.753	0.224	-0.8	16.2	8.6
Sericite-chlorite-clay altered	CCDH5*	64.44	0.596	16.58	3.817	0.031	1.358	3.984	4.317	0.481	0.210	11.0	12.0	9.2
Potassic altered	13IA08	57.35	1.020	17.17	7.685	0.020	3.360	4.153	3.364	2.341	0.164	23.4	5.4	6.8
Potassic altered	15IA01	55.18	0.937	15.45	7.390	0.028	6.267	2.042	3.645	4.023	0.175	20.6	20.3	9.7
Potassic altered	1005	56.47	1.092	19.19	6.929	0.031	1.590	6.833	3.264	1.586	0.131	19.7	2.6	5.4
Diorite	IA84	53.39	0.964	19.38	7.283	0.048	1.855	5.073	4.064	2.202	0.198	21.5	16.2	12.8

Note: Samples marked with * are collected from uninspected drill hole in Cerro Colorado Mine; N.A. = Not analyzed.

Rock unit	Cu ppm	Zn ppm	Ga ppm	Br ppm	Rb ppm	Sr ppm	Y ppm	Zr ppm	Nb ppm	Ba ppm	Pb ppm	Th ppm
Subvolcanic intrusions												
Porphyritic quartz monzonite	4388.4	209.7	28.0	N.A.	24.7	250.2	22.4	153.8	5.0	N.A.	6.3	7.9
Porphyritic quartz monzonite	1856.2	110.7	24.8	N.A.	53.4	400.3	9.7	149.0	3.2	N.A.	10.1	4.1
Porphyritic quartz monzonite	819.7	212.5	22.4	N.A.	53.8	463.2	7.0	150.2	4.5	N.A.	6.9	6.0
Porphyritic quartz monzonite	2243.8	87.2	23.8	N.A.	62.3	489.0	9.0	137.8	4.1	N.A.	12.8	4.3
Porphyritic quartz monzonite	999.8	20.6	24.5	N.A.	127.3	222.6	12.6	138.0	5.3	N.A.	2.8	2.7
Porphyritic quartz monzonite	1030.0	485.7	22.0	-38.3	102.8	156.7	31.8	146.6	7.6	1132.8	124.2	6.3
Porphyritic quartz monzonite	4853.6	117.7	10.1	N.A.	141.6	60.3	16.8	160.7	7.9	N.A.	6.7	15.7
Leucocratic quartz porphyry	156.5	2.7	5.9	N.A.	123.0	23.7	22.2	155.5	10.6	N.A.	0.9	15.6
Leucocratic quartz porphyry	3357.9	0.6	-32.9	N.A.	132.2	74.2	13.8	151.6	8.7	N.A.	7.8	52.9
Leucocratic quartz porphyry	4127.2	85.7	23.9	N.A.	43.6	159.1	10.3	153.9	7.3	N.A.	36.7	7.2
Leucocratic quartz porphyry	1356.0	38.6	21.1	N.A.	34.0	258.8	9.4	145.2	6.5	N.A.	4.5	3.8
Cerro Empexa Formation												
Sericite-chlorite-clay altered	5396.4	47.6	11.7	N.A.	100.2	182.6	24.7	123.4	5.8	N.A.	4.5	6.9
Sericite-chlorite-clay altered	400.5	77.6	18.0	N.A.	25.1	328.3	12.6	179.0	6.5	N.A.	3.3	8.4
Sericite-chlorite-clay altered	1881.7	29.4	15.7	N.A.	9.0	576.1	11.3	152.3	1.3	N.A.	2.1	9.6
Potassic altered	549.6	53.0	16.4	N.A.	201.4	365.0	23.7	134.6	5.3	N.A.	5.2	9.0
Potassic altered	449.8	42.7	19.6	7.8	355.6	241.5	20.7	117.6	5.3	76.8	6.0	5.2
Potassic altered	1082.2	22.9	6.4	N.A.	108.4	472.1	20.3	139.4	3.8	N.A.	2.3	16.6
Diorite	2270.8	66.9	23.4	-9.5	105.4	331.7	21.7	153.0	5.5	610.3	5.3	6.6

Table 4 U–Pb geochronology data for zircons from host rocks and intrusive units in Cerro Colorado mine site

a) Zircon U–Pb results of individual basement granite samples

Sample Name	Th/U	207Pb/206Pb		Error 2σ	206Pb/238U		Error 2σ	207Pb/235U		Error 2σ	238U-206Pb age (Ma)		Error 2σ	235U-207Pb age (Ma)		Error 2σ	Probability of concordance	Remarks
15IA03		**Relatively fresh with localized illitization two-feldspar granite, 890 m below surface**																
15IA03-1	0.56	0.0607	±	0.0051	0.0538	±	0.0013	0.450	±	0.039	337.6	±	8.4	377.5	±	32.8	0.003*	
15IA03-2	0.57	0.0563	±	0.0063	0.0529	±	0.0016	0.410	±	0.048	332.1	±	10.0	349.0	±	40.6	0.310	
15IA03-3	0.45	0.0534	±	0.0032	0.0529	±	0.0011	0.390	±	0.025	332.3	±	6.6	334.2	±	21.2	0.820	
15IA03-4	0.37	0.0560	±	0.0027	0.0481	±	0.0009	0.371	±	0.019	302.6	±	5.5	320.5	±	16.4	0.007*	
15IA03-5	0.39	0.0540	±	0.0045	0.0547	±	0.0013	0.407	±	0.035	343.2	±	8.2	346.8	±	29.8	0.770	
15IA03-9	0.59	0.0532	±	0.0049	0.0539	±	0.0014	0.396	±	0.038	338.7	±	8.8	338.8	±	32.1	0.995	
15IA03-10	0.48	0.0581	±	0.0060	0.0553	±	0.0016	0.442	±	0.047	346.7	±	10.0	371.9	±	39.7	0.120	
15IA03-11	0.62	0.0594	±	0.0051	0.0497	±	0.0013	0.407	±	0.036	312.7	±	8.0	346.8	±	31.1	0.008*	
15IA03-12	0.54	0.0563	±	0.0047	0.0509	±	0.0013	0.395	±	0.035	320.1	±	8.0	338.0	±	29.6	0.140	
15IA03-15	0.68	0.0544	±	0.0035	0.0516	±	0.0011	0.387	±	0.026	324.4	±	6.9	332.5	±	22.5	0.370	
15IA03-16	0.30	0.0599	±	0.0034	0.0881	±	0.0018	0.727	±	0.044	544.2	±	11.2	555.1	±	33.5	0.370	
IA12		**Relatively fresh with localized illitization two-feldspar granite, 774 m below surface**																
IA12-2	0.35	0.0521	±	0.0049	0.0366	±	0.0010	0.263	±	0.026	232.0	±	6.4	237.3	±	23.5	0.600	
IA12-8	0.43	0.0539	±	0.0056	0.0448	±	0.0013	0.333	±	0.036	282.6	±	8.5	291.9	±	31.5	0.480	
IA12-10	0.32	0.0555	±	0.0027	0.0423	±	0.0009	0.324	±	0.017	267.0	±	5.8	284.7	±	15.1	0.004*	
IA12-13	0.33	0.0546	±	0.0028	0.0366	±	0.0008	0.276	±	0.015	231.9	±	5.1	247.4	±	13.6	0.006*	
IA12-16	0.54	0.0505	±	0.0042	0.0507	±	0.0012	0.353	±	0.030	318.7	±	7.3	306.8	±	26.2	0.270	
IA12-17	0.49	0.0550	±	0.0030	0.0406	±	0.0008	0.308	±	0.018	256.6	±	4.9	272.6	±	15.8	0.016*	
IA12-21	0.26	0.0529	±	0.0036	0.0388	±	0.0008	0.284	±	0.020	245.7	±	5.1	253.5	±	17.9	0.310	
IA12-22	0.49	0.0520	±	0.0034	0.0542	±	0.0011	0.388	±	0.026	340.0	±	6.9	332.9	±	22.5	0.440	
IA12-23	0.60	0.0550	±	0.0053	0.0480	±	0.0013	0.364	±	0.036	302.1	±	7.9	314.9	±	31.4	0.330	
IA68		**Moderately epidote-altered two-feldspar granite, 889 m below surface**																
IA68-1	0.70	0.0539	±	0.0024	0.0539	±	0.0011	0.401	±	0.020	338.3	±	6.8	342.2	±	16.7	0.550	
IA68-3	0.59	0.0566	±	0.0031	0.0518	±	0.0011	0.404	±	0.024	325.7	±	7.0	344.8	±	20.2	0.017*	
IA68-5	0.48	0.0545	±	0.0038	0.0542	±	0.0013	0.407	±	0.030	340.1	±	8.0	346.6	±	25.3	0.530	
IA68-9	0.51	0.0571	±	0.0033	0.0476	±	0.0009	0.375	±	0.023	300.1	±	5.7	323.3	±	19.5	0.004*	
IA68-10	0.68	0.0507	±	0.0034	0.0509	±	0.0010	0.356	±	0.025	320.2	±	6.4	309.5	±	21.4	0.220	
IA68-11	0.69	0.0556	±	0.0026	0.0494	±	0.0009	0.379	±	0.019	310.7	±	5.4	326.1	±	16.5	0.021*	
IA68-12	0.52	0.0565	±	0.0050	0.0517	±	0.0013	0.403	±	0.037	324.8	±	8.0	343.7	±	31.9	0.150	
IA68-13	0.64	0.0528	±	0.0028	0.0506	±	0.0009	0.368	±	0.020	318.0	±	5.7	318.5	±	17.6	0.950	
IA68-14	0.54	0.0535	±	0.0062	0.0526	±	0.0016	0.388	±	0.047	330.3	±	9.8	332.9	±	40.1	0.870	
IA68-16	0.24	0.0553	±	0.0040	0.0516	±	0.0011	0.394	±	0.030	324.5	±	7.0	337.1	±	25.5	0.230	

* For basement granite, data points with probability of concordance < 0.1 and > 0.01 are included into calculation

b) Zircon U–Pb results of individual Cerro Empexa Formation (CEF) samples (andesite and subsurface diorite)

Sample Name	Th/U	207Pb/206Pb		Error 2σ	206Pb/238U		Error 2σ	207Pb/235U		Error 2σ	238U-206Pb age (Ma)		Error 2σ	235U-207Pb age (Ma)		Error 2σ	Probability of concordance	Remarks
15IA01		**Potassic altered, phenocrysts and clast-rich CEF andesite, 788 m below surface**																
15IA01-2	0.53	0.0686	±	0.0176	0.0124	±	0.0008	0.118	±	0.031	79.7	±	5.2	112.9	±	30.0	0.018*	
15IA01-13	0.76	0.0640	±	0.0125	0.0118	±	0.0006	0.104	±	0.021	75.7	±	3.7	100.7	±	20.3	0.009*	
15IA01-14	0.75	0.0551	±	0.0086	0.0146	±	0.0006	0.111	±	0.018	93.3	±	3.6	106.7	±	17.2	0.094*	
15IA01-18	0.70	0.0486	±	0.0104	0.0120	±	0.0006	0.080	±	0.018	76.8	±	3.8	78.4	±	17.2	0.840	
		Weighted mean age of late Cretaceous peak									**76.9**	**±**	**2.3**	**MSWD = 0.8**				
IA66		**Potassic altered aphyric CEF andesite, 833 m below surface**																
IA66-1	0.70	0.0577	±	0.0025	0.0719	±	0.0011	0.572	±	0.027	447.5	±	6.9	459.0	±	21.4	0.160	
IA66-2	0.38	0.0562	±	0.0038	0.0969	±	0.0019	0.750	±	0.053	596.2	±	11.6	568.4	±	40.4	0.060*	
IA66-4	0.69	0.0472	±	0.0075	0.0124	±	0.0004	0.081	±	0.013	79.6	±	2.8	79.0	±	12.8	0.910	
IA66-6	0.63	0.0536	±	0.0028	0.0496	±	0.0008	0.366	±	0.020	312.0	±	4.9	317.0	±	17.5	0.480	
IA66-8	0.90	0.0549	±	0.0040	0.0438	±	0.0009	0.331	±	0.025	276.3	±	5.4	290.5	±	21.9	0.130	
IA66-9	0.64	0.0585	±	0.0109	0.0126	±	0.0006	0.101	±	0.019	80.5	±	3.6	98.0	±	18.8	0.046*	
IA66-11	0.63	0.0652	±	0.0127	0.0129	±	0.0006	0.116	±	0.023	82.8	±	4.1	111.5	±	22.5	0.006*	
IA66-14	0.65	0.0521	±	0.0054	0.0746	±	0.0025	0.536	±	0.059	464.0	±	15.5	435.6	±	47.6	0.120	
		Weighted mean age of late Cretaceous peak									**80.6**	**±**	**1.9**	**MSWD = 0.8**				
Weighted mean age of late Cretaceous peak of lower andesite sequence (15IA01 and IA66)											**79.1**	**±**	**2.6**	**MSWD = 1.8**				
13IA07		**Sericite-chlorite-clay altered CEF andesite, close to a section of brecciated CEF, 290 m below surface**																
13IA07-2	0.31	0.0741	±	0.0048	0.1843	±	0.0053	1.883	±	0.135	1,090.2	±	31.5	1,075.1	±	76.9	0.500	
13IA07-3	0.68	0.0496	±	0.0162	0.0117	±	0.0009	0.080	±	0.027	75.1	±	5.5	78.3	±	26.2	0.800	
13IA07-9	0.87	0.0815	±	0.0038	0.2035	±	0.0032	2.288	±	0.114	1,194.4	±	18.9	1,208.5	±	60.0	0.400	
13IA07-11	0.11	0.0663	±	0.0034	0.1407	±	0.0022	1.285	±	0.069	848.7	±	13.4	839.2	±	45.0	0.520	
13IA07-14	2.28	0.0608	±	0.0036	0.0948	±	0.0016	0.795	±	0.050	584.0	±	10.0	594.1	±	37.0	0.450	
13IA07-17	0.72	0.0719	±	0.0183	0.0107	±	0.0007	0.106	±	0.028	68.8	±	4.6	102.7	±	27.0	0.008*	
		Weighted mean age^ of late Cretaceous ages									**71.4**	**±**	**3.5**					
IA84		**Potassic altered porphyritic subsurface diorite, 745 m below surface**																
IA84-1	0.51	0.0532	±	0.0153	0.0116	±	0.0008	0.085	±	0.025	74.3	±	4.8	83.0	±	24.4	0.450	
IA84-5	0.54	0.0504	±	0.0122	0.0120	±	0.0006	0.084	±	0.021	77.1	±	4.2	81.5	±	20.2	0.640	
IA84-7	0.67	0.0489	±	0.0053	0.0114	±	0.0003	0.077	±	0.009	73.3	±	1.9	75.4	±	8.3	0.600	
IA84-9	0.60	0.0722	±	0.0204	0.0104	±	0.0008	0.103	±	0.030	66.6	±	5.1	99.8	±	29.2	0.015*	
IA84-10	0.72	0.0522	±	0.0158	0.0107	±	0.0008	0.077	±	0.024	68.4	±	4.8	75.1	±	23.4	0.540	
IA84-12	0.72	0.0506	±	0.0169	0.0107	±	0.0008	0.075	±	0.026	68.8	±	5.2	73.3	±	25.1	0.700	
IA84-13	0.84	0.0627	±	0.0139	0.0122	±	0.0007	0.106	±	0.024	78.3	±	4.4	102.0	±	23.3	0.030*	

IA84-14	0.87	0.0495	±	0.0051	0.0429	±	0.0012	0.293	±	0.031	270.7	±	7.4	260.6	±	27.8	0.400	
IA84-16	0.84	0.0511	±	0.0160	0.0144	±	0.0010	0.102	±	0.033	92.3	±	6.7	98.3	±	31.6	0.680	
IA84-18	0.57	0.0762	±	0.0222	0.0112	±	0.0009	0.118	±	0.036	72.0	±	5.6	113.3	±	34.3	0.010*	
IA84-19	0.80	0.0704	±	0.0166	0.0123	±	0.0008	0.120	±	0.029	79.1	±	5.0	114.8	±	28.0	0.006*	DC
IA84-20	0.51	0.0598	±	0.0153	0.0109	±	0.0007	0.090	±	0.024	70.2	±	4.4	87.7	±	23.2	0.110	
IA84-21	0.51	0.0441	±	0.0126	0.0105	±	0.0006	0.064	±	0.019	67.5	±	4.1	63.0	±	18.4	0.600	
IA84-22	0.85	0.0530	±	0.0139	0.0111	±	0.0007	0.081	±	0.022	71.1	±	4.4	79.0	±	21.3	0.430	
IA84-25	0.56	0.0534	±	0.0197	0.0109	±	0.0009	0.080	±	0.030	69.8	±	5.6	78.3	±	29.6	0.540	
IA84-26	0.52	0.0437	±	0.0122	0.0113	±	0.0007	0.068	±	0.019	72.2	±	4.3	66.7	±	19.0	0.540	
IA84-29	0.42	0.0534	±	0.0157	0.0117	±	0.0008	0.086	±	0.026	75.3	±	5.0	84.2	±	25.4	0.450	
IA84-31	0.46	0.0435	±	0.0151	0.0115	±	0.0008	0.069	±	0.024	73.4	±	5.1	67.5	±	23.8	0.600	
IA84-34	0.48	0.0542	±	0.0185	0.0111	±	0.0009	0.083	±	0.029	71.4	±	5.5	81.2	±	28.4	0.460	
IA84-35	0.58	0.0685	±	0.0162	0.0113	±	0.0007	0.107	±	0.026	72.3	±	4.6	102.8	±	25.2	0.010*	
IA84-36	0.63	0.0490	±	0.0159	0.0118	±	0.0008	0.080	±	0.026	75.8	±	5.4	78.1	±	25.8	0.850	
IA84-37	0.71	0.0649	±	0.0125	0.0118	±	0.0006	0.106	±	0.021	75.8	±	4.0	102.1	±	20.4	0.005*	
IA84-38	0.78	0.0557	±	0.0108	0.0138	±	0.0007	0.106	±	0.021	88.1	±	4.4	102.0	±	20.4	0.140	
IA84-39	0.92	0.0606	±	0.0129	0.0111	±	0.0006	0.093	±	0.020	71.1	±	4.0	90.1	±	19.8	0.041*	
IA84-40	0.58	0.0582	±	0.0052	0.0431	±	0.0014	0.346	±	0.033	272.1	±	8.9	301.8	±	28.8	0.012*	
		Weighted mean age of late Cretaceous peak									**72.5**	**±**	**1.4**	**MSWD = 2.0**				

^ Error is internal 2σ. Satistically impractical to calculate MSWD value for two data points.

* For host rocks, data points with probability of concordance < 0.1 and > 0.01 are included into calculation

DC – Distinct old core age

c) Zircon U–Pb results of individual volcanic breccia (VBX) samples

Sample Name	Th/U	207Pb/206Pb		Error 2σ	206Pb/238U		Error 2σ	207Pb/235U		Error 2σ	238U-206Pb age (Ma)		Error 2σ	235U-207Pb age (Ma)		Error 2σ	Probability of concordance	Remarks
13IA06		**Phyllic altered pervasively silicified VBX, 60 m below surface**																
13IA06-7	0.70	0.0467	±	0.0188	0.0087	±	0.0007	0.056	±	0.023	55.8	±	4.7	55.3	±	22.7	0.960	
13IA06-9	0.79	0.0600	±	0.0219	0.0092	±	0.0008	0.076	±	0.029	58.9	±	5.1	74.3	±	27.9	0.240	
13IA06-10	1.17	0.0448	±	0.0111	0.0084	±	0.0005	0.052	±	0.013	54.0	±	3.1	51.4	±	13.1	0.680	
13IA06-11	0.71	0.0661	±	0.0181	0.0142	±	0.0010	0.130	±	0.037	91.2	±	6.5	124.0	±	35.0	0.043*	
13IA06-12	0.82	0.0482	±	0.0165	0.0085	±	0.0006	0.057	±	0.020	54.7	±	4.1	56.0	±	19.7	0.890	
13IA06-14	0.80	0.0567	±	0.0179	0.0106	±	0.0008	0.083	±	0.027	67.9	±	5.1	80.6	±	26.2	0.300	Rj
13IA06-18	0.88	0.0654	±	0.0235	0.0101	±	0.0009	0.091	±	0.034	64.5	±	5.9	88.2	±	32.6	0.120	
13IA06-20	0.82	0.0481	±	0.0071	0.0254	±	0.0011	0.169	±	0.026	161.9	±	6.8	158.3	±	24.3	0.740	
13IA06-21	0.85	0.0801	±	0.0215	0.0098	±	0.0008	0.109	±	0.030	63.1	±	4.9	104.7	±	29.3	0.002*	
13IA06-22	1.01	0.0591	±	0.0202	0.0087	±	0.0007	0.071	±	0.025	56.1	±	4.7	69.8	±	24.6	0.240	
		Weighted mean age of late Cretaceous to early Eocene peak									**57.0**	**±**	**3.6**	**MSWD = 3.1**				
IA49		**Phyllic to argillic altered VBX, 147 m below surface**																

IA49-1	0.74	0.0540	±	0.0245	0.0096	±	0.0009	0.072	±	0.033	61.9	±	6.1	70.4	±	32.7	0.580	
IA49-2	0.35	0.0811	±	0.0248	0.0090	±	0.0007	0.100	±	0.032	57.4	±	4.8	96.8	±	30.7	0.007*	
IA49-6	0.44	0.0562	±	0.0215	0.0088	±	0.0008	0.068	±	0.027	56.2	±	5.2	66.6	±	26.2	0.400	
IA49-7	1.05	0.0463	±	0.0203	0.0085	±	0.0008	0.054	±	0.024	54.4	±	5.2	53.5	±	24.0	0.930	
IA49-8	0.43	0.0839	±	0.0261	0.0097	±	0.0009	0.112	±	0.036	62.1	±	5.6	107.8	±	34.9	0.005*	
IA49-10	0.65	0.0407	±	0.0186	0.0090	±	0.0008	0.050	±	0.023	57.5	±	5.4	49.8	±	23.3	0.490	
IA49-11	0.72	0.0655	±	0.0242	0.0098	±	0.0009	0.089	±	0.034	63.0	±	5.7	86.3	±	32.8	0.130	
IA49-13	0.43	0.0701	±	0.0241	0.0090	±	0.0008	0.087	±	0.031	57.8	±	5.1	84.8	±	30.1	0.058*	
IA49-14	0.68	0.0918	±	0.0328	0.0086	±	0.0009	0.109	±	0.040	55.2	±	5.7	104.9	±	39.0	0.007*	
IA49-15	0.91	0.0356	±	0.0160	0.0084	±	0.0007	0.041	±	0.019	53.9	±	4.4	41.0	±	18.8	0.150	
IA49-16	0.66	0.0454	±	0.0243	0.0085	±	0.0009	0.053	±	0.029	54.3	±	5.7*	52.4	±	28.5	0.890	
IA49-17	0.89	0.0373	±	0.0164	0.0093	±	0.0008	0.048	±	0.022	59.8	±	4.9	47.6	±	21.3	0.230	
IA49-20	0.46	0.0575	±	0.0254	0.0097	±	0.0010	0.077	±	0.035	62.1	±	6.4*	75.1	±	34.1	0.420	
IA49-22	0.71	0.0645	±	0.0258	0.0091	±	0.0009	0.081	±	0.034	58.6	±	5.9	79.3	±	32.7	0.180	
IA49-26	0.90	0.0638	±	0.0231	0.0086	±	0.0008	0.076	±	0.028	55.4	±	5.1	74.3	±	27.8	0.150	
IA49-33	0.75	0.0216	±	0.0157	0.0085	±	0.0007	0.025	±	0.018	54.6	±	4.6	25.4	±	18.5	0.001*	
IA49-34	0.78	0.0495	±	0.0219	0.0086	±	0.0008	0.059	±	0.027	55.4	±	4.8	58.1	±	26.2	0.830	
IA49-36	0.63	0.0560	±	0.0137	0.0106	±	0.0006	0.082	±	0.020	67.8	±	3.9	79.6	±	20.0	0.210	Rj
		Weighted mean age of late Cretaceous to early Eocene peak									**57.3**	**±**	**1.5**	**MSWD = 1.3**				
		Weighted mean age of late Cretaceous to early Eocene peak of VBX									**57.2**	**±**	**1.4**	**MSWD = 1.7**				

* For host rocks, data points with probability of concordance < 0.1 and > 0.01 or error > 10.0 % and < 10 % are included into calculation

Rj – Age is statistically rejected during calculation of weighted mean for volcanic breccia unit

d) Zircon U–Pb results of individual porphyritic tonalite (PTN) samples

Sample Name	Th/U	207Pb/206Pb		Error 2σ	206Pb/238U		Error 2σ	207Pb/235U		Error 2σ	238U-206Pb age (Ma)		Error 2σ	235U-207Pb age (Ma)		Error 2σ	Probability of concordance	Remarks
15IA09		**Sericite-chlorite-clay altered PTN collected from 642 m below surface**																
15IA09-6(2)	1.11	0.0449	±	0.0145	0.0083	±	0.0006	0.051	±	0.017	53.3	±	3.7	51.0	±	16.8	0.770	
15IA09-7	0.92	0.0405	±	0.0135	0.0090	±	0.0006	0.050	±	0.017	57.9	±	3.9	50.0	±	17.0	0.330	
15IA09-21	0.89	0.0474	±	0.0129	0.0091	±	0.0006	0.059	±	0.017	58.4	±	3.6	58.7	±	16.3	0.970	DC
15IA09-23	0.43	0.0539	±	0.0101	0.0084	±	0.0004	0.062	±	0.012	53.8	±	2.5	61.4	±	11.9	0.180	
15IA09-26	1.27	0.0468	±	0.0130	0.0080	±	0.0005	0.052	±	0.015	51.3	±	3.2	51.0	±	14.5	0.980	
		Weighted mean age of the Palaeocene to early Eocene ages									**53.8**	**±**	**3.9**	**MSWD = 2.4**				
IA29		**Sericite-chlorite-clay altered PTN collected from 248 m below surface**																
IA29-1	0.79	0.0633	±	0.0195	0.0084	±	0.0007	0.073	±	0.023	54.0	±	4.3	71.9	±	22.9	0.097	
IA29-3	0.91	0.0425	±	0.0125	0.0119	±	0.0008	0.070	±	0.021	76.1	±	4.9	68.3	±	20.6	0.420	DC
IA29-4	0.80	0.0402	±	0.0162	0.0081	±	0.0007	0.045	±	0.018	51.9	±	4.3	44.6	±	18.3	0.400	
IA29-6	0.87	0.0579	±	0.0143	0.0080	±	0.0005	0.064	±	0.016	51.2	±	3.2	62.7	±	15.9	0.130	

IA29-8	0.99	0.0585	±	0.0152	0.0088	±	0.0006	0.071	±	0.019	56.3	±	3.7	69.4	±	18.6	0.130	
IA29-11	0.94	0.0420	±	0.0157	0.0081	±	0.0006	0.047	±	0.018	51.9	±	3.7	46.4	±	17.7	0.520	
IA29-13	0.91	0.0484	±	0.0162	0.0086	±	0.0006	0.058	±	0.020	55.3	±	3.8	56.8	±	19.3	0.870	
IA29-15	0.89	0.0383	±	0.0153	0.0079	±	0.0006	0.041	±	0.017	50.4	±	3.6	41.2	±	16.8	0.250	
IA29-16	0.72	0.0438	±	0.0183	0.0085	±	0.0007	0.051	±	0.022	54.3	±	4.3	50.6	±	21.5	0.720	
IA29-24	0.72	0.0620	±	0.0181	0.0082	±	0.0006	0.070	±	0.021	52.9	±	3.8	69.2	±	20.8	0.099	
		Weighted mean age of the Palaeocene to early Eocene ages									**53.0**	**±**	**1.2**	**MSWD = 1.13**				
IA80		**Sericite-chlorite-clay altered PTN collected from 338 m below surface**																
IA80-1	0.79	0.0558	±	0.0185	0.0083	±	0.0006	0.064	±	0.022	53.3	±	4.0	62.9	±	21.4	0.350	
IA80-2	0.82	0.0529	±	0.0096	0.0081	±	0.0004	0.059	±	0.011	52.0	±	2.3	58.2	±	10.9	0.230	
IA80-5	0.94	0.0583	±	0.0199	0.0088	±	0.0007	0.071	±	0.025	56.7	±	4.4	69.6	±	24.4	0.260	
IA80-6	0.91	0.0373	±	0.0132	0.0086	±	0.0006	0.044	±	0.016	55.2	±	3.6	43.9	±	15.8	0.130	
IA80-8	0.60	0.0570	±	0.0206	0.0083	±	0.0007	0.065	±	0.024	53.2	±	4.3	64.1	±	23.7	0.330	
IA80-10	0.21	0.0522	±	0.0035	0.0302	±	0.0006	0.217	±	0.015	191.6	±	3.9	199.5	±	14.0	0.200	
IA80-12	0.97	0.0517	±	0.0138	0.0088	±	0.0005	0.063	±	0.017	56.3	±	3.4	61.6	±	16.9	0.510	
IA80-16	0.67	0.0478	±	0.0181	0.0085	±	0.0007	0.056	±	0.022	54.3	±	4.2	55.1	±	21.3	0.940	
IA80-20	1.18	0.0426	±	0.0309	0.0078	±	0.0004	0.046	±	0.033	49.8	±	2.8	45.3	±	32.9	0.770	
		Weighted mean age of the Palaeocene to early Eocene ages									**53.2**	**±**	**2.0**	**MSWD = 2.1**				
IA81		**Potassic altered PTN collected from 726 m below surface**																
IA81-1(2)	0.85	0.0496	±	0.0094	0.0089	±	0.0004	0.061	±	0.012	57.3	±	2.7	60.2	±	11.7	0.600	
IA81-9	0.82	0.0503	±	0.0065	0.0088	±	0.0003	0.061	±	0.008	56.5	±	1.8	60.1	±	7.9	0.330	DC
IA81-20	0.60	0.0589	±	0.0167	0.0082	±	0.0006	0.067	±	0.020	52.9	±	3.8	65.7	±	19.3	0.160	
IA81-32	0.65	0.0580	±	0.0142	0.0084	±	0.0005	0.067	±	0.017	54.0	±	3.4	66.1	±	16.8	0.130	
		Weighted mean age of the Palaeocene to early Eocene ages									**55.2**	**±**	**5.8**	**MSWD = 2.1**				
1006		**Sericite-chlorite-clay altered PTN collected from 520 m below surface from an uninspected drill core located W of 11-112 (shown on Fig. 3)**																
1006-1	0.62	0.0518	±	0.0122	0.0085	±	0.0005	0.061	±	0.015	54.4	±	3.2	59.7	±	14.5	0.440	
1006-7	0.97	0.0515	±	0.0112	0.0080	±	0.0004	0.057	±	0.013	51.4	±	2.9	56.1	±	12.6	0.430	
1006-13	0.82	0.0455	±	0.0113	0.0091	±	0.0005	0.057	±	0.015	58.7	±	3.3	56.6	±	14.4	0.760	Rj
1006-16	0.51	0.0452	±	0.0155	0.0081	±	0.0006	0.051	±	0.018	52.2	±	3.8	50.2	±	17.5	0.810	
1006-29	0.66	0.0395	±	0.0136	0.0088	±	0.0006	0.048	±	0.017	56.3	±	3.7	47.4	±	16.6	0.260	
1006-36	0.57	0.0440	±	0.0122	0.0082	±	0.0005	0.050	±	0.014	52.7	±	3.1	49.4	±	13.9	0.620	
1006-39	0.46	0.0492	±	0.0156	0.0084	±	0.0006	0.057	±	0.018	54.1	±	3.8	56.4	±	18.3	0.790	
		Weighted mean age of the Palaeocene to early Eocene ages									**54.1**	**±**	**2.4**	**MSWD = 2.4**				
		Weighted mean age of the Palaeocene to early Eocene ages of PTN									**53.51**	**±**	**0.8**	**MSWD = 1.5**				

DC – Distinct old core age
Rj – Age is statistically rejected during calculation of weighted mean for porphyritic tonalite unit

e) Zircon U–Pb results of individual porphyritic quartz monzonite (PMN) samples

Sample Name	Th/U	207Pb/206Pb		Error 2σ	206Pb/238U		Error 2σ	207Pb/235U		Error 2σ	238U-206Pb age (Ma)		Error 2σ	235U-207Pb age (Ma)		Error 2σ	Probability of concordance	Remarks
13IA02		**Low intensity phyllic altered and silicified PMN collected from 150 m below surface**																
13IA02-1	0.71	0.0624	±	0.0214	0.0076	±	0.0006	0.066	±	0.023	49.0	±	3.8	64.6	±	22.7	0.150	
13IA02-2	0.58	0.0488	±	0.0186	0.0079	±	0.0006	0.053	±	0.021	50.7	±	3.8	52.5	±	20.4	0.850	
13IA02-3	0.57	0.0440	±	0.0090	0.0077	±	0.0004	0.047	±	0.010	49.5	±	2.5	46.4	±	9.7	0.510	
13IA02-5	0.82	0.0414	±	0.0263	0.0100	±	0.0010	0.057	±	0.037	64.4	±	6.1	56.6	±	36.4	0.660	
13IA02-6	0.37	0.0440	±	0.0150	0.0074	±	0.0005	0.045	±	0.016	47.6	±	3.2	44.7	±	15.5	0.700	
13IA02-7	0.91	0.0549	±	0.0171	0.0082	±	0.0006	0.062	±	0.020	52.9	±	3.7	61.4	±	19.6	0.360	
13IA02-8	0.68	0.0513	±	0.0202	0.0080	±	0.0006	0.056	±	0.023	51.1	±	4.0	55.6	±	22.4	0.670	
13IA02-11	0.77	0.0510	±	0.0192	0.0076	±	0.0006	0.053	±	0.020	48.8	±	3.7	52.8	±	20.2	0.680	
13IA02-13	1.22	0.0473	±	0.0139	0.0072	±	0.0005	0.047	±	0.014	46.1	±	3.0	46.5	±	14.0	0.960	
13IA02-14	0.41	0.0534	±	0.0177	0.0077	±	0.0006	0.057	±	0.019	49.5	±	3.6	56.1	±	19.1	0.470	
13IA02-15	0.79	0.0494	±	0.0096	0.0080	±	0.0004	0.054	±	0.011	51.1	±	2.8	53.6	±	10.8	0.620	
13IA02-19	0.75	0.0646	±	0.0242	0.0097	±	0.0009	0.086	±	0.033	62.0	±	5.5	83.8	±	32.3	0.150	DC
13IA02-21	0.46	0.0466	±	0.0138	0.0080	±	0.0005	0.051	±	0.015	51.1	±	3.1	50.6	±	15.3	0.950	
		Youngest gaussian peak age obtained by deconvolution method									**49.65**	**±**	**0.99**	**Fraction = 0.85**	**of**	**13**		
		Subordinate peak age obtained by deconvolution method									**63.1**	**±**	**4.1**	**Fraction = 0.15**	**of**	**13**		
13IA04		**Sericite-chlorite-clay to potassic altered PMN collected from 365 m below surface**																
13IA04-1	0.42	0.0629	±	0.0220	0.0091	±	0.0007	0.079	±	0.028	58.6	±	4.8	77.4	±	27.8	0.150	
13IA04-2	0.65	0.0528	±	0.0030	0.369	±	0.022	0.0507	±	0.0009	319.0	±	5.9	319.1	±	19.3	0.990	DC
13IA04-3	0.46	0.0571	±	0.0184	0.0090	±	0.0007	0.071	±	0.024	58.1	±	4.2	69.9	±	23.1	0.280	
13IA04-4	0.63	0.0613	±	0.0227	0.0087	±	0.0007	0.074	±	0.028	56.0	±	4.7	72.2	±	27.4	0.210	
13IA04-6	0.32	0.0514	±	0.0097	0.0097	±	0.0004	0.069	±	0.013	62.4	±	2.7	67.8	±	13.1	0.390	
13IA04-7	0.83	0.0433	±	0.0108	0.0120	±	0.0006	0.072	±	0.018	77.1	±	3.9	70.4	±	17.9	0.440	DC
13IA04-8	0.61	0.0522	±	0.0238	0.0081	±	0.0008	0.058	±	0.027	51.9	±	4.9	57.4	±	26.7	0.670	
13IA04-9	0.51	0.0484	±	0.0273	0.0077	±	0.0008	0.052	±	0.030	49.5	±	5.0	51.0	±	29.2	0.920	
13IA04-11	0.52	0.0602	±	0.0248	0.0078	±	0.0007	0.065	±	0.027	50.3	±	4.4	63.9	±	26.9	0.290	
13IA04-13	0.61	0.0469	±	0.0273	0.0078	±	0.0008	0.051	±	0.030	50.4	±	5.1	50.2	±	29.7	0.991	
13IA04-14	0.69	0.0531	±	0.0231	0.0082	±	0.0007	0.060	±	0.027	52.6	±	4.6	59.1	±	26.2	0.600	
13IA04-18	1.06	0.0595	±	0.0180	0.0077	±	0.0006	0.063	±	0.020	49.3	±	3.6	62.1	±	19.4	0.170	
		Youngest gaussian peak age obtained by deconvolution method									**51.6**	**±**	**2.4**	**Fraction = 0.63**	**of**	**9**		
		Subordinate peak age obtained by deconvolution method									**60.4**	**±**	**2.2**	**Fraction = 0.37**	**of**	**9**		
13IA11		**Relatively fresh PMN collected from 500 m below surface close to brecciated CEF**																
13IA11-1	0.70	0.0520	±	0.0114	0.0123	±	0.0006	0.088	±	0.020	79.0	±	4.1	86.0	±	19.3	0.440	DC
13IA11-2	0.41	0.0491	±	0.0230	0.0091	±	0.0009	0.062	±	0.029	58.3	±	5.8	60.6	±	29.0	0.870	
13IA11-4	0.60	0.0477	±	0.0088	0.0113	±	0.0005	0.074	±	0.014	72.3	±	3.1	72.6	±	13.8	0.960	DC
13IA11-5	0.43	0.0556	±	0.0142	0.0088	±	0.0005	0.067	±	0.018	56.3	±	3.4	66.1	±	17.4	0.230	
13IA11-6	0.64	0.0478	±	0.0071	0.0112	±	0.0004	0.074	±	0.011	71.9	±	2.6	72.4	±	11.1	0.930	DC

13IA11-8	0.47	0.0481	±	0.0055	0.0114	±	0.0004	0.076	±	0.009	73.0	±	2.3	73.9	±	8.8	0.830	
13IA11-17	0.48	0.0462	±	0.0079	0.0095	±	0.0004	0.061	±	0.011	61.1	±	2.4	59.8	±	10.5	0.800	DC
13IA11-19	0.93	0.0592	±	0.0171	0.0090	±	0.0006	0.073	±	0.022	57.6	±	4.1	71.8	±	21.4	0.160	DC
13IA11-20	0.97	0.0407	±	0.0156	0.0093	±	0.0007	0.052	±	0.020	59.4	±	4.5	51.5	±	20.1	0.410	
13IA11-21	1.04	0.0406	±	0.0141	0.0095	±	0.0007	0.053	±	0.019	60.7	±	4.2	52.4	±	18.6	0.350	
13IA11-22	0.61	0.0563	±	0.0141	0.0094	±	0.0006	0.073	±	0.019	60.0	±	3.6	71.1	±	18.3	0.200	
13IA11-23	0.92	0.0406	±	0.0130	0.0086	±	0.0006	0.048	±	0.016	55.4	±	3.6	47.9	±	15.6	0.320	
13IA11-25	0.16	0.0544	±	0.0044	0.321	±	0.027	0.0428	±	0.0011	270.2	±	6.7	282.7	±	23.8	0.210	
13IA11-26	0.53	0.0443	±	0.0098	0.0127	±	0.0006	0.078	±	0.017	81.4	±	3.6	76.0	±	17.1	0.500	
13IA11-27	0.86	0.0402	±	0.0335	0.0081	±	0.0008	0.045	±	0.037	51.7	±	5.1	44.3	±	37.2	0.680	
13IA11-28	0.70	0.0377	±	0.0218	0.0091	±	0.0007	0.047	±	0.028	58.2	±	4.5	46.8	±	27.3	0.390	
13IA11-30	0.75	0.0419	±	0.0200	0.0091	±	0.0007	0.052	±	0.025	58.1	±	4.2	51.8	±	25.0	0.600	DC
13IA11-32	0.77	0.0577	±	0.0196	0.0079	±	0.0005	0.063	±	0.022	50.6	±	3.4	61.8	±	21.4	0.280	
13IA11-33	0.56	0.0458	±	0.0144	0.0083	±	0.0006	0.052	±	0.017	53.1	±	3.6	51.7	±	16.6	0.860	
13IA11-36	0.81	0.0396	±	0.0170	0.0078	±	0.0006	0.043	±	0.019	50.1	±	4.1	42.4	±	18.5	0.390	
13IA11-37	1.05	0.0498	±	0.0184	0.0080	±	0.0006	0.055	±	0.021	51.4	±	4.1	54.3	±	20.6	0.770	
13IA11-38	0.73	0.0433	±	0.0157	0.0076	±	0.0006	0.046	±	0.017	49.0	±	3.7	45.3	±	16.8	0.640	
13IA11-39	1.30	0.0485	±	0.0130	0.0076	±	0.0005	0.051	±	0.014	48.6	±	3.0	50.1	±	13.8	0.810	
13IA11-41	1.01	0.0474	±	0.0165	0.0071	±	0.0005	0.046	±	0.017	45.7	±	3.3	46.1	±	16.4	0.960	
		Youngest gaussian peak age obtained by deconvolution method									**49.7**	**±**	**1.3**	**Fraction = 0.44**	**of**	**19**		
		Subordinate peak age obtained by deconvolution method									**58.75**	**±**	**1.2**	**Fraction = 0.56**	**of**	**19**		
IA97		**Phyllic altered PMN collected from 374 m below surface close to a section of xenolith-rich quartz porphyry**																
IA97-1	0.70	0.0469	±	0.0032	0.0098	±	0.0003	0.063	±	0.005	62.8	±	1.7	62.3	±	4.5	0.820	DC
IA97-4	0.49	0.0492	±	0.0083	0.0108	±	0.0005	0.074	±	0.013	69.5	±	3.0	72.0	±	12.6	0.670	
IA97-5	0.45	0.0490	±	0.0079	0.0077	±	0.0003	0.052	±	0.009	49.5	±	2.1	51.6	±	8.6	0.620	
IA97-7	1.33	0.0540	±	0.0135	0.0083	±	0.0005	0.062	±	0.016	53.3	±	3.2	60.9	±	15.7	0.310	
IA97-9	0.54	0.0398	±	0.0105	0.0120	±	0.0006	0.066	±	0.018	77.0	±	4.0	64.9	±	17.5	0.140	
IA97-10	0.55	0.0518	±	0.0108	0.0123	±	0.0006	0.087	±	0.019	78.5	±	3.7	85.1	±	18.2	0.440	
IA97-12	0.86	0.0513	±	0.0146	0.0078	±	0.0005	0.055	±	0.016	50.2	±	3.1	54.7	±	15.9	0.550	
IA97-13	0.94	0.0487	±	0.0204	0.0091	±	0.0008	0.061	±	0.026	58.2	±	4.9	59.9	±	25.6	0.880	
IA97-16	1.07	0.0524	±	0.0215	0.0092	±	0.0008	0.067	±	0.028	59.2	±	5.1	65.6	±	27.5	0.630	
IA97-18	0.87	0.0510	±	0.0133	0.0084	±	0.0005	0.059	±	0.016	54.1	±	3.2	58.4	±	15.6	0.560	
IA97-21	0.50	0.0630	±	0.0237	0.0078	±	0.0007	0.068	±	0.026	50.1	±	4.4	66.7	±	25.7	0.180	
IA97-22	0.82	0.0590	±	0.0142	0.0083	±	0.0005	0.067	±	0.017	53.0	±	3.1	65.9	±	16.4	0.095	
IA97-23	0.30	0.0494	±	0.0068	0.0087	±	0.0003	0.059	±	0.008	55.8	±	1.9	58.4	±	8.3	0.510	
		Youngest gaussian peak age obtained by deconvolution method									**52.85**	**±**	**1.1**	**Fraction = 0.78**	**of**	**10**		
		Subordinate peak age obtained by deconvolution method									**62.3**	**±**	**1.7**	**Fraction = 0.22**	**of**	**10**		
		Youngest gaussian peak age of PMN obtained by deconvolution method									**50.29**	**±**	**0.65**	**Fraction = 0.62**	**of**	**51**		
		Subordinate peak age of PMN obtained by deconvolution method									**59.51**	**±**	**0.8**	**Fraction = 0.38**	**of**	**51**		
		Youngest gaussian peak weighted mean age of PMN									**50.37**	**±**	**0.79**	**MSWD = 1.6**				

DC – Distinct old core age

f) Zircon U–Pb results of individual leucocratic quartz porphyry (LQP) samples

Sample Name	Th/U	207Pb/206Pb		Error 2σ	206Pb/238U		Error 2σ	207Pb/235U		Error 2σ	238U-206Pb age (Ma)		Error 2σ	235U-207Pb age (Ma)		Error 2σ	Probability of concordance	Remarks
13IA05		**Phyllic altered LQP (~10% quartz "eyes"), 266 m below surface**																
13IA05-01	0.95	0.0470	±	0.0191	0.0075	±	0.0006	0.048	±	0.020	47.9	±	3.9	48.0	±	19.9	0.996	
13IA05-02	0.77	0.0522	±	0.0147	0.0077	±	0.0005	0.056	±	0.016	49.7	±	3.1	55.0	±	15.9	0.480	
13IA05-4	0.63	0.0518	±	0.0105	0.0115	±	0.0006	0.082	±	0.017	73.9	±	3.7	80.4	±	16.8	0.410	
13IA05-6	0.65	0.0478	±	0.0070	0.0118	±	0.0005	0.078	±	0.012	75.6	±	3.0	76.0	±	11.5	0.940	DC
13IA05-8	1.16	0.0556	±	0.0146	0.0082	±	0.0005	0.063	±	0.017	52.8	±	3.2	62.2	±	16.7	0.240	
13IA05-10	0.68	0.0559	±	0.0173	0.0078	±	0.0005	0.060	±	0.019	50.1	±	3.4	59.3	±	18.8	0.300	
13IA05-11	0.59	0.0500	±	0.0087	0.0118	±	0.0005	0.082	±	0.015	75.9	±	2.9	79.7	±	14.2	0.570	
13IA05-12	0.45	0.0430	±	0.0109	0.0120	±	0.0006	0.071	±	0.018	76.7	±	3.8	69.6	±	18.0	0.410	
13IA05-14	1.26	0.0440	±	0.0116	0.0084	±	0.0004	0.051	±	0.014	54.1	±	2.7	50.6	±	13.5	0.600	
13IA05-16	0.47	0.0501	±	0.0057	0.0144	±	0.0004	0.100	±	0.012	92.4	±	2.6	96.6	±	11.4	0.430	DC
13IA05-17	0.88	0.0512	±	0.0172	0.0095	±	0.0006	0.067	±	0.023	60.8	±	4.0	65.8	±	22.5	0.640	
13IA05-19	1.47	0.0414	±	0.0128	0.0080	±	0.0004	0.046	±	0.014	51.6	±	2.8	45.6	±	14.3	0.380	
13IA05-21	0.47	0.0481	±	0.0111	0.0134	±	0.0006	0.089	±	0.021	85.6	±	4.0	86.3	±	20.3	0.940	
13IA05-23	0.93	0.0599	±	0.0218	0.0085	±	0.0006	0.070	±	0.026	54.7	±	3.9	69.1	±	25.6	0.240	
13IA05-24	0.44	0.0507	±	0.0041	0.0117	±	0.0003	0.082	±	0.007	74.9	±	1.8	79.7	±	6.6	0.110	
13IA05-25	0.85	0.0474	±	0.0208	0.0086	±	0.0006	0.056	±	0.025	55.5	±	4.1	55.8	±	24.8	0.980	
13IA05-26	0.82	0.0492	±	0.0195	0.0082	±	0.0006	0.056	±	0.022	52.6	±	3.7	55.0	±	22.1	0.820	
13IA05-29	0.82	0.0498	±	0.0122	0.0086	±	0.0005	0.059	±	0.015	55.4	±	2.9	58.4	±	14.6	0.660	
13IA05-30	1.16	0.0399	±	0.0125	0.0080	±	0.0005	0.044	±	0.014	51.6	±	3.0	43.9	±	14.0	0.260	
13IA05-31	0.66	0.0541	±	0.0106	0.0080	±	0.0004	0.060	±	0.012	51.6	±	2.4	59.1	±	11.9	0.180	
13IA05-33	0.51	0.0488	±	0.0122	0.0104	±	0.0006	0.070	±	0.018	66.7	±	3.6	68.7	±	17.6	0.810	
13IA05-34	0.52	0.0509	±	0.0094	0.0115	±	0.0005	0.080	±	0.015	73.5	±	3.2	78.6	±	14.9	0.470	
13IA05-43	1.12	0.0611	±	0.0185	0.0082	±	0.0006	0.069	±	0.021	52.6	±	3.8	67.8	±	21.0	0.130	
13IA05-48	0.51	0.0412	±	0.0084	0.0117	±	0.0005	0.066	±	0.014	74.8	±	3.5	65.2	±	13.6	0.130	
		Youngest gaussian peak age obtained by deconvolution method									**52.3**	**±**	**0.88**	**Fraction = 0.93**	**of**	**14**		
		Subordinate peak age obtained by deconvolution method									**60.8**	**±**	**4.2**	**Fraction = 0.07**	**of**	**14**		
13IA10		**Phyllic (to argillic) altered LQP (~5% quartz "eyes"), 70 m below surface**																
13IA10-02	0.47	0.0441	±	0.0180	0.0078	±	0.0006	0.047	±	0.020	49.9	±	4.0	46.9	±	19.4	0.750	
13IA10-03	0.55	0.0535	±	0.0219	0.0076	±	0.0007	0.056	±	0.024	49.0	±	4.3	55.5	±	23.2	0.550	
13IA10-05	0.69	0.0434	±	0.0162	0.0082	±	0.0006	0.049	±	0.019	52.9	±	3.9	48.9	±	18.6	0.650	
13IA10-07	0.62	0.0401	±	0.0152	0.0087	±	0.0006	0.048	±	0.018	55.7	±	4.0	47.6	±	18.3	0.350	
13IA10-09	0.89	0.0385	±	0.0160	0.0084	±	0.0005	0.045	±	0.019	54.0	±	3.4	44.3	±	18.7	0.280	
13IA10-10	0.76	0.0531	±	0.0157	0.0094	±	0.0006	0.069	±	0.021	60.6	±	3.6	67.9	±	20.5	0.450	
13IA10-11	0.63	0.0455	±	0.0164	0.0075	±	0.0005	0.047	±	0.017	48.0	±	3.0	46.5	±	17.1	0.860	

13IA10-12	0.23	0.0490	±	0.0057	0.0343	±	0.0012	0.232	±	0.028	217.6	±	7.4	211.7	±	25.6	0.590	
13IA10-13	0.71	0.0414	±	0.0188	0.0075	±	0.0005	0.043	±	0.020	48.4	±	3.3	42.7	±	19.6	0.550	
13IA10-16	1.78	0.0527	±	0.0084	0.0075	±	0.0003	0.054	±	0.009	48.1	±	2.0	53.8	±	8.8	0.170	
13IA10-17	0.77	0.0396	±	0.0109	0.0086	±	0.0005	0.047	±	0.013	55.0	±	3.2	46.4	±	13.1	0.170	
13IA10-20	0.55	0.0610	±	0.0187	0.0080	±	0.0006	0.067	±	0.021	51.3	±	3.8	66.0	±	20.9	0.140	
		Youngest gaussian peak age obtained by deconvolution method									**48.78**	**±**	**1.3**	**Fraction = 0.56**	**of**	**11**		
		Subordinate peak age obtained by deconvolution method									**55.71**	**±**	**1.9**	**Fraction = 0.44**	**of**	**11**		
Mo6		**Phyllic altered LQP (~10% quartz "eyes"), 347 m below surface in a xenolith and clast-rich section**																
Mo6-4	0.46	0.0611	±	0.0179	0.0084	±	0.0006	0.070	±	0.021	53.7	±	3.8	69.1	±	20.9	0.120	
Mo6-10	0.51	0.0555	±	0.0122	0.0116	±	0.0007	0.089	±	0.020	74.5	±	4.2	86.5	±	19.7	0.190	
Mo6-12	0.64	0.0455	±	0.0101	0.0114	±	0.0006	0.072	±	0.016	73.2	±	3.8	70.2	±	16.0	0.690	DC
Mo6-16	0.70	0.0476	±	0.0081	0.0106	±	0.0005	0.070	±	0.012	68.3	±	3.1	68.6	±	12.1	0.950	
Mo6-19	0.52	0.0532	±	0.0145	0.0082	±	0.0005	0.060	±	0.017	52.4	±	3.3	59.0	±	16.5	0.400	
Mo6-21	0.84	0.0615	±	0.0200	0.0105	±	0.0008	0.089	±	0.030	67.5	±	5.3	86.9	±	29.1	0.160	
Mo6-22	0.77	0.0512	±	0.0102	0.0082	±	0.0004	0.058	±	0.012	52.7	±	2.6	57.2	±	11.7	0.410	
Mo6-27	0.99	0.0486	±	0.0133	0.0079	±	0.0005	0.053	±	0.015	50.5	±	3.2	52.1	±	14.6	0.810	
		Weighted mean age # of the youngest gaussian peak									**52.3**	**±**	**1.5**	**MSWD = 0.65**				
IA76		**Phyllic altered LQP (~5-8% quartz "eyes"), 214 m below surface in a xenolith and clast-rich section**																
IA76-1	0.66	0.0473	±	0.0074	0.0113	±	0.0005	0.074	±	0.012	72.5	±	3.1	72.3	±	11.8	0.970	DC
IA76-4	0.45	0.0524	±	0.0065	0.0488	±	0.0019	0.352	±	0.046	307.0	±	12.1	306.4	±	39.9	0.970	
IA76-7	0.81	0.0504	±	0.0214	0.0108	±	0.0010	0.075	±	0.033	69.2	±	6.6	73.4	±	32.0	0.780	DC
IA76-9	1.16	0.0442	±	0.0151	0.0083	±	0.0006	0.050	±	0.018	53.0	±	3.7	49.8	±	17.4	0.700	
IA76-10	2.80	0.0453	±	0.0142	0.0082	±	0.0005	0.051	±	0.016	52.8	±	3.5	50.9	±	16.3	0.810	
IA76-12	0.50	0.0553	±	0.0040	0.0462	±	0.0010	0.352	±	0.026	291.2	±	6.0	306.4	±	22.9	0.110	DC
IA76-14	0.68	0.0455	±	0.0177	0.0091	±	0.0007	0.057	±	0.023	58.4	±	4.7	56.4	±	22.4	0.850	
IA76-18	0.50	0.0596	±	0.0173	0.0081	±	0.0005	0.067	±	0.020	52.0	±	3.4	65.5	±	19.5	0.150	
IA76-19	0.77	0.0533	±	0.0202	0.0096	±	0.0008	0.071	±	0.027	61.9	±	4.8	69.5	±	26.9	0.550	
IA76-21	0.56	0.0433	±	0.0079	0.0115	±	0.0004	0.068	±	0.013	73.5	±	2.8	67.1	±	12.5	0.290	
IA76-23	0.52	0.0437	±	0.0097	0.0123	±	0.0006	0.074	±	0.017	78.8	±	3.6	72.6	±	16.5	0.420	
IA76-24	0.49	0.0546	±	0.0129	0.0120	±	0.0006	0.090	±	0.022	76.8	±	4.1	87.7	±	21.2	0.270	
		Youngest gaussian peak age obtained by deconvolution method									**52.7**	**±**	**2.1**	**Fraction = 0.62**	**of**	**5**		
		Subordinate peak age obtained by deconvolution method									**60.1**	**±**	**3.5**	**Fraction = 0.38**	**of**	**5**		
		Youngest gaussian peak age of LQP obtained by deconvolution method									**51.74**	**±**	**0.6**	**Fraction = 0.88**	**of**	**34**		
		Subordinate peak age of LQP obtained by deconvolution method									**60.3**	**±**	**2.4**	**Fraction = 0.12**	**of**	**34**		
		Youngest gaussian peak weighted mean age of LQP									**51.73**	**±**	**0.88**	**MSWD = 2.2**				

The sample shows unimodal age distribution, weighted mean is calculated

DC – Distinct old core age

g) Zircon U–Pb results of individual porphyritic granodiorite (PGD) samples

Sample Name	Th/U	207Pb/206Pb		Error 2σ	206Pb/238U		Error 2σ	207Pb/235U		Error 2σ	238U-206Pb age (Ma)		Error 2σ	235U-207Pb age (Ma)		Error 2σ	Probability of concordance	Remarks
IA37		**Low intensity sericite-chlorite-clay altered PGD, 386 m below surface**																
IA37-22	0.86	0.0576	±	0.0250	0.0094	±	0.0009	0.075	±	0.033	60.5	±	5.9	73.2	±	32.6	0.410	
IA37-25	0.92	0.0453	±	0.0208	0.0083	±	0.0007	0.052	±	0.024	53.3	±	4.7	51.4	±	24.0	0.870	
IA37-30	1.24	0.0480	±	0.0159	0.0091	±	0.0006	0.060	±	0.020	58.3	±	4.0	59.3	±	20.0	0.920	
IA37-32	1.13	0.0599	±	0.0223	0.0078	±	0.0007	0.064	±	0.025	50.0	±	4.2	63.3	±	24.2	0.250	
Weighted mean age^ of the youngest gaussian peak											**51.5**	**±**	**3.1**					
Weighted mean age^ ## of the subordinate peak											**59.0**	**±**	**3.3**					
IA47		**Relatively unaltered PGD, 70 m below surface**																
IA47-1	0.90	0.0493	±	0.0165	0.0081	±	0.0007	0.055	±	0.019	52.0	±	4.8	54.3	±	18.9	0.790	
IA47-2	0.85	0.0449	±	0.0181	0.0085	±	0.0008	0.053	±	0.022	54.8	±	5.4	52.3	±	21.7	0.810	
IA47-9	1.15	0.0591	±	0.0204	0.0073	±	0.0006	0.059	±	0.021	46.9	±	3.9	58.7	±	20.8	0.230	
IA47-13	1.23	0.0576	±	0.0168	0.0081	±	0.0006	0.064	±	0.019	52.0	±	3.9	63.3	±	19.0	0.210	
IA47-14	0.61	0.0432	±	0.0159	0.0080	±	0.0006	0.048	±	0.018	51.5	±	4.0	47.4	±	17.8	0.630	
IA47-20	0.85	0.0634	±	0.0248	0.0090	±	0.0009	0.079	±	0.032	57.7	±	5.6	76.8	±	31.0	0.190	
IA47-25	1.04	0.0411	±	0.0203	0.0079	±	0.0007	0.045	±	0.022	50.4	±	4.5	44.2	±	22.2	0.560	
Weighted mean age # of the youngest gaussian peak											**51.5**	**±**	**3.0**	**MSWD = 2.0**				
Youngest gaussian peak age of PGD obtained by deconvolution method											**50.98**	**±**	**1.7**	**Fraction = 0.70**	**of**	**11**		
Subordinate peak age of PGD obtained by deconvolution method											**58.1**	**±**	**3.2**	**Fraction = 0.30**	**of**	**11**		
Youngest gaussian peak weighted mean age of PGD											**51.0**	**±**	**1.5**	**MSWD = 1.16**				

^ Error is internal 2σ. Satistically impractical to calculate MSWD value for two data points.

\# The sample shows unimodal age distribution, weighted mean is calculated

\## The sample shows bimodal age distribution, however the number of data is insuffucuent for the deconvolution algorithm, so the two peak ages were calculated separately

Table 5 SHRIMP U–Th–Pb dating results for zircon grains from a porphyritic tonalite, a porphyritic quartz monzonite and a leucocratic quartz porphyry

a) Data for zircon grain #1 from 15IA09 (Porphyritic tonalite)

Spot # [sample-grain. spot]	% 206Pb$_c$	ppm U	ppm Th	(207Pb-corrected) ppm 206Pb*	232Th /238U	(1) 206Pb/238U Age		(2) 206Pb/238U Age		(1) 207Pb/206Pb Age		(1) 208Pb/232Th Age		% Discor-dant	Total 238U /206Pb	±%
IA09-1.1	0.03	46	38	0.33	0.84	53.4	±2.4	53.4	±2.4	53.8	±239	53.9	±8	+1	120	4.5
IA09-1.2	0.19	66	42	0.48	0.66	54.3	±2.3	54.2	±2.3	72.5	±260	50.2	±9	+25	118	4.2
IA09-1.3	0.07	62	48	0.44	0.81	53.0	±1.9	53.0	±1.9	66.5	±231	53.2	±9	+20	121	3.6

b) Data for zircon grain #11 from 13IA02 (Porphyritic quartz monzonite)

Spot # [sample-grain. spot]	% 206Pb$_c$	ppm U	ppm Th	(207Pb-corrected) ppm 206Pb*	232Th /238U	(1) 206Pb/238U Age		(2) 206Pb/238U Age		(1) 207Pb/206Pb Age		(1) 208Pb/232Th Age		% Discor-dant	Total 238U /206Pb	±%
IA2-11.1	0.03	127	111	0.85	0.90	50.0	±1	50.0	±1	46.6	±319	50.2	±9	-7	128	2.7
IA2-11.2	0.04	70	32	0.46	0.47	49.0	±3	49.0	±3	63.7	±362	48.3	±13	+23	131	5.5
IA2-11.3	0.14	61	31	0.40	0.53	49.5	±2	49.5	±2	43.5	±363	50.5	±14	-14	129	3.1
IA2-11.4	0.14	127	122	0.84	1.00	49.9	±1	49.9	±1	74.1	±298	48.0	±8	+33	129	2.8
IA2-11.5	0.05	119	85	0.83	0.74	52.4	±3	52.4	±3	61.3	±370	52.7	±23	+15	122	5.2
IA2-11.6	0.03	142	135	0.95	0.98	49.8	±1	49.8	±1	51.4	±382	51.8	±8	+3	129	2.5

c) Data for zircon grain #3 from 13IA10 (Leucocratic quartz porphyry)

Spot # [sample-grain. spot]	% 206Pb$_c$	ppm U	ppm Th	(207Pb-corrected) ppm 206Pb*	232Th /238U	(1) 206Pb/238U Age		(2) 206Pb/238U Age		(1) 207Pb/206Pb Age		(1) 208Pb/232Th Age		% Discor-dant	Total 238U /206Pb	±%
IA10-3.1	--	54	20	0.36	0.39	49.6	±2	49.6	±2	31.8	±298	46.7	±8	-56	129	3.7
IA10-3.2	0.31	279	197	1.85	0.73	49.5	±1	49.6	±1	40.7	±139	49.3	±6	-22	129	2.1
IA10-3.3	0.42	91	60	0.58	0.68	47.4	±2	47.4	±2	56.3	±340	47.3	±9	+16	135	4.9
IA10-3.4	0.07	114	143	0.76	1.29	49.9	±2	49.9	±2	31.8	±242	49.4	±6	-57	129	3.9

Errors are 1-sigma; Pb$_c$ and Pb* indicate the common and radiogenic portions, respectively.
Error in Standard calibration was 0.39% (not included in above errors but required when comparing data from different mounts).
(1) Common Pb corrected using measured 204Pb.
(2) Common Pb corrected by assuming 206Pb/238U-207Pb/235U age-concordance

Spot # [sample-grain. spot]	Total 207Pb /206Pb	±%	(1) 238U /206Pb*	±%	(1) 207Pb* /206Pb*	±%	(1) 207Pb* /235U	±%	(1) 206Pb* /238U	±%	error correlation
IA09-1.1	0.0473	10	120	4.5	0.0471	10	0.0540	11	0.00832	4.5	0.4
IA09-1.2	0.0486	10	118	4.2	0.0475	11	0.0553	12	0.00845	4.2	0.4
IA09-1.3	0.0476	10	121	3.6	0.0473	10	0.0539	10	0.00826	3.6	0.3

Spot # [sample-grain. spot]	Total 207Pb /206Pb	±%	(1) 238U /206Pb*	±%	(1) 207Pb* /206Pb*	±%	(1) 207Pb* /235U	±%	(1) 206Pb* /238U	±%	error correlation
IA2-11.1	0.0473	13	129	2.7	0.0469	13	0.0504	14	0.00778	2.7	0.2
IA2-11.2	0.0473	15	131	5.5	0.0473	15	0.0498	16	0.00763	5.5	0.3
IA2-11.3	0.0481	15	130	3.1	0.0469	15	0.0498	16	0.00771	3.1	0.2
IA2-11.4	0.0481	12	129	2.8	0.0475	13	0.0509	13	0.00777	2.8	0.2
IA2-11.5	0.0475	15	122	5.2	0.0472	16	0.0532	16	0.00817	5.2	0.3
IA2-11.6	0.0472	16	129	2.5	0.0470	16	0.0503	16	0.00776	2.5	0.2

Spot # [sample-grain. spot]	Total 207Pb /206Pb	±%	(1) 238U /206Pb*	±%	(1) 207Pb* /206Pb*	±%	(1) 207Pb* /235U	±%	(1) 206Pb* /238U	±%	error correlation
IA10-3.1	0.0467	12	129	3.7	0.0467	12	0.0497	13	0.00772	3.7	0.3
IA10-3.2	0.0495	4	130	2.1	0.0468	6	0.0498	6	0.00771	2.1	0.3
IA10-3.3	0.0503	13	136	4.9	0.0471	14	0.0480	15	0.00738	4.9	0.3
IA10-3.4	0.0476	10	129	3.9	0.0467	10	0.0500	11	0.00777	3.9	0.4

Part III

Porphyry copper deposit formed at magmatic temperatures under hydraulic fracturing conditions in Cerro Colorado copper mine, northern Chile, revealed by fluid inclusion microthermometry

1 Introduction

There is a clear spatial relationship between porphyry copper metallogenic belts and belts of arc magmatism parallel to convergent plate margins (Fig. 1) (e.g., Richards, 2011a, 2013; Sillitoe, 2010, 2012). Moreover, early in the study of copper porphyry deposits (PCDs) some workers proposed that the magmatic-hydrothermal brecciation commonly observed associated with PCDs might indicate a direct link between volcanic eruption and PCD formation (e.g., Sillitoe, 1973, 1985). However, although there is a clear general link between the locations of the volcanic arcs and PCDs, many studies have proposed that the conditions needed for PCD formation are actually characteristic of times when volcanism was suppressed or absent (e.g., Cloos, 2001; Cooke et al., 2005; Sillitoe, 2010).

Active volcanism would clearly suppress the likelihood of PCD formation if most of the metal was released in volcanic ash and lava before sufficient concentrations had been built up in the country rocks (e.g., Richards, 2005; Sillitoe, 2010). Some workers have emphasised that releasing copper-bearing volcanic gasses into the atmosphere may also significantly reduce the possibility of forming a PCD (e.g., Williams-Jones & Heinrich, 2005; Audetat et al., 2008). The role of gasses is particularly important, because many studies have identified the volcanic gas phase as the main carrier for copper in PCDs (e.g., Williams-Jones & Heinrich, 2005; Simon et al., 2006; Audetat et al., 2008; Landtwing et al., 2010; Seo et al., 2012; Vigneresse et al., 2014). Alternative genetic models for PCDs propose brine fluids are the main medium for Cu transport (Cline & Bodnar, 1991; Hedenquist & Lowenstern, 1994; Shinohara, 1994; Leuchbaumer & Audetat, 2012; Blundy et al., 2015). In such cases, volcanic degassing would not necessarily hinder PCD development.

The relationship between PCD formation and volcanism is an important part of identifying places for future exploration, and the starting point for many of these discussions is estimating temperatures and pressures associated with PCD formation. The primary source of information on PCD formation conditions is the analysis of fluid inclusions that were trapped at the time of mineralisation. Copper and iron sulphide ore minerals of PCDs are commonly crystallised as an important constituent of dominantly quartz veins. Quartz is transparent and stable over a wide range of temperatures. This means that any fluids trapped during its growth as fluid inclusions can be observed in situ over a wide range of temperatures and the information used to estimate the conditions at which fluid became trapped. Analyses of quartz fluid inclusions in vein material associated with PCD formation generally show trapping temperatures of 300–400 ˚C (e.g., Ulrich et al., 2002; Landtwing et al., 2005; Rusk et al 2008) and this is taken to be the formation temperature for PCDs by many workers.

The 300–400°C temperature range corresponds to a drastic drop in the solubility of copper-chloride species in hydrothermal ore fluid (e.g., Crerer & Barnes, 1976; Hemley & Hunt, 1992; Hezarkhani et al., 1999; Brugger et al., 2007). This decrease in solubility can explain the supply of metal ions required for the ore formation. A second chemical consideration that underlines the potential importance of this temperature range in mineralisation is the supply of sulphur. Both the sulphide ions required for metal sulphide formation and the acid required for the widespread alteration seen around PCDS are generally thought to be provided as a result of the disproportionation reaction of SO_2 with a hydrothermal fluid forming H_2S and H_2SO_4:

$$4SO_2 + 4H_2O = H_2S + 3H_2SO_4$$

(e.g., Holland, 1965; Landtwing et al, 2005; Kouzmanov & Pokrovski, 2012). This reaction occurs at temperatures ≤ 400 ˚C.

Despite this good general agreement between the theoretical considerations and observations of natural systems suggesting PCD formation around 300–400 °C, there is also a significant body of fluid inclusion data suggesting that chalcopyrite-bearing veins from PCDs can form at significantly higher temperatures reaching magmatic temperatures (e.g., Roedder 1971, 1972; Sheppard et al., 1971; Hedenquist & Lowenstern 1994; Landtwing et al., 2010; Kouzmanov & Pokrovski, 2012). The link between these high temperatures and copper mineralisation is unclear.

Fluid inclusions can also be used to derive pressure estimates. The interpretation of pressures in terms of depth depends primarily on the density assumed for the overlying rock and fluid. The two common assumptions are hydrostatic, which implies fluid connected to the surface, and lithostatic, which implies the fluid is overlain by rock. Short-lived changes in pressure due to dynamic fluid processes may also have a significant effect.

The present study uses microthermometry to investigate *P–T* formation conditions of ore-bearing quartz vein samples from the hypogene zone of the Cerro Colorado porphyry copper mine, in N. Chile. The samples were collected from drill cores archived at the mine site—material that has not previously been available for academic research. I find evidence for mineralisation associated with temperatures in excess of 500°C and pressure that varies from sub-hydrostatic to supra-lithostatic. These results have implications both for potential links between active volcanism and PCD formation and the mechanism for supplying sulphur in PCDs.

2 Study area

Cerro Colorado porphyry copper mine (CMCC), a BHP Billiton property, is the northernmost copper mine which is currently being exploited in Chile (Fig. 36a). The geology of the mine area can be summarised as follows (see Part II of this study and Bouzari & Clark, 2002 for more details). The main copper host, the Cerro Empexa Formation, is a thick regional volcanic sequence of Cretaceous age, composed mainly of andesitic volcanic and minor continental siliciclastic sedimentary rock units (Tomlinson et al., 2001; Bouzari & Clark, 2002, 2006; Charrier et al., 2007). Cutting this basement unit, there are several breccia and porphyritic bodies recognised in CMCC. The oldest is a locally exposed ca. 57 Ma volcanic-related breccia unit. Two main porphyritic intrusions associated with PCD formation were identified: a ca. 53.5 Ma tonalite followed by a ca. 50 Ma quartz monzonite (Fig. 36b). The quartz monzonite porphyritic body has an ultrafine-grained matrix, suggesting rapid crystallisation probably due to a rapid reduction in pressure.

3. Analytical method

3.1 Samples selection

The six samples selected for fluid inclusions studies are all chalcopyrite-bearing quartz veins, some of which also contain molybdenite, and were collected from three of the major units exposed in the CMCC mine site: the Cerro Empexa andesitic host rock, and the two subvolcanic intrusions: the porphyritic tonalite and porphyritic quartz monzonite. PCD sulphide deposition is generally thought to occur in the temperature range 300–400 °C, where disproportionation of SO_2 gives sulphuric acid as a by-product. The acid triggers more intense alteration that shifts the environment to a sericite-stable domain (Richards, 2011a). The best domain to examine this process is the stockwork quartz veins within the quartz–sericitic (phyllic) alteration domain, which belongs to the main hydrothermal alteration and mineralisation phase of CMCC.

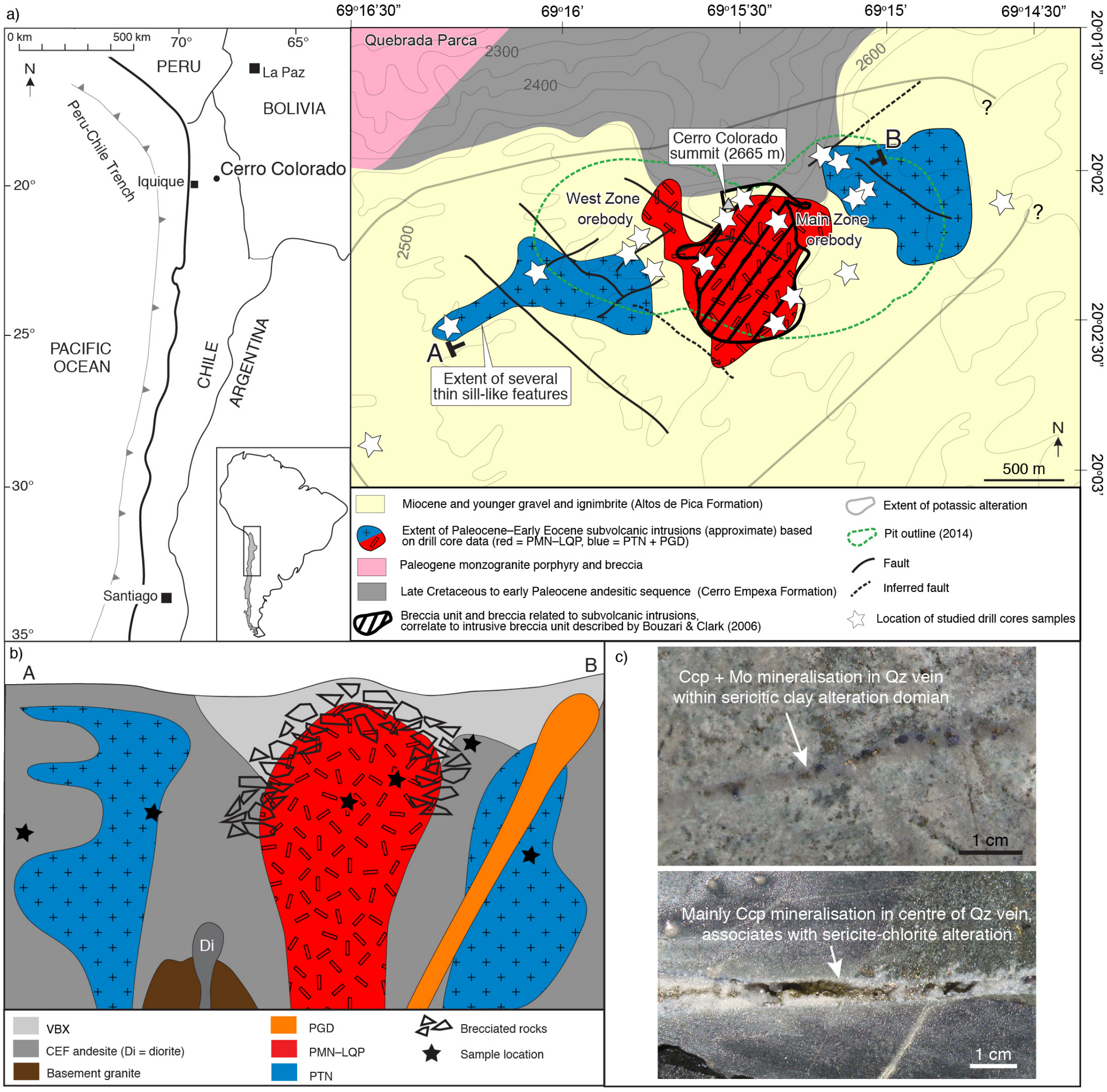

Figure 36 **a)** Location of Cerro Colorado porphyry copper mine in South America, and local geological map of Cerro Colorado area; **b)** Schematic cross section of A–B transect from a). Locations of vein samples used in this study are indicated. **c)** Two examples of ore mineral-bearing quartz veins from the sericitic alteration domain.

Sample descriptions and locations are listed in Table 6. Five of the vein samples dominantly consist of coarse-grained (ca. 500 μm) quartz, with minor, < 5 vol% fine-grained sericite. The veins also contain chalcopyrite, and locally also contain grains of pyrite and molybdenite. These veins collected from phyllic alteration zones are closely associated with a sericite- (± clay) rich wall rock, which is cut by the stockwork quartz veins. The remaining sample, V58, has similar assemblages but contains around 10 % of ca. 1 mm biotite forming in the quartz vein.

All vein samples consist of coarse vuggy quartz and most vein samples show a clear central line indicating where quartz grains met after growing from both sizes grow towards the central opening. The main sulphide mineral growth occurs near the centre of the veins. With the exception of V58, the vein samples show a sharp boundary with the wall rock and clear alteration halos were not observed in hand specimens. Based on the mineral assemblages and vein features the main set of sampled veins can be defined as transitional—veins that formed in a transitional domain between the high-temperature potassic alteration domain and sericitic to argillic alteration domain. This type of vein is referred to as B-type by many workers (Gustafson & Hunt, 1975; Gustafson & Quiroga G., 1995; Seedorff et al., 2005). The presence of sericite in the wall rock indicates that these transitional veins formed at relatively shallow levels and low temperatures in association with hydrolytic alteration. Vein 58 shows a more irregular vein–wallrock boundary. Together with the presence of biotite, these features suggest vein V58 formed at a higher temperatures than the other samples (Seedorff et al., 2005), under conditions transitional between the potassic domain and B-type veins (Gustafson & Quiroga G., 1995; Seedorff et al., 2005).

3.2 Fluid inclusion microthermometry

Due to the special properties of the H_2O–NaCl system, during the ascent of fluid from a magma source to the surface, a magmatic brine fluid experiencing a drop in temperature and pressure will separate into two immiscible saline fluids: a low-density low-salinity vapour, and a high-density hypersaline brine (e.g., Sourirajan & Kennedy, 1962; Bodnar et al., 1985; Driesner, 2007; Driesner & Heinrich, 2007). Within the two-phase field, the compositions of the brine and gas will be determined by the original composition and the *P–T* conditions (e.g., Sourirajan & Kennedy, 1962; Bodnar et al., 1985; Vityk & Bodnar, 1995). The depth of alteration and mineralisation in PCDs clearly falls in the two immiscible fluid field (e.g., Bodnar et al., 1985; Hedenquist & Lowenstern, 1994, Cline, 1995) and by determining two of the three variables, *P, T* and salinity, at the time when the coexisting immiscible pair formed, the remaining variable can be obtained. Such conditions can be treated as the entrapment condition of the hydrothermal alteration fluid (e.g., Bodnar et al., 1985; Vityk & Bodnar, 1995).

In the case of a hypersaline inclusion containing a gas bubble and daughter salt crystal(s) in a liquid-dominant fluid, measuring the temperature at which the salt(s) in the inclusion completely melt or dissolve gives the halite homogenisation temperature (T_m Halite) (assuming the daughter crystal is halite). The salinity can then be determined by using known relationships between T_m Halite and composition (e.g., Bodnar et al., 1985; Bodnar & Vitky, 1994). The temperature at which the gas bubble phase in the hypersaline fluid disappears, marks the temperature at which the gas and liquid mixture becomes homogenised and lies on the critical curve. This homogenisation temperature (T_h L–V) can be taken as the temperature at which the inclusion was trapped, provided that no re-equilibration of fluid inclusions occurred after trapping (e.g., Bodnar et al., 1985; Bodnar & Vitky, 1994). After obtaining the temperature of inclusion entrapment and the salinity, the trapping pressure can then be determined using the *P–T–X* phase relationships of the H_2O–NaCl system (e.g., Bodnar et al., 1985; Vityk & Bodnar, 1995).

3.3 Sample preparation

Entrapment pressure, temperature and salinities of 3-phase (3-P)—gas, liquid, and solid halite—hypersaline fluid inclusions were determined using microthermometry as discussed below. The quartz vein samples were first polished on one side and then mounted in Crystal Bonde and cut into 200–300 µm thick slices for double-side polishing. Microtextural observations were carried out before the samples were immersed in acetone to dissolve the Crystal Bonde and detach the sample from the glass slide.

3.4 Microtextural Observations

The quartz veins were examined under reflected and polarized light combined with cathodoluminescence (CL) images. The microtextures suggest that there were multiple stages of quartz growth (Fig. 37, 38). The first stage is associated with a mosaic quartz pattern (Q1), which may indicate recrystallisation from an amorphous silica state (Dong et al., 1995). The quartz grains generally show homogenous CL and are fine-grained. A second stage is characterised by growth of euhedral quartz grains (Q2), which show clear growth zone patterns in CL images. Small pockets of quartz (Q3), which do not show clear CL patterns, fill pore spaces between the well-formed quartz. All three of these stages are cut by quartz-filled fractures (Q4). This final phase of quartz shows only weak luminescence and has highly irregular outlines where it is in contact with Q2 and Q3 quartz. These features are described by some workers as splatter and cobweb microtextures. Therefore, microtextural observations suggest the veins formed in four distinct stages with a period of fracturing, dilation and partial dissolution of Q2 and Q3 quartz prior to the final stage of quartz precipitation.

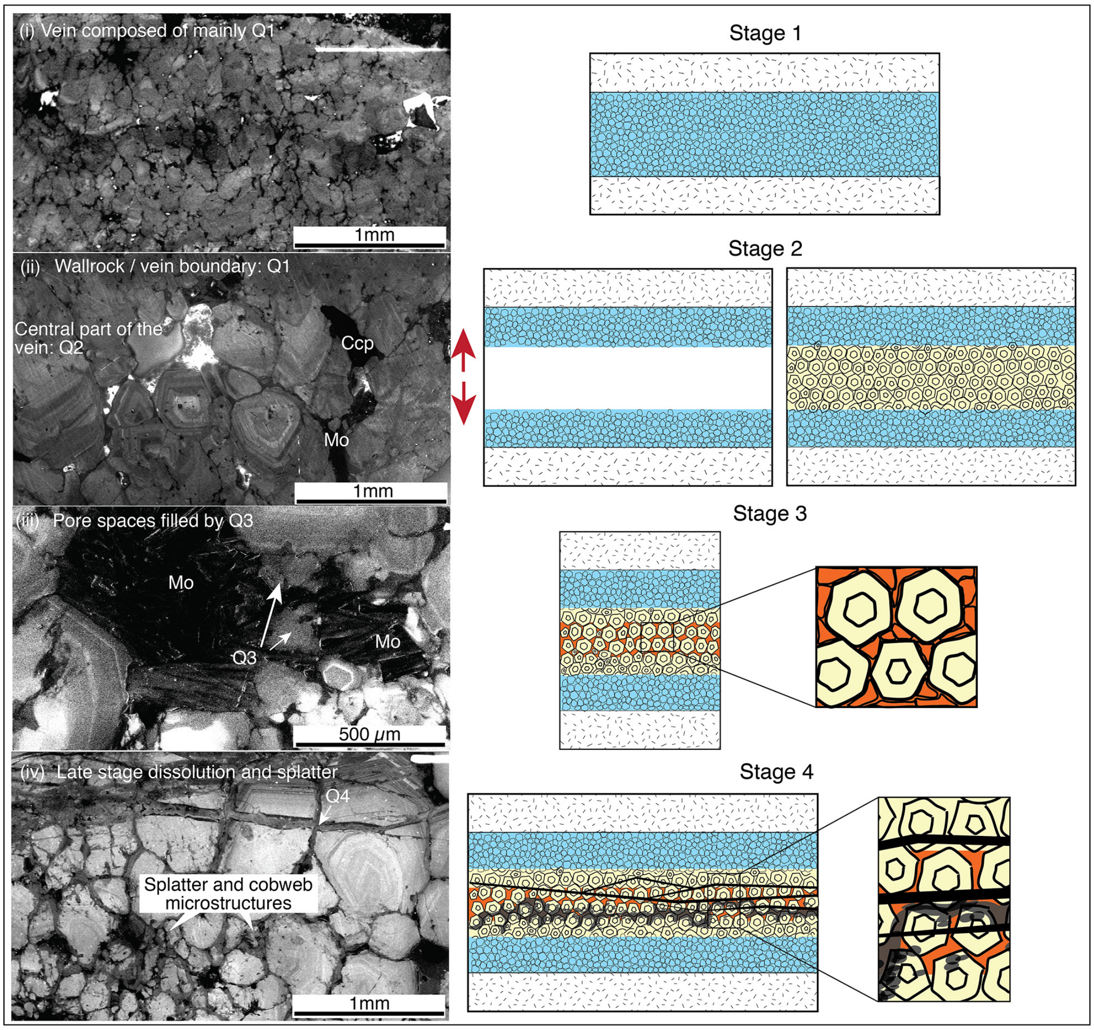

Fig. 37 CL images (L) and cartoon (R) summarising the features of 4-stage quartz growth.

(i) Quartz vein consisting entirely of Q1 quartz growth. Grains are irregular and CL image does not show clear patterns.

(ii) Quartz vein that shows two stages of quartz growth: mosaic and homogeneous quartz (Q1) that formed close to the rock-vein boundary; and euhedral quartz grains of the Q2 domain that shows clear growth zoning under CL. Molybdenite and chalcopyrite form along quartz grain boundaries of Q2.

(iii) Quartz without clear CL microtextures partially fills the pore spaces forming pockets of Q3.

(iv) A final quartz domain (Q4) showing dull CL cuts through euhedral Q2. The splatter and cobweb microtextures of Q4 suggest some degree of dissolution and reprecipitation.

Chalcopyrite and molybdenite grains are mainly associated with the central region of the Q2 quartz domain (Fig. 37). These minerals occur mainly as large grains deposited along the Q2 quartz grain boundaries, but also occur as small inclusions within quartz grains and within fluid inclusions (Fig. 39 a, b). These microtextural observations suggest that Q2 quartz growth is coeval with the sulphide ore deposition. Therefore, fluid inclusions within this quartz can potentially be used to estimate the formation conditions of both the quartz and sulphide minerals.

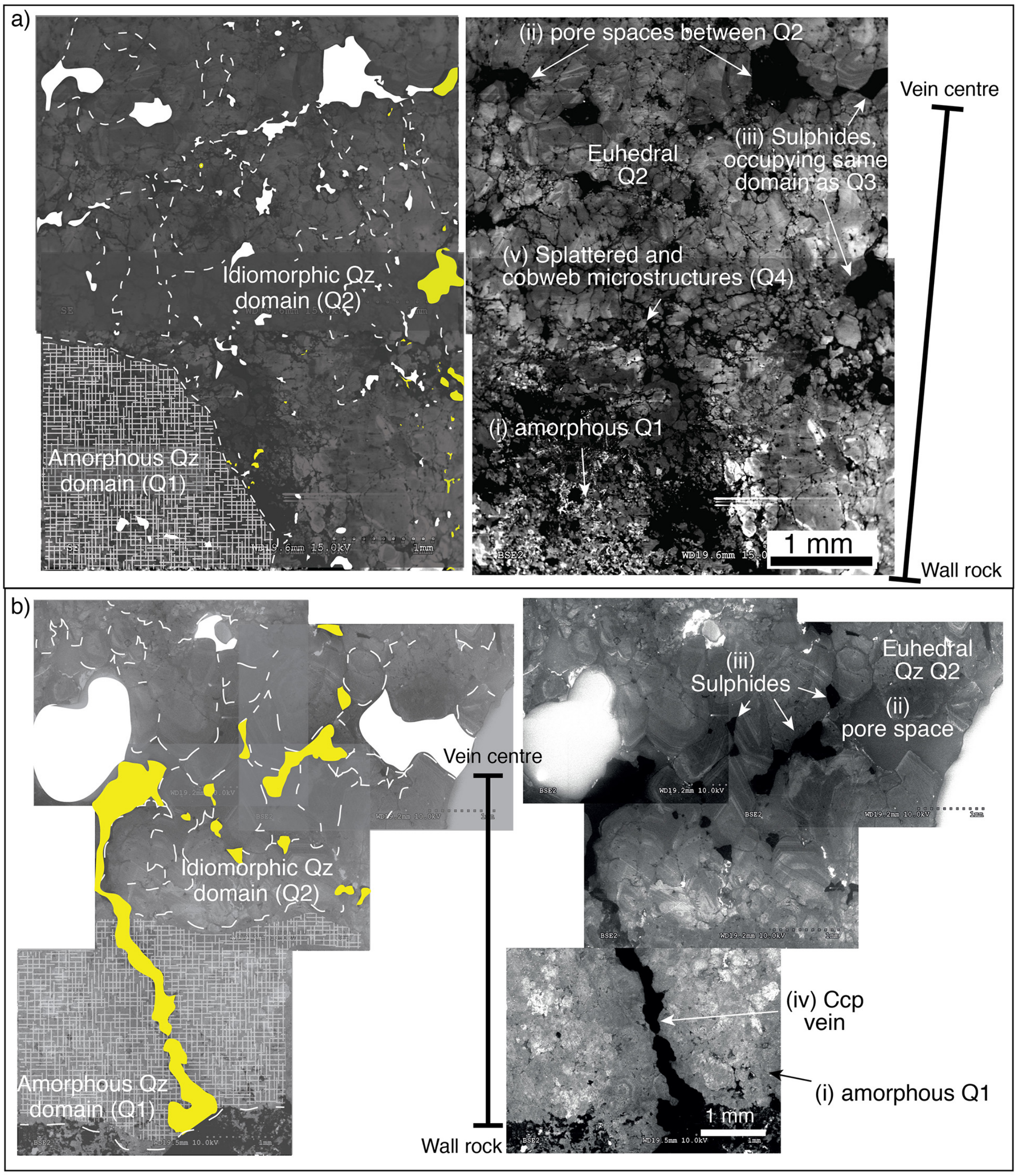

(Refer to next page for figure captions)

Figure 38. CL images and corresponding sketches of two quartz veins, V146 and 13011, from wall rock to vein centre showing the main features.

(i) Quartz grains closer to the wall rock show a blurred and amorphous mosaic microtexture (Q1)

(ii) A central porous domain with euhedral quartz (Q2).

(iii) Sulphide minerals form along quartz grain boundaries infilling former pore spaces, sharing same microtextural domain as Q3 (see Fig. 37 iii).

(iv) A chalcopyrite vein penetrating through the outer quartz layer suggests the outer Q1 layer precipitated before the Q2 central region. Chalcopyrite and molybdenite grains grew at the same time or after the Q2 region.

(v) The presence of splatter and cobweb textures indicate partial dissolution and reprecipitation of quartz (Q4). The presence of these features suggests the vein experienced hydraulic fracturing after the euhedral Q2 quartz formation.

CL images are important to help identify primary inclusions formed at the same time as the surrounding quartz. Firstly, inclusion trails that crosscut growth zonation shown in CL are clearly secondary. In contrast, inclusions that formed along the growth zone domains are likely to be primary. I focused on inclusions with good microtextural evidence for being primary, and inclusions that show rounded to sub-rounded or negative crystal shapes (Fig. 39d). Irregular shaped fluid inclusions were avoided due to the possibility of necking (loss of volume) or post-trapping re-equilibration of P–T conditions (Sterner & Bodnar, 1989; Sterner et al., 1995; Vityk & Bodnar 1995; Bodnar, 2003) (Fig. 39 h, i). In addition, during heating a limited number of 3-P inclusions showed the disappearance of the gas vapour bubble first before full halite dissolution. In such cases, the 3-P inclusions cannot represent the corresponding liquid of a gas–brine immiscible pair, because they cannot have formed in phase equilibrium (Bodnar, 2003). This implies the inclusions have undergone volume loss and they are excluded from the discussion.

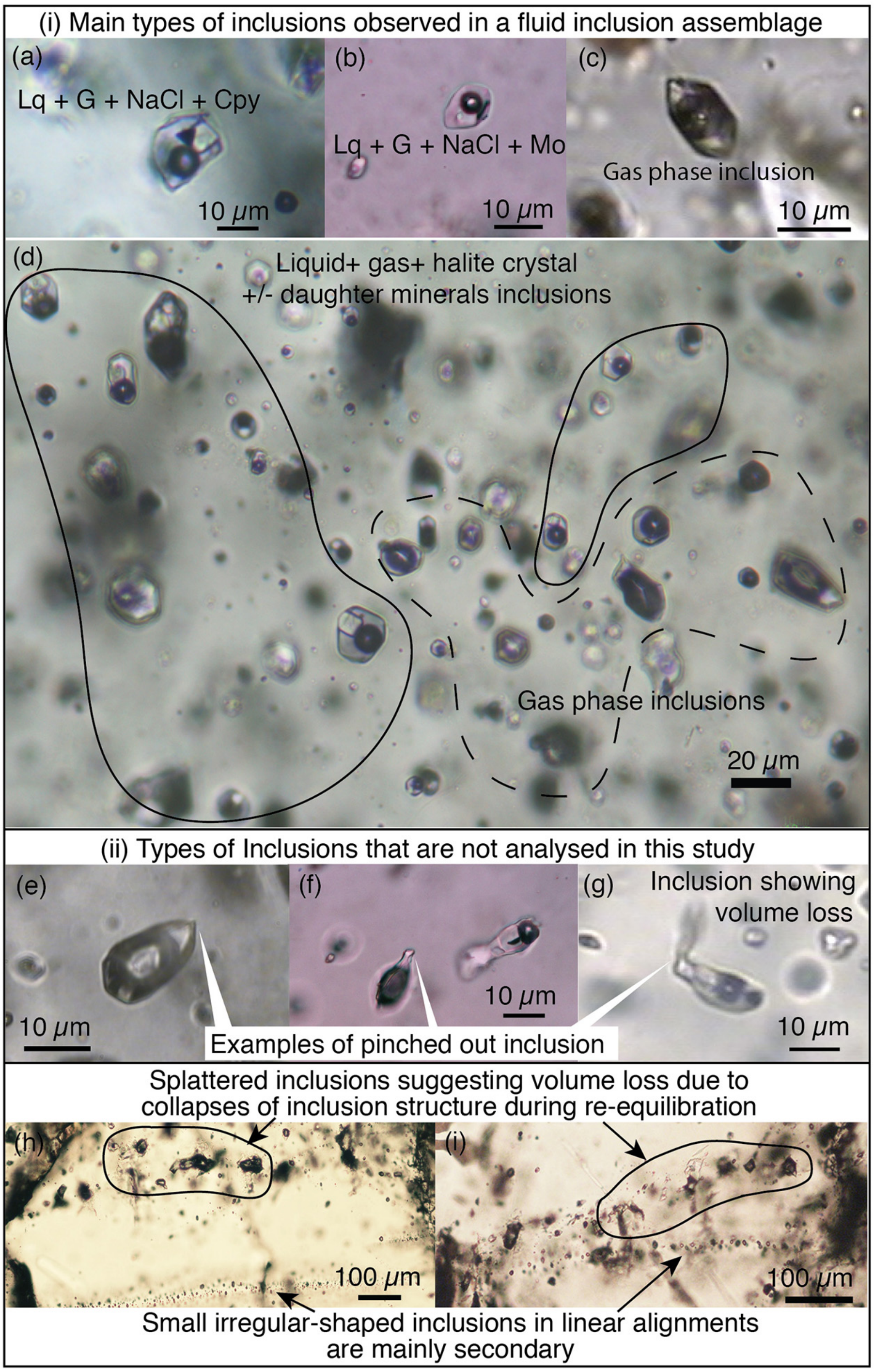

Figure 39 Different types of fluid inclusions observed in quartz. **(a)**, **(b)** Examples of 3-P (L–V–H) inclusions, which is the study target type. It is common to observe the occurrences of sulphides in the 3-P inclusions. The dark grain with a triangular section shown in (a) is chalcopyrite and the dark flaky grain in (b) is molybdenite. **(c)** An example of a gas phase inclusion. Together with 3-P inclusions, such inclusions make up a fluid inclusion assemblage (d). **(e)**–**(i)** Examples of inclusions that show apparent volume loss. This could happen due to necking or re-equilibration of fluid inclusions (see text).

3.5 Analytical approach

In the quartz vein samples selected for microthermometry analysis, both 3-P hypersaline brine fluids and also gas dominated low salinity vapour inclusions are present (Fig. 39d). The presence of both types of inclusion supports the idea that these veins formed in the 2-immiscible fluid field. The occurrences of daughter sulphide minerals (i.e. chalcopyrite, molybdenite, pyrite) (Fig. 39 a, b) within some inclusions shows a direct link between the formation of these inclusions and mineralisation.

The current study focuses on observing the high-density hypersaline 3-phase brine inclusions. Petrographic observations of these fluid inclusions show that the majority of the inclusion assemblages contain a liquid, a gas bubble, and a daughter salt crystal or crystals. Locally opaque sulphide crystal are also present in the inclusions (Fig. 39 a, b). A few inclusions show more than one type of daughter salt crystals, suggesting some inclusions may contain KCl, which is common in magmatic derived fluid (e.g., Bodnar, 2003), or less likely, $CaCl_2$. In this study, I focus on the H_2O–NaCl system, and only measured inclusions that contain a clear cubic-shaped halite crystal (NaCl), which is the most abundant salt crystal observed in the fluid inclusions. A minimal amount of KCl will only contribute to an insignificant amount of excess thermodynamic energy of mixing, and thus is possible to neglect its affect on the results (Evans & Powell, 2006).

The presence of CO_2 in the fluid inclusion will have a significant influence on the determination of trapping pressure (e.g., Roedder & Bodnar, 1997; Bodnar, 2003). The presence of CO_2 in the fluids was checked before microthermometry observations using laser Raman spectroscopy. Raman spectral peaks for CO_2 at around 1388.2 cm^{-1} and 1285.4 cm^{-1} (subject to Raman spectral shift due to different CO_2 concentration) (Fall et al., 2011) were checked for. No CO_2 was detected in any of the 3-P inclusions. CO_2 was found in 8 % of the low salinity vapour-rich inclusions. The current study focuses on hypersaline inclusions and analysing these inclusions assuming a H_2O–NaCl system is considered to be sufficient.

Salt melting temperatures (T_m) were measured when the halite crystals in the 3-P inclusions completely dissolved upon heating. Homogenisation temperatures (T_h) were measured when the gas phase bubbles in the 3-phase inclusions disappeared upon heating. All salinity and trapping pressure calculations were performed using software SoWat designed for fluid properties in the H_2O–NaCl system (Driesner, 2007; Driesner & Heinrich, 2007).

Altogether 182 inclusions, which homogenised by vapour disappearance following halite dissolution, were tested. The homogenisation sequence of these inclusions suggests that they were trapped in a normal temperature-decrease environment (e.g., Bodnar, 1994). All but 13 inclusions were analysed at Nagoya University using a Linkam THMS 600 heating stage setup. A further 13 inclusions were analysed at Bristol University using Linkam TS 1200. To check for consistency of the results measured in the two different laboratories, five inclusions with $T_h \leq 550^\circ C$ were analysed using both instruments. The results obtained from two independent laboratories show differences of ≤ 10°C. Limited number of analysed inclusions that homogenised by halite dissolution following vapour disappearance were also recorded.

4 Results

The measured temperatures (T_m and T_h) and calculated salinities and trapping pressure are summarized in Table 7 and Fig. 40. The main features are as follows.

The halite dissolution temperatures (T_mHalite) lie between 168˚C and 378˚C, corresponding to a salinity range of 30.4–44.7 wt% NaCl. This is a commonly reported range in PCD environments (e.g., Gustafson & Hunt, 1975; Heinrich et al., 1992; Rusk et al., 2008; Landtwing et al., 2010). 41 % of the inclusions yield T_h L-V of 240–391 ˚C, indicating a relatively low range of trapping pressures from ca. 30–190 bars. In contrast, 58% of the inclusions show homogenisation temperatures (T_h L-V) higher than 422˚C, which combined with the dissolution temperatures, imply trapping pressures of ca. 250 to ≥ 1000 bars, with an average of ca. 600 bars. There is a noticeable gap in the recorded homogenisation temperatures between about 390°C and 420°C. A few inclusions showed homogenisation temperatures above 580˚C. This is the high-temperature limit for accurate measurement on the Linkam THMS 600, and their T_h L–V are recorded as 580˚C. To obtain a better understanding of these high-T inclusions a limited number were measured using the Linkam THMS 1200 at Bristol University with a higher temperature capability. The results for T_h L–V mainly fall in the range 540–700 ˚C, with one high-T outlier at 768 ˚C. The results show that a significant proportion of the high T inclusions were trapped at magmatic temperatures up to 700 ˚C, much higher than generally assumed for PCD formations.

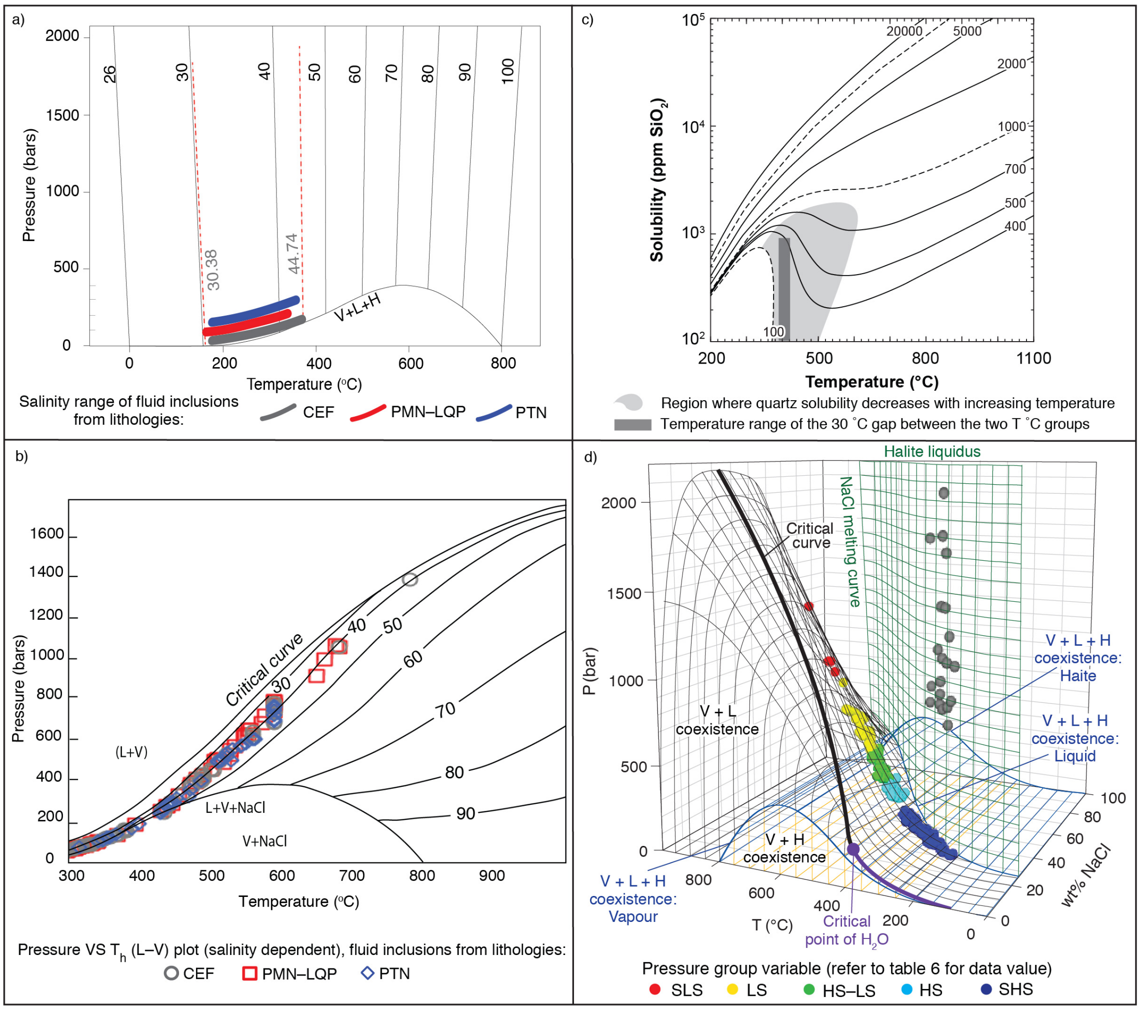

Figure 40

(a) Halite liquidi showing the salinity of a liquid in the indicated salinity in equilibrium with halite in the NaCl-H_2O system. The approximate salinities of the fluid inclusions can be derived according to their T_mHalite (after Bodnar, 2003; Becker et al., 2008).

(b) Formation pressure obtained by plotting *T-X* results from fluid inclusion analysis from this study on a *P-T* isoplethal projection of the high-salinty H_2O-NaCl system (labels on lines represent wt.%NaCl) (after Bodnar et al., 1985; Bodnar, 2003). An apparent temperature gap between 385–420°C implies the presence of two trapping temperature groups.

(c) Solubility of quartz in aqueous fluids as function of temperature at pressure indicated. Shaded region shows the temperature range where T_h L-V was not recorded in this study. The temperature and pressures inferred by my measurements fall into the range of retrograde SiO_2 solubility (e.g., Fournier, 1985, 1999; Richards, 2011a; Sillitoe, 2010; Landtwing et al., 2005), suggesting the lack of fluid inclusions trapped in the temperature range 385–420°C may be due to dissolution of quartz (graph is modified after Dolejš & Manning, 2010). (Continued on next page)

d) *P-T-X* results from fluid inclusion analysis plotted on the NaCl-H_2O phase diagram (from Driesner & Heinrich, 2007). Different colours represent pressure groups relative to estimated hydrostatic and lithostatic pressure. For a range of formation depths of 1.88–3 km (refer to text and Fig. 40c) the results indicate a spread across a wide range of pressures: subhydrostatic (SHS) in dark blue, hydrostatic (HS) in light blue, between hydrostatic and lithostatic (HS–LS) in green, lithostatic (LS) in yellow and (SLS) supralithostatic in red. The actual pressure data plotted in corresponding pressure fields (and colours) are given in Table 7. Grey dots show the estimated *P-T-X* conditions of the recorded fluid inclusions homogenised by halite dissolution, the results are not discussed in detail. Purple line is the boiling curve of H_2O, and is linked to the critical curve of the H2O–NaCl system by the critical point of H_2O shown in purple dot.

5 Discussions

5.1 Formation depth estimation and pressure fluctuation

The CMCC area is composed of a series of subvolcanic to volcanic rocks, with andesitic lava and porphyritic dacite being the most common. Taking the range of andesite, granodiorite and quartz diorite densities to be 2.65–2.81 Mg/m^3 (Wohletz & Heiken, 1992), and assuming lithostatic pressures, the high temperature population of fluid inclusions indicates shallow crustal formation at depths of about 0.86–3.8 km and the lower temperature population implies even shallower depths of about 70–680 m. When the lower temperature population group was recalculated assuming hydrostatic pressure, the inferred formation depth becomes 0.2–1.83 km, which overlaps with the estimated depth given by the high temperature group. The two groups of inclusions could therefore represent fluids trapped when there was an opening to the surface of the earth (hydrostatic) and when this pathway was sealed (lithostatic).

According to phase equilibrium of SiO_2 in H_2O system (Cline et al., 1992; Fournier, 1999; Akinfiev & Diamond, 2009; Dolejš & Manning, 2010), the solubility of SiO_2 in aqueous fluids has a local maximum in the temperature range of 375–410°C at pressures range 100–500 bars (Fig. 40c). Following the same SiO_2 solubility trend, this may imply that at ca.

250–300 bars (the pressures indicated by salinity of fluid inclusions, see Fig. 40b), precipitation of SiO_2 phases will be limited in this temperature range and this may account for the bimodal homogenisation temperatures. In such cases, the wide range of homogenisation temperatures can be seen as a continuum without a clear grouping.

A plot of all the calculated pressures, including those associated with both high- and low-T_m groups, against the depth at which veins were collected, shows a large range of pressures and no clear relationship with either lithostatic or hydrostatic pressure gradients (Fig. 41). To assess their significance, I use an independent estimate of paleodepth (Fig. 41) based on the amount of erosion since the intrusion around 50 Ma. I considered three different scenarios.

Scenario 1 (Fig. 41a, b, orange shade)

Based on fission track results, Maksaev & Zentilli (1999) estimate the maximum erosion in Northern Chile (21°S) was 2–4 km (one of the four areas of analysis) during late Eocene to Oligocene (50–30 Ma). The other 3 groups of data indicate 1.5–3 km of erosion. They suggest after a period of relatively rapid exhumation that lasted until late Miocene (i.e. from ca. 30 Ma to ca. 9 Ma), the average erosion rate reduced to 50 m/Myr. All their estimations assume a geothermal gradient of 30 °C/km. The total eroded depth is estimated to be: (2–4 km) + 50 m x 20 Myr = 3–5 km (for simplicity, the slow erosion Oligocene–late Miocene period is taken as 20 Ma) for the fastest exhumed group, and (1.5–3 km) + 50 m x 20 Myr = 2.5–4 km for the remaining 3 groups of samples.

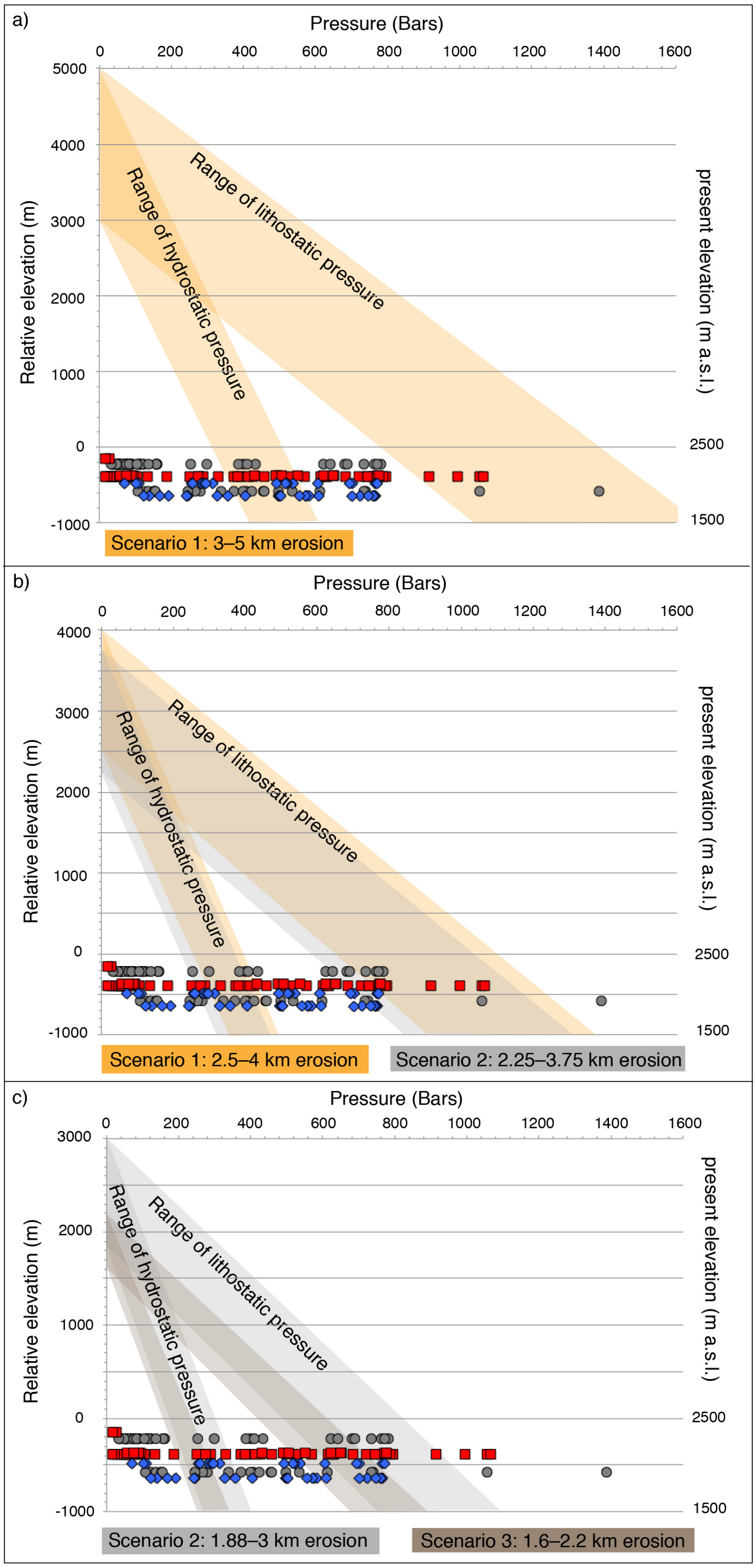

Figure 41 Range of formation pressure derived from fluid inclusion analysis plotted against depth for several scenarios. Zero marked on the depth axes corresponds to a height of 2500 m above sea level, which is an estimate of the height of the mine site before excavation. The negative values below zero are depth of veins collected (thus analysed fluid inclusions). The positive values above zero are estimated eroded mass since 50 Ma. Calculations of the ranges of lithostatic and hydrostatic pressures of each scenario are given in supplementary sheet 4.

a) Scenario 1 assumes 3–5 km maximum erosion suggested by Maksaev & Zentilli (1999). The lithostatic and hydrostatic pressure gradient zones are shaded in orange.

b) Besides the area that has experienced maximum exhumation rate, 2.5–4 km erosion is calculated for other areas of the same study. The lithostatic and hydrostatic pressure gradient zones for such erosion rate are shaded in orange. Scenario 2 assumes geothermal gradient was 40˚C/ km instead of 30˚C/ km adopted by Maksaev & Zentilli (1999). The recalculated maximum eroded mass for Scenario 1 in (a) is 2.25–3.75 km. The corresponding pressure gradients are shaded in grey.

c) Similarly, recalculation of the eroded mass for the non-maximum rate regions in Maksaev & Zentilli (1999) is 1.88–3 km, assuming geothermal gradient was 40˚C/ km. The lithostatic and hydrostatic pressure gradients are shaded in grey. Scenario 3 assumes 1.6–2.2 km erosion calculated from Victor et al. (2004) and Arancibia et al. (2006), the corresponding pressure gradients are shaded in brown.

Scenario 2 (Fig. 41b & c, grey shade)

Victor et al. (2004) studied the uplift rate of Precordillera (20°–21°S) and suggested the estimate of the geothermal gradient given by Maksaev & Zentilli (1999) was too low for an active arc system. Rothstein & Manning (2003) present summaries of several studies of geothermal gradients in active arcs and the following the following: 30–35 °C/km, 45 °C/km, 50 °C/km. These results imply a more suitable estimate of exhumation can be obtained by recalculating the Maksaev & Zentilli (1999) estimation using a higher geothermal gradient. Here I recalculated the depth using an average of 40°C/km. The total eroded depth is estimated to be [(2–4 km) + 1 km] x (30/40) = 2.25–3.75 km for the fastest exhumed group, and similarly, [(1.5–3 km) + 1 km] x (30/40) = 1.88–3 km for the remaining 3 groups of samples.

Scenario 3 (lowest estimate, Fig. 41c, brown shade)

Based on the geochemical data by Haschke & Gunther (2003), Victor et al. (2004) calculated the erosion from Eocene to Oligocene in the region 20°–22°S in Chile was 1.2 ± 0.3 km. Arancibia et al. (2006) suggest that from Oligocene to late Miocene, the erosion rate in the Precordillera was around 35 m/Myr. This contrasts with the estimate given by Maksaev & Zentilli (1999) of 50 m/Myr. Using these lowest estimates, the total removal since ca. 50 Ma is calculated to be (0.9–1.5 km) + 35 m x 20 Myr = 1.6–2.2 km.

All the above calculations neglect the period since late Miocene (ca. 9 Ma onwards) when the region then changed to hyperarid conditions (e.g., Arancibia et al., 2006). Previous studies suggest the erosion rate during this period did not exceed 0.7–1 m/Myr (Schlungger et al., 2006; Kober et al., 2006).

From the graphs plotted for the recalculated estimates of Maksaev & Zentilli (1999) (Fig. 41b) and the lowest estimates (Fig. 41c), it is clear that the pressure stretches across a whole range from subhydrostatic, to between hydrostatic and lithostatic, and up to supralithostatic pressure at a paleodepth range of ca. 2–4 km. There is no clear division into separate groups. Such large variations of fluid pressure could be explained by hydraulic fracturing events caused by fluid accumulation and overpressure of rocks, followed by rock fracturing and a resulting sudden large drop in pressure (Dilles, 1987; Fournier, 1999).

When rock failure happens due to fluid overpressure, the pressure of the fluid instantly drops due to the creation of an open space. The increase in permeability provides a pathway for fluid to flow (e.g., Sibson, 1981; Sibson et al., 1988). Fluid pressure above lithostatic pressure is likely to induce rock fracture (Blake, 1984; Druitt & Sparks, 1984; Fournier, 1999). Hydraulic fracturing acts as a valve providing pathways for fluid fluxes and this process has been reported in previous studies (e.g., Sibson, 1981; Fournier, 1999; Weisheit et al., 2013; Sachau et al., 2015).

My results concur with the proposal of many previous authors (e.g., Singer et al., 2008) that PCDs are formed at shallow crustal levels around 1.5–2.5 km up to 4 km. Bouzari and Clark (2006) suggest that Cerro Colorado PCD was formed at paleo-depths of 2.5–3 km. Such shallow conditions imply that mineralisation is likely to have undergone periodic fracturing. The suggestion of hydraulic fracturing causing a drop in pressure and instant fluid release into the passages created is also compatible with the idea that the copper mineralisation in CMCC is related to a decompression event caused by degassing (for details refer to Part II).

Irregular inclusion textures have been observed but not analysed (Fig. 39 h, i). The occurrences of these inclusions suggest the system has partially undergone re-equilibration, which are the results of inclusion internal overpressure or underpressure (e.g., Sterner & Bodnar, 1989; Vityk & Bodnar, 1995). These observations lend further support to the idea that the system has undergone fluctuations in pressure, causing volume loss in part of the inclusions (i.e. pinched inclusions, or collapse of inclusion).

5.2 Evolution of quartz veins and precipitation of sulphide minerals

The first stage of quartz growth was recrystallised from an amorphous silica phase (Q1), followed by the second stage of euhedral quartz growth (Q2), where a wide range of pressures from subhydrostatic to supralithostatic pressure have been measured. This Q2 stage was likely formed by repeated fracturing (opening) inducing fluid flow, which explains the fluid inclusions formed in underpressure and overpressure conditions. The open space gradually closed due to precipitation of quartz, trapping inclusions that record a whole range of pressures in between hydrostatic to lithostatic conditions. The formation of chalcopyrite and molybdenite is mainly associated with the third quartz domain (Q3) stage characterised by euhedral quartz and the sulphide minerals are mainly found in pore spaces in between quartz crystals. Fluid inclusions analysed from the quartz with no clear CL patterns, directly surrounding these sulphide grains, gave mainly high T_m (Fig. 42a, b). This suggests the main stage mineralisation is associated with a high temperature fluid flowing into the pore spaces.

The final stage of quartz evolution is related to fracturing and dissolution of the existing quartz. In the CL images, significantly darker bands showing sharp contact cutting through Q2 is clearly observed. The dark Q4 also formed dissolution rims around Q2 and Q3 quartz grain boundaries. As Q2 has experienced multiple hydraulic fracturing, new hot fluid introduced into pore spaces then formed Q3, and it is possible that the hydraulic fracturing and dissolution domain Q4 was formed contemporaneously with Q2 and Q3. To resolve this issue, more microtextural observations on quartz veins have to be done.

5.3 Fluid of direct magmatic origin forms PCD at high temperature

41 % of fluid inclusions recorded a range 240–391 ˚C. This temperature range apparently agrees with many previous authors that in PCDs, hydrothermal fluid seems to be related to the main phase mineralisation. Microtextural observations suggest fluid inclusions of this temperature range are trapped in the euhedral quartz (Q2) domain (Fig. 42a). This lower temperature group of fluid inclusions is also microtexturally associated with dissolution of earlier quartz domains along grain boundaries, and hydraulic fracturing of quartz. The former fractures are now filled by secondary quartz, and locally chalcopyrite and molybdenite. This Q4 domain of reprecipitated quartz shows darker CL (Fig. 42 c, d) and can be correlated with the fracture-filling quartz domain reported in Landtwing et al. (2005). These authors reported the presence of sulphides in the dissolution and re-precipitation domain of quartz growth, which led to their conclusion that hydrothermal alteration phase is responsible for copper mineralisation (Landtwing et al., 2005).

However, the occurrences of high (up to 700 ˚C) temperature fluids recorded in the main-stage mineralised quartz veins, which agree with the high temperature range summarized in some older literatures, confer with previous suggestions that the ore forming fluid had a magmatic origin (Roedder, 1971, 1972; Hedenquist & Lowenstern 1994). This suggests the mineralisation had already commenced at magmatic temperatures.

The source of sulphur from the magmatic-hydrothermal system that allows deposition of chalcopyrite is generally considered to originate from the disproportionation reaction of SO_2 to give H_2S and H_2SO_4 at hydrothermal temperatures. The reason for this idea is based on the ability for the magma to retain most of the Cu until late stage fractionation, suggesting Cu has not undergone early segregation and thus most of the S in the magma should occur as oxidized species, which promotes higher Cu solubility in the brine rich ore fluids (Zajacz et al., 2011; Audetat & Simon, 2012), allowing the Cu to be retained in the volatile saturated magma (e.g., Cline, 1995).

Instead of the commonly accepted theory that copper mineralisation occurs when the fluid temperature dropped to the 400 °C hydrothermal temperature, my results suggest the ore-forming fluids exsolved from a magmatic source directly initiate chalcopyrite deposition at magmatic temperatures. This implies another mechanism of S^{2-} supply is required. This implication agrees with the suggestion of a second phase of sulphur input during mineralisation processes (e.g., Hattori & Keith, 2001; Collins et al., 2012; Henley et al., 2015; Blundy et al., 2015). The late sulphur phase may be related to degassing (e.g., Collins et al., 2012; Henley et al., 2015; Blundy et al., 2015) or directly associated with mafic magma eruption (e.g., Hattori & Keith, 2001, Nadeau et al., 2016).

It is reported by various studies that the formation of breccia-related or vein-type ore formation may be the result of multiple hydrofracturing events (e.g., Jebrak, 1997; Chi & Xue, 2011; Faleiros et al., 2014; Sun & Liu, 2014). Such rock deformation will locally and for a short period of time cause an underpressure lower than hydrostatic pressure (Chi & Xue, 2011). Faleiros et al. (2014) has reported experimental results of fluid inclusions trapped in mineralised quartz veins that show a group of subhydrostatic pressures, together with a range of recorded pressures in between hydrostatic to lithostatic pressures. The fluid inclusion results of this study show a wide range of formation pressures suggesting hydraulic fracturing activity during mineralisation. Such conditions can be achieved during the emplacement of the volcanic-related breccia unit and also the monzonitic subvolcanic intrusion in CMCC, both of which show evidence for intense brecciation and large amounts of volatile release. Furthermore, the observations providing a direct link between mineralisation and high temperature fluids add further support to the idea of the release of a late phase S^{2-} supplying fluid exsolved directly from the magma, inducing eruption, devolatilisation and likely brecication, at the same time causing Cu deposition.

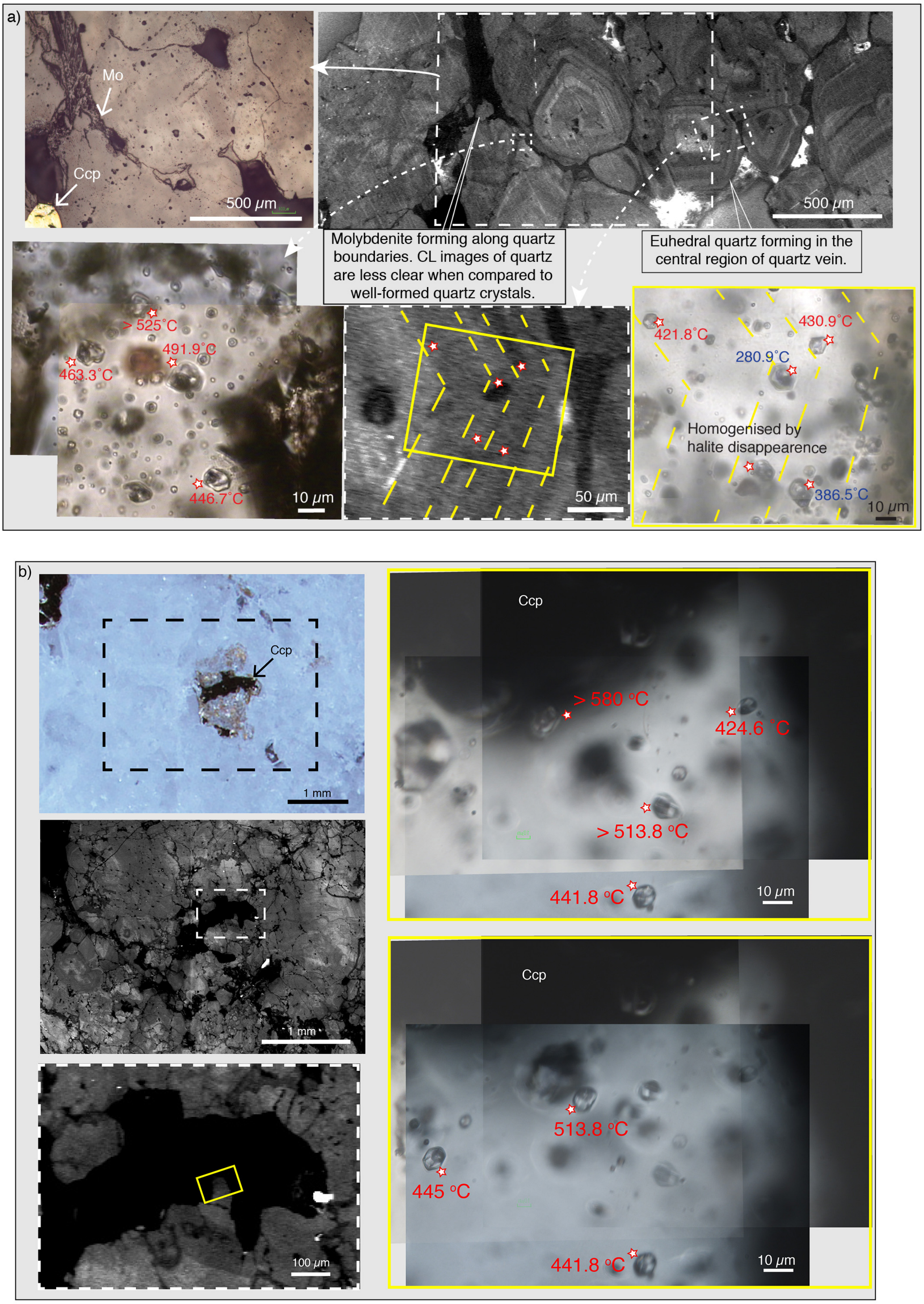

Molybdenite forming along quartz boundaries. CL images of quartz are less clear when compared to well-formed quartz crystals.

Euhedral quartz forming in the central region of quartz vein.

(Refer to next page for figure captions)

Figure 42 Reflected light, transmitted light and CL images showing examples of analysed fluid inclusion locations from (a) 13011, (b) V146, (c) V100 and (d) 13V12. Dotted white rectangular box on the CL images correspond to the location of reflected light images; solid yellow rectangular boxes show the enlarged transmitted light images on which the measured fluid inclusions are indicated by white stars with red outlines and, when appropriate, are also shown on the corresponding CL images. CL patterns are traced on the transmitted images to show the relative location of fluid inclusions. Fluid inclusions trapped along the quartz growth boundaries are more likely to be primary.

(a) Example where the recorded high and low temperatures do not show clear relationship with CL zoning. Area adjacent to sulphide, with unclear CL patterns, shows more consistent high temperature inclusions. These features are also demonstrated in **(b)**, which shows consistent high fluid inclusion temperatures measured in the Q3 domain sitting next to a chalcopyrite. The two transmitted light images show the same field of view at different depths of the same section. The positions of the chalcopyrite and the fluid inclusion at the bottom (441.8 ˚C) are useful markers to recognise the locations of the other inclusions.

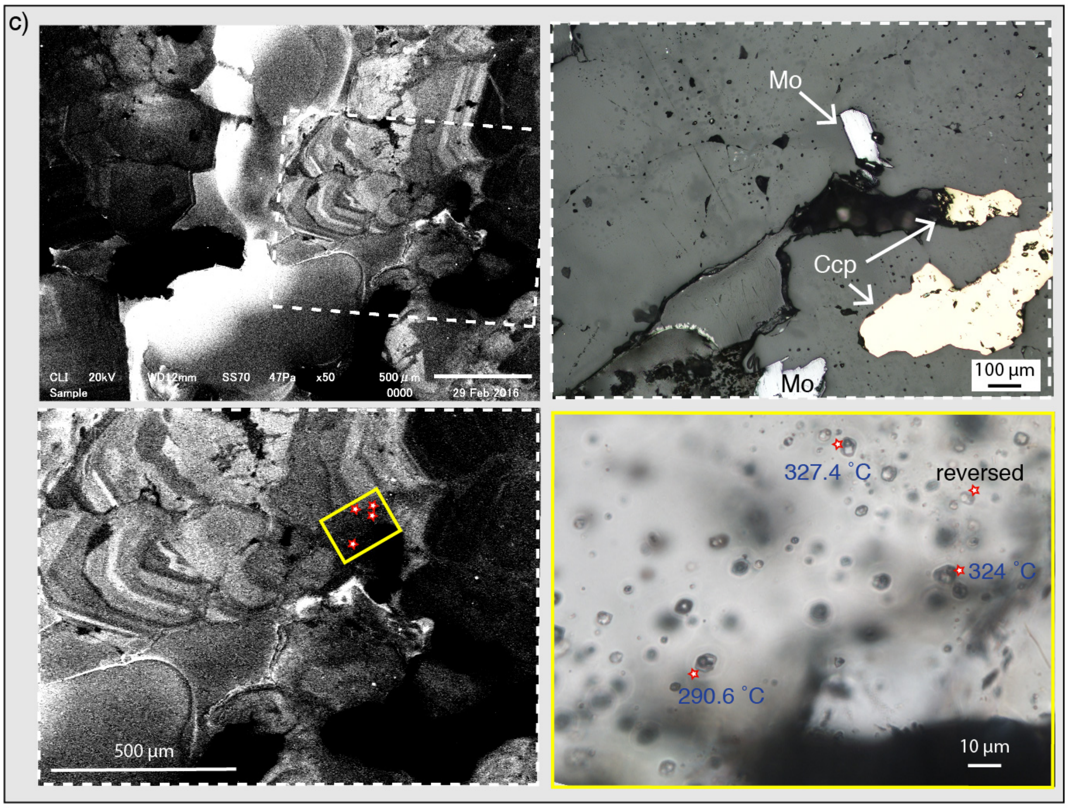

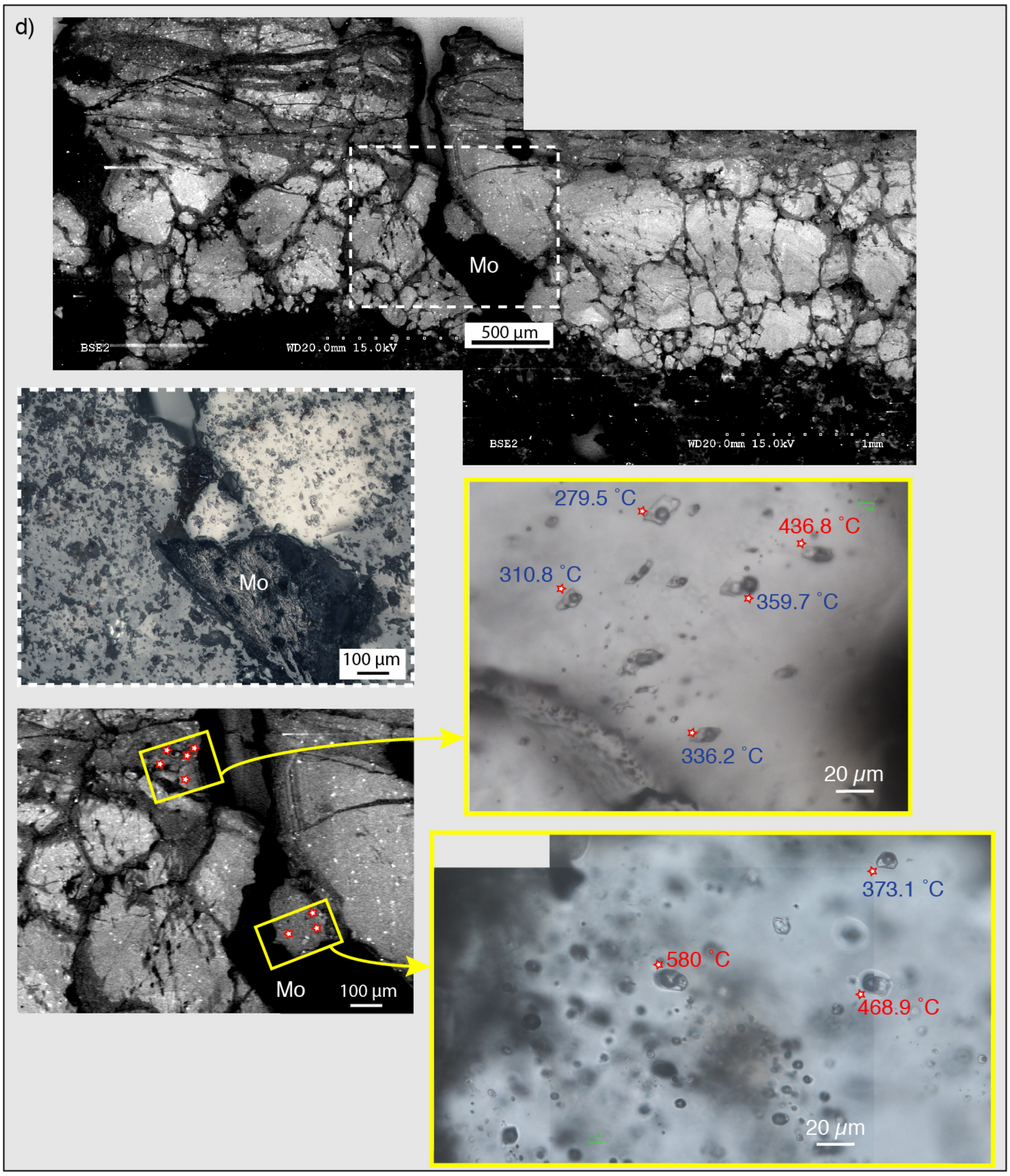

Figure 42 c, d) Two examples where low-temperature fluid inclusions were recorded in close relation with sulphides. **(c)** Quartz adjacent to the vein centre, a domain where Q2 has undergone dissolution. Three low-temperature inclusions were recorded in this domain. A molybdenite grain is present in the same dark CL. **(d)** Similar features to (c) showing 4 low-temperature fluid inclusions recorded in the Q3 domain where type Q4 domains are also present. In contrast, high-temperature fluid inclusions are present in the irregular infilling Q3 quartz domain that shows weak homogenous CL adjacent to a molybdenite grain.

6 Conclusions

The widely varying formation pressures recorded by fluid inclusion microthermometry in this study stretches from subhydrostatic pressure to supralithostatic pressure. The majority lie in between hydrostatic and lithostatic. I propose the mineralised veins were formed during fracturing caused by fluid overpressure, which may be induced by a late stage sulphur-rich fluid influx during mineralisation. This is supported by the microtextural observations of mineralised quartz veins suggesting copper mineralisation is associated with the later stage (Q3) of the vein evolution. Fluids with temperatures of up to 700°C were recorded in Q3 quartz occupying pore spaces between grains of earlier Q2 quartz, suggesting a late phase hot fluid was released into the system inducing mineralisation. The rupture as a consequence of over pressure, would cause a large instant drop of pressure and enhance fluid flow within the space created by the rupture. The introduction of hot fluid at close to magmatic temperatures resulting in hydrofracturing of the rock is most likely during active volcanism. Therefore, the results of the fluid inclusion studies point to a close association between copper mineralisation and active volcanism in agreement with the conclusions of Part II of this thesis.

Table 6 Descriptions and locations of samples used in microthermometry study

Table 7 Whole set of recorded fluid inclusion temperatures and the calculated corresponding salinities and entrapment pressures. Abbreviations used: A = adjacent to sulphide minerals; L = temperature limit of heating stage; B = temperature at which inclusion burst or the sample showed burning of remnant adhesive; SHS = sub-hydrostatic pressure; HS = hydrostatic pressure; LS = lithostatic pressure; SLS = supra-lithostatic pressure.

Table 6 Sample locations and descriptions of the ore-bearing quartz veins used in microthermometry study

Vein sample #	Rock type	Metallic Minerals	Associate wall rock alteration	Drill core #	Drilling elevation (m a.s.l.)	sample depth (m)	sample elevation (m a.s.l.)	Quartz vein feature descriptions
V151	CEF–andesite	Ccp, Py	Qz-Ser-Clay	11-112	2527	605	1922	Sharp vein-wallrock boundary. Lack alteration halo. Coarse quartz grains. Centre of Qz vein cut by Bt vein suggest a later stage hot fluid passed through.
13V12	CEF–andesite	Ccp, Py, Mo	Qz-Ser-Clay	11-097A	2364	85	2279	Sharp vein-wallrock boundary. Lacking alteration halo. Coarse quartz grains. Centre line is not obvious
13001	PMN–LQP	Ccp, Py	Qz-Ser-Clay	11-075	2409	60	2349	Sharp vein-wallrock boundary. Lack alteration halo. Mainly amorphous, only 2 inclusions measured
13011	PMN–LQP	Ccp, Py, Mo	Qz-Ser-Clay	11-075	2409	297	2112	Sharp vein-wallrock boundary. Lacking alteration halo, coarse quartz grains. Centre of vein is vuggy.
V100	PMN–LQP	Ccp, Py, Mo	Qz-Ser-Clay	11-081	2394	266	2128	Similar to 13011 but vein-wallrock boundary less sharp. The vein is more vuggy than 13011, the "centre" line is closer to one side of the wallrock.
V58	PTN	Ccp, Bn, Py, Mo	Qz-Bt-(greenish) Ser	GT08-10	2470	614	1856	Vein is irregular; coarse quartz grains, centre line is present in some segments. Features of A–B vein transition. May have formed earlier in the PCD system compared to the rest of the samples (Gustafson & Hunt, 1975; Gustafson & Quiroga G., 1995)
V146	PTN	Ccp, Bn, Mo	Qz-Ser-Clay	11-100	2360	343	2017	Sharp vein-wallrock boundary. Lacking alteration halo; coarse quartz grains; the vein is vuggy, centre line is not obvious.

Table 7 Halite melting temperatures and homogenisation temperatures of measured fluid inclusions and their calculated equivalent salinities and entrapment pressures

Tested inclusions sample-inclusion #	Tm Halite (˚C)	Th L-V (˚C)	NaCl (wt %)	Pressure (bars)	Remarks		P range group
					adj. S	Limit	
V151-1	350	550	41.9447	612.436	A	B	LS
V151-2	322	495	39.463	454.555	A		HS–LS
V151-3	358	768	42.7092	1387.98	A		SLS
V151-4	323	670	39.5465	1056.63	A		SLS
V151-5	3183	480	39.1328	408.739	A		HS–LS
V151-6	304.2	466.4	38.039	371.77	A		HS–LS
V151-7	296.4	515	37.4514	533.778	A		LS
V151-8	329.3	478.6	40.0811	398.766	A		HS–LS
V151-9	292	454	37.1295	337.891	A		HS
V151-10	277.3	352	36.1021	122.61	A		SHS
V151-11	287.9	503	36.8355	498.13	A		HS–LS
V151-12	317.6	580	39.1001	740.235	A	L	LS
V151-13	302.6	493.1	37.9167	458.411	A		HS–LS
V151-14	288.8	373.1	36.8995	153.497	A		SHS
V151-15	294	362.4	37.275	135.883	A		SHS
V151-16	276.9	371.6	36.0752	152.591	A		SHS
V151-17	288.6	432.8	36.8853	279.378	A		HS
V151-18	287.5	374	36.8072	155.193	A		SHS
V151-19	273.2	426.4	35.8284	266.908	A		HS
V151-20	325.5	580	39.7568	733.659	A	L	LS
V151-21	301.6	482	37.8407	422.75		B	HS–LS
V151-22	259.2	339.7	34.9344	107.523			SHS
V151-23	358	427	42.7092	244.539			HS
13V12-1	319.4	477.7	39.2476	400.787	A		HS–LS
13V12-2	286.8	580	36.7576	763.015	A		LS
13V12-3	336.8	550	40.7374	623.266	A		LS
13V12-4	378.1	580	44.7382	682.174	A		LS
13V12-5	312.8	550	38.7124	641.139	A		LS
13V12-6	185.5	289.1	31.1126	56.8152	A		SHS
13V12-7	263.4	480.6	35.1962	433.359	A		HS–LS
13V12-8	323.9	580	39.6219	735.015	A		LS
13V12-9	248.5	464.7	34.2915	385.11	A		HS–LS
13V12-10	199.7	370.7	31.7487	159.149			SHS
13V12-11	240.5	320.4	33.8324	85.2813			SHS
13V12-12	208.4	371.9	32.1596	160.457			SHS
13V12-13	289	325.6	36.9138	87.4432			SHS
13V12-14	241.5	342.6	33.8888	112.911			SHS
13V12-15	229.5	339.4	33.2298	109.53			SHS
13V12-16	214.4	348.2	32.453	122.861			SHS
13V12-17	219.2	290.5	32.6939	56.7633			SHS
13V12-18	245.1	343.9	34.0942	114.388			SHS
13V12-19	213.8	260.5	32.4233	35.3005			SHS
13V12-20	212.3	302.1	32.3494	67.604			SHS
13V12-21	227.2	312.1	33.1078	76.9819			SHS
13V12-22	241.6	290.3	33.8945	55.609			SHS
13V12-23	248.5	286.3	34.2915	52.0111			SHS
13V12-24	257.6	292.1	34.8361	56.3251			SHS
13V12-25	232.2	287.3	33.3747	53.5486			SHS
13V12-26	242.9	306.1	33.9682	69.9635			SHS
13V12-27	236.4	263.6	33.604	36.5066			SHS
13V12-28	218.5	276.2	32.6584	45.5278			SHS
13V12-29	230.3	309.8	33.2725	74.4064			SHS
13V12-30	242.7	312.2	33.9568	76.1908			SHS

Tested inclusions	Tm Halite	Th L-V	NaCl	Pressure	Remarks		P range
sample-inclusion #	(˚C)	(˚C)	(wt %)	(bars)	adj. S	Limit	group
13V12-31	252.5	272.3	34.5279	41.5286			SHS
13V12-32	254.5	580	34.6478	782.306	A	L	LS
13V12-33	211.2	468.9	32.2955	408.986	A		HS–LS
13V12-34	218.2	282.9	32.6432	50.5891	A		SHS
13V12-35	238.4	345.2	33.7148	116.742	A		SHS
13V12-36	224.5	324.3	32.9663	90.8208	A		SHS
13V12-37	281.9	301.8	36.4157	63.4132	A		SHS
13V12-38	308.2	424.6	38.3489	254.155	A		HS
13V12-39	371.8	580	44.0856	689.032	A	L	LS
13V12-40	244.4	373.1	34.0539	158.964	A		SHS
13V12-41	225.2	279.5	33.0028	47.7213			SHS
13V12-42	242.1	310.8	33.9228	74.7671			SHS
13V12-43	233.2	319.9	33.4289	85.1793			SHS
13V12-44	178.2	254.1	30.8014	32.4223			SHS
13V12-45	236.9	318.1	33.6316	82.9265			SHS
13V12-46	242.7	359.7	33.9568	137.523			SHS
13V12-47	252.7	436.8	34.5398	298.525			HS
13V12-48	275.1	580	35.9546	770.52		L	LS
13V12-49	233	336.2	33.418	105.048			SHS
13011-1	324	670	39.6303	1055.56	A		SLS
13011-2	293	665	37.202	1065.89	A		SLS
13011-3	310	562	38.4902	684.032	A		LS
13011-4	287	568	36.7718	720.551	A		LS
13011-5	302	540	37.8711	614.411	A		LS
13011-6	311	650	38.5692	995.08	A		SLS
13011-7	273	540	35.8152	631.033	A		LS
13011-8	348	639	41.7575	915.592	A		LS
13011-9	297	544	37.4959	631.114	A		LS
13011-10	279	479.8	36.2172	424.929			HS–LS
13011-11	325	518.6	39.7146	528.88			LS
13011-12	313	580	38.7284	743.924		L	LS
13011-13	200	280	31.7626	48.9748			SHS
13011-14	289.5	580	36.9495	761.196		L	LS
13011-15	285	325.5	36.6311	87.6921			SHS
13011-16	282	303.6	36.4226	65.078			SHS
13011-17	263	334.2	35.171	100.107			SHS
13011-18	293.2	361.8	37.2166	135.081			SHS
13011-19	219.6	253.8	32.7142	31.3124			SHS
13011-20	211.7	275.3	32.32	45.1053			SHS
13011-21	211.4	251.5	32.3053	30.2737			SHS
13011-22	183.2	298.1	31.0134	64.9716			SHS
13011-23	168	227	30.3834	19.861			SHS
13011-24	170	223	30.4638	18.3459			SHS
13011-25	213.8	270.2	32.4233	41.4795			SHS
13011-26	249.6	318.5	34.356	82.5465			SHS
13011-27	244.8	336.1	34.0769	104.023			SHS
13011-28	228.7	308.1	33.1872	72.7501			SHS
13011-29	239.2	280.9	33.7595	48.2253			SHS
13011-30	226.3	386.5	33.0604	185.816			SHS
13011-31	214	293.6	32.4332	59.6682			SHS
13011-32	291.7	421.8	37.1078	251.685			HS
13011-33	279.5	430.9	36.2512	276.754			HS
13011-34	290.2	302.8	36.9997	63.7425			SHS
13011-35	256.1	500	34.7447	501.666		B	HS–LS
13011-36	249.2	291.1	34.3325	55.9133			SHS
13011-37	298.6	437.5	37.615	288.964			HS
13011-38	231.2	307.3	33.3208	71.8066			SHS

Tested inclusions sample-inclusion #	Tm Halite (˚C)	Th L-V (˚C)	NaCl (wt %)	Pressure (bars)	Remarks		P range group
					adj. S	Limit	
13011-39	275.9	463.3	36.008	372.164	A		HS–LS
13011-40	292.2	525	37.1439	569.522	A	B	LS
13011-41	294.5	491.9	37.3116	458.304	A		HS–LS
13011-42	239.6	446.7	33.7819	330.094	A		HS
13011-43	312.7	580	38.7044	744.161	A	L	LS
13011-44	282.3	471	36.4433	394.82	A		HS–LS
13011-45	252.7	464.3	34.5398	382.584	A		HS–LS
13011-46	230.1	580	33.2618	794.117	A	L	LS
13011-47	245.1	472.5	34.0942	412.109	A		HS–LS
13011-48	300.4	432.1	37.75	274.491	A		HS
13011-49	243.5	580	34.0024	787.902	A	L	LS
13011-50	270.2	580	35.6317	773.485	A	L	LS
13011-51	218.3	292.2	32.6483	58.263	A		SHS
13001-1	168	247.4	30.3834	29.0035			SHS
13001-2	192.8	219.6	31.4344	16.8752			SHS
V100-1	274.1	580	35.888	771.134	A		LS
V100-2	288.2	518.7	36.8568	550.469	A		LS
V100-3	260.5	544.3	35.0149	652.342	A		LS
V100-4	232.1	327.4	33.3693	94.0476	A		SHS
V100-5	241.2	290.6	33.8718	55.8798	A		SHS
V100-6	234.6	324	33.5051	89.8238	A		SHS
V100-7	248.7	497.6	34.3032	496.248	A		HS–LS
V100-8	277	538.2	36.0819	622.706	A		LS
V100-9	341.7	510	41.1777	490.423	A		HS–LS
V100-10	257.4	501.5	34.8239	506.269	A		HS–LS
V100-11	282.9	482.4	36.4849	431.983	A		HS–LS
V100-12	280.6	546.8	36.3264	650.422	A		LS
V100-13	233.2	312.1	33.4289	76.6449	A		SHS
V100-14	266	580	35.361	775.944	A	L	LS
V146-1	267.4	308.6	35.4506	70.923			SHS
V146-2	356.6	550	42.5736	606.754		B	LS
V146-3	294.2	435.1	37.2896	283.867			HS
V146-4	245	430.7	34.0884	283.708			HS
V146-5	297.1	424.6	37.5033	256.98	A		HS
V146-6	280.7	513.8	36.3332	537.742	A		LS
V146-7	310.6	513.8	38.5376	521.938	A	B	HS–LS
V146-8	280	445	36.2853	314.929	A		HS
V146-9	253	341	34.5578	109.788	A		SHS
V146-10	325.6	441.8	39.7653	291.94	A		HS
V146-11	358.6	580	42.7675	702.803	A	L	LS
V146-12	307.6	427	38.302	260.008	A		HS
V146-13	283.1	508.2	36.4987	517.778	A		HS–LS
V146-14	367.9	580	43.6892	693.185	A	L	LS
V146-15	288	501.3	36.8426	492.426	A		HS–LS
V146-16	261.8	436.6	35.0958	295.94	A		HS
V146-17	246.8	334.6	34.1924	101.94	A		SHS
V146-18	281	580	36.3538	766.812	A	L	LS
V146-19	275.6	580	35.988	770.212	A	L	LS
V58-1	366	460.8	43.4981	326.964	A		HS
V58-2	316	422	38.9699	246.072	A		HS
V58-3	231.4	360.2	33.3316	139.346			SHS
V58-4	265.8	391.7	35.3482	191.347			SHS
V58-5	309.7	506	38.4665	496.897			HS–LS
V58-6	320.4	421	39.3302	242.62			HS
V58-7	212	348.2	32.3347	123.038			SHS
V58-8	282	580	36.4226	766.168	A	L	LS
V58-9	336.8	580	40.7374	723.724	A	L	LS

Tested inclusions sample-inclusion #	Tm Halite (˚C)	Th L-V (˚C)	NaCl (wt %)	Pressure (bars)	Remarks		P range group
					adj. S	Limit	
V58-10	332.7	534.5	40.376	575.442	A	B	LS
V58-11	290.5	580	37.0212	760.514	A	L	LS
V58-12	351.1	541.3	42.0484	583.365	A		LS
V58-13	331.3	533.4	40.254	572.85	A		LS
V58-14	319.9	478.8	39.2889	404.024	A		HS–LS
V58-15	301.5	522.7	37.8332	556.603	A		LS
V58-16	272	501.4	35.7494	499.944	A		HS–LS
V58-17	368.3	554	43.7296	608.973	A	B	LS
V58-18	312.8	462.5	38.7124	356.246	A		HS–LS
V58-19	291.8	580	37.115	759.62	A	L	LS
V58-20	366.3	520	43.5283	503.905	A	B	HS–LS
V58-21	288.5	382.2	36.8782	169.265	A		SHS
V58-22	307.3	580	38.2786	748.354	A	L	LS
V58-23	358.5	580	42.7578	702.904	A	L	LS
V58-24	248.2	350.6	34.2739	123.517	A		SHS

Abbreviations used: A = adjacent to sulphide minerals; L = temperature limit of heating stage;
B = temperature at which inclusion burst or the sample showed burning of remnant adhesive;
SHS = sub-hydrostatic pressure; HS = hydrostatic pressure; LS = lithostatic pressure; SLS = supra-lithostatic pressure.

Acknowledgement

I would like to express my most sincere gratitude towards my supervisor Prof. Simon Wallis for all his guidance and invaluable advices throughout my study. He showed me the way to become a real researcher and scientist, to think critically and work conscientiously. Without him this project could not have possibly proceeded to completion. I would also like to thank Dr. Brian Tattitch, my second supervisor at the University of Bristol, for inspiring me with a lot of ideas especially regarding the interesting NaCl–H_2O system, and offering guidance on the analytical techniques in Part 3 of this study; let alone always providing first hand help whenever I was traveling to Bristol.

I would like to acknowledge Prof. Koshi Yamamoto and Prof. Makoto Takeuchi for the generous guidance during XRF analysis and zircon analysis at the geochemistry labs at Nagoya University; and Prof. Hiroshi Hidaka and Dr. Kenji Horie for the assistance in SHRIMP analysis at National Institute of Polar Research. Thank Dr. Takayoshi Nagaya, Prof. Hidekazu Yoshida, Masumi Nozaki, Dr. Stuart Kearns, Dr. Amy Glimmer for assisting CL imaging in SEM labs at Nagoya University and Bristol University; Dr. Hiroshi Mori, to be the first person to show me the techniques on fluid inclusion analysis; Ilona Sakaguchi and Natsuko Takagi, for assisting on sample preparation work. I thank all current and ex-members of the Petrology group at Nagoya University, my days in Nagoya have been colourful because of all of them.

Special appreciation is dedicated to Prof. Steve Sparks, Prof. Jon Blundy, Prof. Donald Hutton, Dr. Ian Parkinson, Dr. Frances Cooper, Dr. Alison Rusk, Dr. Dan Condon (British Geological Survey), Dr. Simon Tapster (British Geological Survey) and all other members of the Bristol–BHP Billiton Porphyry Copper Deposit research group. During my several visits to Bristol University, I have received very insightful comments and constructive suggestions through discussions. I owe my sincere gratitude to Dr. Ian Parkinson, Dr. Amy Glimmer and Rebecca Perkins, for offering much help on chemistry labwork at Bristol University; and Dr. Vladimir Matjuschkin for guiding me through the amazing but complicated sulphur chemistries. Together with Dr. Marit van Zalinge, Dr. Hart Chen and Dr. Honchin Ng, they provided me with huge comfort and mental support during my stay abroad. Because of all of them, I was never alone in the UK.

I wish to extend my gratitude to Alberto Ruggigro, Thiago Oliveira, Emilio Gonzales, Victoria Quintana, Julio Cabeza, Mario Avendaño, Guilherme Santos, Analia Delsouc, Freddy Escobar, Tomas Moreno Araos and Victor Bustamante for logistic help and mine geology discussions at Cerro Colorado Mine, N. Chile; Prof. Donald Hutton, and

of course my two supervisors Simon and Brian, for guidance and accompany in Chile during field work.

My family and friends in Hong Kong, thanks for the encouragement and support through these years and letting me chase my dream for this once in my life. Thank Dr. Denise Tang, Dr. Jean Wong, Dr. Samuel Ng, Dennis Leung, S.F. Cheuk and Trudy Kwong for motivational sharing and assistance. Last but not least, I would like to express my deepest gratitude to my dearest mister, Bart Drieghe, for all his understanding, love and care, for always standing by my side walking me through ups and downs. I would not have managed my study without him, who has always taken care of our home.

This work is mainly funded by BHP Billiton and a Japanese MEXT scholarship. Additional support was provided by a grant under the scheme of ProjecTerrae offered by Mr. Jacky S.L. Chan.

References

Agemar, T., Wörner, G., Heumann, A., 1999. Stable isotopes and amphibole chemistry on hydrothermally altered granitoids in the North Chilean Precordillera: a limited role for meteoric water? *Contributions To Mineralogy and Petrology* **136**, 331–344.

Akinfiev, N.N., Diamond, L.W., 2009. A simple predictive model of quartz solubility in water–salt–CO2 systems at temperatures up to 1000 °C and pressures up to 1000 MPa. *Geochemica et Cosmochimica Acta* **73**, 1597–1608.

Al-Farawati, R., van den Berg, C.M.G., 1999. Metal-sulphide complexation in seawater. *Marine Chemistry* **63**, 331–352.

Amilibia, A., Sabat, F., McClay, K.R., Muñoz, J.A., Chong, G., 2008. The role of inherited tectono-sedimentary architecture in the development of the central Andean mountain belt: Insights from the Cordillera de Domeyko. *Journal of Structural Geology* **30**, 1520–1539.

Arancibia, G, Matthews, S J, Pérez de Arce, C., 2006. K–Ar and ^{40}Ar/ ^{39}Ar geochronology of supergene processes in the Atacama Desert, Northern Chile: tectonic and climatic relations. *Journal of the Geological Society*, London. **163,** 107–118.

Audètat, A., Pettke, T., Heinrich, C.A., Bodnar, R.J., 2008. The Composition of Magmatic-Hydrothermal Fluids in Barren and Mineralized Intrusions. *Economic Geology* **103**, 877–908.

Audètat, A., Simon, A.C., 2012 Magmatic Controls on Porphyry Copper Genesis. *Society of Economic Geologists Special Publication* **16**, 553–572

Bacon, C.R., Lowenstern, J.B., 2005. Late Pleistocene granodiorite source for recycled zircon and phenocrysts in rhyodacite lava at Crater Lake, Oregon. *Earth and Planetary Science Letters* **233**, 277–293.

Ballard, J.R., Palin, J.M., Williams, I.S., Campbell, I.H., Faunes, A., 2001. Two ages of porphyry intrusion resolved for the super-giant Chuquicamata copper deposit of northern Chile by ELA-ICP-MS and SHRIMP. *Geology* **29**, 383–386.

Barra, F., Alcota, H., Rivera, S., Valencia, V., Munizaga, F., Maksaev, V., 2013. Timing and formation of porphyry Cu–Mo mineralization in the Chuquicamata district, northern Chile: new constraints from the Toki cluster. *Mineralium Deposita* **48,** 629–651.

Becker, S.P., Fall, A., Bodnar, R.J., 2008. Synthetic Fluid Inclusions. XVII.1 PVTX Properties of High Salinity H2O-NaCl Solutions (> 30 wt % NaCl): Application to

Fluid Inclusions that Homogenize by Halite Disappearance from Porphyry Copper and Other Hydrothermal Ore Deposits. *Economic Geology* **103**, 539–554.

Bertrand, G., Guillou-Frottier, L., Loiselet, C., 2014. Distribution of porphyry copper deposits along the western Tethyan and Andean subduction zones: Insights from a paleotectonic approach. *Ore Geology Reviews* **60**, 174–190.

Black, L.P., Kamo, S.L., Allen, C.M., Davis, D.W., Aleinikoff, J.N., Valley, J.W., Mundil, R., Campbell, I.H., Korsch, R.J., Williams, I.S., Foudoulis, C., 2004. Improved ^{206}Pb/^{238}U microprobe geochronology by the monitoring of a trace-element related matrix effect; SHRIMP, ID-TIMS, ELA-ICP-MS, and oxygen isotope documentation for a series of zircon standards. *Chemical Geology* **205**, 115–140.

Blake, S., 1984. Volatile oversaturation during the evolution of silicic magma chamber as an eruption trigger. *Journal of Geophysical Research* **89**, B10, 8237–8244

Blundy, J.D., Mavrogenes, J., Tattitch, B., Sparks, S., Gilmer, A., 2015. Generation of porphyry copper deposits by gas–brine reaction in volcanic arcs. *Nature Geoscience* **8**, 235–240.

Bodnar, R.J., 1994. Synthetic fluid inclusions: XII. The system H_2O-NaCI. Experimental determination of the halite liquidus and isochores for a 40 wt% NaCl solution. *Geochimica et Cosmochimica Acta* **58**, 1053–1063.

Bodnar, R. J., 2003. Introduction to aqueous-electrolyte fluid inclusions. *In*: I. Samson, A. Anderson, and D. Marshall, Eds., *Fluid Inclusions: Analysis and Interpretation,* Mineralogical Association of Canada Short Course **32**, 81–100

Bodnar, R.J., Burnham, C.W., Sterner S.M., 1985. Synthetic fluid inclusions in natural quartz. III. Determination of phase equilibrium properties in the system H_2O-NaCI to 1000°C and 1500 bars. *Geochimica et Cosmochimica Acta* **49**, 1861–1873.

Bolhar, R., Ring, U., Allen, C.M., 2010. An integrated zircon geochronological and geochemical investigation into the Miocene plutonic evolution of the Cyclades, Aegean Sea, Greece: Part 1: Geochronology. *Contributions To Mineralogy and Petrology* **160**, 719–742.

Boric, R., Díaz, J., Becerra, H., Zentilli, M., 2009. Geology of the Ministro Hales Mine (MMH), Chuquicamata District, Chile, XII Congreso Geológico Chileno, Santiago.

Bouzari, F., Clark, A.H., 2002. Anatomy, evolution and metallogenic significance of the supergene ore body of the Cerro Colorado porphyry copper deposit, I Region, northern Chile. *Economic Geology* **97**, 1701–1740.

Bouzari, F., Clark, A.H., 2006. Prograde Evolution and Geothermal Affinities of a Major Porphyry Copper Deposit: The Cerro Colorado Hypogene Protore, I Región, Northern Chile. *Economic Geology* **101**, 95–134.

Brauhart, C.W., Huston, D.L., Groves, D.I., Mikucki, E.J., Gardoll, S.J. 2001. Geochemical Mass-Transfer Patterns as Indicators of the Architecture of a Complete Volcanic-Hosted Massive Sulfide Hydrothermal Alteration System, Panorama District, Pilbara, Western Australia. *Economic Geology* **96**, 1263–1278.

Brugger, J., Etschmann, B., Liu, W., Testemale, D., Hazemann, J.L., Emerich, H., van Beek, W., Proux, O., 2007. An XAS study of the structure and thermodynamics of Cu(I) chloride complexes in brines up to high temperature (400 °C, 600 bar). *Geochemica et Cosmochimica Acta* **71**, 4920–4941.

Buckley, A.N., Woods, R., 1984. An X-ray photoelectron spectroscopic study of the oxidation of chalcopyrite. *Australian Journal of Chemistry* **37**, 2403–2413

Candela, P.A., 1989. Calculation of magmatic fluid contributions to porphyry-type ore systems: predicting fluid inclusion chemistries. *Geochemical Journal* **23**, 295–305.

Campbell, I.H., Ballard, J., Palin, J.M., Allen, C., Faunes, A., 2006. U–Pb zircon geochronology of granitic rocks from the Chuquicamata–El Abra porphyry copper belt of northern Chile: excimer laser ablation ICP-MS analysis. *Economic Geology* **101**, 1327–1344.

Campos, E., Wijbrans, J., Andriessen, P.A.M., 2009. New thermochronologic constraints on the evolution of the Zaldívar porphyry copper deposit, Northern Chile. *Mineralium Deposita* **44**, 329–342.

Camus, F., 2005. The Andean porphyry systems, in: Porter, T.M. (Ed.), *Super Porphyry Copper & Gold Deposits: A Global Perspective.* PGC Publishing, Adelaide, pp. 45–63.

Camus, F., Dilles, J.H. 2001. A Special Issue Devoted to Porphyry Copper Deposits of Northern Chile: Preface. *Economic Geology* **96**, 233–237.

Carlier, G., Grandin, G., Laubacher, G., Marocco, R., Megard, F., 1982. Present knowledge of the magmatic evolution of the eastern Cordillera of Perú. *Earth-Science Reviews* **18**, 253–283.

Cashman, K.V., 1992. Groundmass crystallization of Mount St. Helens dacite, 1980–1986: a tool for interpreting shallow magmatic processes. *Contributions To Mineralogy and Petrology* **109**, 431–449.

Cashman, K.V. 2004. Volatile controls on magma ascent and eruption, in: Sparks, R.S.J., Hawkesworth, C.J. (Eds.), *The State of the Planet: Frontiers and Challenges in*

Geophysics. American Geophysical Union Geophysical Monograph Series 150, 109–124.

Cashman, K. V., Blundy, J. D., 2000. Degassing and crystallization of ascending andesite and dacite. *Philosophical Transactions of the Royal Society* **358**, 1487–1513.

Charlier, B.L.A., Wilson, C.J.N., Lowenstern, J.B., Blake, S., van Calsteren, P.W., Davidson, J.P., 2005. Magma generation at a large, hyperactive silicic volcano (Taupo, New Zealand) revealed by U/Th and U/Pb systematics in zircons. *Journal of Petrology* **46**, 3–32.

Charrier, R., Pinto, L., Rodrigues, M.P., 2007. Tectonostratigraphic evolution of the Andean Orogen in Chile, in: Moreno, T., Gibbons, W. (Eds.), *The Geology of Chile.* The Geological Society, London, pp. 21–114.

Chew, D.M., Schaltegger, U., Košler, J., Whitehouse, M.J., Gutjahr, M., Spikings, R.A., Mišković, A., 2007. U–Pb geochronologic evidence for the evolution of the Gondwanan margin of the north-central Andes. *GSA Bulletin* **119**, 697–711.

Chi, G & Xue, C., 2011. An overview of hydrodynamic studies of mineralization, *Geoscience Frontiers* **2,** 423–438

Chiaradia, M., Caricchi, L., 2017. Stochastic modelling of deep magmatic controls on porphyry copper deposit endowment. *Scientific Reports* **7**, 44523

Chiaradia, M., Schaltegger, U., Spikings, R., Wotzlaw, J.-F., Ovtcharova, M., 2013. How accurately can we date the duration of magmatic-hydrothermal events in porphyry systems?—An invited paper. *Economic Geology* **108**, 565–584.

Chiaradia, M., Ulianov, A., Kouzmanov, K., Be, B., 2012. Why large porphyry Cu deposits like high Sr/Y magmas? *Scientific Reports* **2,** 685.

Clark, A.H., Archibald, D.A., Lee, A.W., Farrar, E., Hodgson, C.J., 1998. Laser probe 40 Ar/ 39 Ar ages of early- and late-stage alteration assemblages, Rosario porphyry copper-molybdenum deposit, Collahuasi District, I Region, Chile. *Economic Geology* **93**, 326–337.

Clark, A.H., Farrar, E., Kontak, D.J., Langridge, R.J., Arenas, F.M.J., France, L.J., McBride, S.L., Woodman, P.L., Wasteneys, H.A., Sandeman, H.A., Archibald, D.A., 1990. Geologic and geochronologic constraints on the metallogenic evolution of the Andes of southeastern Peru. *Economic Geology* **85**, 1520–1583.

Cline, J.S., 1995. Genesis of porphyry copper deposits: the behavior ofwater, chloride, and copper in crystallizing melts. In: Pierce, F.W., Bolm, J.G. (Eds.), *Porphyry Copper Deposits of the American Cordillera.* Arizona Geological Society Digest **20**, pp. 69–82.

Cline, J.S., Bodnar, R.J., 1991. Can economic porphyry copper mineralization be generated by a typical calc-alkaline melt? *Journal of Geophysical Research* **96**, 8113–8126.

Cline, J.S., Bodnar, B.J., 1994. Direct Evolution of Brine from a Crystallizing Silicic Melt at tha Questa, New Mexico, Molybdenum Deposit. *Economic Geology* **89**, 1780–1802.

Cline, J.S., Bodnar, R.J., Rimstidt, J.D., 1992. Numerical Simulation of Fluid Flow and Silica Transport and Deposition in Boiling Hydrothermal Solutions: Application to Epithermal Gold Deposits. *Journal of Geophysical Research* **97**, 9085–9103.

Cloos, M., 2001. Bubbling Magma Chambers, Cupolas, and Porphyry Copper Deposits, *International Geology Review* **43**, 285–311.

Collins, S.J., Maclennan, J., Pyle, D.M., Barnes, S.J., Upton B.G.J., 2012. Two phases of sulphide saturation in Re´union magmas: Evidence from cumulates, *Earth and Planetary Science Letters* **337–338**, 104–113.

CMCC 2014. Geologia Cerro Colorado. Internal workshop material .

Coira, B., Davidson, C., Mpodozis, C., Ramos, V., 1982. Tectonic and magmatic evolution of the Andes of northern Argentina and Chile. *Earth-Science Reviews* **18**, 303–332.

Cooke, D.R., Heithersay, P.S., Wolfe, R., Calderon, A.L., 1998. Australian and western Pacific porphyry Cu-Au deposits. *Journal of Australian Geology & Geophysics* **17,** 97–104.

Cooke, D.R., Hollings, P., Walshe, J.L., 2005. Giant Porphyry Deposits: Characteristics, Distribution, and Tectonic Controls. *Economic Geology* **100**, 801–818.

Cornejo, P., Tosdal, R., Mpodozis, C., Tomlinson, A.J., Rivera, O., 1997. El Salvador porphyry copper revisited: Geologic and geochronologic framework. *International Geology Review* **39**, 22–54.

Cotton, W.B., 2003. Near infrared and XRD quantification of porphyry copper alteration at Cerro Colorado and Spence, Chile, PhD thesis. University of Colorado, Boulder, USA.

Crerar, D.A., Barnes, H.L., 1976. Ore solution chemistry V. Solubilities of chalcopyrite and chalcocite assemblages in hydrothermal solution at 200 °C to 350 °C. *Economic Geology* **71**, 772–794.

Cuadra, C.P., 1986. Geocronología K–Ar del yacimiento El Teniente y áreas adyacentes. *Revista Geológica de Chile* **27**, 3–26.

Cuadra, C.P., Rojas, G.S., 2001. Oxide mineralization at the Radomiro Tomic porphyry copper deposit, Northern Chile. *Economic Geology* **96**, 387–400.

Defant, M.J., Drummond, M.S., 1990. Derivation of some modern arc magmas by melting of young subducted lithosphere. *Nature* **347**, 662–665.

Derakhshani, R., Abdolzadeh, M., 2009. Geochemistry, mineralization and alteration zones of darrehzar porphyry copper deposit, Kerman, Iran. *Journal of Applied Sciences* **9**, 1628–1646.

Dilles, J.H., 1987. Petrology of the Yerington Batholith, Nevada: Evidence for Evolution of Porphyry Copper Ore Fluids. *Economic Geology* **82**, 1750–1789.

Dilles, J.H., Tomlinson, A.J., Martin, M.W., Blanco, N., 1997. El Abra and Fortuna Complexes: A porphyry copper batholith sinistrally displaced by the Falla Oeste, *VIII Congreso Geológico Chileno, Proceedings*, **3**, pp. 1883–1887.

Dolejš, D., Manning, C.M., 2010. Thermodynamic Model for Mineral Solubility in Aqueous Fluids: Theory, Calibration and Application to Model Fluid-Flow Systems. *Geofluids* **10**, 20–40.

Dong, G., Morrison, G., Jaireth, S., 1995. Quartz Textures in Epithermal Veins, Queensland—Classification, Origin, and Implication. *Economic Geology* **90**, 1841–1856.

Driesner, T., 2007. The system H_2O–NaCl. Part II: Correlations for molar volume, enthalpy, and isobaric heat capacity from 0 to 1000 °C, 1 to 5000 bar, and 0 to 1 X_{NaCl}, *Geochimica et Cosmochimica Acta* **71**, 4902–4919

Driesner, T., Heinrich, C.A., 2007. The system H_2O–NaCl. Part I: Correlation formulae for phase relations in temperature–pressure–composition space from 0 to 1000°C, 0 to 5000 bar, and 0 to 1 X_{NaCl}, *Geochimica et Cosmochimica Acta* **71** 4880–4901

Druitt, T.H., Sparks, R.S.J., 1984. On the formation of calderas during ignimbrite eruptions. *Nature* **310**, 679 – 681.

Drummond, S., Ohmoto, H., 1985. Chemical evolution and mineral deposition in boiling hydrothermal systems. *Economic Geology* **80**, 126–147.

Etschmann, B.E., Liu, W., Testemale, D., Müller, H., Rae, N.A., Proux, O., Hazemann, J.L., Brugger, J., 2010. An in situ XAS study of copper(I) transport as hydrosulfide complexes in hydrothermal solutions (25–592 °C, 180–600 bar): Speciation and solubility in vapor and liquid phases. *Geochemica et Cosmochimica Acta* **74**, 4723–4739.

Evans, K., Powell, R., 2006. A method for activity calculations in saline and mixed solvent solutions at elevated temperature and pressure: A framework for geological phase equilibria calculations. *Geochemica et Cosmochimica Acta* **70**, 5488–5506.

Frank, M.R., Vaccaro, D.M., 2012. An experimental study of high temperature potassic alteration. *Geochimica et Cosmochimica Acta* **83**, 195–204.

Faleiros, A.M., Campanha, G.A.C., Faleiros, F.M., Bello, R.M.S., 2014. Fluid regimes, fault-valve behavior and formation of gold-quartz veins—The Morro do Ouro Mine, Ribeira Belt, Brazil. *Ore Geology Reviews* **56**, 442–456.

Fall, A., Tattitch, B., Bodnar, R.J., 2011. Combined microthermometric and Raman spectroscopic technique to determine the salinity of H_2O–CO_2–NaCl fluid inclusions based on clathrate melting. *Geochimica et Cosmochimica Acta* **75**, 951–964.

Fournier, R.O., 1985. The behavior of silica in hydrothermal solutions. *Reviews in Economic Geology* **2**, 45–61.

Fournier, R.O., 1999. Hydrothermal processes related to movement of fluid from plastic into brittle rock in the magmatic–epithermal environment. *Economic Geology* **94**, 1193–1212.

Galli, C., 1968. Carta Geológica de Chile: Cuadrángulo Juan de Morales, Provincia de Tarapacá, Escala 1:50,000. Instituto de Investigaciones Geológicas de Chile, Carta 18, 53 p.

Gehrels, G.E., Blakey, R., Karlstrom, K.E., Timmons, J.M., Dickinson, B., Pecha, M. 2011. Detrital zircon U-Pb geochronology of Paleozoic strata in the Grand Canyon, Arizona. *Lithosphere* **3**, 183–200.

Gelcich, S.H., Davis, D.W., Spooner, E.T.C., 2003. New U–Pb ages for host rocks, mineralization and alteration of iron oxide (Cu-Au) deposits in the Coastal Cordillera of northern Chile, *South American Symposium on Isotope Geology* **4**, Salvador de Bahia, Brazil, pp. 63–66.

Gifkins, C.C., Allen, R.L., 2001. Textural and Chemical Characteristics of Diagenetic and Hydrothermal Alteration in Glassy Volcanic Rocks: Examples from the Mount Read Volcanics, Tasmania. *Economic Geology* **96**, 973–1002.

Gill, R., 2010. *Igneous Rocks and Processes: A Practical Guide.* Wiley-Blackwell, Chichester, UK.

Grant, J.A., 1986. The Isocon Diagram—A Simple Solution to Gresens' Equation for Metasomatic Alteration. *Economic Geology* **81**, 1976–1982.

Gresens, R.L., 1967. Composition-volume relationships of metasomatism. *Chemical Geology* **2**, 47–55.

Gustafson, L.B., Hunt, J.P., 1975. The porphyry copper deposit at El Salvador, Chile. *Economic Geology* **70**, 857–912.

Gustafson, L.B., Quiroga G., J., 1995. Patterns of Mineralization and Alteration below the Porphyry Copper Orebody at El Salvador, Chile. *Economic Geology* **90**, 2–16.

Halter, W.E., Heinrich, C.A., Pettke, T., 2005. Magma evolution and the formation of porphyry Cu–Au ore fluids: evidence from silicate and sulfide melt inclusions. *Mineralium Deposita* **39**, 845–863.

Hammer, J.E., Rutherford, M.J., 2002. An experimental study of the kinetics of decompression-induced crystallization in silicic melt. *Journal of Geophysical Research* **107**, B1, ECV 8-1–ECV 8–24.

Hansen, J., 2015. A numerical approach to sill emplacement in isotropic media: Do saucer-shaped sills represent 'natural' intrusive tendencies in the shallow crust? *Tectonophysics* **664**, 125–138.

Harris, A.C., Allen, C.A., Bryan, S.E., Campbell, I.H., Holcombe, R.J., Palin, M.J., 2004. Measuring the longevity of regional volcanism hosting the Bajo de la Alumbrera Cu-Au deposit: Implications for the genesis of porphyry ore deposits. *Mineralium Deposita* **39**, 46–67.

Harris, A.C., Dunlap, W.J., Reners, P.W., Allen, C.M., Cooke, D.R., White, N.C., Campbell, I.H., Golding, S.D., 2008. Multimillion year thermal history of a porphyry copper deposit: Application of U–Pb, 40Ar/39Ar and (U–Th)/He chronometers, Bajo de la Alumbrera copper-gold deposit, Argentina. *Mineralium Deposita* **43,** 295–314.

Haschke, M., Gu¨nther, A., 2003. Balancing crustal thickening in arcs by tectonic vs. magmatic means*, Geology* **31**, 933 – 936.

Haschke, M.R., Scheuber, E., Gu ̈nther, A., Reutter, K.J., 2002a. Evolutionary cycles during the Andean orogeny: repeated slab breakoff and flat subduction? *Terra Nova* **14**, 49–55.

Haschke, M.R., Siebel, W., Gu ̈nther, A., Scheuber, E., 2002b. Repeated crustal thickening and recycling during the Andean orogeny in north Chile (21°–26°S). *Journal of Geophysical Research* **107**, B1–2019.

Hattori, K.H., Keith, J.D., 2001. Contribution of mafic melt to porphyry copper mineralization: evidence from Mount Pinatubo, Philippines, and Bingham Canyon, Utah, USA. *Mineralium Deposita* **36**, 799–806.

Hedenquist, J.W., Arribas Jr., A., Reynolds, T.J., 1998. Evolution of an Intrusion-Centered Hydrothermal System: Far Southeast-Lepanto Porphyry and Epithermal Cu-Au Deposits, Philippines. *Economic Geology* **93**, 373–404.

Hedenquist, J.W., Lowenstern, J.B., 1994. The role of magmas in the formation of hydrothermal ore deposits. *Nature* **370**, 519–527.

Heinrich, C.A., Gu̇nther, D., Audétat, A., Ulrich, T., Frischknecht, R., 1999. Metal fractionation between magmatic brine and vapor, determined by microanalysis of fluid inclusions. *Geology* **27**, 755–758.

Heinrich, C.A., Ryan, C., Mernagh, T.P., Eadington, P.J., 1992. Segregation of Ore Metals between Magmatic Brine and Vapor: A Fluid Inclusion Study Using PIXE Microanalysis. *Economic Geology* **87**, 1566–1583.

Hemley, J.J., Hunt, J.P., 1992. Hydrothermal Ore-Forming Processes in the Light of Studies in Rock-Buffered Systems: II . Some General Geologic Applications. *Economic Geology* **87**, 23–43.

Henley, R.W., King, P.L., Wykes, J.L., Renggli, C.J., Brink, F.J., Clark, D.A., Troitzsch, U., 2015. Porphyry copper deposit formation by sub-volcanic sulphur dioxide flux and chemisorption. *Nature Geoscience* **8**, 210–215.

Hezarkhani, A., Williams-Jones, A.E., Gammons, C.H., 1999. Factors controlling copper solubility and chalcopyrite deposition in the Sungun porphyry copper deposit, Iran. *Mineralium Deposita* **34**, 770–783.

Holland, H.D., 1965. Some applications of thermochemical data to problems of ore deposits II. Mineral assemblages and the composition of ore forming fluids. *Economic Geology* **60**, 1101–1166.

Horie, K., Takehara, M., Suda, Y., Hidaka, H., 2013. Potential Mesozoic reference zircon from the Unazuki plutonic complex: geochronological and geochemical characterization. *Island Arc* **22**, 292–305.

Horn, I., von Blanckenburg, F., 2007. Investigation on elemental and isotopic fractionation during 196 nm femtosecond laser ablation multiple collector inductively coupled plasma mass spectrometry. *Spectrochimica Acta Part B* **62**, 410–422.

Huete, C., Maksaev, V., Moscoso, R., Ulricksen, C., Vergara, H., 1977. Antecedentes geocronológicos de rocas intrusivas y volcánicas de la Cordillera de los Andes comprendida entre la Sierra de Moreno y el Rio Loa, y los 21o y 22o de latitud Sur, II Región, Chile. *Revista Geológica de Chile* **4**, 35–41.

Humphreys, M. C. S., Brooker, R. A., Fraser, D. G., Burgisser, A., Mangan M. T., McCammon, C., 2015. Coupled Interactions between Volatile Activity and Fe Oxidation State during Arc Crustal Processes. Journal of Petrology 56, 795–814.

Isacks, B.L., 1988. Uplift of the Central Andean Plateau and Bending of the Bolivian Orocline. *Journal of Geophysical Research* **93,** 3211–3231.

Iwano, H., Orihashi, Y., Hirata, T., Ogasawara, M., Danhara, T., Horie, K., Hasebe, N., Sueoka, S., Tamura, A., Hayasaka, Y., Katsube, A., Ito, H., Tani., K., Kimura, J.I., Chang, Q., Kouchi, Y., Haruta, Y., Yamamoto, K., 2013. An inter-laboratory evaluation of OD-3 zircon for use as a secondary U–Pb dating standard. *Island Arc* **22**, 382–394.

James, D.E., Sacks, S., 1999. Cenozoic formation of the central Andes: A geophysical perspective, in: Skinner, B.J. (Ed.), *Geology and Ore Deposits of the Central Andes,* Society of Economic Geologists Special Publication, pp. 1–25.

Jébrak, M., 1997. Hydrothennal breccias in vein-type ore deposits: A review of mechanisms, morphology and size distribution. *Ore Geology Reviews* **12**, 111–134.

Kay, S.M., Mpodozis, C., 2001. Central Andean Ore Deposits Linked to Evolving Shallow Subduction Systems and Thickening Crust. *GSA Today* **11**, 4–9.

Kay, S.M., Mpodozis, C., Coira, B., 1999. Magmatism, tectonism, and mineral deposits of the Central Andes (22°–33°S latitude). in: Skinner, B.J. (Ed.), *Geology and Ore Deposits of the Central Andes*, Society of Economic Geologists Special Publication, pp. 27–59.

Kay, S.M., Ramos, V.A., Mpodozis, C., Sruoga, P., 1989. Late Palaeozoic to Jurassic silicic magmatism at the Gondwana margin: Analogy to the middle Proterozoic in North America? *Geology* **17**, 324–328.

Kerr, P.F., Kulp, J.L., Patterson, C.M., Wright, R.J., 1950. Hydrothermal Alteration at Santa Rita, New Mexico. *Geological Society of America Bulletin* **61**, 275–347.

Kober, F., Ivy-Ochs, S., Schlunegger, F., Baur, H., Kubik, P.W., Wieler, R., 2007. Denudation rates and a topography-driven rainfall threshold in northern Chile: Multiple cosmogenic nuclide data and sediment yield budgets. *Geomorphology* **83**, 97–120

Kouchi, Y., Orihashi, Y., Obara, H., Fujimoto, T., Haruta, Y., Yamamoto, K., 2015. Zircon U–Pb dating by 213 nm Nd: YAG laser ablation inductively coupled plasma mass spectrometry: Optimization of the analytical condition to use NIST SRM 610 forPb/U fractionation correction. *Chikyukagaku (Geochemistry)* **49**, 19–35.

Kouzmanov, K., Pokrovski, G.S., 2012. Hydrothermal Controls on Metal Distribution in Porphyry Cu (-Mo-Au) Systems. In: Hedenquist, J.F., Harris, M., Camus, F. (eds). *Geology and Genesis of Major Copper Deposits and Districts of the World, A Tribute to Richard H. Sillitoe.* Society of Economic Geologists Special Publication **16**, 573–618.

Landtwing, M.R., Furrer, C., Redmond, P.B., Pettke, T., Guillong, M., Heinrich, C.A., 2010. The Bingham Canyon Porphyry Cu-Mo-Au Deposit. III. Zoned Copper-Gold Ore Deposition by Magmatic Vapor Expansion. *Economic Geology* **105**, 91–118.

Landtwing, M. R., Pettke, T., Halter, W.E., Heinrich, C.A., Redmond, P.B., Einaudi, M.T., Kunze, K., 2005. Copper deposition during quartz dissolution by cooling magmatic–hydrothermal fluids: The Bingham porphyry. *Earth and Planetary Science Letters* **235**, 229– 243.

Lee, R.G., 2008. Genesis of the El Salvador Porphyry Copper Deposit, Chile and Distribution of Epithermal Alteration at Lassen Peak, California, PhD Thesis. Oregon state university.

Le Maitre, R.W., 1989. *A Classification of Igneous Rocks and Glossary of Terms.* Blackwell, Oxford.

Lerchbaumer, L., Aude´tat, A., 2012. High Cu concentrations in vapor-type fluid inclusions: An artifact? *Geochimica et Cosmochimica Acta* **88**, 255–274.

Lewis, W. J., 1899. *A Treatise on Crystallography.* Vol 2 Cambridge University Press 615 pp.

Lortie, R.B., Clark, A.H., 1987. Strata-Bound Cupriferous Sulfide Mineralization Associated with Continental Rhyolitic Volcanic Rocks, Northern Chile: I. The Jardín Copper-Silver Deposit. *Economic Geology* **82,** 546–570.

Lowell, J.D., Guilbert, J.M., 1970. Lateral and vertical alteration-mineralization zoning in porphyry ore deposits. *Economic Geology* **65**, 373–408.

Ludwig, K.R. 1998. On the treatment of concordant uranium-lead ages. *Geochimica et Cosmochimica Acta* **62**, 665–676.

Ludwig, K.R., 2012. *User's Manual for ISOPLOT 3.75—A Geochronological Toolkit for Microsoft Excel.* Berkeley Geochronology Center, Special Publication **5**, 75 p.

Lukács R., Harangi, S., Bachmann, O., Guillong, M., Danišík, M., Buret, Y., von Quadt, A., Dunkl, I., Fodor, L., Sliwinski, J., Soós, I., Szepesi, J., 2015. Zircon geochronology and geochemistry to constrain the youngest eruption events and magma evolution of the Mid-Miocene ignimbrite flare-up in the Pannonian Basin, eastern central Europe. *Contributions to Mineralogy and Petrology* **170**, 1-26.

Madeisky, H.E., 1996, A lithogeochemical and radiometric study of hydrothermal alteration and metal zoning at the Cinola epithermal gold deposit, Queen Charlotte Islands, British Columbia, in: Coyner, A.R., Fahey, P.L. (Eds.), *Geology and Ore Deposits of the American Cordillera*, v.3, pp. 1153–1185.

Maksaev, V., 1990. Metallogenic, geological evolution and thermochronology of the Chilean Andes between latitudes 21°and 26°S, and the origin of major porphyry copper deposits, PhD Thesis. Dalhousie University, Canada.

Maksaev, V., Almonacid, T.A., Munizaga, F., Valencia, V., McWilliams, M., Barra, F., 2010. Geochronological and thermochronological constraints on porphyry copper mineralization in the Domeyko alteration zone, northern Chile. *Andean Geology* **37**, 144–176.

Maksaev, V., Munizaga, F., Fanning, M., Palacios, C., Tapia, J., 2006. SHRIMP U–Pb dating of the Antucoya porphyry copper deposit: new evidence for an Early Cretaceous porphyry-related metallogenic epoch in the Coastal Cordillera of northern Chile. *Mineralium Deposita* **41**, 637–644.

Maksaev, V., Munizaga, F., McWilliams, M., Fanning, M., Mathur, R., Rutz, J., Zentilli, M., 2004. New Chronology for El Teniente, Chilean Andes, from U–Pb, 40Ar/39Ar, Re–Os, and Fission-Track Dating: Implications for the Evolution of a Supergiant Porphyry Cu-Mo Deposit, in: Sillitoe, R.H., Perelló, J., Vidal, C.E. (Eds.), *Andean Metallogeny: New Discoveries, Concepts, and Updates*. Society of Economic Geologists Special Publication, pp. 15–54.

Maksaev, V., Munizaga, F., Tassinari, C., 2014. Timing of the magmatism of the paleo-Pacific border of Gondwana: U–Pb geochronology of Late Paleozoic to Early Mesozoic igneous rocks of the north Chilean Andes between 20° and 31°S. *Andean Geology* **41**, 447–506.

Maksaev, V., Townley, B., Palacios, C., Camus, F., 2007. Metallic ore deposits, in: Moreno, T., Gibbons, W. (Eds.), *The Geology of Chile.* The Geological Society, London, pp. 179-199.

Maksaev, V., Zentilli, M., 1999. Fission Track Thermochronology of the Domeyko Cordillera, Northern Chile: Implications for Andean Tectonics and Porphyry Copper Metallogenesis. *Exploration and Mining Geology* **8**, 65–89.

Marschik, R., Fontboté, L., 2001. The Candelaria-Punta del Cobre iron oxide Cu-Au(-Zn-Ag) deposits, Chile. *Economic Geology* **96**, 1799–1826.

Masterman, G.J., Cooke, D.R., Berry, R.F., Clark, A.H., Archibald, D.A., Mathur, R., Walshe, J.L., Durán, M., 2004. 40Ar/39Ar and Re–Os Geochronology of Porphyry

Copper-Molybdenum Deposits and Related Copper-Silver Veins in the Collahuasi District, Northern Chile. *Economic Geology* **99**, 673–690.

Mathur, R., Marschik, R., Ruiz, J., Munizaga, F., Leveille, R.A., Martin, W., 2002. Age of Mineralization of the Candelaria Fe Oxide Cu-Au Deposit and the Origin of the Chilean Iron Belt, Based on Re–Os Isotopes. *Economic Geology* **97**, 59–71.

Mathur, R., Ruiz, J., Munizaga, F., 2000. Relationship between copper tonnage of Chilean base-metal porphyry deposits and Os isotope ratios. *Geology* **28**, 555–558.

Matjuschkin, V., Blundy, J.D., Brooker, R.A., 2016. The effect of pressure on sulphur speciation in mid to deep-crustal arc magmas and implications for the formation of porphyry copper deposits. *Contributions To Mineralogy and Petrology* **171**:66, pp 25.

Matthews, W.A., Guest, B, 2016. A Practical Approach for Collecting Large-n Detrital Zircon U-Pb Data sets by Quadrupole LA-ICP-MS. Geostandards and *Geoanalytical Research* **41**, 161–180.

Mattinson, J. M., Graubard, C. M., Parkinson, D. L., McClelland, W. C., 1996. U-Pb reverse discordance in zircons: the role of fine-scale oscillatory zoning and sub-micron transport of Pb, in: Basu, A.R., Hart, S.R., (Eds.), *Earth Processes: Reading the Isotopic Code*, Geophysical Monograph Series Volume 95, American Geophysical Union, pp. 355–370.

McInnes, B.I.A., Evans, N.J., Fu, F.Q., Garwin, S., Belousova, E., Griffin, W.L., Bertens, A., Sukarna, D., Permanadewi, S., Andrew, R.L., Deckart, K., 2005. Thermal History Analysis of Selected Chilean, Indonesian and Iranian Porphyry Cu-Mo-Au Deposits, in: Porter, T.M. (Ed.), *Super Porphyry Copper & Gold Deposits: A Global Perspective*, PGC Publishing, Adelaide, pp. 1–16.

Menand, T., 2011. Physical controls and depth of emplacement of igneous bodies: A review. *Tectonophysics* **500,** 11–19.

Meyer, C., Hemley, J.J., 1967. Wall rock alteration, in: H.L., B. (Ed.), *Geochemistry of hydrothermal ore deposits*. Holt, Rinehart and Winston, New York, pp. 166–232.

Miller, J.S., Matzel, J.E.P., Miller, C.F., Burgess, S.D., Miller, R.B., 2007. Zircon growth and recycling during the assembly of large, composite arc plutons. *Journal of Volcanology and Geothermal Research* **167**, 282–299.

Mortimer, C., Farrar, E., Saric, N., 1974. K–Ar ages from Tertiary lavas of the northernmost Chilenean Andes. *Geologische Rundschau* **63**, 395–420.

Mountain, B. W., Seward, T. M., 1999. The hydrosulphide/ sulphide complexes of copper (I): experimental determination of the stoichiometry an stability at 22 °C and reassessment of high temperature data. *Geochemica et Cosmochimica Acta* **63**, 11–29.

Mountain, B. W., Seward, T. M., 2003. Hydrosulphide/ sulphide complexes of copper(I): experimental confirmation of the stoichiometry and stability of $Cu(HS)_2^-$ to elevated temperatures. *Geochemica et Cosmochimica Acta* **67**, 3005–3014.

Mpodozis, C., Arriagada, C., Basso, M., Roperch, P., Cobbold, P., Reich, M., 2005. Late Mesozoic to Paleogene stratigraphy of the Salar de Atacama basin, Antofagasta, northern Chile: Implications for the tectonic evolution of the central Andes. *Tectonophysics* **399**, 125–154.

Mpodozis, C., Cornejo, P., 2012. Cenozoic Tectonics and Porphyry Copper Systems of the Chilean Andes, in: Hedenquist, J.W., Harris, M., Camus, F. (Eds.), *Geology and Genesis of Major Copper Deposits and Districts of the World: A Tribute to Richard H. Sillitoe.* Society of Economic Geologists Special Publication, pp. 329–360.

Mpodozis, C., Kay, S.M. 1990. Provincias magmáticas ácidas y evolución tectónica de Gondwana: Andes chilenos (28–31°S). *Revista Geologica de Chile* **17**, 153–180

Mpodozis, C., Ramos, V. A. 1989. The Andes of Chile and Argentina. In: Ericksen, G. E., Cañas, M. T. & Reinemund (eds). *Geology of the Andes and its Relation to Hydrocarbon and Energy Resources.* Houston, Texas. Circum-Pacific Council for Energy and Hydrothermal Resources, Earth Science Series **11**, 59–90.

Mungall, J.E., 2002. Roasting the mantle: Slab melting and the genesis of major Au and Au-rich Cu deposits. *Geology* **30**, 915–918.

Munizaga, F., Maksaev, V., Fanning, C.M., Giglio, S., Yaxley, G., Tassinari, C.C.G., 2008. Late Paleozoic– Early Triassic magmatism on the western margin of Gondwana: Collahuasi area, Northern Chile. *Gondwana Research* **13**, 407–427.

Muñoz, J.O., 1975. On Stratiform copper deposits of Chile. *Annales de la Société Géologique de Belgique* T. **98**, 17–21.

Murray, B.P., Busby, C.J., Ferrari, L., Solari, L.A., 2013. Synvolcanic crustal extension during the mid-Cenozoic ignimbrite flare-up in the northern Sierra Madre Occidental, Mexico: Evidence from the Guazapares Mining District region, western Chihuahua. *Geosphere* **9**, 1201–1235.

Nadeau, O., Williams-Jones, A.E., Stix, J., 2010. Sulphide magma as a source of metals in arc-related magmatic hydrothermal ore fluids. *Nature Geoscience* **3**, 501–505.

Nadeau, O., Stix, J., Williams-Jones, A.E., 2016. Links between arc volcanoes and porphyry-epithermal ore deposits. *Geology* **44**, 11–14.

O'Driscoll, L.J., Richards, M.A., Humphreys, E.D., 2012. Nazca–South America interactions and the late Eocene–late Oligocene flat-slab episode in the central Andes. *Tectonics* **31**, TC2013.

Oliveros, V., Féraud, G., Aguirre, L., Ramírez, L., Fornari, M., Palacios, C., Parada, M., 2008. Detailed 40Ar/39Ar dating of geologic events associated with the Mantos Blancos copper deposit, northern Chile. *Mineralium Deposita* **43**, 281–293.

Orihashi, Y., Nakai, S., Hirata, T., 2008. U-Pb Age Determination for Seven Standard Zircons using Inductively Coupled Plasma–Mass Spectrometry Coupled with Frequency Quintupled Nd-YAG (λ= 213 nm) Laser Ablation System: Comparison with LA-ICP-MS Zircon Analyses with a NIST Glass Reference Material. *Resource Geology* **58**, 101–123.

Ossandón, G., Fréraut, R., Gustafson, L., Lindsay, D., Zentilli, M., 2001. Geology of the Chuquicamata mine: A progress report. *Economic Geology* **96**, 240–270.

Pardo-Casas, F., Molnar, P., 1987. Relative Motion of the Nazca (Farallon) and South American Plates since Late Cretaceous Time. *Tectonics* **6**, 233–248.

Pearce, J.A., 1996. A user's guide to basalt discrimination diagrams, in: Wyman, D.A. (Ed.), *Trace Element Geochemistry of Volcanic Rocks: Applications for Massive Sulphide Exploration.* Geological Association of Canada, Short Course Notes **12**, pp. 79–113.

Perelló, J., Martini, R., Arcos, R., Muhr, R., 2003. Buey Muerto: porphyry copper mineralization in the Early Cretaceous arc of northern Chile, Actas X Congreso Geológico Chileno, Concepción, Chile.

Petersen, C.R., Rivera, S.L., Peri, M.A., 1996. Chimborazo copper deposit, Region II, Chile: Exploration and geology, in: Camus, F., Sillitoe, R.H., Petersen, R. (Eds.), *Andean Copper Deposits: New Discoveries, Mineralization, Styles and Metallogeny.* Society of Economic Geologists Special Publication **5**, pp. 71–80.

Pohl, W.L., 2011. *Economic Geology: Principles and Practice*. John Wiley and Sons Ltd, West Sussex, UK

Proffett, J.M., 2009. High Cu grades in porphyry Cu deposits and their relationship to emplacement depth of magmatic sources. *Geology* **37**, 675–678.

Quang, C.X., Clark, A.H., Lee, J.K.W., Guillén B., J., 2003. 40Ar– 39Ar ages of hypogene and supergene mineralization in the Cerro Verde-Santa Rosa porphyry Cu-Mo cluster, Arequipa, Peru. *Economic Geology* **98**, 1683–1696.

Reynolds, P., Ravenhurst, c., Zentilli, M., Lindsay, D., 1998. High-precision 40Ar/39Ar dating of two consecutive hydrothermal events in the Chuquicamata porphyry copper system, Chile. *Chemical Geology* **148**, 45–60.

Richards, J.P., 2003. Tectono-magmatic precursors for porphyry Cu-(Mo-Au) deposit formation. *Economic Geology* **98**, 1515–1533.

Richards, J.P., 2005. Cumulative Factors in the Generation of Giant Calc-alkaline Porphyry Cu Deposits, in: Porter, T.M. (Ed.), *Super Porphyry Copper & Gold Deposits: A Global Perspective*. PGC Publishing, Adelaide, pp. 7–25.

Richards, J.P., 2011a. Magmatic to hydrothermal metal fluxes in convergent and collided margins. *Ore Geology Reviews* **40**, 1–26.

Richards, J.P., 2011b. High Sr/Y arc magmas and porphyry Cu ± Mo ± Au deposits: just add water. *Economic Geology* **106**, 1075–1081.

Richards, J.P., 2013. Giant ore deposits formed by optimal alignments and combinations of geological processes. *Nature Geoscience* **6**, 911–916.

Richards, J.P., Boyce, A.J., Pringle, M.S., 2001. Geologic evolution of the Escondida area, northern Chile: A model for spatial and temporal localization of porphyry Cu mineralization. *Economic Geology* **96**, 271–305.

Richards, J.P., Kerrich, R., 2007. Special Paper: Adakite-Like Rocks: Their Diverse Origins and Questionable Role in Metallogenesis. *Economic Geology* **102,** 537–576.

Richards, J.P., Noble, S.R., Pringle, M.S., 1999. A Revised Late Eocene Age for Porphyry Cu Magmatism in the Escondida Area, Northern Chile. *Economic Geology* **94,** 1231–1248.

Rivera, S., Pardo, R., 2004. Discovery and Geology of the Toki porphyry Copper Deposits, Chuquicamata District, Northern Chile, in: Sillitoe, R.H., Perelló, J., Vidal, C.E. (Eds.), *Andean Metallogeny: New Discoveries, Concepts, and Update*. Society of Economic Geologists Special Publication, pp. 199–211.

Rivera, S.L., Alcota, H., Proffett, J., Díaz, J., Leiva, G., Vergara, M., 2012. Update of the geologic setting and porphyry Cu-Mo deposits of the Chuquicamata District, northern Chile, in: Hedenquist, J.W., Harris, M., Camus, F. (Eds.), *Geology and Genesis of Major Copper Deposits and Districts of the World: A Tribute to Richard H. Sillitoe*. Society of Economic Geologists Special Publication **16,** pp. 19–54.

Roedder, E., 1971. Fluid inclusion studies on the porphyry type deposits at Bingham. Utah, Butte, Montana, and Climax, Colorado. *Economic Geology* **66**, 66–120.

Roedder, E., 1972. Composition of fluid inclusions. *U.S. Geological Survey Professional Paper* **440JJ**. 189 p.

Roedder, E., Bodnar, R.J., 1997. Fluid inclusion studies of hydrothermal ore deposits, in: Barnes, H.L. (Ed.), *Geochemistry of hydrothermal ore deposits.* John Wiley & Sons, Inc. New York, pp. 657–698.

Rohrlach, B.D., Loucks, B.R., 2005. Muti-Million-Year Cyclic Ramp-Up of Volatiles in a Lower Crustal Magma Reservoir Trapped Below the Tampakan Copper-Gold Deposit by Mio–Pliocene Crustal Compression in the Southern Phillippines. in: Porter, T.M. (Ed.), *Super Porphyry Copper & Gold Deposits: A Global Perspective.* PGC Publishing, Adelaide. pp. 369–407.

Rose, A.W., Burt, D.M., 1979. Hydrothermal alteration, in: H.L., B. (Ed.), *Geochemistry of Hydrothermal Ore Deposits,* 2nd edition. John Wiley and Sons, New York, pp. 173–235.

Rosenbaum, G., Giles, D., Saxon, M., Betts, P.G., Weinberg, R.F., Duboz, C., 2005. Subduction of the Nazca Ridge and the Inca Plateau: Insights into the formation of ore deposits in Peru. *Earth and Planetary Science Letters* **239**, 18–32.

Rosera, J.M., Coleman, D.S., Stein, H.J., 2013. Re-evaluating genetic models for porphyry Mo mineralization at Questa, New Mexico: Implications for ore deposition following silicic ignimbrite eruption. *Geochemistry Geophysics Geosystems* **14**, 787–805

Rossignol, C., Bourquin, S., Poujol, M., Hallot, E., Dabard, M.-P., Nalpas, T., 2016. The volcaniclastic series from the luang prabang basin, Laos: A witness of a Triassic magmatic arc? *Journal of Asian Earth Sciences* **120**, 159–183.

Rothstein, D.A., Manning, C.E., 2003. Geothermal gradients in continental magmatic arcs: Constraints from the eastern Peninsular Ranges batholith, Baja California, México, in: Johnson, S.E., Paterson, S.R., Fletcher, J.M., Girty, G.H., Kimbrough, D.L., and Martín-Barajas, A., eds., *Tectonic evolution of northwestern México and the southwestern USA.* Boulder, Colorado, Geological Society of America Special Paper **374**, pp. 337–354.

Rowland, M.G., Clark, A.H., 2001. Temporal overlap of supergene alteration and high-sulfidation mineralization in the Spence porphyry copper deposit, II Region, Chile, *GSA Annual Meeting* **33**, A-358.

Rusk, B.G., Reed, M.H., Dilles, J.H., 2008. Fluid Inclusion Evidence for Magmatic-Hydrothermal Fluid Evolution in the Porphyry Copper-Molybdenum Deposit at Butte, Montana. *Economic Geology* **103,** 307–334.

Sachau, T., Bons, P.D., Gomez-Rivas, E., 2015. Transport efficiency and dynamics of hydraulic fracture networks. *Frontiers in Physics* **3**, art. 63.

Sambridge, M.S., Compston, W., 1994. Mixture modeling of multi-component data sets with application to ion-probe zircon ages. *Earth and Planetary Science Letters* **128**, 373–390.

Sapiie, B., Cloos, M., 2004. Strike-slip faulting in the core of the Central range of west New Guinea: Ertsberg Mining District, Indonesia. *GSA Bulletin* **116**, 277–293.

Scheuber, E., Reutter, K.J., 1992. Magmatic arc tectonics in the Central Andes between 21o and 25oS. *Tectonophysics* **205**, 127–140.

Schlunegger, F., Zeilinger, G., Kounov, A., Kober, F., Hu¨sser, B., 2006. Scale of relief growth in the forearc of the Andes of Northern Chile (Arica latitude, 18°S) *Terra Nova* **18**, 217–223.

Seedorff, E., Dilles, J.H., Proffett, Jr., J.M., Einaudi, M.T., Zurcher, L., Stavast, W.J.A., Johnson, D.A., Barton, M.D. 2005. Porphyry Deposits: Characteristics and Origin of Hypogene Features. In: Hedenquist, J.W., Thompson, J.F.H., Goldfarb, R.J., Richards, J.P. (Ed) *Economic Geology 100th Anniversary Volume*. Society of Economic Geologists. pp. 251–298

Segerstrom, K., 1959. Geología del Cuadrángulo Los Loros. Instituto de Investigaciones Geológicas, Carta Geológica de Chile 1:1–33, Santiago.

Seo, J.H., Guillong, M., Heinrich, C.A., 2012. Separation of Molybdenum and Copper in Porphyry Deposits: The Roles of Sulfur, Redox, and pH in Ore Mineral Deposition at Bingham Canyon. *Economic Geology* **107**, 333–356.

Shinohara, H., 1994. Exsolution of immiscible vapor and liquid phases from a crystallizing silicate melt: Implications for chlorine and metal transport. *Geochemica et Cosmochimica Acta* **58**, 5215–5221.

Shinohara, H., Hedenquist, J.W., 1997. Constraints on Magma Degassing beneath the Far Southeast Porphyry Cu–Au Deposit, Philippines. *Journal of Petrology* **38**, 1741–1752.

Shinohara, H., Kazahaya, K., Lowenstern, J.B., 1995. Volatile transport in a convecting magma column: Implications for porphyry Mo mineralization. *Geology* **23**, 1091–1094.

Sheppard, S.M.F., Nielsen, R.L., Taylor, Jr., H.P., 1971. Hydrogen and Oxygen Isotope Ratios in Minerals from Porphyry Copper Deposits. *Economic Geology* **66**, 515–542.

Sibson, R.H., 1981, Fluid flow accompanying faulting: Field evidence and models, in Simpson, D.W., and Richards, P.G., eds., *Earthquake prediction: An international review:* American Geophysical Union, Maurice Ewing Series, pp. 593–603.

Sibson, R.H., Robert, F., Poulsen, K.H., 1988. High-angle reverse faults, fluid-pressure cycling, and mesothermal gold-quartz deposits. *Geology* **16**, 551–555.

Sillitoe, R.H., 1973. The Tops and Bottoms of Porphyry Copper Deposits. *Economic Geology* **68**, 799–815.

Sillitoe, R.H., 1974. Tectonic segmentation of the Andes: implications for magmatism and metallogeny. *Nature* **250**, 542–545.

Sillitoe, R. H., 1985. Ore-Related Breccias in Volcanoplutonic Arcs. *Economic Geology* **80**, 1467–1514.

Sillitoe, R.H., 1988. Epochs of intrusion-related copper mineralization in the Andes. *Journal of South American Earth Sciences* **1**, 89–108.

Sillitoe, R.H., 1994. Erosion and collapse of volcanoes: Causes of telescoping in intrusion-centered ore deposits. *Geology* **22**, 945–948.

Sillitoe, R.H., 2010. Porphyry copper systems. *Economic Geology* 105, 3–41.

Sillitoe, R.H., 2012. Copper Provinces, in: Hedenquist, J.W., Harris, M., Camus, F. (Eds.), *Geology and Genesis of Major Copper Deposits and Districts of the World: A Tribute to Richard H. Sillitoe*. Society of Economic Geologists Special Publication, pp. 1–18.

Sillitoe, R.H., Clark, A.H., 1969. Copper and Copper-Iron Sulphides as the Initial Products of Supergene Oxidation, Cipiapó Mining District, Northern Chile. *The American Mineralogist* **54**, 1684–1710.

Sillitoe, R.H., Mortensen, J.K., 2010. Longevity of Porphyry Copper Formation at Quellaveco, Peru. *Economic Geology* **105**, 1157–1162.

Sillitoe, R.H. & Perelló, J. 2005. Andean copper province: tectonomagmatic settings, deposit types, Metallogeny, exploration, and discovery, in: Hedenquist J.W., et al. (Eds.), *Economic Geology One Hundredth Anniversary Volume (1905-2005)*, pp. 845–890.

Simmons, A.T., Tosdal, R.M., Wooden, J.L., Mattos, R., Concha, O., McCracken, S., Beale, T., 2013. Punctuated Magmatism Associated with Porphyry Cu-Mo Formation in the Paleocene to Eocene of Southern Peru. *Economic Geology* **108**, 625–639.

Simon A. C., Pettke T., Candela P. A., Piccoli P. M., Heinrich C. A., 2006. Copper partitioning in a melt–vapor–brine–magnetite–pyrrhotite assemblage. *Geochimica et Cosmochimica Acta* **70**, 5583–5600.

Singer, D.A., Berger, V.I., Moring, B.C., 2008. Porphyry copper deposits of the world: database and grade and tonnage models: *U.S.G.S Open-File Report* 2008–1155.

Sinha, A.K., Wayne, D.M., Hewitt, D.A., 1992. The hydrothermal stability of zircon: Preliminary experimental and isotopic studies. *Geochemica et Cosmochimica Acta* **56**, 3551–3560.

Skewes, M.A., Stern, C.R. 1994. Tectonic trigger for the formation of late Miocene Cu-rich breccia pipes in the Andes of central Chile. *Geology* **22**, 551–554

Solomon, M., 1990. Subduction, arc reversal, and the origin of porphyry copper-gold deposits in island arcs. *Geology* **18**, 630–633.

Sourirajan, S., Kennedy, G.C., 1962. The system H_2O–NaCl at elevated temperatures and pressures. *American Journal of Science* **260**, 115–141.

Steinberger, I., Hinks, D., Driesner, T., Heinrich, C.A., 2013. Source Plutons Driving Porphyry Copper Ore Formation: Combining Geomagnetic Data, Thermal Constraints, and Chemical Mass Balance to Quantify the Magma Chamber Beneath the Bingham Canyon Deposit. *Economic Geology* **108**, 605–624.

Sterner, S.M., Bodnar, R.J., 1989. Synthetic fluid inclusions. VII. Re-equilibration of fluid inclusions in quartz during laboratory simulated metamorphic burial and uplift. *Journal of Metamorphic Geology* **7**, 243–260.

Sterner, S.M., Hall, D.L, Keppler, H., 1995. Compositional re-equilibration of fluid inclusions in quartz. *Contributions to Mineralogy and Petrology* **119**, 1–15.

Sun, T., Liu, L., 2014. Delineating the complexity of Cu–Mo mineralization in a porphyry intrusion by computational and fractal modeling: A case study of the Chehugou deposit in the Chifeng district, Inner Mongolia, China. *Journal of Geochemical Exploration* **144**, Part A, 128–143.

Tapster, S., Condon, D.J., Naden, J., Noble, S.R., Petterson, M.G., Roberts, N.M.W., Saunders, A.D., Smith, D.J., 2016. Rapid thermal rejuvenation of high-crystallinity magma linked to porphyry copper deposit formation, evidence from the Koloula Porphyry Prospect, Solomon Islands. *Earth and Planetary Science Letters* **442**, 206–217.

Tomlinson, A.J., Martin, M.W., Blanco, N., Perez de Arce, C., 2001. U–Pb and K–Ar geochronology from the Cerro Empexa Formation, 1st and 2nd Regions, Precordillera, Northern Chile, 3. *South American symposium on isotope geology, Pucon (Chile)*, Extended abstract.

Tosdal, R.M., Richards, J.P., 2001. Magmatic and structural controls on the development of porphyry Cu ± Mo ± Au deposits. In: Richards, J.P., Tosdal, R.M. (Eds.), *Structural Controls on Ore Genesis: Society of Economic Geologists.* Reviews in Economic Geology **14**, pp. 157–181.

Ullrich, T.D., Clark, A.H., 1999. The Candelaria copper-gold deposit, Region III, Chile: Paragenesis, geochronology and fluid composition, in: Stanley, C.J.e.a. (Ed.), *Mineral Deposits: Processes to Processing*. A.A.Balkema, Rotterdam, pp. 201–204.

Ulrich, T., Gu ̈nther, A., Heinrich, C.A., 1999. Gold concentrations of magmatic brines and the metal budget of porphyry copper deposits. *Nature* **399**, 676–679.

Ulrich, T.D., Gu ̈nther, D., Heinrich, C.A., 2002. The evolution of a porphyry Cu-Au deposit, based on LA-ICP-MS analysis of fluid inclusions: Bajo de la Alumbrera, Argentina (corrected version of Economic Geolology 96 (2001) 1743–1774), *Economic Geology* **97**, 1888–1920.

Ulrich, T., Heinrich, C.A., 2001. Geology and Alteration Geochemistry of the Porphyry Cu-Au Deposit at Bajo de la Alumbrera, Argentina. *Economic Geology* **96**, 1719–1742.

Valencia, V.A., Noguez-Alcántara, B., Barra, F., Ruiz, J., Gehrels, G., Quintanar, F., Valencia-Moreno, M. 2006. Re–Os molybdenite and LA-ICPMS-MC U–Pb zircon geochronology for the Milpillas porphyry copper deposit: insights for the timing of mineralization in the Cananea District, Sonora, Mexico. *Revista Mexicana de Ciencias Geológicas* **223**, 39–53.

Vergara, M., Drake, R., 1978. Edades postasio–argón y su implicancia en la geología regional de Chile. *Comunicaciones,* Departamento de Geología, Universidad de Chile, Santiago **23**, 1–11.

Victor, P., Oncken, O., Glodny, J., 2004. Uplift of the western Altiplano plateau: Evidence from the Precordillera between 20° and 21°S (northern Chile) *Tectonics*. **23**, TC4004

Vigneresse, J.-L.; Tikoff, B.; Ame ́glio, L., 1999. Modification of the regional stress field by magma intrusion and formation of tabular granitic plutons. *Tectonophysics* **302**, 203–224.

Vigneresse, J.-L., Truche, L., Chattaraj, P.K., 2014. Metal (copper) segregation in magmas. *Lithos* **208–209**, 462–470.

Vila, T., Lindsay, N., Zamora, R., 1996. Geology of the Manto Verde copper deposit, northern Chile: a specularite-rich, hydrothermal- tectonic breccia related to the Atacama Fault Zone, in: Camus, F., Sillitoe, R.H., Petersen, R. (Eds.), *Andean Copper Deposits: New Discoveries, Mineralization, Styles and Metallogeny.* Society of Economic Geologists Special Publication **5**, pp. 157–170.

Vityk, M.O., Bodnar, R.J., 1995. Textural evolution of synthetic fluid inclusions in quartz during re-equilibration, with applications to tectonic reconstruction. *Contributions to Mineralogy and Petrology* **121**, 309–323.

von Quadt, A., Erni, M., Martinek, K., Moll, M., Peytcheva, I., Heinrich, C.A., 2011. Zircon crystallization and the lifetimes of ore-forming magmatic-hydrothermal systems. *Geology* **39**, 731–734.

Warren, I., Simmons, S.F., Mauk, J.L., 2007. Whole-Rock Geochemical Techniques for Evaluating Hydrothermal Alteration, Mass Changes, and Compositional Gradients Associated with Epithermal Au-Ag Mineralization. *Economic Geology* **102**, 923–948.

Wendt, I., Carl, C., 1991. The statistical distribution of the mean squared weighted deviation. *Chemical Geology* (Isotope Geoscience Section) **86**, 275–285.

Weisheit, A., Bons, P.D., Elburg, M.A., 2013. Long-lived crustal-scale fluid flow: the hydrothermal mega-breccia of Hidden Valley, Mt. Painter Inlier, South Australia. *International Journal of Earth Sciences (Geologische Rundschau)* **102**, 1219–1236.

Wiedenbeck, M., Allé, P., Corfu, F., Griffin, W.L., Meier, M., Oberli, F., von Quadt, A., Roddick, J.C., Spiegel, W., 1995. Three natural zircon standards for U–Th–Pb, Lu–Hf, trace element and REE analyses. *Geostandards Newsletter* **19**, 1–23.

Wilkinson, J.J., 2001. Fluid inclusions in hydrothermal ore deposits. *Lithos* **55**, 229–272.

Wilkinson, J.J., 2013. Triggers for the formation of porphyry ore deposits in magmatic arcs. *Nature Geoscience* **6**, 917–925.

Williams-Jones A. E., Heinrich C. A., 2005. Vapor transport of metals and the formation of magmatic-hydrothermal ore deposits. *Economic Geology* **100,** 1287–1312.

Williamson, B.J., Herrington, R.J., Morris, A., 2016. Porphyry copper enrichment linked to excess aluminium in plagioclase. *Nature Geoscience* **9**, 237–241.

Winchester, J.A., Floyd, P.A., 1977. Geochemical discrimination of different magma series and their differentiation products using immobile elements. *Chemical Geology* **20**, 325–343.

Wohletz, K., Heiken, G., 1992. Surface Manifestations of Geothermal Systems. In: *Volcanology and Geothermal Energy*. University of California Press. p.128

Wörner, G., Hammerschmidt, K., Henjes-Kunst, F., Lezaun, J., Wilke, H., 2000. Geochronology (40Ar/39Ar, K-Ar and He-exposure ages) of Cenozoic magmatic rocks from Northern Chile (18-22°S): implications for magmatism and tectonic evolution of the central Andes. *Revista geológica de Chile* **27**, 205–240.

Yamamoto, K., Morishita, T., 1997. Preparation of standard compositions for the trace element analysis by X-ray fluorescence. *Journal of Geological Society of Japan* **103**, 1037–1045 (in Japanese, abstract in English).

Zajacz, Z., Seo, J.H., Candela, P.A., Piccoli, P.M., Tossell, J.A., 2011. The solubility of copper in high-temperature magmatic vapors: A quest for the significance of various chloride and sulfide complexes. *Geochimica et Cosmochimica Acta* **75**, 2811–2827.

Zellmer, G.F., Edmonds, M., Straub, S.M., 2015. Volatiles in subduction zone magmatism, in: Zellmer, G.F., Edmonds, M., Straub, S.M. (Eds.), *The Role of Volatiles in the Genesis, Evolution and Eruption of Arc Magmas.* Geological Society, London, pp. 1–17.

Zentilli, M., Boric, R., Heaman, L., Mathur, R., Hanley, J., 2015. New Development on the Geology of MMH: is it the "missing half" of Chuquicamata?, Extended Abstract, *SIM2 Exploration Andina: nuevos hallazgos y actualizaciones,* 14th Chilean Geological Congress, La Serena, Chile.

Zentilli, M., Graves, M.C., Lindsay, D.D., Ossandon, G., Camus, F., 1995. Recurrent mineralization in the Chuquicamata porphyry copper system: Restrictions on genesis from mineralogical, geochemical and isotopic studies, in: Clark, A.R. (Ed.), *Proceedings of giant ore deposits II: Controls of the scale of orogenic magmatic hydrothermal mineralization.* Queens University, Kingston, Ontario, pp. 86–111.

Zentilli, M., Krogh, T., Maksaev, V., Alpers, C., 1994. Uranium–lead dating of zircons from the Chuquicamata and La Escondida porphyry copper deposits, Chile: inherited zircon cores of Paleozoic ages with Tertiary overgrowths. *Comunicaciones*, Departamento de Geología, Universidad de Chile, Santiago **45**, 101–110.

Zimmerer, M.J., McIntosh, W.C., 2013. Geochronologic evidence of upper-crustal in situ differentiation: Silicic magmatism at the Organ caldera complex, New Mexico. *Geosphere* **9**, 155–169.

Zweng, P.L., Clark, A.H., 1995. Hypogene evolution of the Toquepala porphyry copper-molybdenum deposit, Moquegua, southern Peru, in: Pierce, F.W., Bolm, J.G. (Eds.), *Porphyry Copper Deposits of the American Cordillera,* Arizona Geological Society Digest **20**, Arizona, pp. 566-612.

Supplementary sheet 1 Summary of published ages in N. Chile

a) Summary of published U–Pb age data in N. Chile

Region	Latitude (S)	Longitude (W)		Rock type (or pluton name)	Method	Age (Ma) (± 2σ)	Reference
Cerro Verde- Santa Rosa	16° 31' 52"	71° 35' 57"	(Approx.)	premineralization pluton	U–Pb	67 ± 1	References within Sillitoe, 1988
Cerro Verde- Santa Rosa	16° 31' 52"	71° 35' 57"	(Approx.)	ore related intrusion	U–Pb	60 ± 1	References within Sillitoe, 1988
Cuajone	17° 1' 13.4"	70° 43' 33.12"		granodiorite	U–Pb LA-ICPMS	65.1 ± 0.8	Simmons et al., 2013
Cuajone	17° 1' 24.77"	70° 43' 23.74"		porphyry intrusions	U–Pb LA-ICPMS	53.5 ± 0.58	Simmons et al., 2013
Cuajone	17° 1' 50.38"	70° 42' 15.82"		intrusive andesite	U–Pb LA-ICPMS	56.2 ± 0.5	Simmons et al., 2013
Cuajone	17° 1' 54.24"	70° 42' 36.21"		porphyry intrusions	U–Pb LA-ICPMS	56.2 ± 0.7	Simmons et al., 2013
Toquepala	17° 13' 49.71"	70° 36' 53.86"		latite porphyry	U–Pb LA-ICPMS	54.3 ± 0.6	Simmons et al., 2013
Toquepala	17° 14' 4.6"	70° 36' 45.93"		dacite porphyry	U–Pb LA-ICPMS	56.8 ± 0.6	Simmons et al., 2013
Toquepala	17° 14' 7.15"	70° 36' 59.23"		diorite	U–Pb LA-ICPMS	61.4 ± 0.8	Simmons et al., 2013
Cuajone	17° 2' 6.21"	70° 42' 12.31"		porphyry intrusions	U–Pb LA-ICPMS	55.6 ± 0.6	Simmons et al., 2013
Cuajone	17° 2' 6.9"	70° 43' 59.14"		diorite	U–Pb LA-ICPMS	64.2 ± 0.9	Simmons et al., 2013
Quellaveco	17° 6' 16"	70° 37' 25"	(approx.)	late mineral porphyry	U–Pb	54.34 ± 0.63	Sillitoe & Mortensen, 2010
Quellaveco	17° 6' 16"	70° 37' 25"	(approx.)	intermediate porphyry	U–Pb	55.9 ± 0.31	Sillitoe & Mortensen, 2010
Quellaveco	17° 6' 16"	70° 37' 25"	(approx.)	early porphyry	U–Pb	58.41 ± 0.53	Sillitoe & Mortensen, 2010
Quellaveco	17° 6' 16"	70° 37' 25"	(approx.)	premineral granodiorite	U–Pb	59.46 ± 0.24	Sillitoe & Mortensen, 2010
Rosario	20° 57′ 54.34″	68° 42′ 28.01″		Rhyolitic porphyry	U–Pb SHRIMP	303.9 ± 3.0	Munizaga et al., 2008
Rosario	20° 58′ 04.34″	68° 42′ 24.01″		Rhyolitic porphyry	U–Pb SHRIMP	308.5 ± 2.2	Munizaga et al., 2008
Rosario	20° 58′ 04.34″	68° 42′ 24.01″		Rhyolitic porphyry	U–Pb SHRIMP	304.6 ± 3.2	Munizaga et al., 2008
Rosario	20° 58′ 08.70″	68° 42′ 17.56″		Rhyolitic porphyry	U–Pb SHRIMP	298.3 ± 2.1	Munizaga et al., 2008
Ujina	20° 59′ 21.05″	68° 38′ 09.68″		Dacitic porphyry	U–Pb SHRIMP	296.9 ± 4.3	Munizaga et al., 2008
Quebrada Blanca	20° 59′ 59.33″	68° 49′ 01.01″		Granitic porphyry	U–Pb SHRIMP	303.2 ± 2.0	Munizaga et al., 2008
Characolla	20° 50′ 22.34″	68° 45′ 10.00″		Granitic porpyhry	U–Pb SHRIMP	243.2 ± 2.1	Munizaga et al., 2008
Characolla	20° 50′ 49.68″	68° 45′ 05.31″		Granitic porpyhry	U–Pb SHRIMP	248.7 ± 3.3	Munizaga et al., 2008
La Profunda	21° 00′ 04.34″	68° 36′ 54.02″		Dacitic porpyhry	U–Pb SHRIMP	244.8 ± 2.5	Munizaga et al., 2008
Los Colorados	21° 01′ 53.71″	68° 50′ 39.72″		Granitic porphyry	U–Pb SHRIMP	292.7 ± 1.9	Munizaga et al., 2008
El Loa	21° 09′ 54.54″	68° 39′ 42.14″		Rhyolitic porphyry	U–Pb SHRIMP	297.6 ± 2.4	Munizaga et al., 2008
Los Colorados	21° 02′ 09.81″	68° 50′ 39.71″		Rhyolitic porphyry	U–Pb SHRIMP	307.9 ± 2.8	Munizaga et al., 2008
Los Colorados	21° 02′ 09.83″	68° 51′ 00.67″		Dacite	U–Pb SHRIMP	298.8 ± 2.2	Munizaga et al., 2008
El Abra	21° 55' 14"	68° 49' 57"	(approx.)	(Cotari granodiorite)	U–Pb ID-TIMS	37.5 ± 0.5	Dilles et al., 1997
Chuquicamata	22° 18' 20"	68° 54' 10"	(approx.)	(Oeste porphyry)	U–Pb	33.5 ± 0.2	Rivera et al., 2012
Chuquicamata	22° 18' 20"	68° 54' 10"	(approx.)	(Chuqui's Este porphyhy)	U—Pb TIMS and LA-ICPMS	34.6 ± 0.2	Zentilli et al., 2015
Chuquicamata	22° 18' 20"	68° 54' 10"	(approx.)		U—Pb	32.5 ± 5	Zentilli et al., 1994
Chuquicamata	22° 18' 20"	68° 54' 10"	(approx.)	(Los Picos quartz monzodiorite)	U–Pb SHRIMP	43.1 ± 0.6	Campbell et al., 2006
Chuquicamata	22° 18' 20"	68° 54' 10"	(approx.)	(Los Picos quartz monzodiorite)	U–Pb LA-ICPMS	41.8 ± 0.3	Campbell et al., 2006
Chuquicamata	22° 18' 20"	68° 54' 10"	(approx.)	(Los Picos quartz monzodiorite)	U–Pb LA-ICPMS	42.2 ± 0.2	Campbell et al., 2006
Chuquicamata	22° 18' 20"	68° 54' 10"	(approx.)	(Antena granodiorite)	U–Pb LA-ICPMS	38.8 ± 0.6	Campbell et al., 2006
Chuquicamata	22° 18' 20"	68° 54' 10"	(approx.)	(Antena granodiorite)	U–Pb ID-TIMS	39.3 ± 0.4	Dilles et al., 1997
Chuquicamata	22° 18' 20"	68° 54' 10"	(approx.)	(Fiesta hornblende granodiorite)	U–Pb LA-ICPMS	39.4 ± 0.5	Campbell et al., 2006
Chuquicamata	22° 18' 20"	68° 54' 10"	(approx.)	(Fiesta hornblende granodiorite)	U–Pb LA-ICPMS	38.2 ± 0.3	Campbell et al., 2006
Chuquicamata	22° 18' 20"	68° 54' 10"	(approx.)	(Fiesta hornblende granodiorite)	U–Pb ID-TIMS	37.6 ± 0.7	Dilles et al., 1997
Chuquicamata	22° 18' 20"	68° 54' 10"	(approx.)	(San Lorenzo rhyodacitic porphyry)	U–Pb LA-ICPMS	38.2 ± 0.8	Campbell et al., 2006
Chuquicamata	22° 18' 20"	68° 54' 10"	(approx.)	(East porphyry)	U–Pb SHRIMP	35.2 ± 0.4	Ballard et al., 2001
Chuquicamata	22° 18' 20"	68° 54' 10"	(approx.)	(East porphyry)	U–Pb LA-ICPMS	34.6 ± 0.3	Ballard et al., 2001
Chuquicamata	22° 18' 20"	68° 54' 10"	(approx.)	(West porphyry)	U–Pb SHRIMP	34 ± 0.3	Ballard et al., 2001
Chuquicamata	22° 18' 20"	68° 54' 10"	(approx.)	(West porphyry)	U–Pb LA-ICPMS	33.5 ± 0.2	Ballard et al., 2001
Chuquicamata	22° 18' 20"	68° 54' 10"	(approx.)	(Bench porphyry)	U–Pb SHRIMP	34.1 ± 0.3	Ballard et al., 2001
Chuquicamata	22° 18' 20"	68° 54' 10"	(approx.)	(Bench porphyry)	U–Pb LA-ICPMS	33.3 ± 0.3	Ballard et al., 2001
Chuquicamata	22° 18' 20"	68° 54' 10"	(approx.)	(RT major)	U–Pb SHRIMP	35 ± 0.3	Campbell et al., 2006
Chuquicamata	22° 18' 20"	68° 54' 10"	(approx.)	(RT major)	U–Pb LA-ICPMS	34.3 ± 0.3	Campbell et al., 2006
Chuquicamata	22° 18' 20"	68° 54' 10"	(approx.)	(RT minor)	U–Pb SHRIMP	33.9 ± 0.4	Campbell et al., 2006
Chuquicamata	22° 22′45″	68°54′50″	(approx.)	(MM porphyry)	U–Pb LA-ICPMS	38.9 ± 0.4	Boric et al., 2009
Chuquicamata	22° 22′45″	68°54′50″	(approx.)	(Quartz porphyry in Ministro Hales)	U–Pb LA-ICPMS	35.5 ± 0.6	Boric et al., 2009
Chuquicamata	22° 18' 20"	68° 54' 10"	(approx.)	(Opache porphyry)	U–Pb SHRIMP	37.3 ± 1	Campbell et al., 2006
Chuquicamata	22° 18' 20"	68° 54' 10"	(approx.)	(Opache porphyry)	U–Pb LA-ICPMS	37.7 ± 0.6	Campbell et al., 2006
Mina Ministro Hales	22° 22' 45"	68° 54' 50"	(approx.)	Granodiorite (MM porphyry)	U—Pb TIMS and LA-ICPMS	35.03 ± 0.34	Zentilli et al., 2015
Mina Ministro Hales	22° 22' 45"	68° 54' 50"	(approx.)	Granodiorite (MM porphyry)	U—Pb TIMS and LA-ICPMS	38.9 ± 0.4	Zentilli et al., 2015
Mina Ministro Hales	22° 22' 45"	68° 54' 50"	(approx.)	quartz porphyry (Quartz porphyry)	U—Pb TIMS	35.3 ± 3.5	Zentilli et al., 2015
Mina Ministro Hales	22° 22' 45"	68° 54' 50"	(approx.)	Argillized feldspar porphyry (Dacite porphyry)	U—Pb TIMS and LA-ICPMS	33.7 ± 0.8	Zentilli et al., 2015
Toki	22° 23' 56.94"	68° 57' 26.11"	(approx.)	(Toki tonalite)	U–Pb SHRIMP	38.8 ± 0.5	Rivera & Pardo, 2004
Toki	22° 23' 56.94"	68° 57' 26.11"		(Quetena)	U–Pb ID-TIMS	38.6 ± 0.7	Barra et al., 2013
Toki	22° 25' 00"	68° 56'00"	(approx.)		U–Pb isoprobe ICP	38.0 ± 2.2	Barra et al., 2013
Toki	22° 25' 00"	68° 56' 00"	(approx.)		U–Pb isoprobe ICP	38.6 ± 1.9	Barra et al., 2013
Toki	22° 25' 00"	68° 56' 00"	(approx.)		U–Pb isoprobe ICP	39.9 ± 1.5	Barra et al., 2013
Toki	22° 25' 00"	68° 56' 00"	(approx.)		U–Pb isoprobe ICP	39.5 ± 1.8	Barra et al., 2013
Toki	22° 25' 00"	68° 56' 00"	(approx.)		U–Pb isoprobe ICP	39.0 ± 1.3	Barra et al., 2013
Toki	22° 25' 00"	68° 56' 00"	(approx.)		U–Pb isoprobe ICP	39.4 ± 3.0	Barra et al., 2013
Toki	22° 25' 00"	68° 56' 00"	(approx.)		U–Pb isoprobe ICP	39.6 ± 1.6	Barra et al., 2013
Toki	22° 25' 00"	68° 56' 00"	(approx.)		U–Pb isoprobe ICP	38.2 ± 0.8	Barra et al., 2013
Toki	22° 25' 00"	68° 56' 00"	(approx.)		U–Pb isoprobe ICP	40.2 ± 2.8	Barra et al., 2013
Toki	22° 25' 00"	68° 56' 00"	(approx.)		U–Pb isoprobe ICP	39.9 ± 2.2	Barra et al., 2013
Toki	22° 25' 00"	68° 56' 00"	(approx.)		U–Pb isoprobe ICP	39.2 ± 1.1	Barra et al., 2013
Toki	22° 25' 00"	68° 56' 00"	(approx.)		U–Pb isoprobe ICP	38.6 ± 1.5	Barra et al., 2013
Toki	22° 25' 00"	68° 56' 00"	(approx.)		U–Pb isoprobe ICP	40.0 ± 2.0	Barra et al., 2013

Toki	22° 25' 00"	68° 56' 00"	(approx.)		U–Pb isoprobe ICP	39.6 ± 1.4	Barra et al., 2013
Toki	22° 25' 00"	68° 56' 00"	(approx.)		U–Pb isoprobe ICP	39.9 ± 1.7	Barra et al., 2013
Toki	22° 25' 00"	68° 56' 00"	(approx.)		U–Pb isoprobe ICP	39.9 ± 2.7	Barra et al., 2013
Toki	22° 25' 00"	68° 56' 00"	(approx.)		U–Pb isoprobe ICP	37.3 ± 1.0	Barra et al., 2013
Toki	22° 25' 00"	68° 56' 00"	(approx.)		U–Pb isoprobe ICP	37.7 ± 1.4	Barra et al., 2013
Toki	22° 25' 00"	68° 56' 00"	(approx.)		U–Pb isoprobe ICP	37.5 ± 0.7	Barra et al., 2013
Antucoya	22° 26' 18"	69° 55' 37"	(approx)	mineralised granodiorite porphyry	U–Pb SHRIMP	142.7 ± 1.6	Maksaev et al., 2006
Antucoya	22° 26' 18"	69° 55' 37"	(approx)	mineralised tonolite porphyry	U–Pb SHRIMP	140.6 ± 1.5	Maksaev et al., 2006
Antucoya	22° 26' 18"	69° 55' 37"	(approx)	post mineralisation dacite	U–Pb SHRIMP	141.9 ± 1.4	Maksaev et al., 2006
Zaldivar	24° 15' 39.65"	69° 3' 43.44"		(Llamo porphyry)	U–Pb	38.7 ± 1.3	Richards et al., 1999
Zaldivar	24° 12' 11.64"	69° 3' 43.34"		Premineralization (Zaldivar porphyry)	U–Pb	290 ± 4	Richards et al., 1999
Zaldivar	24° 12' 11.64"	69° 3' 36.25"		Premineralization (Antigua porphyry)	U–Pb	288 ± 18	Richards et al., 1999
Escondida	24° 14' 59.9"	69° 4' 56.05"		dacitic quartz feldspar porphyry (Escondida porphyry)	U–Pb	37.9 ± 1.1	Richards et al., 1999
Escondida	24° 15' 39.65"	69° 3' 43.44"		altered rhyolite quartz feldspar porphyry	U–Pb	34.7 ± 1.7	Richards et al., 1999
	26° 07' 21.74"	70° 31' 53.93"		Muscovite leucogranite (Pan de Azúcar pluton)	U–Pb SHRIMP	269.5 ± 4	Maksaev et al., 2014
	26° 16' 27.71"	70° 39' 22.80"		Muscovite-biotite monzogranite (Pan de Azúcar pluton)	U–Pb SHRIMP	276.6 ± 3.6	Maksaev et al., 2014
	26° 18' 22.54"	70° 27' 05.87"		Biotite-muscovite leucogranite (Cerros del Vetado Pluton)	U–Pb SHRIMP	246.5 ± 4	Maksaev et al., 2014
	26° 20' 58.88"	69° 15' 42.50"		Biotite monzogranite (Pedernales batholith)	U–Pb SHRIMP	280.6 ± 4.2	Maksaev et al., 2014
	26° 22' 07.72"	69° 16' 37.94"		Hornblende-biotite quartz monzodiorite (Pedernales batholith)	U–Pb SHRIMP	287 ± 4.2	Maksaev et al., 2014
	26° 22' 41.05"	70° 27' 36.16"		Biotite monzogranite (Cerros del Vetado pluton)	U–Pb SHRIMP	237 ± 4	Maksaev et al., 2014
	26° 23' 34.30"	69° 29' 24.72"		Foliated biotite-hornblende tonalite (Sierra Castillo batholith)	U–Pb SHRIMP	285.3 ± 6.4	Maksaev et al., 2014
El Salvador Mine	26° 15' 13.51"	69° 33' 46.34"		Rhyolite (Cerro Indio Muerto rhyolite)	U–Pb SHRIMP	59.1 ± 1.9	Cornejo et al., 1997
El Salvador Mine	26° 13' 10.44"	69° 31' 59.80"		(Old Camp porphyry)	U–Pb SHRIMP	42.3 ± 1.3	Cornejo et al., 1997
El Salvador Mine	26° 14' 27.44"	69° 33' 29.54"		(X porphyry)	U–Pb SHRIMP	41.8 ± 2.3	Cornejo et al., 1997
Cerro Pelado	26° 12' 55.39"	69° 32' 28.92"		Altered quartz-sanidine rhyolite porphyry	U–Pb MC-ICP-MS	43 ± 2	Cornejo et al., 1997
El Salvador Mine	26° 13' 10.44"	69° 31' 59.80"		(Old Camp porphyry)	U–Pb MC-ICP-MS	43 ± 1	Cornejo et al., 1997
El Salvador Mine	26° 14' 27.44"	69° 33' 29.54"		(X porphyry)	U–Pb MC-ICP-MS	41 ± 2	Cornejo et al., 1997
El Salvador Mine	26° 14' 25.49"	69° 33' 29.89"		(L porphyry)	U–Pb MC-ICP-MS	41 ± 2	Cornejo et al., 1997
El Salvador Mine	26° 24' 00"	69° 56' 00"	(approx)	Latite	U–Pb	41.6 ± 0.5	Lee, 2008
	26° 28' 19.36"	69° 17' 50.67"		Andesitic dike (Dike in La Tabla Fm.)	U–Pb SHRIMP	264.6 ± 7	Maksaev et al., 2014
	26° 28' 53.10"	69° 19' 25.75"		Biotite-hornblende monzogranite (Pedernales batholith)	U–Pb SHRIMP	264.9 ± 7	Maksaev et al., 2014
Manto Verde	26° 50' 00"	70° 30' 00"	(approx.)	Quartz monzonite to granodiorite	U–Pb	128.9 ± 0.6	Gelcich et al., 2003
Manto Verde	26° 50' 00"	70° 30' 00"	(approx.)	Quartz monzonite to granodiorite	U–Pb	126.4 ± 0.5	Gelcich et al., 2003
	26° 50' 46.18"	69° 08' 50.32"		Biotite monzogranite (Caballo Muerto Pluton)	U–Pb SHRIMP	263.5 ± 3.4	Maksaev et al., 2014
	27° 08' 21.17"	69° 22' 05.53"		Biotite monzogranite (El Hielo batholith)	U–Pb SHRIMP	267.9 ± 3.8	Maksaev et al., 2014
Bajo de la Alumbrera	27° 19' 00"	66° 34' 00"	(approx.)	porphyry intrusion (P2)	U–Pb LA-ICPMS	7.92 ± 0.14	Harris et al., 2004
Bajo de la Alumbrera	27° 19' 00"	66° 34' 00"	(approx.)	late pulse intrusion (P3)	U–Pb LA-ICPMS	6.96 ± 0.09	Harris et al., 2004
Bajo de la Alumbrera	27° 19' 00"	66° 34' 00"	(approx.)	porphyry intrusion (P2)	U–Pb LA-ICPMS	7.216 ± 0.018	von Quadt et al., 2011
Bajo de la Alumbrera	27° 19' 00"	66° 34' 00"	(approx.)	porphyry intrusion (EP3)	U–Pb LA-ICPMS	7.126 ± 0.016	von Quadt et al., 2011
Bajo de la Alumbrera	27° 19' 00"	66° 34' 00"	(approx.)	porphyry intrusion (P2)	U–Pb	8.02 ± 0.14	Harris et al., 2004
Bajo de la Alumbrera	27° 19' 00"	66° 34' 00"	(approx.)	porphyry intrusion (P2)	U–Pb	7.98 ± 0.14	Harris et al., 2004
Bajo de la Alumbrera	27° 19' 00"	66° 34' 00"	(approx.)	porphyry intrusion (P3)	U–Pb	7.1 ± 0.07	Harris et al., 2004
	28° 39' 59.13"	70° 10' 55.94"		Biotite-bearing mylonitized tonalite (Quebrada Pintado tonalite)	U–Pb SHRIMP	258.9 ± 5	Maksaev et al., 2014
Tricolor	28° 57' 17.79"	70° 52' 44.28"		tonalitic porphyry	U–Pb LA-ICPMS	108.5 ± 3.4	Maksaev et al., 2010
West of Tricolor	28° 57' 23.83"	70° 53' 2.45"		granodiorite	U–Pb LA-ICPMS	99.6 ± 1.8	Maksaev et al., 2010
	28° 58' 18.69"	70° 09' 44.14"		Biotite monzogranite (Chollay batholith)	U–Pb SHRIMP	244 ± 2.8	Maksaev et al., 2014
Dos Amigos mine pit	28° 59' 10.62"	70° 52' 47.06"		granodioritic porphyry	U–Pb LA-ICPMS	106.1 ± 3.5	Maksaev et al., 2010
Dos Amigos mine pit	28° 59' 4.03"	70° 52' 46.72"		tonalitic porphyry	U–Pb LA-ICPMS	104 ± 3.5	Maksaev et al., 2010
Pajonales	29° 07' 10.2"	70° 57' 10.82"		Cachiyuyo batholith	U–Pb LA-ICPMS	99.1 ± 1.9	Maksaev et al., 2010
	29° 08' 19.52"	70° 22' 41.82"		Biotite monzogranite (Guachicay pluton)	U–Pb SHRIMP	315.7 ± 4.6	Maksaev et al., 2014
	29° 09' 16.19"	70° 21' 31.11"		Biotite-hornblende tonalite (Guanta pluton)	U–Pb SHRIMP	307.1 ± 4.8	Maksaev et al., 2014
	29° 10' 10.89"	70° 20' 59.70"		Muscovite-biotite monzogranite (Burro Muerto pluton)	U–Pb SHRIMP	286.3 ± 6.2	Maksaev et al., 2014
	29° 20' 25.47"	70° 19' 14.69"		Biotite syenogranite (Guanta pluton)	U–Pb SHRIMP	311.9 ± 6	Maksaev et al., 2014
	29° 24' 29.70"	70° 14' 24.51"		Syenogranite (La Coneja pluton; Colorado unit)	U–Pb SHRIMP	229.6 ± 5.2	Maksaev et al., 2014
El Teniente	34° 5' 19''	70° 27' 45''	(approx.)	(A porphyry)	U–Pb SHRIMP	6.46 ± 0.11	Maksaev et al., 2004
El Teniente	34° 5' 19''	70° 27' 45''	(approx.)	(A porphyry)	U–Pb SHRIMP	5.67 ± 0.19	Maksaev et al., 2004
El Teniente	34° 5' 19''	70° 27' 45''	(approx.)	(Sewell stock)	U–Pb SHRIMP	6.15 ± 0.08	Maksaev et al., 2004
El Teniente	34° 5' 19''	70° 27' 45''	(approx.)	(Sewell stock)	U–Pb SHRIMP	5.59 ± 0.17	Maksaev et al., 2004
El Teniente	34° 5' 19''	70° 27' 45''	(approx.)	Central quartz diorite-tonalite	U–Pb SHRIMP	6.28 ± 0.16	Maksaev et al., 2004
El Teniente	34° 5' 19''	70° 27' 45''	(approx.)	Central quartz diorite-tonalite	U–Pb SHRIMP	5.5 ± 0.24	Maksaev et al., 2004
El Teniente	34° 5' 19''	70° 27' 45''	(approx.)	Northern quartz diorite-tonalite	U–Pb SHRIMP	6.11 ± 0.13	Maksaev et al., 2004
El Teniente	34° 5' 19''	70° 27' 45''	(approx.)	Northern quartz diorite-tonalite	U–Pb SHRIMP	5.49 ± 0.19	Maksaev et al., 2004
El Teniente	34° 5' 19''	70° 27' 45''	(approx.)	Dacite porphyry (Teniente dacite porphyry)	U–Pb SHRIMP	5.28 ± 0.1	Maksaev et al., 2004
El Teniente	34° 5' 19''	70° 27' 45''	(approx.)	dacite dike	U–Pb SHRIMP	4.82 ± 0.09	Maksaev et al., 2004

b) Summary of published K–Ar or Ar–Ar age data in N. Chile

Region	Latitude (S)	Longitude (W)		Rock type (or pluton name)	Material	Stage	Method	Age (Ma) (± 2σ)	Reference
Santa Rosa	15° 45' 41"	70° 45' 55"	(approx.)		Sericite	Hydrothermal event	Ar–Ar	62.2 ± 2.9	Quang et al., 2003
Santa Lucia District	15° 40' 00"	70° 36" 50"		Monzogabbro	Orthoclase		Ar–Ar total fusion	30.28 ± 0.61	Clark et al., 1990
Santa Lucia District	15° 38' 15"	70° 38" 40"		Microdiorite	Hornblende		Ar–Ar total fusion	28.21 ± 3.4	Clark et al., 1990
Santa Lucia District	15° 41' 20"	70° 38" 30"		Microdiorite	Hornblende		Ar–Ar total fusion	26.45 ± 2.7	Clark et al., 1990
Santa Lucia District	15° 39' 10"	70° 34" 05"		intrusive andesite	Hornblende		Ar–Ar total fusion	26.8 ± 1.3	Clark et al., 1990
Santa Lucia District	15° 40' 00"	70° 40" 51"		rhyolitic tuff	Whole rock		Ar–Ar total fusion	26.83 ± 0.28	Clark et al., 1990
Santa Lucia District	15° 40' 00"	70° 40" 51"			Sericite	phyllic alteration	Ar–Ar total fusion	23.5 ± 0.52	Clark et al., 1990
Santa Lucia District	15° 34' 22"	70° 35" 10"		rhyolitic tuff	Biotite		Ar–Ar total fusion	21.59 ± 0.88	Clark et al., 1990
Santa Lucia District	15° 44' 20"	70° 34" 30"		intrusive rhyolite	Biotite		Ar–Ar total fusion	6.97 ± 0.5	Clark et al., 1990
Cerro Verde	16° 31' 52"	71° 35' 57"	(approx.)		Sericite	Hydrothermal event	Ar–Ar	61.8 ± 0.7	Quang et al., 2003

Cerro Verde	16° 31' 52"	71° 35' 57"	(approx.)		Sericite	Hydrothermal event	Ar–Ar	62 ± 1.1	Quang et al., 2003
Cerro Verde- Santa Rosa	16° 31' 52"	71° 35' 57"	(approx.)			premineralization	K–Ar	60.4 ± 3.0	References within Sillitoe, 1988
Cerro Verde- Santa Rosa	16° 31' 52"	71° 35' 57"	(approx.)			premineralization	K–Ar	60.3 ± 2.0	References within Sillitoe, 1988
Cerro Verde- Santa Rosa	16° 31' 52"	71° 35' 57"	(approx.)			premineralization	K–Ar	58.2 ± 2.0	References within Sillitoe, 1988
Cerro Verde- Santa Rosa	16° 31' 52"	71° 35' 57"	(approx.)			potassic alteration	K–Ar	59.7 ± 2.4	References within Sillitoe, 1988
Cerro Verde- Santa Rosa	16° 31' 52"	71° 35' 57"	(approx.)			potassic alteration	K–Ar	58.3 ± 1.9	References within Sillitoe, 1988
Cacachara-Pavico district	16° 37' 59"	70° 03' 05"		Andesite	Biotite		K–Ar	8.316 ± 0.586	Clark et al., 1990
Cacachara-Pavico district	16° 38' 17"	70° 04' 14"		Dacite	Biotite		K–Ar	7.035 ± 0.430	Clark et al., 1990
Cacachara-Pavico district	16° 38' 40"	70° 03' 26"		Dacitic ash-flow tuff	Biotite		K–Ar	6.617 ± 0.146	Clark et al., 1990
Cacachara-Pavico district	16° 39' 41"	70° 05' 03"		Dacitic crystal-vitric tuff	Biotite		K–Ar	6.476 ± 0.181	Clark et al., 1990
Cuajone	17° 1' 53"	70° 42' 34"	(approx.)			premineralization	K–Ar	59.3 ± 2.0	References within Sillitoe, 1988
Cuajone	17° 1' 53"	70° 42' 34"	(approx.)			potassic alteration	K–Ar	52.2 ± 1.6	References within Sillitoe, 1988
Cuajone	17° 1' 53"	70° 42' 34"	(approx.)		Sericite	Hydrothermal event	Ar–Ar	52.8 ± 1	Clark et al., 1990
Quellaveco	17° 6' 16"	70° 37' 25"	(approx.)			premineralization	K–Ar	55.1 ± 2.3	References within Sillitoe, 1988
Quellaveco	17° 6' 16"	70° 37' 25"	(approx.)			magmatic, potassic to sericitic alteration	K–Ar	53.6 ± 11.6	References within Sillitoe, 1988
Quellaveco	17° 6' 16"	70° 37' 25"	(approx.)		Sericite	Sericitic alteration	K–Ar	55.4 ± 2.1	References within Sillitoe, 1988
Toquepala	17° 14' 42"	70° 37' 3"	(approx.)			premineralization	K–Ar	60.1 ± 1.8	References within Sillitoe, 1988
Toquepala	17° 14' 42"	70° 37' 3"	(approx.)			premineralization	K–Ar	58.6 ± 1.9	References within Sillitoe, 1988
Toquepala	17° 14' 42"	70° 37' 3"	(approx.)		Biotite	Hydrothermal event	Ar–Ar	55.9 (± ?)	Zweng & Clark, 1995
Toquepala	17° 14' 42"	70° 37' 3"	(approx.)		Sericite	Hydrothermal event	Ar–Ar	55 (± ?)	Zweng & Clark, 1995
Ilo-Ite and Cocachacra districts	17° 34' 18"	71° 21' 25"		Diorite	Hornblende		K–Ar	158.4 ± 4.9	Clark et al., 1990
Ilo-Ite and Cocachacra districts	17° 34' 18"	71° 21' 25"		Diorite	Biotite		K–Ar	157.6 ± 4.7	Clark et al., 1990
Ilo-Ite and Cocachacra districts	17° 34' 34"	71° 06' 59"		Granodiorite	Hornblende		K–Ar	151.3 ± 4.9	Clark et al., 1990
Ilo-Ite and Cocachacra districts	17° 40' 43"	71° 17' 19"		Granodiorite-tonalite	Hornblende		K–Ar	105.6 ± 3.2	Clark et al., 1990
Ilo-Ite and Cocachacra districts	17° 40' 43"	71° 17' 19"		Granodiorite-tonalite	Biotite		K–Ar	103.6 ± 3.0	Clark et al., 1990
Ilo-Ite and Cocachacra districts	17° 37' 18"	71° 10' 57"		Granodiorite-tonalite	Biotite		K–Ar	96.1 ± 2.9	Clark et al., 1990
Ilo-Ite and Cocachacra districts	17° 01' 46"	71° 41' 58"		Granodiorite	Biotite (+ chlorite)		K–Ar	156.4 ± 4.6	Clark et al., 1990
Toquepala-Cuajone district	17° 13' 17"	70° 39' 06"		Quartz monzodiorite	Biotite		K–Ar	58.7 ± 1.9	Clark et al., 1990
Toquepala-Cuajone district	17° 14' 00"	70° 36' 30"		Dacite	Biotite		K–Ar	57.1 ± 0.57	Clark et al., 1990
Toquepala-Cuajone district	17° 01' 38"	70° 42' 26"		Quartz vein envelope	Muscovite		K–Ar	52.3 ± 1.6	Clark et al., 1990
Lluta (Cercana) district	17° 48' 48"	70° 00' 17"		Monzodiorite	Biotite		K–Ar	60.33 ± 1.30	Clark et al., 1990
Lluta (Cercana) district	17° 50' 28"	70° 06' 13"		Monzodiorite	Biotite		K–Ar	60.9 ± 1.83	Clark et al., 1990
Ataspaca-Caplina district	17° 43' 36"	69° 55' 16"		Quartz monzodiorite	Biotite		K–Ar	42.58 ± 0.96	Clark et al., 1990
Ataspaca-Caplina district	17° 42' 24"	69° 55' 01"		Quartz monzodiorite	Biotite		K–Ar	39.15 ± 0.85	Clark et al., 1990
Ataspaca-Caplina district	17° 42' 24"	69° 55' 01"			Biotite	Potassic alteration zone	K–Ar	40.65 ± 0.88	Clark et al., 1990
Mocha	19° 48' 00"	69° 16' 01.2"	(Approx.)		Sericite	Sericitic alteration	K–Ar	58.0 ± 2.6	References within Sillitoe, 1988
Mocha	19° 48' 00"	69° 16' 01.2"	(Approx.)		Sericite	Sericitic alteration	K–Ar	57.8 ± 0.9	References within Sillitoe, 1988
Queen Elizabeth	19° 52' 00"	68° 58' 00"	(Approx.)			magmatic	K–Ar	37.1 ± 0.6	References within Sillitoe, 1988
La Planada	19° 58' 00"	69° 05' 00"	(Approx.)			potassic alteration	K–Ar	31.9 ± 0.7	References within Sillitoe, 1988
Cerro Colorado	20° 2' 41"	69° 15' 35"	(approx)	tonolite to monzonitic porphyry	Biotite and sericite (hydrothermal)		Ar–Ar	51.8 ± 0.5	Bouzari & Clark, 2002
Cerro Colorado	20° 2' 41"	69° 15' 35"	(approx)	Andesite dyke	Biotite		Ar-Ar	51.8 ± 0.4	Cotton, 2003
Cerro Colorado	20° 2' 41"	69° 15' 35"	(approx)	Brecciated quartz porphyry (Central Breccia)	Muscovite (hydrothermal)		Ar-Ar	51.5 ± 0.2	Cotton, 2003
Cerro Colorado	20° 2' 41"	69° 15' 35"	(approx)		Biotite (hydrothermal)		Ar-Ar	50.18 ± 1.95	Bouzari & Clark, 2006
Cerro Colorado	20° 2' 41"	69° 15' 35"	(approx)		Muscovite (hydrothermal)		Ar-Ar	51.8 ± 0.6	Bouzari & Clark, 2006
Cerro Colorado	20° 2' 41"	69° 15' 35"	(approx)		Muscovite and Chlorite (hydrothermal)		Ar-Ar	51.8 ± 0.5	Bouzari & Clark, 2006
Cerro Colorado	20° 2' 41"	69° 15' 35"	(approx)	evolved granitoid	Biotite		Ar–Ar	67.98 ± 0.18	Agemar et al., 1999
Cerro Colorado	20° 2' 41"	69° 15' 35"	(approx)	mafic alkali gabbro	Biotite		Ar–Ar	68.08 ± 0.18	Agemar et al., 1999
Cerro Colorado	20° 2' 41"	69° 15' 35"	(approx)		Biotite		K–Ar	62.2 ± 2.4	Huete et al., 1977
Cerro Colorado	20° 2' 41"	69° 15' 35"	(approx)		Biotite		K–Ar	65.1 ± 1.8	Huete et al., 1977
Rosario	20° 57' 14.02"	68° 42' 23.84"	(approx.)	Collahuasi Porphyry	Biotite (hydrothermal)	Potassic Alteration	Ar–Ar	32.9 ± 0.5	Clark et. al., 1998
Rosario	20° 57' 14.02"	68° 42' 23.84"	(approx.)	Collahuasi Porphyry	Muscovite	Phyllic Alteration	Ar–Ar	32.9 ± 0.6	Clark et. al., 1998
Rosario	20° 57' 14.02"	68° 42' 23.84"	(approx.)	Andesite	Biotite	Biotite Alteration	K–Ar	34.2 ± 1.5	Unpublished report by Munchmeyer et. al., cited in Clark et al., 1998
Rosario	20° 57' 39.69"	68° 41' 57.71"		Collahuasi Porphyry	Illite	Biotite-Orthoclase alteration	Ar–Ar	34.1 ± 0.6	Masterman et. al., 2004
Rosario	20° 57' 49.99"	68° 42' 13.31"		Collahuasi Porphyry	Hypogene alunite	Argillic Alteration	Ar–Ar	32.6 ± 0.3	Masterman et. al., 2004
Rosario	20° 57' 14.02"	68° 42' 23.84"	(approx.)	Collahuasi Porphyry	Whole rock	Magmatic emplacement	K–Ar	59.4 ± 1.2	Vergara & Drake, 1978
Rosario	20° 57' 46.44"	68° 42' 10.09"		Rosario Porphyry	Biotite		Ar–Ar	34.4 ± 0.3	Masterman et. al., 2004
Ujina	20° 58' 51.29"	68° 38' 03.65"		Inca Porphyry	Biotite	Magmatic emplacement	Ar–Ar	34.7 ± 0.3	Masterman et. al., 2004
La Grande	20° 58' 14.53"	68° 43' 01.85"		Sandstone	Hypogene alunite	Argillic Alteration	Ar–Ar	32.7 ± 1.6	Masterman et. al., 2004
Quebrada Blanca	20° 59' 08.34"	68° 48' 27.29"	(approx.)	Granodiorite porphyry	Biotite (hydrothermal)	Phyllic Alteration	Ar–Ar	34.9 ± 0.4	Maksaev, 1990
Quebrada Blanca	20° 59' 08.34"	68° 48' 27.29"	(Approx.)			magmatic to potassic alteration	K–Ar	38 ± 2	References within Sillitoe, 1988
Ujina	20° 59' 01.32"	68° 38' 14.15"		Ujina Porphyry	Biotite		Ar–Ar	35.2 ± 0.3	Masterman et. al., 2004
La Profunda	21° 00' 02.48"	68° 37' 13.39"		Biotite Granite	Biotite	Pluton cooling age	Ar–Ar	80.4 ± 3.5	Masterman et. al., 2004
Puntillas	21° 55' 00"	69° 49' 59"	(Approx.)			potassic alteration	K–Ar	132 ± 8	References within Sillitoe, 1988
El Abra Mine	21° 55' 14"	68° 49' 57"		dacitic porphyry	Biotite		Ar–Ar	36.8 (± ?)	Maksaev, 1990
El Abra	21° 55' 14"	68° 49' 57"	(Approx.)			premineralization	K–Ar	35.3 ± 0.5	References within Sillitoe, 1988
El Abra	21° 55' 14"	68° 49' 57"	(Approx.)			potassic alteration	K–Ar	36.3 to 34.3	References within Sillitoe, 1988
El Abra	21° 55' 14"	68° 49' 57"	(Approx.)			potassic alteration	K–Ar	34.0 ± 0.5	References within Sillitoe, 1988
El Abra	21° 55' 14"	68° 49' 57"	(Approx.)			post mineralization	K–Ar	36.8 ± 0.7	References within Sillitoe, 1988
Chuquicamata	22° 16' 36"	68° 53' 47"			Biotite		Ar–Ar Plateau age	31.9 ± 0.5	Barra et al., 2013
Chuquicamata	22° 16' 38"	68° 53' 45"			K-feldspar		Ar–Ar Plateau age	30.6 ± 0.3	Barra et al., 2013
Chuquicamata	22° 16' 38"	68° 53' 45"			Biotite		Ar–Ar Plateau age	31.8 ± 0.4	Barra et al., 2013
Chuquicamata	22° 16' 38"	68° 53' 45"			Muscovite		Ar–Ar Plateau age	30.6 ± 0.4	Barra et al., 2013
Chuquicamata	22° 16' 39"	68° 53' 49"			K-feldspar		Ar–Ar Plateau age	30.6 ± 0.4	Barra et al., 2013
Chuquicamata	22° 16' 39"	68° 53' 49"			K-feldspar		Ar–Ar Plateau age	30.7 ± 0.6	Barra et al., 2013
Chuquicamata	22° 16' 54"	68° 53' 59"			Muscovite		Ar–Ar Plateau age	31.1 ± 0.7	Barra et al., 2013
Chuquicamata	22° 16' 54"	68° 53' 59"			Muscovite		Ar–Ar Plateau age	30.8 ± 0.4	Barra et al., 2013
Chuquicamata	22° 17' 6"	68° 54' 6"			Muscovite		Ar–Ar Plateau age	31.7 ± 0.7	Barra et al., 2013
Chuquicamata	22° 17' 47.57"	68° 54' 08.09"	(Approx.)			premineralization	K–Ar	38.0 ± 0.3	References within Sillitoe, 1988
Chuquicamata	22° 17' 47.57"	68° 54' 08.09"	(Approx.)			premineralization	K–Ar	37.8 ± 0.6	References within Sillitoe, 1988

Chuquicamata	22° 17' 47.57"	68° 54' 08.09"	(Approx.)			premineralization	K–Ar	36.2 ± 1.4	References within Sillitoe, 1988
Chuquicamata	22° 17' 47.57"	68° 54' 08.09"	(Approx.)			premineralization	K–Ar	35.9 ± 0.1	References within Sillitoe, 1988
Chuquicamata	22° 17' 47.57"	68° 54' 08.09"	(Approx.)			magmatic	K–Ar	33.8 ± 1.3	References within Sillitoe, 1988
Chuquicamata	22° 17' 47.57"	68° 54' 08.09"	(Approx.)			potassic alteration	K–Ar	32.6 ± 0.9	References within Sillitoe, 1988
Chuquicamata	22° 17' 47.57"	68° 54' 08.09"	(Approx.)			potassic alteration	K–Ar	31.2 ± 1.3	References within Sillitoe, 1988
Chuquicamata	22° 17' 47.57"	68° 54' 08.09"	(Approx.)			potassic alteration	K–Ar	34.4 ± 0.9	References within Sillitoe, 1988
Chuquicamata	22° 17' 47.57"	68° 54' 08.09"	(Approx.)		Sericite	Sericitic alteration	K–Ar	29.9 ± 0.5	References within Sillitoe, 1988
Chuquicamata	22° 17' 47.57"	68° 54' 08.09"	(Approx.)		Sericite	Sericitic alteration	K–Ar	28.0 ± 1.1	References within Sillitoe, 1988
Chuquicamata	22° 17' 47.57"	68° 54' 08.09"	(Approx.)		Sericite	Sericitic alteration	K–Ar	31.0 ± 1.2	References within Sillitoe, 1988
Chuquicamata	22° 17' 47.57"	68° 54' 08.09"	(approx.)		Chalcopyrite	Potassic alteration	Ar–Ar	33.4 ± 0.3	Reynolds et al., 1998
Chuquicamata	22° 17' 47.57"	68° 54' 08.09"	(approx.)		Pyrite	Qtz sericitic alteration	Ar–Ar	31.1 ± 0.3	Reynolds et al., 1998
Chuquicamata	22° 17' 47.57"	68° 54' 08.09"				sericite alteration	Ar–Ar	31 (± ?)	Zentilli et al., 1995
Chuquicamata	22° 17' 47.57"	68° 54' 08.09"			K-feldspar and biotite	K alteration	Ar–Ar	34 (± ?)	Zentilli et al., 1995
Chuquicamata	22° 17' 47.57"	68° 54' 08.09"			Hypogene alunite		Ar–Ar	31.7 (± ?)	Zentilli et al., 2015
Chuquicamata	22° 17' 47.57"	68° 54' 08.09"			K-feldspar		Ar–Ar	31.4 ± 0.2	Maksaev, 1990
Chuquicamata	22° 17' 47.57"	68° 54' 08.09"			Biotite		Ar–Ar	31.7 ± 0.4	Maksaev, 1990
Chuquicamata	22° 17' 47.57"	68° 54' 08.09"			Sericite	main stage mineralization	Ar–Ar	31.1 ± 0.2	Ossandón et al., 2001
Chuquicamata	22° 18' 20"	68° 54' 10"	(approx.)	(Antena granodiorite)	Biotite		K–Ar	39.6 to 39	Dilles et al., 1997
Chuquicamata	22° 18' 20"	68° 54' 10"	(approx.)	(Fiesta hornblende granodiorite)	Biotite		K–Ar	37.9 to 37.3	Dilles et al., 1997
Chuquicamata	22° 18' 20"	68° 54' 10"	(approx.)	Granodiorite porphyry	Biotite and sericite		K–Ar	38.5 to 37.1	Dilles et al., 1997
El Abra	21° 55' 14"	68° 49' 57"	(approx.)	(El Abra granodiorite)	Biotite		K–Ar	40 to 38	Dilles et al., 1997
El Abra	21° 55' 14"	68° 49' 57"	(approx.)	(Cotari granodiorite)	Biotite		K–Ar	37.3 to 36.5	Dilles et al., 1997
Chuquicamata	22° 18' 20"	68° 54' 10"	(approx.)	(East porphyry)	K-feldspar	potassic alteration	Ar–Ar	33.7 ± 0.2	Reynolds et al., 1998
Chuquicamata	22° 18' 20"	68° 54' 10"	(approx.)	(East porphyry)	K-feldspar	potassic alteration	Ar–Ar	33.4 ± 0.4	Reynolds et al., 1998
Chuquicamata	22° 18' 20"	68° 54' 10"	(approx.)	(East porphyry)	K-feldspar	potassic alteration	Ar–Ar	32.1 ± 0.2	Reynolds et al., 1998
Chuquicamata	22° 18' 20"	68° 54' 10"	(approx.)	(East porphyry)	K-feldspar	potassic alteration	Ar–Ar	33.6 ± 0.2	Reynolds et al., 1998
Chuquicamata	22° 18' 20"	68° 54' 10"	(approx.)	(East porphyry)	Biotite	potassic alteration	Ar–Ar	31.9 ± 0.2	Reynolds et al., 1998
Chuquicamata	22° 18' 20"	68° 54' 10"	(approx.)	(East porphyry)	Biotite	potassic alteration	Ar–Ar	32.8 ± 0.2	Reynolds et al., 1998
Chuquicamata	22° 18' 20"	68° 54' 10"	(approx.)	(East porphyry)	Biotite	potassic alteration	Ar–Ar	34 ± 0.4	Reynolds et al., 1998
Chuquicamata	22° 18' 20"	68° 54' 10"	(approx.)	(East porphyry)	Biotite	potassic alteration	Ar–Ar	35.2 ± 0.2	Reynolds et al., 1998
Chuquicamata	22° 18' 20"	68° 54' 10"	(approx.)	(East porphyry)	Biotite	potassic alteration	Ar–Ar	33.9 ± 0.3	Reynolds et al., 1998
Chuquicamata	22° 18' 20"	68° 54' 10"	(approx.)	(East porphyry)	K-feldspar	sericite alteration	Ar–Ar	31.6 ± 0.3	Reynolds et al., 1998
Chuquicamata	22° 18' 20"	68° 54' 10"	(approx.)	(East porphyry)	K-feldspar	sericite alteration	Ar–Ar	30.9 ± 0.2	Reynolds et al., 1998
Chuquicamata	22° 18' 20"	68° 54' 10"	(approx.)	(East porphyry)	Sericite	sericite alteration	Ar–Ar	31.1 ± 0.2	Reynolds et al., 1998
Chuquicamata	22° 18' 20"	68° 54' 10"	(approx.)	(East porphyry)	Biotite	sericite alteration	Ar–Ar	31.2 ± 0.2	Reynolds et al., 1998
Chuquicamata	22° 18' 20"	68° 54' 10"	(approx.)	(Bench porphyry)	K-feldspar	potassic alteration	Ar–Ar	33.1 ± 0.2	Reynolds et al., 1998
Chuquicamata	22° 18' 20"	68° 54' 10"	(approx.)	(RT major)	Sericite	sericite alteration	Ar–Ar	31.8 ± 0.3	Cuadra & Rojas, 2001
Toki	22° 23' 56.94"	68° 57' 26.11"	(approx.)		Sericite	D-vein halo	Ar–Ar	34.5 ± 0.2	Rivera & Pardo, 2004
Toki	22° 23' 57"	68° 57' 18"			Biotite		Ar–Ar Plateau age	36.2 ± 0.4	Barra et al., 2013
Toki	22° 24' 20"	68° 58' 1"			Biotite		Ar–Ar Plateau age	36.1 ± 0.4	Barra et al., 2013
Toki	22° 24' 55"	68° 56' 20"			Plagioclase		Ar–Ar Plateau age	36.1 ± 0.5	Barra et al., 2013
Buey Muerto	22° 26' 18"	69° 55' 37"	(approx.)		Biotite (hydrothermal)		Ar–Ar	137 ± 4	Perelló et al., 2003
Buey Muerto	22° 26' 18"	69° 55' 37"	(approx.)		Sericite (hydrothermal)		Ar–Ar	132 ± 4	Perelló et al., 2003
Gatico	22°28' 13"	70°13' 23"	(Approx.)		Amphibole	hydrothermal	K–Ar	167 ± 7	References within Sillitoe, 1988
Spence	22° 40' 00"	69° 20' 00"	(approx)		Hypogene alunite		Ar–Ar	33.2 ± 1.9	Rowland & Clark, 2001
Spence	22° 40' 00"	69° 20' 00"	(approx)		Hypogene alunite		Ar–Ar	33.4 ± 1.1	Rowland & Clark, 2001
Spence	22° 40' 00"	69° 20' 00"	(approx)		Hypogene alunite		Ar–Ar	35.6 ± 1.4	Rowland & Clark, 2001
Spence	22° 40' 00"	69° 20' 00"	(approx)	pre-mineralization stock	Biotite		Ar–Ar	57 ± 0.7	Rowland & Clark, 2001
Spence	22° 40' 00"	69° 20' 00"	(approx)	late mineralization stock	Biotite		Ar–Ar	56.6 ± 0.6	Rowland & Clark, 2001
Mantos Blancos	23° 25' 27"	70° 02' 53"		Mafic dyke	Amphibole		Ar–Ar	142.7 ± 2	Oliveros et al., 2008
Mantos Blancos	23° 25' 35"	70° 03' 09"		Basic dyke	Sericite		Ar–Ar	155.4 ± 0.6	Oliveros et al., 2008
Mantos Blancos	23° 25' 35"	70° 03' 09"		Basic dyke	Sericite		Ar–Ar	154.7 ± 1.2	Oliveros et al., 2008
Mantos Blancos	23° 25' 35"	70° 03' 09"		Rhyolitic dome	Sericite		Ar–Ar	155.4 ± 0.7	Oliveros et al., 2008
Mantos Blancos	23° 25' 35"	70° 03' 09"		Rhyolitic dome	Sericite		Ar–Ar	156.6 ± 0.5	Oliveros et al., 2008
Mantos Blancos	23° 25' 45"	70° 03' 32"		Basic dyke	Sericite		Ar–Ar	101.6 ± 5.0 (?)	Oliveros et al., 2008
Mantos Blancos	23° 27' 06"	70° 05' 27"		Granodiorite	Amphibole		Ar–Ar	142.2 ± 1	Oliveros et al., 2008
Mantos Blancos	23° 27' 23"	70° 05' 03"		Metandesite	Amphibole		Ar–Ar	142.5 ± 0.6	Oliveros et al., 2008
Mantos Blancos	23° 27' 28"	70° 04' 56"		Diorite	Amphibole		Ar–Ar	141.6 ± 0.6	Oliveros et al., 2008
Mantos Blancos	23° 28' 59"	70° 09' 11"		Granodiorite	Biotite		Ar–Ar	148.2 ± 0.6	Oliveros et al., 2008
Mantos Blancos	23° 29' 07"	70° 08' 38"		Granodiorite (?)	Sericite		Ar–Ar	145.6 ± 0.8	Oliveros et al., 2008
Mantos Blancos	23° 29' 07"	70° 08' 38"		Granodiorite (?)	Sericite		Ar–Ar	147.1 ± 0.6	Oliveros et al., 2008
Mantos Blancos	23° 29' 59"	70° 03' 24"		Andesitic lava	Plagioclase		Ar–Ar	156.3 ± 1.4	Oliveros et al., 2008
Mantos Blancos	23° 29' 59"	70° 03' 24"		Andesitic lava	Sericite		Ar–Ar	147.5 ± 0.5 (?)	Oliveros et al., 2008
Mantos Blancos	23° 29' 59"	70° 03' 24"		Andesitic lava	Sericite		Ar–Ar	126.2 ± 0.5 (?)	Oliveros et al., 2008
Zaldivar	24° 15' 39.65"	69° 3' 43.44"		(Llamo porphyry)	Biotite		Ar–Ar	37.4 ± 0.18	Richards et al., 1999
Chimborazo	24° 8' 30.44"	69° 8' 23.15"		andesitic feldspar-biotite-quartz porphyry	Biotite		Ar–Ar	38.09 ± 0.3	Richards et al., 1999
Chimborazo	24° 07' 00"	69° 26' 00''	(approx.)	late hornblende-porphyritic diorite	Hornblende		K–Ar	38.8 ± 3.4	Petersen et al., 1996
Zaldivar	24° 12' 18.13"	69° 3' 55.75"		(Llamo porphyry)	Biotite	magmatic	Ar–Ar plateau	36.6 ± 0.9	Campos et al., 2009
Zaldivar	24° 12' 18.79"	69° 3' 46.89"		(Llamo porphyry)	Biotite	magmatic	Ar–Ar plateau	36 ± 0.3	Campos et al., 2009
Zaldivar	24° 12' 17.81"	69° 3' 43.34"		(Llamo porphyry)	Biotite	magmatic	Ar–Ar plateau	36.6 ± 0.4	Campos et al., 2009
Zaldivar	24° 12' 19.76"	69° 3' 52.91"		(Llamo porphyry)	Biotite	magmatic	Ar–Ar plateau	37.7 ± 0.4	Campos et al., 2009
Zaldivar	24° 12' 19.43"	69° 3' 53.27"		(Llamo porphyry)	Biotite	magmatic	Ar–Ar plateau	37.1 ± 0.5	Campos et al., 2009
Zaldivar	24° 12' 18.13"	69° 3' 53.98"		(Llamo porphyry)	Biotite	magmatic	Ar–Ar plateau	36.5 ± 0.5	Campos et al., 2009
Zaldivar	24° 12' 14.89"	69° 3' 39.79"		(Llamo porphyry)	Biotite	hydrothermal	Ar–Ar plateau	35.6 ± 0.7	Campos et al., 2009
Escondida	24° 15' 34.77"	69° 3' 52.3"		andesite	Biotite	Biotite	K–Ar	39.1 ± 2.2	References within Richards et al., 1999
Escondida	24° 14' 54.14"	69° 4' 09.37"		alunite vein	Alunite	hypogene advanced argillic	K–Ar	38.3 ± 3	References within Richards et al., 1999
Escondida	24° 14' 59.49"	69° 4' 30.94"		alunite vein	Alunite	hypogene advanced argillic	K–Ar	35.7 ± 2.8	References within Richards et al., 1999
Escondida	24° 14' 28.11"	69° 4' 57.55"		andesite	whole rock	Biotite with chlorite	K–Ar	35.4 ± 3.6	References within Richards et al., 1999
Escondida	24° 15' 54''	69° 4' 18''	(approx.)	andesite	whole rock		K–Ar	34.6 ± 3.6	References within Richards et al., 1999

Escondida	24° 16' 24.84"	69° 3' 12.25"		dacite ignimbrite	Sericite	propylitic to sericitic	K–Ar	33.7 ± 2.8	References within Richards et al., 1999
Escondida	24° 14' 26.49"	69° 4' 43.26"		breccia	Biotite	biotite (mineralized)	K–Ar	33.7 ± 2.6	References within Richards et al., 1999
Escondida	24° 15' 54''	69° 4' 18''	(approx.)	(Escondida porphyry)	whole rock		K–Ar	33.6 ± 3.4	References within Richards et al., 1999
Escondida	24° 15' 46.14"	69° 4' 11.81"		andesite	Biotite	Biotite with chlorite	K–Ar	33.2 ± 2.8	References within Richards et al., 1999
Escondida	24° 15' 39.64"	69° 4' 15.36"		andesite	Biotite	Biotite with chlorite and sericite	K–Ar	32.8 ± 2.6	References within Richards et al., 1999
Escondida	24° 15' 54''	69° 4' 18''	(approx.)	(Colorado Grande porphyry)	Biotite	Biotite	K–Ar	31.9 ± 2.4	References within Richards et al., 1999
Escondida	24° 15' 54''	69° 4' 18''	(approx.)	(Escondida porphyry)	whole rock		K–Ar	31.8 ± 2.4	References within Richards et al., 1999
Escondida	24° 15' 55.91"	69° 3' 26.07"		rhyolitic porphyry	Sericite	strong advanced argillic with sericite	K–Ar	31.6 ± 3.2	References within Richards et al., 1999
Escondida	24° 15' 39.65"	69° 3' 50.53"		late dacitic dyke	Sericite	weak sericite with chl	K–Ar	31.5 ± 2.8	References within Richards et al., 1999
Escondida	24° 15' 39.65"	69° 3' 54.08"		late dacitic dyke	whole rock	weak sericitic	K–Ar	31 ± 2.8	References within Richards et al., 1999
Escondida	24° 15' 54''	69° 4' 18''	(approx.)	Hornblende diorite	Hornblende		Ar–Ar	38.28 ± 0.32	Richards et al., 2001
Escondida	24° 15' 54''	69° 4' 18''	(approx.)	Hornblende diorite	Hornblende		Ar–Ar	37.87 ± 0.28	Richards et al., 2001
Escondida	24° 15' 54''	69° 4' 18''	(approx.)	Hornblende diorite	Hornblende		Ar–Ar	37.94 ± 0.34	Richards et al., 2001
Escondida	24° 15' 54''	69° 4' 18''	(approx.)	Porphyritic andesite dike	Hornblende		Ar–Ar	36.94 ± 0.46	Richards et al., 2001
Escondida	24° 15' 54''	69° 4' 18''	(approx.)	Porphyritic dacite dike	Hornblende		Ar–Ar	37.01 ± 0.88	Richards et al., 2001
Escondida	24° 15' 54''	69° 4' 18''	(approx.)	Hornblende diorite	Hornblende		Ar–Ar	38.25 ± 0.88	Richards et al., 2001
Escondida	24° 15' 54''	69° 4' 18''	(approx.)	Hornblende gabbro	Hornblende		Ar–Ar	76.9 ± 1.2	Richards et al., 2001
Escondida	24° 15' 54''	69° 4' 18''	(approx.)	Hornblende gabbro	Hornblende		Ar–Ar	74 ± 2	Richards et al., 2001
Escondida	24° 15' 54''	69° 4' 18''	(approx.)	Dacite porphyry	Hornblende		Ar–Ar	267.6 ± 4.3	Richards et al., 2001
El Salvador Mine	26° 12' 55.71"	69° 32' 29.64"		Quartz-sanidine porphyry	Whole rock	sericitically altered	K–Ar	42.1 ± 1.2	Cornejo et al., 1997
El Salvador Mine	26° 12' 50.58"	69° 32' 21.37"		Quartz-sanidine rhyolite porphyry	Sanidine plus altered plagioclase		K–Ar	45.3 ± 2	Cornejo et al., 1997
El Salvador Mine	26° 13' 15.26"	69° 32' 15.32"		Old Camp quartz-plagioclase porphyry dike	Whole rock		K–Ar	43.9 ± 1.5	Cornejo et al., 1997
El Salvador Mine	26° 14' 25.49"	69° 33' 29.89"		Granodioritic porphyry (L porphyry)	Biotite		K–Ar	41.2 ± 1.1	Cornejo et al., 1997
El Salvador Mine	26° 14' 27.44"	69° 33' 29.54"		Granodioritic porphyry (X porphyry)	Biotite		K–Ar	41.6 ± 1.2	Cornejo et al., 1997
El Salvador Mine	26° 13' 51.14"	69° 33' 04.14"		Biotite dacitic porphyry (A porphyry)	Biotite		K–Ar	43.8 ± 1.2	Cornejo et al., 1997
El Salvador Mine	26° 14' 01.73"	69° 33' 06.64"		Biotite dacitic porphyry (fine grained A- or L- porphyry)	Biotite		K–Ar	41.1 ± 1.3	Cornejo et al., 1997
El Salvador Mine	26° 13' 54.88"	69° 33' 03.94"		Biotite dacitic porphyry (coarse grained A- or L- porphyry)	Biotite		K–Ar	41.2 ± 1.3	Cornejo et al., 1997
El Salvador Mine	26° 13' 51.31"	69° 33' 10.77"		Granodioritic porphyry	Biotite		K–Ar	38.3 ± 1.2	Cornejo et al., 1997
El Salvador Mine	26° 13' 16.35"	69° 32' 24.05"		Quartz-plagioclase porphyry (Old Camp porphyry)	Sericite		K–Ar	42.1 ± 2.6	Gustafson & Hunt (1975) (recalculated by Cornejo et al. (1997))
El Salvador Mine	26° 13' 51.86"	69° 33' 00.30"		Granodioritic porphyry (Colina de Cobre (Cu Hill))	Biotite		K–Ar	41.6 ± 1.8	Gustafson & Hunt (1975) (recalculated by Cornejo et al. (1997))
El Salvador Mine	26° 14' 32.52"	69° 33' 09.06"		(K porphyry)	Sericite		K–Ar	41.9 ± 1	Gustafson & Hunt (1975) (recalculated by Cornejo et al. (1997))
El Salvador Mine	26° 14' 31.97"	69° 33' 05.82"		(L porphyry)	Amphibole		K–Ar	43.2 ± 5.6	Gustafson & Hunt (1975) (recalculated by Cornejo et al. (1997))
El Salvador Mine	26° 15' 24.17"	69° 33' 56.91"		(L porphyry (Quebrada Granito))	Amphibole		K–Ar	43.2 ± 2.6	Gustafson & Hunt (1975) (recalculated by Cornejo et al. (1997))
El Salvador Mine	26° 15' 24.17"	69° 33' 56.91"		(L porphyry (Quebrada Granito))	Biotite		K–Ar	43.1 ± 1.2	Gustafson & Hunt (1975) (recalculated by Cornejo et al. (1997))
El Salvador Mine	26° 14' 33.60"	69° 33' 21.18"		Biotitized andesite	Biotite		K–Ar	41.8 ± 2.64	Gustafson & Hunt (1975) (recalculated by Cornejo et al. (1997))
El Salvador Mine	26° 14' 44.07"	69° 33' 38.64"		"Latite" dike	Biotite		K–Ar	42 ± 1.0	Gustafson & Hunt (1975) (recalculated by Cornejo et al. (1997))
Potrerillos	26° 29' 54''	69° 23' 58''	(Approx.)			magmatic	K–Ar	38.6 ± 0.6	References within Sillitoe, 1988
Potrerillos	26° 29' 54''	69° 23' 58''	(Approx.)			potassic alteration	K–Ar	34.9 ± 0.5	References within Sillitoe, 1988
San Pedro de Cachiyuyo	26° 45' 00''	69° 54' 00''	(Approx.)		Sericite	Sericitic alteration	K–Ar	66.5 ± 1.0	References within Sillitoe, 1988
Candaleria	26° 48' 0"	69° 34' 0"	(approx.)	biotite assicite with chalcopyrite	Biotite (hydrothermal)		Ar–Ar	115.1 ± 0.2	Marschik & Fontboté, 2001
Candaleria	26° 48' 0"	69° 34' 0"	(approx.)		Biotite (hydrothermal)		Ar–Ar	114.2 ± 0.8	Ullrich & Clark, 1999
Candaleria	26° 48' 0"	69° 34' 0"	(approx.)		Biotite (hydrothermal)		Ar–Ar	114.1 ± 0.7	Ullrich & Clark, 1999
Candaleria	26° 48' 0"	69° 34' 0"	(approx.)		Biotite (hydrothermal)		Ar–Ar	111 ± 1.7	Ullrich & Clark, 1999
Candaleria	26° 48' 0"	69° 34' 0"	(approx.)		Biotite (hydrothermal)		Ar–Ar	110.7 ± 1.6	Ullrich & Clark, 1999
Manto Verde	26° 50' 00"	70° 30' 00"	(approx.)	Altered Andesite	Whole rock		K–Ar	117 ± 3	Vila et al., 1996
Manto Verde	26° 50' 00"	70° 30' 00"	(approx.)	Altered Andesite	Whole rock		K–Ar	121 ± 3	Vila et al., 1996
Caehiyuyo de Llampos	27° 8' 54''	69° 57' 42''	(Approx.)			magmatic	K–Ar	62.1 ± 1.0	References within Sillitoe, 1988
Bajo de la Alumbrera	27° 19' 00"	66° 34' 00"	(approx.)	porphyry intrusion (P3)	biotite	potassic alteration	Ar–Ar	7.12 ± 0.13	Harris et al., 2008
Bajo de la Alumbrera	27° 19' 00"	66° 34' 00"	(approx.)	porphyry intrusion (P3)	alkali feldspar		Ar–Ar	6.82 ± 0.05	Harris et al., 2008
Bajo de la Alumbrera	27° 19' 00"	66° 34' 00"	(approx.)	porphyry intrusion (P3)	alkali feldspar		Ar–Ar	6.64 ± 0.09	Harris et al., 2008
Candaleria	27° 20' 00"	70° 25' 00"	(approx.)	biotite assicite with chalcopyrite	Biotite (hydrothermal)		Ar–Ar	115.1 ± 0.2	Marschik & Fontboté, 2001
Candaleria	27° 20' 00"	70° 25' 00"	(approx.)		Biotite (hydrothermal)		Ar–Ar	114.2 ± 0.8	Ullrich & Clark, 1999
Candaleria	27° 20' 00"	70° 25' 00"	(approx.)		Biotite (hydrothermal)		Ar–Ar	114.1 ± 0.7	Ullrich & Clark, 1999
Candaleria	27° 20' 00"	70° 25' 00"	(approx.)		Biotite (hydrothermal)		Ar–Ar	111 ± 1.7	Ullrich & Clark, 1999
Candaleria	27° 20' 00"	70° 25' 00"	(approx.)		Biotite (hydrothermal)		Ar–Ar	110.7 ± 1.6	Ullrich & Clark, 1999
Cabeza de Vaca	27° 39' 12.74"	70° 2' 18.43"	(Approx.)		Sericite	Sericitic alteration	K–Ar	63.5 ± 7.0	References within Sillitoe, 1988
Tricolor	28° 57' 17.12"	70° 52' 38.03"		biotitized rock	Biotite (hydrothermal)		Ar–Ar	104.1 ± 5.1	Maksaev et al., 2010
Tricolor	28° 57' 18.72"	70° 52' 41.86"		altered porphyry	Biotite (hydrothermal)		Ar–Ar	97.1 ± 2.5	Maksaev et al., 2010
Tricolor	28° 57' 18.72"	70° 52' 41.86"		altered porphyry	Muscovite (hydrothermal)		Ar–Ar	96.3 ± 3.7	Maksaev et al., 2010
Tricolor	28° 57' 19.65"	70° 52' 42.62"		foliated porphyry	Biotite (hydrothermal)		Ar–Ar	105.4 ± 4.9	Maksaev et al., 2010
Dos Amigos	28° 58' 40.63"	70° 52' 38.47"		hydrothermal breccia	Sericite (hydrothermal)		Ar–Ar	85.8 ± 1.2	Maksaev et al., 2010
Dos Amigos mine pit	28° 59' 10.62"	70° 52' 47.06"		altered porphyry	Biotite (hydrothermal)		Ar–Ar	96.9 ± 1.4	Maksaev et al., 2010
Dos Amigos	28° 59' 12.59"	70° 52' 36.01"		altered porphyry	Sericite (hydrothermal)		Ar–Ar	96.1 ± 1	Maksaev et al., 2010
West of Tricolor	28° 57' 23.83"	70° 53' 2.45"		unaltered Cachiyuyo batholith	Biotite		Ar–Ar	96.9 ± 3.9	Maksaev et al., 2010
Domeyko	29° 0' 0"	71° 3' 0"	(Approx.)		Sericite	Sericitic alteration	K–Ar	106 ± 10	References within Sillitoe, 1988
Domeyko	29° 0' 0"	71° 3' 0"	(Approx.)		Sericite	Sericitic alteration	K–Ar	97 ± 20	References within Sillitoe, 1988
Pajonales	29° 7' 10.2"	70° 57' 10.82"	(Approx.)			magmatic	K–Ar	97 ± 1	References within Sillitoe, 1988
Pajonales	29° 7' 10.2"	70° 57' 10.82"	(Approx.)		Sericite	Sericitic alteration	K–Ar	97 ± 20	References within Sillitoe, 1988
Pajonales	29° 7' 10.2"	70° 57' 10.82"		unaltered Cachiyuyo batholith	Biotite		Ar–Ar	94.8 ± 0.9	Maksaev et al., 2010
Los Loros	29° 44' 30"	71° 05' 30"	(Approx.)			magmatic	K–Ar	91.1 ± 0.6	References within Sillitoe, 1988
El Indio	29° 46' 50''	69° 56' 58''	(Approx.)			premineralization	K–Ar	16.6 ± 0.7 to 11.0	References within Sillitoe, 1988
El Indio	29° 46' 50''	69° 56' 58''	(Approx.)			magmatic	K–Ar	12.6 ± 0.6	References within Sillitoe, 1988
El Indio	29° 46' 50''	69° 56' 58''	(Approx.)			propylitic alteration	K–Ar	10.7 ± 0.7	References within Sillitoe, 1988
El Indio	29° 46' 50''	69° 56' 58''	(Approx.)		Sericite	Sericitic alteration	K–Ar	8.6 ± 0.4	References within Sillitoe, 1988
Andacollo	30° 15' 00"	71° 25' 00"	(Approx.)			premineralization	K–Ar	105 ± 3	References within Sillitoe, 1988
Andacollo	30° 15' 00"	71° 25' 00"	(Approx.)		Sericite	Sericitic alteration	K–Ar	112 ± 10	References within Sillitoe, 1988
La Loica	31° 04' 00"	70° 43' 00"	(Approx.)			magmatic	K–Ar	35.3 ± 0.5	References within Sillitoe, 1988
Llamuco	31° 41' 16"	70° 46' 23"	(Approx.)		Sericite	Sericitic alteration	K–Ar	63.5 ± 1.0	References within Sillitoe, 1988
Los Pelambres	31° 42' 50"	70° 29' 20"	(Approx.)			premineralization	K–Ar	17 to 8	References within Sillitoe, 1988

Los Pelambres	31° 42' 50"	70° 29' 20"	(Approx.)			potassic alteration	K–Ar	10.2 ± 0.2	References within Sillitoe, 1988
Los Pelambres	31° 42' 50"	70° 29' 20"	(Approx.)			potassic alteration	K–Ar	9.9 ± 0.2	References within Sillitoe, 1988
Rio Blanco-Los Bronces	33° 8' 20"	70° 16' 40"	(Approx.)			premineralization	K–Ar	22 to 16	References within Sillitoe, 1988
Rio Blanco-Los Bronces	33° 8' 20"	70° 16' 40"	(Approx.)			premineralization	K–Ar	20.1 ± 2.0 to 8.6 ±	References within Sillitoe, 1988
Rio Blanco-Los Bronces	33° 8' 20"	70° 16' 40"	(Approx.)			premineralization	K–Ar	7.4 ± 0.1	References within Sillitoe, 1988
Rio Blanco-Los Bronces	33° 8' 20"	70° 16' 40"	(Approx.)			magmatic	K–Ar	5.15 ± 0.2	References within Sillitoe, 1988
Rio Blanco-Los Bronces	33° 8' 20"	70° 16' 40"	(Approx.)			potassic alteration	K–Ar	5.2 ± 0.3	References within Sillitoe, 1988
Rio Blanco-Los Bronces	33° 8' 20"	70° 16' 40"	(Approx.)			magmatic	K–Ar	4.6 ± 0.1	References within Sillitoe, 1988
Rio Blanco-Los Bronces	33° 8' 20"	70° 16' 40"	(Approx.)			post mineralization	K–Ar	5.0 ± 0.2 to 3.9 ±	References within Sillitoe, 1988
El Teniente	34° 02' 04.94''	70° 19' 20.83''		(La Huifa breccia pipe)	Biotite		Ar–Ar Plateau age	6.97 ± 0.1	Maksaev et al., 2004
El Teniente	34° 5' 19''	70° 27' 45''	(approx.)	Biotitized andesite	Biotite		Ar–Ar Total fusion age	4.76 ± 0.12	Maksaev et al., 2004
El Teniente	34° 5' 19''	70° 27' 45''	(approx.)	Biotitized andesite	Biotite		Ar–Ar Total fusion age	5.09 ± 0.12	Maksaev et al., 2004
El Teniente	34° 5' 19''	70° 27' 45''	(approx.)	Biotitized andesite	Sericite		Ar–Ar Total fusion age	5.58 ± 0.14	Maksaev et al., 2004
El Teniente	34° 5' 19''	70° 27' 45''	(approx.)	Biotitized andesite	Biotite		Ar–Ar Total fusion age	4.76 ± 0.1	Maksaev et al., 2004
El Teniente	34° 5' 19''	70° 27' 45''	(approx.)	Biotitized andesite	Sericite		Ar–Ar Total fusion age	4.85 ± 0.1	Maksaev et al., 2004
El Teniente	34° 5' 19''	70° 27' 45''	(approx.)	Biotitized andesite	Biotite		Ar–Ar Total fusion age	4.73 ± 0.18	Maksaev et al., 2004
El Teniente	34° 5' 19''	70° 27' 45''	(approx.)	Biotitized andesite	Biotite		Ar–Ar Total fusion age	5.5 ± 0.24	Maksaev et al., 2004
El Teniente	34° 5' 19''	70° 27' 45''	(approx.)	Biotitized andesite	Biotite		Ar–Ar Total fusion age	4.93 ± 0.14	Maksaev et al., 2004
El Teniente	34° 5' 19''	70° 27' 45''	(approx.)	(Braden pipe)	Sericite		Ar–Ar Total fusion age	5.42 ± 0.12	Maksaev et al., 2004
El Teniente	34° 5' 19''	70° 27' 45''	(approx.)	Central quartz diorite-tonalite	Sericite		Ar–Ar Total fusion age	4.66 ± 0.1	Maksaev et al., 2004
El Teniente	34° 5' 19''	70° 27' 45''	(approx.)	Central quartz diorite-tonalite	Sericite		Ar–Ar Total fusion age	4.8 ± 0.18	Maksaev et al., 2004
El Teniente	34° 5' 19''	70° 27' 45''	(approx.)	Northern quartz diorite-tonalite	Sericite		Ar–Ar Total fusion age	10.07 ± 0.62	Maksaev et al., 2004
El Teniente	34° 5' 19''	70° 27' 45''	(approx.)	Northern quartz diorite-tonalite	Sericite		Ar–Ar Total fusion age	5.94 ± 0.44	Maksaev et al., 2004
El Teniente	34° 5' 19''	70° 27' 45''	(approx.)	Northern quartz diorite-tonalite	Sericite		Ar–Ar Total fusion age	5.26 ± 0.82	Maksaev et al., 2004
El Teniente	34° 5' 19''	70° 27' 45''	(approx.)	Northern quartz diorite-tonalite	Sericite		Ar–Ar Total fusion age	5.25 ± 0.36	Maksaev et al., 2004
El Teniente	34° 5' 19''	70° 27' 45''	(approx.)	Northern quartz diorite-tonalite	Sericite		Ar–Ar Total fusion age	5.07 ± 0.22	Maksaev et al., 2004
El Teniente	34° 5' 19''	70° 27' 45''	(approx.)	Northern quartz diorite-tonalite	Sericite		Ar–Ar Total fusion age	4.67 ± 0.18	Maksaev et al., 2004
El Teniente	34° 5' 19''	70° 27' 45''	(approx.)	(Sewell stock)	Biotite		Ar–Ar Total fusion age	5.27 ± 0.08	Maksaev et al., 2004
El Teniente	34° 5' 19''	70° 27' 45''	(approx.)	(Sewell stock)	Biotite		Ar–Ar Total fusion age	5.32 ± 0.1	Maksaev et al., 2004
El Teniente	34° 5' 19''	70° 27' 45''	(approx.)	(Sewell stock)	Sericite		Ar–Ar Total fusion age	4.91 ± 0.2	Maksaev et al., 2004
El Teniente	34° 5' 19''	70° 27' 45''	(approx.)	(Sewell stock)	Biotite		Ar–Ar Total fusion age	4.71 ± 0.08	Maksaev et al., 2004
El Teniente	34° 5' 19''	70° 27' 45''	(approx.)	(Sewell stock)	Sericite		Ar–Ar Total fusion age	12.26 ± 0.74	Maksaev et al., 2004
El Teniente	34° 5' 19''	70° 27' 45''	(approx.)	Dacite porphyry (Teniente dacite porphyry)	Sericite		Ar–Ar Total fusion age	4.94 ± 0.14	Maksaev et al., 2004
El Teniente	34° 5' 19''	70° 27' 45''	(approx.)	Dacite porphyry (Teniente dacite porphyry)	Biotite		Ar–Ar Total fusion age	5.4 ± 0.42	Maksaev et al., 2004
El Teniente	34° 5' 19''	70° 27' 45''	(approx.)	Dacite porphyry (Teniente dacite porphyry)	Sericite		Ar–Ar Total fusion age	4.6 ± 0.08	Maksaev et al., 2004
El Teniente	34° 5' 19''	70° 27' 45''	(approx.)	Dacite porphyry (Teniente dacite porphyry)	Sericite		Ar–Ar Total fusion age	5.1 ± 0.28	Maksaev et al., 2004
El Teniente	34° 5' 19''	70° 27' 45''	(approx.)	Dacite porphyry (Teniente dacite porphyry)	Sericite		Ar–Ar Total fusion age	6.35 ± 0.62	Maksaev et al., 2004
El Teniente	34° 5' 19''	70° 27' 45''	(approx.)	Dacite porphyry (Teniente dacite porphyry)	Biotite		Ar–Ar Total fusion age	4.93 ± 0.24	Maksaev et al., 2004
El Teniente	34° 5' 19''	70° 27' 45''	(approx.)	Dacite porphyry (Teniente dacite porphyry)	Sericite		Ar–Ar Total fusion age	5.09 ± 0.32	Maksaev et al., 2004
El Teniente	34° 5' 19''	70° 27' 45''	(approx.)	Dacite porphyry (Teniente dacite porphyry)	Sericite		Ar–Ar Total fusion age	4.68 ± 0.06	Maksaev et al., 2004
El Teniente	34° 5' 19''	70° 27' 45''	(approx.)	Dacite dike	Sericite		Ar–Ar Total fusion age	4.39 ± 0.34	Maksaev et al., 2004
El Teniente	34° 5' 19''	70° 27' 45''	(approx.)	Dacite dike	Sericite		Ar–Ar Total fusion age	8.4 ± 1.4	Maksaev et al., 2004
El Teniente	34° 5' 19''	70° 27' 45''	(approx.)	Dacite dike	Sericite		Ar–Ar Total fusion age	4.8 ± 0.14	Maksaev et al., 2004
El Teniente	34° 5' 19''	70° 27' 45''	(approx.)	Biotitized andesite (Biotitized host)	Biotite		Ar–Ar Plateau age	4.78 ± 0.14	Maksaev et al., 2004
El Teniente	34° 5' 19''	70° 27' 45''	(approx.)	Biotitized andesite (Biotitized host)	Biotite		Ar–Ar Plateau age	4.69 ± 0.1	Maksaev et al., 2004
El Teniente	34° 5' 19''	70° 27' 45''	(approx.)	Coarse-grained biotite-quartz vein (Biotitized host)	Biotite		Ar–Ar Plateau age	4.68 ± 0.1	Maksaev et al., 2004
El Teniente	34° 5' 19''	70° 27' 45''	(approx.)	Gabbro (Biotitized host)	Biotite	Potassic alteration (biotite magnetite)	Ar–Ar Plateau age	4.46 ± 0.22	Maksaev et al., 2004
El Teniente	34° 5' 19''	70° 27' 45''	(approx.)	Hydrothermal breccia (Sewell stock)	Biotite		Ar–Ar Plateau age	5.69 ± 0.08	Maksaev et al., 2004
El Teniente	34° 5' 19''	70° 27' 45''	(approx.)	Unmineralized tonalite (Sewell stock)	Biotite		Ar–Ar Plateau age	5.63 ± 0.12	Maksaev et al., 2004
El Teniente	34° 5' 19''	70° 27' 45''	(approx.)	Unmineralized tonalite (Sewell stock)	Biotite		Ar–Ar Plateau age	5.47 ± 0.12	Maksaev et al., 2004
El Teniente	34° 5' 19''	70° 27' 45''	(approx.)	Coarse-grained hydrothermal biotite vein (Sewell stock)	Biotite		Ar–Ar Plateau age	5.06 ± 0.12	Maksaev et al., 2004
El Teniente	34° 5' 19''	70° 27' 45''	(approx.)	Coarse-grained hydrothermal biotite (Sewell stock)	Biotite		Ar–Ar Plateau age	4.74 ± 0.1	Maksaev et al., 2004
El Teniente	34° 5' 19''	70° 27' 45''	(approx.)	(Sewell stock)	Biotite	Potassic alteration (biotite-magnetite)	Ar–Ar Plateau age	4.62 ± 0.12	Maksaev et al., 2004
El Teniente	34° 5' 19''	70° 27' 45''	(approx.)	(Sewell stock)	Biotite		Ar–Ar Plateau age	4.69 ± 0.1	Maksaev et al., 2004
El Teniente	34° 5' 19''	70° 27' 45''	(approx.)	(Sewell stock)	Sericite	Pervasive quartz-sericite-smectite alteration	Ar–Ar Plateau age	4.37 ± 0.1	Maksaev et al., 2004
El Teniente	34° 5' 19''	70° 27' 45''	(approx.)	(Sewell stock)	Sericite	Pervasive quartz-sericite alteration	Ar–Ar Plateau age	4.62 ± 0.12	Maksaev et al., 2004
El Teniente	34° 5' 19''	70° 27' 45''	(approx.)	(Sewell stock)	Sericite	Pervasive quartz-sericite alteration	Ar–Ar Plateau age	4.55 ± 0.12	Maksaev et al., 2004
El Teniente	34° 5' 19''	70° 27' 45''	(approx.)	(Sewell stock)	Sericite	Pervasive quartz-sericite alteration	Ar–Ar Plateau age	4.54 ± 0.12	Maksaev et al., 2004
El Teniente	34° 5' 19''	70° 27' 45''	(approx.)	(Sewell stock)	Sericite	Pervasive quartz-sericite alteration	Ar–Ar Plateau age	4.47 ± 0.1	Maksaev et al., 2004
El Teniente	34° 5' 19''	70° 27' 45''	(approx.)	(Sewell stock)	Biotite		Ar–Ar Plateau age	4.72 ± 0.12	Maksaev et al., 2004
El Teniente	34° 5' 19''	70° 27' 45''	(approx.)	(A porphyry)	Biotite		Ar–Ar Plateau age	4.93 ± 0.12	Maksaev et al., 2004
El Teniente	34° 5' 19''	70° 27' 45''	(approx.)	Central quartz diorite-tonalite	Sericite	pervasive quartz-sericite-smectite alteration	Ar–Ar Plateau age	4.55 ± 0.1	Maksaev et al., 2004
El Teniente	34° 5' 19''	70° 27' 45''	(approx.)	Northern quartz diorite-tonalite	Sericite		Ar–Ar Plateau age	4.74 ± 0.12	Maksaev et al., 2004
El Teniente	34° 5' 19''	70° 27' 45''	(approx.)	Fine-grained hydrothermal biotite (Teniente dacite porphyry)	Biotite		Ar–Ar Plateau age	4.77 ± 0.14	Maksaev et al., 2004
El Teniente	34° 5' 19''	70° 27' 45''	(approx.)	Fine-grained hydrothermal biotite (Teniente dacite porphyry)	Sericite		Ar–Ar Plateau age	4.4 ± 0.1	Maksaev et al., 2004
El Teniente	34° 5' 19''	70° 27' 45''	(approx.)	Coarse-grained hydrothermal sericite (Teniente dacite porphyry)	Sericite		Ar–Ar Plateau age	4.69 ± 0.12	Maksaev et al., 2004
El Teniente	34° 5' 19''	70° 27' 45''	(approx.)	Coarse-grained biotite (Teniente dacite porphyry)	Biotite		Ar–Ar Plateau age	4.69 ± 0.12	Maksaev et al., 2004
El Teniente	34° 5' 19''	70° 27' 45''	(approx.)	Sericite halo of quartz-chalcopyrite-molybdenite vein (Teniente dacite porphyry)	Sericite		Ar–Ar Plateau age	4.65 ± 0.12	Maksaev et al., 2004
El Teniente	34° 5' 19''	70° 27' 45''	(approx.)	Quartz-sericite vein (Teniente dacite porphyry)	Sericite		Ar–Ar Plateau age	4.61 ± 0.14	Maksaev et al., 2004
El Teniente	34° 5' 19''	70° 27' 45''	(approx.)	Sericitic halo of molybdenite-chalcopyrite vein (Teniente dacite porphyry)	Sericite		Ar–Ar Plateau age	4.57 ± 0.12	Maksaev et al., 2004
El Teniente	34° 5' 19''	70° 27' 45''	(approx.)	(Teniente dacite porphyry)	Biotite		Ar–Ar Plateau age	4.69 ± 0.18	Maksaev et al., 2004
El Teniente	34° 5' 19''	70° 27' 45''	(approx.)	Sericitized halo of chalcopyrite vein (Braden pipe)	Sericite		Ar–Ar Plateau age	4.81 ± 0.1	Maksaev et al., 2004
El Teniente	34° 5' 19''	70° 27' 45''	(approx.)	Sericite alteration of fragment (Braden pipe)	Sericite		Ar–Ar Plateau age	4.75 ± 0.12	Maksaev et al., 2004
El Teniente	34° 5' 19''	70° 27' 45''	(approx.)	Tourmalinized breccia (Braden pipe)	Sericite		Ar–Ar Plateau age	4.68 ± 0.12	Maksaev et al., 2004
El Teniente	34° 5' 19''	70° 27' 45''	(approx.)	Sericitized border of andesite fragment (Marginal breccia)	Sericite		Ar–Ar Plateau age	4.67 ± 0.22	Maksaev et al., 2004
El Teniente	34° 5' 19''	70° 27' 45''	(approx.)	Sericite alteration of fragment (Marginal breccia)	Sericite		Ar–Ar Plateau age	4.6 ± 0.1	Maksaev et al., 2004
El Teniente	34° 5' 19''	70° 27' 45''	(approx.)	Sericitized border of andesite fragment (Braden pipe)	Sericite		Ar–Ar Plateau age	4.6 ± 0.06	Maksaev et al., 2004
El Teniente	34° 5' 19''	70° 27' 45''	(approx.)	Bedded horizon (Braden pipe)	Sericite		Ar–Ar Plateau age	4.58 ± 0.12	Maksaev et al., 2004
El Teniente	34° 5' 19''	70° 27' 45''	(approx.)	Hydrothermal breccia (Braden pipe)	Sericite		Ar–Ar Plateau age	4.49 ± 0.1	Maksaev et al., 2004

El Teniente	34° 5' 19''	70° 27' 45''	(approx.)	Dike with pervasive quartz-sericite alteration (late dyke)	Sericite		Ar–Ar Plateau age	4.61 ± 0.12	Maksaev et al., 2004
El Teniente	34° 5' 19''	70° 27' 45''	(approx.)	late dacite stock	Biotite		Ar–Ar Plateau age	4.58 ± 0.1	Maksaev et al., 2004
El Teniente	34° 5' 19''	70° 27' 45''	(approx.)	Dike with quartz-sericite-carbonate alteration (late dyke)	Sericite		Ar–Ar Plateau age	4.56 ± 0.12	Maksaev et al., 2004
El Teniente	34° 5' 19''	70° 27' 45''	(approx.)	Sericitized halo of quartz vein within dike (late dyke)	Sericite		Ar–Ar Plateau age	4.52 ± 0.12	Maksaev et al., 2004
El Teniente	34° 5' 19''	70° 27' 45''	(approx.)	Late dacite stock	Sericite	Quartz-sericite alteration	Ar–Ar Plateau age	4.46 ± 0.1	Maksaev et al., 2004
El Teniente	34° 5' 19''	70° 27' 45''	(approx.)	Late dacite stock	Sericite	Quartz-sericite alteration	Ar–Ar Plateau age	4.55 ± 0.12	Maksaev et al., 2004
El Teniente	34° 5' 19''	70° 27' 45''	(approx.)	Postmineralization hornblende rich andesitic dike	Hornblende		Ar–Ar Plateau age	3.85 ± 0.18	Maksaev et al., 2004
El Teniente	34° 5' 19''	70° 27' 45''	(approx.)	(Teniente dacite porphyry)	Biotite		K–Ar	4.6 ± 0.1	Cuadra, 1986
El Teniente	34° 5' 19''	70° 27' 45''	(approx.)	(La Huifa Breccia pipe)	Biotite		K–Ar	7.0 ± 0.5	Cuadra, 1986
El Teniente	34° 5' 19''	70° 27' 45''	(approx.)	(Marginal breccia)	sericitic whole rock		K–Ar	4.7 ± 0.1	Cuadra, 1986
El Teniente	34° 5' 19''	70° 27' 45''	(approx.)	(Braden pipe)	sericitic whole rock		K–Ar	4.5 ± 0.1	Cuadra, 1986
El Teniente	34° 5' 19''	70° 27' 45''	(approx.)	(Sewell stock)	biotite whole-rock		K–Ar	7.1 ± 0.5	Cuadra, 1986

c) Summary of published Re–Os age data in N. Chile

Region	**Latitude (S)**	**Longitude (W)**		**Rock type (or pluton name)**	**Material**	**Stage (Molybdenite mineralization, otherwise specified)**	**Method**	**Age (Ma) (± 2σ)**	**Reference**
Cerro Colorado	20° 2' 41''	69° 15' 35''	(approx.)		Molybdenite		Re–Os	55.5 ± 0.3	Cotton, 2003
Collahuasi (Rosario)	20° 57' 35.82"	68° 41' 55.71"	(approx.)		Molybdenite		Re–Os	33.3 ± 0.2	Masterman et al., 2004
Chuquicamata	22° 17' 00"	68° 54' 00"			Molybdenite		Re–Os	32.2 ± 0.2	Barra et al., 2013
Chuquicamata	22° 17' 00"	68° 54' 00"			Molybdenite		Re–Os	31.7 ± 0.2	Barra et al., 2013
Chuquicamata	22° 16' 49"	68° 54' 4"			Molybdenite		Re–Os	32.9 ± 0.2	Barra et al., 2013
Chuquicamata	22° 16' 49"	68° 54' 4"			Molybdenite		Re–Os	31.9 ± 0.2	Barra et al., 2013
Chuquicamata	22° 17' 0"	68° 54' 2"			Molybdenite		Re–Os	32.2 ± 0.2	Barra et al., 2013
Chuquicamata	22° 17' 47.57"	68° 54' 08.09"	(approx.)		Pyrite	Quartz sericitic alteration	Re–Os	31 ± 2	Mathur et al., 2000
Chuquicamata	22° 17' 47.57"	68° 54' 08.09"	(approx.)		Chalcopyrite	Orthoclase biotite alteration	Re–Os	33 (± ?)	Mathur et al., 2000
Chuqucamata	22° 17' 47.57"	68° 54' 08.09"	(approx.)		Molybdenite		Re–Os	34.8 ± 0.2	Mathur et al., 2000
Chuquicamata	22° 17' 6"	68° 54' 6"			Molybdenite		Re–Os	32 ± 0.2	Barra et al., 2013
Chuquicamata	22° 17' 47.57"	68° 54' 08.09"			Molybdenite		Re–Os	33.4 (± ?)	Campbell et al., 2006
Chuquicamata	22° 17' 47.57"	68° 54' 08.09"			Molybdenite		Re–Os	31.1 (± ?)	Campbell et al., 2006
Chuquicamata	22° 17' 47.57"	68° 54' 08.09"			Molybdenite		Re–Os	34.9 ± 0.17	Writ. commum. with Ruiz, cited in Ossandón et al., 2001
Mina Ministro Hales	22° 22' 45"	68° 54' 50"			Molybdenite		Re–Os	31 ± 2	Zentilli et al., 2015
Mina Ministro Hales	22° 22' 45"	68° 54' 50"			Molybdenite		Re–Os	34.2 ± 3.1	Unpublished reported by Tobey, cited in Zentilli et al., 2015
Quetena	22° 23' 50"	68° 57' 5"			Molybdenite		Re–Os	37.9 ± 0.2	Barra et al., 2013
Quetena	22° 23' 57"	68° 57' 18"			Molybdenite		Re–Os	37.9 ± 0.2	Barra et al., 2013
Genoveva	22° 24' 20"	68° 58' 1"			Molybdenite		Re–Os	38 ± 0.2	Barra et al., 2013
Toki	22° 24' 3"	68° 56' 34"			Molybdenite		Re–Os	38.1 ± 0.2	Barra et al., 2013
Quetena	22° 24' 3"	68° 57' 37"			Molybdenite		Re–Os	38.4 ± 0.2	Barra et al., 2013
Miranda	22° 24' 33"	68° 56' 2"			Molybdenite		Re–Os	36.5 ± 0.2	Barra et al., 2013
Miranda	22° 24' 39"	68° 56' 7"			Molybdenite		Re–Os	36 ± 0.2	Barra et al., 2013
Toki	22° 24' 42"	68° 56' 30"			Molybdenite		Re–Os	37.7 ± 0.2	Barra et al., 2013
Miranda	22° 24' 46"	68° 55' 52"			Molybdenite		Re–Os	36.2 ± 0.2	Barra et al., 2013
Toki	22° 24' 55"	68° 56' 20"			Molybdenite		Re–Os	37.9 ± 0.2	Barra et al., 2013
Genoveva	22° 24' 7"	68° 58' 8"			Molybdenite		Re–Os	38.1 ± 0.2	Barra et al., 2013
Toki	22° 25' 8"	68° 56' 27"			Molybdenite		Re–Os	37.9 ± 0.2	Barra et al., 2013
Opache	22° 26' 23"	68° 57' 52"			Molybdenite		Re–Os	36.4 ± 0.2	Barra et al., 2013
Opache	22° 26' 23"	68° 58' 1"			Molybdenite		Re–Os	36.8 ± 0.2	Barra et al., 2013
Opache	22° 26' 36"	68° 57' 57"			Molybdenite		Re–Os	37.6 ± 0.2	Barra et al., 2013
Opache	22° 26' 36"	68° 57' 57"			Molybdenite		Re–Os	37.5 ± 0.2	Barra et al., 2013
El Salvador	26° 13' 52.26"	69° 33' 25.8"	(approx.)		Pyrite/ Chalcopyrite	Quartz sericitic/ Orthoclase Biotite alteration	Re–Os	39.2 ± 2	Mathur et al., 2000
Candelaria	26° 48' 0"	69° 34' 0"	(approx.)		Molybdenite		Re–Os	114.2 ± 0.6	Mathur et al., 2002
Candelaria	26° 48' 0"	69° 34' 0"	(approx.)		Molybdenite		Re–Os	115.14 ± 0.18	Mathur et al., 2002
El Teniente	34° 5' 19''	70° 27' 45''	(approx.)	Breccia, potassic altered (Sewell stock)	Molybdenite		Re–Os	6.31 ± 0.03	Maksaev et al., 2004
El Teniente	34° 5' 19''	70° 27' 45''	(approx.)	Breccia, potassic altered (Sewell stock)	Molybdenite		Re–Os	5.6 ± 0.02	Maksaev et al., 2004
El Teniente	34° 5' 19''	70° 27' 45''	(approx.)	Mo vein, host quartz-sericite altered (Sewell stock)	Molybdenite		Re–Os	4.89 ± 0.08	Maksaev et al., 2004
El Teniente	34° 5' 19''	70° 27' 45''	(approx.)	Qtz-Mo vein, host potassic altered (Teniente dacite porphyry)	Molybdenite		Re–Os	4.87 ± 0.03	Maksaev et al., 2004
El Teniente	34° 5' 19''	70° 27' 45''	(approx.)	Mo vein in biotitized gabbro	Molybdenite		Re–Os	4.83 ± 0.03	Maksaev et al., 2004
El Teniente	34° 5' 19''	70° 27' 45''	(approx.)	Mo-Cpy vein with sericite halo (Teniente dacite porphyry)	Molybdenite		Re–Os	4.78 ± 0.03	Maksaev et al., 2004
El Teniente	34° 5' 19''	70° 27' 45''	(approx.)	Mo (minor cpy) vein, sericite halo (Teniente dacite porphyry)	Molybdenite		Re–Os	4.42 ± 0.02	Maksaev et al., 2004
El Teniente	34° 5' 19''	70° 27' 45''	(approx.)	Qtz-Mo-cpy vein, host quartz-sericite altered (Northern quartz diorite-tonalite porp	Molybdenite		Re–Os	4.42 ± 0.02	Maksaev et al., 2004

Supplementary table 2 Geochemical data extracted from CMCC mine report

The CMCC data are ICP–MS whole rock analyses measured in SGS CIMM T&S (SGS, Centro de Investigación Minera y Metalúrgica, Tecnologías y Servicios S.A.) in Antofagasta.

Drill core # - Rock unit	SiO[2] mass %	TiO[2] mass %	Al[2]O[3] mass %	Fe[2]O[3] mass %	MnO mass %	MgO mass %	CaO mass %	Na[2]O mass %	K[2]O mass %	P[2]O[5] mass %
11-075-PTO 1	70.44	0.083	12.47	2.34	0.013	1.28	0.45	6.63	1.78	0.092
11-075-PTO 1	67.69	0.117	14.57	2.16	0.012	1.53	0.49	6.40	2.51	0.115
11-075-PTO 1	68.57	0.117	13.02	2.63	0.011	1.71	0.41	5.88	3.13	0.115
11-075-PTO 1	68.16	0.083	14.23	2.96	0.010	1.49	0.42	5.53	2.59	0.115
11-075-PTO 1	68.27	0.083	14.40	2.82	0.011	1.34	0.45	5.66	2.43	0.115
11-075-PTO 1	67.97	0.083	14.66	3.37	0.007	1.16	0.42	4.43	3.31	0.160
11-075-PTO 1	71.74	0.067	12.06	2.20	0.006	1.13	0.48	4.97	2.71	0.229
11-075-PTO 1	70.75	0.083	13.09	2.40	0.007	0.93	0.41	5.11	2.66	0.137
11-075-PTO 1	70.53	0.083	13.26	2.54	0.007	0.85	0.48	4.87	2.78	0.183
11-075-PTO 1	70.44	0.083	12.98	3.12	0.006	0.60	0.38	4.81	2.99	0.183
11-075-PTO 1	68.62	0.083	13.87	3.53	0.006	0.88	0.45	4.85	3.11	0.183
11-075-PTO 1	69.15	0.100	13.60	3.52	0.009	1.01	0.43	4.07	3.51	0.183
11-075-PTO 1	69.42	0.100	13.17	4.45	0.009	1.11	0.48	3.33	3.29	0.229
11-075-PTO 1	68.18	0.067	14.87	4.79	0.010	0.61	0.45	2.62	3.81	0.183
11-075-PTO 1	67.72	0.117	14.23	2.57	0.019	1.49	0.71	5.28	3.18	0.252
11-075-PTO 1	72.87	0.100	11.09	3.02	0.011	0.93	0.41	3.84	3.13	0.183
11-075-PTO 1	73.31	0.117	10.47	2.37	0.014	1.14	0.46	4.68	2.88	0.137
11-075-PTO 1	70.68	0.133	12.60	2.26	0.025	1.18	0.48	5.77	2.37	0.092
11-075-PTO 1	68.24	0.083	14.27	2.92	0.013	1.26	0.45	5.01	3.20	0.137
11-075-PTO 1	67.90	0.100	15.12	2.34	0.017	1.21	0.49	5.37	2.93	0.115
11-075-PTO 1	70.16	0.100	13.21	2.80	0.016	1.18	0.42	4.83	2.78	0.092
11-075-PTO 1	69.09	0.100	14.68	2.43	0.014	1.18	0.45	4.96	2.59	0.092
11-075-PTO 1	68.25	0.067	13.81	4.15	0.012	1.09	0.41	4.64	3.05	0.115
11-075-PTO 1	68.76	0.133	13.66	3.13	0.016	1.28	0.50	4.93	3.01	0.160
11-075-PTO 1	66.34	0.133	16.08	2.63	0.014	1.33	0.69	5.72	2.57	0.092
11-075-PTO 1	67.92	0.150	14.36	2.76	0.020	1.31	0.90	5.76	2.23	0.183
11-075-PTO 1	67.90	0.150	14.13	3.20	0.015	1.09	0.74	5.62	2.54	0.183
11-075-PTO 1	67.02	0.133	15.68	2.26	0.014	1.33	0.85	5.89	2.31	0.092
11-075-PTO 1	67.74	0.150	14.78	2.66	0.017	1.09	0.78	5.66	2.49	0.206
11-075-PTO 1	68.23	0.150	14.23	2.12	0.016	1.24	0.78	6.09	2.52	0.206
11-075-PTO 1	70.80	0.150	12.28	1.69	0.014	1.39	0.73	5.76	2.59	0.183
11-075-PTO 1	69.11	0.183	13.04	2.37	0.015	1.51	0.83	5.73	2.61	0.183
11-075-PTO 1	70.04	0.167	13.04	1.86	0.014	1.56	0.76	5.65	2.41	0.092
11-075-PTO 1	69.77	0.183	13.26	1.66	0.013	1.59	0.78	5.99	2.24	0.092
11-075-PTO 1	69.15	0.167	13.64	1.86	0.016	1.72	0.66	5.77	2.46	0.137
11-075-PTO 1	65.92	0.150	16.31	2.92	0.014	1.59	0.60	4.81	3.13	0.137
11-075-PTO 1	69.50	0.150	13.51	2.32	0.016	1.19	0.53	5.58	2.55	0.229
11-075-PTO 1	68.25	0.133	14.68	2.86	0.019	1.43	0.59	4.53	2.94	0.160
11-075-PTO 1	69.72	0.133	13.74	2.67	0.015	1.51	0.45	4.46	2.75	0.137
11-075-PTO 1	67.81	0.100	15.00	2.79	0.015	1.56	0.53	5.15	2.49	0.137
11-075-PTO 1	72.80	0.133	13.62	1.73	0.007	1.13	0.24	1.02	4.78	0.115
11-075-PTO 1	69.62	0.067	14.15	1.86	0.013	1.01	0.46	5.28	2.98	0.137
11-075-PTO 1	70.38	0.083	13.19	2.23	0.010	1.28	0.67	5.06	2.43	0.252
11-075-PTO 1	70.14	0.100	13.15	2.79	0.009	1.09	0.70	4.83	2.64	0.137
11-075-PTO 1	70.80	0.067	13.49	2.70	0.007	0.75	0.52	4.27	2.79	0.183
11-075-PTO 1	68.05	0.067	15.44	2.13	0.011	1.06	0.71	5.86	2.08	0.160
11-075-PTO 1	73.04	0.083	11.85	1.80	0.009	1.03	0.55	5.07	2.02	0.137
11-075-PTO 1	70.64	0.067	13.32	2.02	0.007	0.90	0.55	5.62	2.34	0.137
11-075-PTO 1	74.56	0.067	10.45	1.20	0.006	0.88	0.42	5.76	2.16	0.092
11-075-PTO 1	70.04	0.067	14.25	2.32	0.007	0.76	0.53	5.32	2.22	0.069
11-075-PTO 1	69.47	0.117	13.93	2.46	0.013	1.34	0.83	5.54	1.82	0.069
11-075-PTO 1	71.07	0.100	12.87	2.79	0.011	1.16	0.62	4.53	2.32	0.115
11-075-PTO 1	68.94	0.083	14.55	3.75	0.010	1.14	0.41	3.73	2.90	0.069
11-075-PTO 1	73.42	0.117	10.81	2.95	0.011	1.43	0.49	3.81	2.48	0.069
11-075-PTO 1	72.16	0.083	11.98	2.57	0.010	1.21	0.46	4.35	2.69	0.069
11-075-PTO 1	69.99	0.067	14.40	1.44	0.008	0.83	0.76	6.30	1.72	0.069
11-075-PTO 1	69.22	0.067	14.45	3.73	0.009	0.96	0.46	3.83	2.73	0.115
11-075-PTO 1	68.04	0.067	15.15	5.48	0.012	0.76	0.42	1.67	3.82	0.160
11-075-PTO 1	71.67	0.083	12.94	2.44	0.017	0.83	0.41	4.22	2.81	0.160
11-075-PTO 1	69.40	0.067	13.98	2.96	0.020	0.99	0.57	4.68	2.72	0.183
11-075-PTO 1	73.56	0.067	11.90	1.67	0.010	0.71	0.38	4.83	2.34	0.115
11-075-PTO 1	71.50	0.067	12.74	2.42	0.011	0.86	0.36	4.58	2.90	0.137

Drill core # - Rock unit	SiO[2] mass %	TiO[2] mass %	Al[2]O[3] mass %	Fe[2]O[3] mass %	MnO mass %	MgO mass %	CaO mass %	Na[2]O mass %	K[2]O mass %	P[2]O[5] mass %
11-075-PTO 1	72.35	0.083	12.17	2.20	0.012	0.91	0.63	4.77	2.31	0.137
11-075-PTO 1	73.25	0.083	11.83	1.10	0.014	0.99	0.64	5.45	2.06	0.160
11-075-PTO 1	72.37	0.067	12.04	2.10	0.015	1.03	0.46	4.72	2.63	0.160
11-075-PTO 1	69.62	0.067	14.15	1.86	0.013	1.01	0.46	5.28	2.98	0.137
11-075-PTO 1	69.84	0.067	14.27	2.17	0.013	1.01	0.55	4.69	2.84	0.137
11-075-PTO 1	73.20	0.083	11.45	2.56	0.007	0.70	0.34	3.60	3.54	0.115
11-075-PTO 1	70.05	0.067	13.98	2.27	0.009	0.83	0.50	4.61	3.17	0.092
11-075-PTO 1	71.19	0.083	13.11	3.05	0.009	0.81	0.39	3.14	3.69	0.115
11-075-PTO 1	68.32	0.050	15.66	2.12	0.010	1.08	0.69	5.04	2.51	0.115
11-075-PTO 1	70.32	0.067	14.08	3.16	0.008	0.86	0.35	3.14	3.46	0.137
11-075-PTO 1	63.90	0.117	18.74	2.99	0.011	1.18	0.60	4.41	3.52	0.115
11-075-PTO 1	71.05	0.083	13.91	2.85	0.008	0.86	0.45	3.63	2.66	0.092
11-075-PTO 1	69.77	0.083	14.70	2.62	0.009	0.95	0.39	4.30	2.67	0.092
11-075-PTO 1	70.44	0.083	14.34	3.25	0.007	0.80	0.28	2.83	3.47	0.092
11-075-PTO 1	67.05	0.067	15.02	6.76	0.010	0.70	0.24	1.89	3.76	0.092
11-075-PTO 1	70.03	0.083	14.62	2.92	0.010	0.83	0.41	4.10	2.49	0.092
11-075-PTO 1	72.76	0.083	13.36	2.20	0.008	0.80	0.38	3.53	2.40	0.069
11-075-PTO 1	71.64	0.083	14.02	1.67	0.009	0.91	0.46	4.91	1.81	0.069
11-075-PTO 1	72.02	0.067	13.25	3.23	0.007	0.93	0.31	2.66	3.05	0.069
11-075-PTO 1	71.88	0.067	13.47	2.57	0.009	0.75	0.42	4.18	2.17	0.069
11-075-PTO 1	72.14	0.067	13.81	2.24	0.007	0.80	0.31	3.38	2.73	0.092
11-075-PTO 1	71.29	0.083	13.96	2.43	0.008	1.06	0.45	3.44	2.75	0.115
11-075-PTO 1	71.54	0.083	14.11	1.33	0.010	1.06	0.76	4.92	1.67	0.092
11-075-PTO 1	73.28	0.083	12.89	1.49	0.008	0.73	0.56	4.96	1.52	0.069
11-075-PTO 1	70.13	0.067	13.40	4.53	0.010	0.85	0.48	3.59	2.47	0.069
11-075-PTO 1	72.53	0.083	13.25	2.06	0.009	0.90	0.34	3.60	2.71	0.115
11-075-PTO 1	72.51	0.083	13.49	2.23	0.009	0.75	0.36	3.07	2.99	0.092
11-075-PTO 1	72.64	0.100	13.06	2.04	0.010	0.99	0.35	3.40	2.90	0.092
11-075-PTO 1	73.83	0.083	12.07	2.07	0.008	0.90	0.28	3.05	3.20	0.092
11-075-PTO 1	73.21	0.067	12.98	1.64	0.013	0.90	0.34	4.08	2.26	0.092
11-075-PTO 1	73.13	0.083	12.02	3.19	0.011	0.90	0.29	2.71	3.12	0.137
11-075-PTO 1	71.92	0.100	13.32	1.53	0.015	1.09	0.49	3.86	3.10	0.160
11-075-PTO 1	73.95	0.100	12.19	1.64	0.010	0.88	0.52	3.37	2.70	0.229
11-075-PTO 1	74.24	0.067	12.38	1.04	0.005	0.66	0.46	5.07	1.52	0.137
11-075-PTO 1	73.91	0.050	12.47	1.80	0.007	0.85	0.45	3.53	2.31	0.206
11-075-PTO 1	71.90	0.067	13.89	2.49	0.007	0.80	0.32	3.13	2.85	0.137
11-075-PTO 1	71.01	0.050	14.61	2.10	0.006	0.70	0.41	4.30	2.29	0.115
11-075-PTO 1	73.15	0.067	12.77	2.03	0.006	0.63	0.38	4.34	2.07	0.137
11-075-PTO 1	72.17	0.100	13.26	1.94	0.010	1.01	0.66	4.22	2.00	0.206
11-075-PTO 1	73.08	0.167	12.55	1.70	0.012	1.34	0.76	3.76	2.06	0.160
11-075-PTO 1	73.16	0.183	12.17	1.56	0.012	1.19	0.88	4.50	1.78	0.137
11-075-PTO 1	71.44	0.183	13.60	2.02	0.011	1.38	0.76	3.76	2.32	0.115
11-075-PTO 1	70.78	0.183	13.17	2.10	0.015	1.92	0.94	3.63	2.43	0.412
11-075-PTO 1	70.32	0.167	13.76	3.47	0.016	1.82	0.49	1.66	3.63	0.252
11-075-PTO 1	71.13	0.117	13.68	2.66	0.009	1.09	0.55	2.76	3.31	0.275
11-075-PTO 1	71.19	0.117	13.36	3.75	0.012	1.09	0.34	2.02	3.54	0.160
11-075-PTO 1	62.80	0.133	20.48	4.82	0.027	1.51	0.46	2.05	3.05	0.252
11-075-PTO 1	71.01	0.133	15.23	2.56	0.012	0.83	0.49	3.38	1.79	0.137
11-075-PTO 1	71.20	0.234	13.11	2.67	0.018	1.56	0.63	3.81	2.23	0.115
11-075-PTO 1	63.14	0.267	20.12	2.54	0.026	1.76	0.92	4.53	2.16	0.115
11-075-PTO 1	72.86	0.133	13.45	1.92	0.012	0.91	0.63	3.95	1.51	0.206
11-075-PTO 1	66.63	0.117	19.56	1.94	0.011	0.53	0.99	4.19	1.45	0.160
11-075-PTO 1	67.64	0.100	18.97	2.04	0.007	0.50	1.40	3.37	1.35	0.206
11-075-PTO 1	69.83	0.250	15.17	2.13	0.016	1.39	1.55	3.49	1.59	0.160
11-075-PTO 1	64.46	0.234	19.37	2.40	0.018	1.26	1.30	4.52	1.87	0.160
11-075-PTO 1	64.33	0.217	19.67	3.15	0.019	1.38	1.23	3.34	2.13	0.115
11-075-PTO 1	65.94	0.217	18.44	2.73	0.021	1.34	1.25	3.45	2.06	0.137
11-075-PTO 1	67.16	0.200	17.46	2.82	0.015	1.19	0.97	3.05	2.61	0.115
11-075-PTO 1	61.42	0.250	20.92	2.76	0.024	1.49	1.68	4.70	2.18	0.160
11-075-PTO 1	69.29	0.267	15.70	2.00	0.017	1.06	1.22	3.96	1.95	0.115
11-075-PTO 1	63.32	0.267	19.41	2.82	0.019	1.61	1.53	4.38	2.11	0.137
11-075-PTO 1	64.06	0.200	19.27	3.07	0.018	1.38	1.22	3.94	2.29	0.137
11-075-PTO 1	62.03	0.267	20.88	2.50	0.025	1.14	1.64	4.80	2.10	0.206
11-075-PTO 1	63.52	0.167	19.93	3.42	0.024	1.09	0.87	3.83	2.59	0.137
11-075-PTO 1	67.56	0.217	16.16	2.32	0.019	1.29	1.41	4.08	2.34	0.183
11-075-PTO 1	67.94	0.234	15.65	2.06	0.019	1.13	1.53	4.81	2.08	0.137
11-081 PQZ	74.99	0.083	11.83	1.72	0.006	1.26	0.31	2.84	2.28	0.183

Drill core # - Rock unit	SiO[2] mass %	TiO[2] mass %	Al[2]O[3] mass %	Fe[2]O[3] mass %	MnO mass %	MgO mass %	CaO mass %	Na[2]O mass %	K[2]O mass %	P[2]O[5] mass %
11-081 PQZ	71.94	0.133	14.25	3.95	0.010	0.66	0.24	0.77	3.40	0.160
11-081 PQZ	74.06	0.083	12.55	2.33	0.006	0.88	0.36	2.43	2.63	0.183
11-081 PQZ	72.60	0.117	12.87	2.10	0.007	0.99	0.56	3.44	2.59	0.229
11-081 PQZ	74.79	0.133	11.28	2.13	0.011	0.91	0.42	3.69	1.95	0.183
11-081 PQZ	74.66	0.117	11.28	2.69	0.007	0.93	0.31	1.83	3.49	0.183
11-081 PQZ	73.81	0.133	11.51	3.50	0.006	0.86	0.32	1.29	3.85	0.206
11-081 PQZ	70.80	0.150	14.61	3.35	0.007	0.81	0.28	1.43	3.89	0.183
11-081 PQZ	70.83	0.133	14.23	4.26	0.008	0.73	0.27	0.77	4.12	0.160
11-081 PQZ	71.39	0.133	13.15	5.28	0.009	0.41	0.25	0.36	4.32	0.183
11-081 PQZ	72.91	0.133	13.09	3.33	0.007	0.70	0.35	0.85	3.99	0.137
11-081 PQZ	73.31	0.133	11.75	3.36	0.006	0.71	0.21	1.37	4.51	0.137
11-081 PQZ	72.71	0.133	12.11	2.89	0.006	0.96	0.24	1.48	4.83	0.137
11-081 PQZ	69.10	0.133	15.95	3.87	0.006	0.65	0.39	2.04	3.20	0.160
11-081 PQZ	73.20	0.117	11.36	4.86	0.004	0.61	0.27	0.88	4.07	0.137
11-081 PQZ	70.55	0.133	13.87	2.76	0.007	0.95	0.31	2.52	4.25	0.160
11-081 PQZ	70.08	0.133	15.19	3.25	0.007	0.90	0.31	1.56	3.91	0.160
11-081 PQZ	71.02	0.117	14.32	3.16	0.005	0.83	0.28	1.56	4.05	0.160
11-081 PQZ	71.76	0.100	14.02	2.66	0.005	0.88	0.25	2.05	3.61	0.160
11-081 PQZ	71.96	0.100	13.55	1.84	0.007	1.08	0.38	3.06	3.36	0.160
11-081 PQZ	68.04	0.117	17.01	2.52	0.007	1.13	0.42	1.97	4.12	0.183
11-081 PQZ	69.54	0.117	16.48	1.84	0.009	0.85	0.28	2.53	3.70	0.160
11-081 PQZ	69.10	0.100	15.91	1.97	0.010	1.16	0.48	3.06	3.53	0.183
11-081 PQZ	69.01	0.117	15.44	2.77	0.007	1.18	0.36	2.56	3.87	0.183
11-081 PQZ	67.05	0.133	17.40	4.09	0.008	0.93	0.32	0.85	4.55	0.160
11-081 PQZ	69.87	0.133	15.17	3.90	0.005	1.24	0.38	0.35	4.29	0.160
11-081 PQZ	73.59	0.133	13.00	2.64	0.005	1.21	0.18	0.31	4.29	0.137
11-081 PQZ	73.83	0.133	13.09	2.70	0.006	0.86	0.29	0.27	4.14	0.160
11-081 PQZ	72.12	0.133	13.87	2.75	0.006	1.11	0.48	0.80	4.08	0.160
11-081 PQZ	68.01	0.133	16.97	3.92	0.005	0.98	0.36	0.38	4.59	0.160
11-081 PQZ	67.29	0.133	17.76	2.95	0.008	1.14	0.46	1.19	4.41	0.160
11-081 PQZ	71.87	0.100	13.70	2.03	0.007	1.08	1.43	1.85	3.30	0.137
11-081 PQZ	71.69	0.117	13.66	2.46	0.009	1.34	0.77	1.58	3.71	0.160
11-081 PQZ	72.00	0.117	14.04	2.54	0.013	1.19	0.35	1.50	3.54	0.206
11-081 PQZ	71.83	0.117	13.89	1.97	0.007	1.41	0.36	2.28	3.47	0.160
10-054 PQZ	69.83	0.117	16.12	3.17	0.009	0.93	0.29	1.09	3.76	0.183
10-054 PQZ	69.39	0.117	16.08	3.59	0.014	1.04	0.34	0.82	3.90	0.206
10-054 PQZ	72.64	0.100	13.28	3.73	0.009	0.63	0.28	0.70	3.96	0.160
10-054 PQZ	70.05	0.117	15.02	3.96	0.010	0.93	0.29	1.01	3.90	0.206
10-054 PQZ	70.35	0.100	15.72	3.25	0.010	0.83	0.34	1.36	3.38	0.160
10-054 PQZ	69.28	0.100	16.10	3.53	0.010	0.85	0.31	1.46	3.73	0.137
10-054 PQZ	69.87	0.117	15.87	3.09	0.007	0.93	0.32	1.44	3.70	0.160
10-054 PQZ	70.80	0.100	14.59	3.17	0.010	0.96	0.39	2.56	2.78	0.137
10-054 PQZ	76.38	0.117	10.24	2.62	0.007	0.71	0.20	1.51	3.60	0.115
10-054 PQZ	69.62	0.100	15.42	2.60	0.008	0.88	1.51	1.51	3.76	0.092
10-054 PQZ	69.75	0.100	15.46	4.07	0.009	0.99	0.29	1.20	3.48	0.137
10-054 PQZ	70.51	0.100	15.10	2.16	0.009	1.11	0.59	2.94	2.78	0.206
10-054 PQZ	71.75	0.100	14.25	2.04	0.009	1.16	0.49	2.83	2.71	0.160
10-054 PQZ	70.06	0.100	15.57	2.67	0.010	1.09	0.43	2.16	3.26	0.137
10-054 PQZ	71.60	0.100	14.64	1.64	0.007	1.08	0.43	3.10	2.71	0.183
10-054 PQZ	69.22	0.100	15.27	2.69	0.009	1.01	1.74	1.90	3.43	0.137
10-054 PQZ	72.21	0.117	13.59	2.89	0.009	1.23	0.31	1.67	3.37	0.115
10-054 PQZ	74.02	0.100	12.53	2.12	0.008	1.13	0.32	2.12	3.00	0.160
10-054 PQZ	69.78	0.117	15.61	3.46	0.008	0.90	0.39	1.66	3.40	0.183
10-054 PQZ	71.43	0.117	13.53	2.54	0.013	1.51	0.38	3.09	2.81	0.092
10-054 PQZ	70.01	0.117	15.29	2.40	0.007	1.53	0.32	2.62	3.12	0.092
10-054 PQZ	69.67	0.100	15.29	3.09	0.011	1.33	0.35	2.39	3.17	0.115
10-054 PQZ	69.74	0.100	15.63	3.06	0.009	1.14	0.39	1.86	3.41	0.160
10-054 PQZ	69.62	0.100	15.82	2.67	0.008	0.99	0.49	2.32	3.25	0.229
10-054 PQZ	69.66	0.100	15.80	3.02	0.007	0.81	0.50	1.62	3.71	0.275
10-054 PQZ	69.60	0.100	15.89	2.97	0.008	0.86	0.41	1.90	3.58	0.183
10-054 PQZ	69.36	0.117	15.51	3.49	0.007	0.80	0.49	1.85	3.70	0.183
10-054 PQZ	70.10	0.100	15.34	2.26	0.007	1.04	0.46	2.94	3.04	0.206
10-054 PQZ	70.11	0.117	15.65	2.63	0.007	0.98	0.42	1.95	3.46	0.183
10-054 PQZ	70.07	0.100	15.83	2.85	0.008	1.09	0.34	1.24	3.83	0.137
10-054 PQZ	67.41	0.117	16.63	3.53	0.024	1.08	0.55	2.21	3.82	0.137
10-054 PQZ	69.83	0.117	15.36	3.72	0.008	0.80	0.45	0.93	4.13	0.160
10-054 PQZ	70.69	0.117	14.98	2.87	0.007	0.99	0.39	1.73	3.55	0.160
10-054 PQZ	70.14	0.117	15.19	3.80	0.007	0.75	0.43	1.04	3.84	0.183

Drill core # - Rock unit	SiO[2] mass %	TiO[2] mass %	Al[2]O[3] mass %	Fe[2]O[3] mass %	MnO mass %	MgO mass %	CaO mass %	Na[2]O mass %	K[2]O mass %	P[2]O[5] mass %
10-054 PQZ	68.67	0.117	15.78	3.90	0.008	0.85	0.39	1.82	3.78	0.183
CEF										
11-097 K-altered	54.88	0.384	21.67	7.69	0.023	2.19	2.00	4.19	2.57	0.229
11-097 K-altered	53.12	0.450	22.26	7.88	0.026	2.69	2.63	3.19	3.42	0.160
11-097 K-altered	58.29	0.484	17.08	9.26	0.034	2.12	2.71	3.07	2.55	0.206
11-097 K-altered	59.44	0.367	17.10	7.95	0.022	1.89	1.76	4.33	2.73	0.229
11-097 K-altered	55.21	0.400	21.71	6.85	0.024	1.99	2.01	4.31	3.08	0.229
11-097 K-altered	54.42	0.400	21.07	8.48	0.019	1.86	2.24	4.41	2.71	0.229
11-097 K-altered	52.59	0.400	23.66	7.31	0.018	1.76	2.38	4.93	2.55	0.229
11-097 K-altered	52.01	0.434	22.86	8.46	0.028	2.09	1.76	4.74	3.20	0.229
11-097 K-altered	59.60	0.367	18.86	7.13	0.016	1.41	1.87	3.96	2.37	0.229
11-097 K-altered	57.27	0.384	19.65	7.85	0.018	1.77	2.11	3.68	2.88	0.206
11-097 K-altered	58.17	0.384	18.80	8.24	0.021	1.94	1.67	3.80	2.60	0.206
11-097 K-altered	48.70	0.434	24.53	10.52	0.027	2.30	1.87	3.75	3.46	0.229
11-097 K-altered	53.35	0.434	22.37	8.45	0.024	2.27	2.35	3.19	3.17	0.206
11-097 K-altered	52.81	0.450	22.71	8.56	0.024	2.39	2.49	3.26	2.92	0.206
11-097 K-altered	51.99	0.417	23.79	8.24	0.022	2.27	2.20	3.87	2.81	0.229
11-097 K-altered	49.32	0.434	25.11	8.62	0.023	2.62	2.25	3.30	3.94	0.206
11-097 K-altered	57.38	0.367	19.54	7.93	0.018	1.77	1.96	3.55	3.08	0.229
11-097 K-altered	58.00	0.367	18.35	8.54	0.020	1.77	2.10	3.53	2.94	0.206
11-097 K-altered	58.40	0.384	18.27	8.91	0.021	1.76	1.97	3.73	2.17	0.206
11-097 K-altered	54.78	0.484	19.41	9.41	0.026	2.22	2.84	3.64	2.79	0.229
11-097 K-altered	51.10	0.450	23.00	9.44	0.029	2.21	2.76	3.71	2.94	0.206
11-097 K-altered	53.08	0.550	21.41	9.25	0.029	2.44	3.39	3.15	2.32	0.206
11-097 K-altered	59.10	0.450	18.40	7.33	0.024	2.09	2.77	2.87	2.60	0.183
11-097 K-altered	62.09	0.467	15.27	6.71	0.046	1.38	4.17	3.15	2.36	0.183
11-097 K-altered	54.76	0.434	21.56	8.06	0.023	1.96	2.32	3.69	2.81	0.206
11-097 K-altered	56.56	0.400	21.33	6.52	0.020	1.77	2.48	4.03	2.53	0.183
11-097 K-altered	56.27	0.434	20.71	7.11	0.020	1.87	2.36	4.03	2.81	0.206
11-097 K-altered	51.62	0.417	22.98	8.44	0.022	2.12	2.27	4.34	3.42	0.206
11-097 K-altered	50.28	0.384	24.15	8.92	0.020	2.11	2.29	3.83	3.66	0.183
11-097 K-altered	61.52	0.334	18.71	6.13	0.018	1.77	2.07	2.93	2.20	0.137
11-097 K-altered	65.69	0.434	13.74	6.09	0.020	2.40	2.63	2.62	2.05	0.160
11-097 K-altered	62.51	0.534	15.36	6.43	0.024	2.49	3.13	2.78	2.39	0.183
11-097 K-altered	63.73	0.517	14.98	5.85	0.025	2.30	3.08	3.14	2.01	0.183
11-097 K-altered	64.40	0.450	15.00	5.40	0.022	2.12	2.76	3.52	1.94	0.206
11-097 K-altered	61.35	0.500	15.91	6.59	0.022	2.60	2.76	3.19	2.71	0.183
11-097 K-altered	62.46	0.534	14.85	7.26	0.024	2.72	3.20	2.29	2.31	0.160
11-097 K-altered	62.43	0.517	14.96	6.93	0.025	2.49	3.48	2.66	2.14	0.183
11-097 K-altered	63.34	0.467	14.95	6.55	0.023	2.19	3.40	2.87	1.86	0.183
11-097 K-altered	65.76	0.417	14.59	4.98	0.020	1.89	3.30	3.05	1.64	0.183
11-097 K-altered	64.91	0.384	14.53	6.36	0.021	1.76	2.97	3.05	1.66	0.183
11-097 K-altered	64.09	0.484	14.96	5.85	0.027	2.16	2.88	2.91	2.28	0.183
11-097 K-altered	64.74	0.467	14.27	6.43	0.022	1.99	2.77	3.09	1.89	0.160
11-097 K-altered	64.86	0.384	14.98	5.59	0.022	1.79	2.91	3.48	1.63	0.183
11-097 K-altered	65.74	0.417	14.34	5.25	0.019	1.84	2.78	3.50	1.75	0.183
11-097 K-altered	64.28	0.467	14.45	6.45	0.026	2.21	2.66	2.84	2.28	0.160
11-097 K-altered	65.99	0.400	14.02	5.86	0.021	1.86	2.62	3.11	1.78	0.160
11-097 K-altered	65.53	0.400	14.00	6.10	0.022	1.92	2.71	3.30	1.66	0.160
11-097 K-altered	64.68	0.467	13.94	6.48	0.023	2.19	3.22	3.03	1.64	0.160
11-097 K-altered	61.88	0.534	15.06	7.18	0.026	2.39	3.68	3.11	1.81	0.160
11-097 K-altered	63.15	0.484	14.74	6.68	0.024	2.40	3.22	3.02	1.93	0.183
11-097 K-altered	65.95	0.417	14.70	5.36	0.022	2.22	2.21	2.37	2.41	0.160
11-097 K-altered	68.43	0.400	13.91	4.82	0.021	2.16	1.71	1.44	2.81	0.137
11-097 K-altered	67.25	0.500	14.32	5.06	0.030	2.44	2.49	0.89	2.71	0.137
11-097 K-altered	64.80	0.434	15.29	6.13	0.026	2.39	2.21	1.83	2.55	0.160
11-097 K-altered	63.62	0.500	15.97	5.96	0.027	1.92	2.70	2.55	2.40	0.183
11-097 K-altered	64.80	0.484	14.76	5.78	0.043	1.92	2.83	2.88	2.14	0.183
11-097 K-altered	66.35	0.484	14.74	4.90	0.021	2.32	2.22	2.21	2.41	0.160
11-097 K-altered	64.55	0.567	15.36	5.10	0.022	2.82	2.45	1.93	2.87	0.160
11-097 K-altered	63.37	0.550	15.29	5.40	0.025	2.39	3.46	3.34	1.84	0.160
11-097 K-altered	67.06	0.500	13.60	4.55	0.022	2.01	3.23	3.17	1.53	0.160
11-097 K-altered	64.49	0.500	14.83	5.28	0.022	1.77	3.36	3.86	1.53	0.183
11-097 K-altered	61.09	0.634	15.68	6.46	0.025	2.17	3.90	3.98	1.70	0.183
11-097 K-altered	64.20	0.550	13.85	6.49	0.021	2.14	3.13	3.56	1.72	0.160
11-097 K-altered	60.76	0.617	15.13	7.39	0.024	2.90	3.60	3.17	2.07	0.160
11-097 K-altered	61.88	0.567	14.62	7.09	0.024	3.13	2.87	2.90	2.58	0.160

Drill core # - Rock unit	SiO[2] mass %	TiO[2] mass %	Al[2]O[3] mass %	Fe[2]O[3] mass %	MnO mass %	MgO mass %	CaO mass %	Na[2]O mass %	K[2]O mass %	P[2]O[5] mass %
11-097 K-altered	61.35	0.584	15.46	6.59	0.025	2.92	3.13	3.21	2.40	0.160
11-097 K-altered	64.81	0.500	13.19	6.99	0.024	2.95	1.79	3.14	2.22	0.206
11-097 K-altered	62.40	0.484	15.38	6.51	0.024	3.00	1.92	3.64	2.24	0.229
11-097 K-altered	61.36	0.450	17.21	6.41	0.045	2.95	1.67	3.14	2.39	0.206
11-078 SCC- altered	65.83	0.183	17.97	2.80	0.011	3.60	0.42	0.66	4.12	0.229
11-078 SCC- altered	66.79	0.167	18.06	2.54	0.008	3.12	0.41	0.77	3.76	0.206
11-078 SCC- altered	66.62	0.183	18.06	3.12	0.012	3.22	0.45	0.92	3.02	0.229
11-078 SCC- altered	69.40	0.150	16.40	2.75	0.009	3.10	0.34	0.63	2.84	0.206
11-078 SCC- altered	69.39	0.167	16.27	2.53	0.007	3.12	0.35	0.49	3.30	0.206
11-078 SCC- altered	67.74	0.167	17.23	2.40	0.006	3.12	0.42	0.61	3.98	0.160
11-078 SCC- altered	65.99	0.167	18.21	2.75	0.006	3.07	0.39	0.57	4.49	0.183
11-078 SCC- altered	66.81	0.183	17.84	3.46	0.009	2.35	0.29	0.53	4.17	0.183
11-078 SCC- altered	68.03	0.167	17.42	2.62	0.006	2.92	0.27	0.46	3.78	0.160
11-078 SCC- altered	70.03	0.183	16.55	2.37	0.005	2.24	0.28	0.54	3.45	0.183
11-078 SCC- altered	70.57	0.150	16.27	2.47	0.005	2.77	0.32	0.32	2.78	0.160
11-078 SCC- altered	70.24	0.150	15.72	2.64	0.006	3.20	0.32	0.55	2.81	0.183
11-078 SCC- altered	69.40	0.167	16.21	2.17	0.006	3.03	0.34	0.36	3.95	0.183
11-078 SCC- altered	69.69	0.150	17.04	2.67	0.005	1.96	0.35	0.51	3.24	0.206
11-078 SCC- altered	75.97	0.150	14.02	1.94	0.005	1.38	0.29	0.32	1.58	0.160
11-078 SCC- altered	75.02	0.150	11.51	2.14	0.007	2.27	0.43	0.24	3.79	0.252
11-078 SCC- altered	72.79	0.200	13.68	2.75	0.009	2.62	0.43	0.61	2.45	0.298
11-078 SCC- altered	77.19	0.250	8.37	2.73	0.014	2.42	1.32	1.00	2.22	0.321
11-078 SCC- altered	72.22	0.183	14.10	2.85	0.005	1.87	1.46	0.28	2.57	0.298
11-078 SCC- altered	68.90	0.350	14.74	4.06	0.025	2.74	0.73	1.06	2.85	0.367
11-078 SCC- altered	72.03	0.217	13.77	2.36	0.013	2.30	0.45	0.50	3.88	0.298
11-078 SCC- altered	72.24	0.217	13.09	2.54	0.012	2.50	0.48	0.66	3.81	0.275
11-078 SCC- altered	74.71	0.150	12.92	2.85	0.005	1.79	0.35	0.23	2.59	0.229
11-078 SCC- altered	70.03	0.133	15.99	2.39	0.005	2.04	1.89	0.28	2.84	0.229
11-078 SCC- altered	76.11	0.117	12.49	3.05	0.005	0.58	0.48	0.20	2.48	0.321
11-078 SCC- altered	70.68	0.150	13.23	2.93	0.024	3.60	1.90	0.86	2.19	0.252
11-078 SCC- altered	72.80	0.133	11.51	2.16	0.017	2.98	2.38	0.93	2.69	0.229
11-078 SCC- altered	72.77	0.133	13.64	2.02	0.014	2.49	1.02	1.23	2.24	0.275
11-078 SCC- altered	76.03	0.100	12.75	1.79	0.009	1.26	1.13	0.67	1.78	0.298
11-078 SCC- altered	68.73	0.167	17.74	2.09	0.009	1.28	0.27	0.61	4.81	0.137
11-078 SCC- altered	77.27	0.117	11.73	1.80	0.009	1.63	0.14	0.32	2.76	0.046
11-078 SCC- altered	74.21	0.117	12.60	2.43	0.007	2.42	1.65	0.28	1.92	0.183
11-078 SCC- altered	73.33	0.150	12.49	2.04	0.006	3.02	0.27	0.26	4.08	0.183
11-078 SCC- altered	72.44	0.150	13.83	2.02	0.011	2.40	0.36	0.27	4.11	0.229
11-078 SCC- altered	75.64	0.150	12.00	1.67	0.007	1.13	0.10	0.58	4.43	0.115
11-078 SCC- altered	72.39	0.150	14.02	2.14	0.007	2.06	0.31	0.19	4.40	0.160
11-078 SCC- altered	66.49	0.200	16.97	2.83	0.010	3.07	1.34	0.43	4.20	0.275
11-078 SCC- altered	70.56	0.167	15.23	2.24	0.006	2.57	0.34	0.23	4.25	0.229
11-078 SCC- altered	68.32	0.150	16.27	3.02	0.014	2.37	0.71	0.26	4.51	0.206
11-078 SCC- altered	71.20	0.167	14.40	2.36	0.017	2.21	0.36	0.26	4.65	0.206
11-078 SCC- altered	65.85	0.217	20.48	2.30	0.006	1.76	0.38	0.28	4.23	0.321
11-078 SCC- altered	58.02	0.217	26.30	3.00	0.007	2.40	0.42	0.30	4.95	0.206
11-078 SCC- altered	55.60	0.183	28.34	3.30	0.007	2.32	0.35	0.20	5.36	0.160
11-078 SCC- altered	74.84	0.200	10.68	1.86	0.004	2.02	1.05	0.23	4.81	0.137
11-078 SCC- altered	57.81	0.167	28.34	3.03	0.008	1.69	0.35	0.18	4.00	0.252
11-078 SCC- altered	59.17	0.167	28.34	2.23	0.007	1.28	0.59	0.20	3.64	0.206
11-078 SCC- altered	56.98	0.167	28.34	2.54	0.009	1.82	1.01	0.20	4.49	0.252
11-078 SCC- altered	60.27	0.150	26.74	2.26	0.006	1.44	0.25	0.18	4.35	0.183
11-078 SCC- altered	57.79	0.167	26.70	3.75	0.006	2.01	0.32	0.20	4.69	0.206
11-078 SCC- altered	58.90	0.167	28.34	2.83	0.006	0.99	0.43	0.19	3.69	0.275
11-097 SCC- altered	71.12	0.250	11.32	3.80	0.018	4.46	0.95	1.52	2.22	0.160
11-097 SCC- altered	69.13	0.234	12.70	4.42	0.022	4.46	1.22	1.63	1.86	0.160
11-097 SCC- altered	68.90	0.250	12.60	4.70	0.025	4.38	1.39	1.67	1.77	0.137
11-097 SCC- altered	70.75	0.284	11.36	4.17	0.021	3.73	1.68	1.77	1.90	0.160
11-097 SCC- altered	67.45	0.183	14.62	3.49	0.013	3.45	0.60	3.37	2.48	0.160
11-097 SCC- altered	69.73	0.250	12.13	4.46	0.023	4.21	1.48	1.69	1.71	0.137
11-097 SCC- altered	64.62	0.284	15.29	5.00	0.026	4.59	1.71	1.95	2.19	0.160
11-097 SCC- altered	60.47	0.267	20.84	5.38	0.026	2.94	1.87	1.54	2.34	0.160
11-097 SCC- altered	71.89	0.234	12.17	4.30	0.019	2.52	1.22	1.23	2.11	0.137
11-097 SCC- altered	70.94	0.300	12.51	4.33	0.020	2.49	1.50	1.44	2.13	0.160
11-097 SCC- altered	68.08	0.267	14.25	4.68	0.023	2.98	1.76	1.50	2.13	0.160
11-097 SCC- altered	62.21	0.267	19.20	5.15	0.026	3.08	2.03	1.52	2.18	0.160
11-097 SCC- altered	67.21	0.267	15.17	4.80	0.022	2.94	1.76	1.43	2.06	0.160
11-097 SCC- altered	66.42	0.250	16.06	4.60	0.020	2.85	1.76	1.55	2.17	0.137

Drill core # - Rock unit	SiO[2] mass %	TiO[2] mass %	Al[2]O[3] mass %	Fe[2]O[3] mass %	MnO mass %	MgO mass %	CaO mass %	Na[2]O mass %	K[2]O mass %	P[2]O[5] mass %
11-097 SCC- altered	61.97	0.250	19.48	5.15	0.019	2.98	1.78	1.60	2.43	0.160
11-097 SCC- altered	67.58	0.267	14.59	4.80	0.020	2.90	1.78	1.42	2.31	0.160
11-097 SCC- altered	68.11	0.284	16.40	5.30	0.016	1.48	1.16	0.92	2.00	0.160
11-097 SCC- altered	64.89	0.267	17.91	4.70	0.020	2.90	1.50	1.31	2.17	0.160
11-097 SCC- altered	66.01	0.267	16.70	4.70	0.019	2.85	1.54	1.27	2.30	0.160
11-097 phyllic altered	75.62	0.167	12.75	2.82	0.009	0.36	0.46	0.77	2.72	0.137
11-097 phyllic altered	77.95	0.234	9.96	3.16	0.004	0.50	0.42	0.71	2.77	0.115
11-097 phyllic altered	73.52	0.284	12.98	3.47	0.008	1.18	0.53	0.85	2.87	0.137
11-097 phyllic altered	76.05	0.250	9.45	3.57	0.016	2.65	0.56	0.97	2.17	0.137
11-097 phyllic altered	69.48	0.284	13.40	5.45	0.019	2.84	0.70	1.19	2.34	0.137
11-097 phyllic altered	67.97	0.317	13.79	6.63	0.021	2.75	0.59	1.09	2.49	0.160
11-097 phyllic altered	68.71	0.267	14.06	5.42	0.019	3.02	0.57	1.19	2.41	0.160
11-097 phyllic altered	70.70	0.267	12.81	4.95	0.018	2.65	0.69	1.50	2.08	0.160
11-097 phyllic altered	70.63	0.300	12.62	5.06	0.020	2.62	0.81	1.52	2.07	0.160
11-097 phyllic altered	69.02	0.300	13.59	5.26	0.021	2.62	0.85	1.86	2.14	0.160
11-097 phyllic altered	68.28	0.300	14.32	5.02	0.018	2.69	1.11	1.85	2.08	0.160
11-097 phyllic altered	69.55	0.300	12.98	5.39	0.021	2.47	1.25	1.87	1.83	0.160
11-097 phyllic altered	67.91	0.317	14.55	5.29	0.034	2.69	1.18	1.73	1.98	0.160
11-097 phyllic altered	69.24	0.317	13.21	4.96	0.023	2.72	1.41	1.79	1.99	0.160
11-097 phyllic altered	69.07	0.350	13.47	5.08	0.024	2.54	1.43	1.77	1.94	0.160
11-097 phyllic altered	63.30	0.350	16.63	5.86	0.028	3.05	2.76	1.91	1.77	0.160
11-097 phyllic altered	65.35	0.350	14.55	6.29	0.029	2.87	2.88	1.75	1.59	0.160
11-097 phyllic altered	67.63	0.367	13.98	5.56	0.027	2.75	2.39	1.39	1.57	0.160
11-097 phyllic altered	63.48	0.367	16.02	6.28	0.030	3.27	2.95	1.52	1.72	0.183
11-097 phyllic altered	64.41	0.367	15.17	6.32	0.028	3.12	2.42	1.86	1.95	0.183
11-097 phyllic altered	66.23	0.367	14.51	5.90	0.027	2.57	1.99	1.90	2.12	0.206
11-097 phyllic altered	66.72	0.450	13.57	5.85	0.029	3.00	2.63	1.50	1.90	0.183
11-097 phyllic altered	66.19	0.350	14.27	6.08	0.031	3.10	2.01	1.54	2.07	0.183
11-097 phyllic altered	65.42	0.267	15.38	5.78	0.032	2.82	2.24	1.59	2.12	0.183
11-097 phyllic altered	63.77	0.284	16.44	6.15	0.031	2.64	2.27	1.64	2.42	0.183
11-097 phyllic altered	65.87	0.234	15.48	5.06	0.026	2.70	2.70	1.73	1.84	0.183

Supplementary Sheet 3 Full raw dataset for U–Pb age dating

a) Granite dataset

(1 marks data with probability of concordance < 0.01)

(* For host rocks and basement, probability of concordance < 0.1 and > 0.01, and error > 10.0 % and < 10 % are included in calculation)

	Sample Name	Th/U	207Pb/206Pb		Error 2σ	206Pb/238U		Error 2σ	207Pb/235U		Error 2σ	238U-206Pb age (Ma)		Error 2σ	235U-207Pb age (Ma)		Error 2σ
*	15IA03-1	0.56	0.0607	±	0.0051	0.0538	±	0.0013	0.450	±	0.039	337.6	±	8.4	377.5	±	32.8
	15IA03-2	0.57	0.0563	±	0.0063	0.0529	±	0.0016	0.410	±	0.048	332.1	±	10.0	349.0	±	40.6
	15IA03-3	0.45	0.0534	±	0.0032	0.0529	±	0.0011	0.390	±	0.025	332.3	±	6.6	334.2	±	21.2
*	15IA03-4	0.37	0.0560	±	0.0027	0.0481	±	0.0009	0.371	±	0.019	302.6	±	5.5	320.5	±	16.4
	15IA03-5	0.39	0.0540	±	0.0045	0.0547	±	0.0013	0.407	±	0.035	343.2	±	8.2	346.8	±	29.8
1	15IA03-6	0.47	0.0626	±	0.0033	0.0495	±	0.0010	0.428	±	0.024	311.6	±	6.1	361.6	±	20.6
1	15IA03-7	0.31	0.0603	±	0.0029	0.0519	±	0.0010	0.431	±	0.022	325.9	±	6.0	363.9	±	18.6
1	15IA03-8	0.42	0.0682	±	0.0045	0.0618	±	0.0014	0.581	±	0.040	386.3	±	8.8	464.9	±	32.2
	15IA03-9	0.59	0.0532	±	0.0049	0.0539	±	0.0014	0.396	±	0.038	338.7	±	8.8	338.8	±	32.1
	15IA03-10	0.48	0.0581	±	0.0060	0.0553	±	0.0016	0.442	±	0.047	346.7	±	10.0	371.9	±	39.7
*	15IA03-11	0.62	0.0594	±	0.0051	0.0497	±	0.0013	0.407	±	0.036	312.7	±	8.0	346.8	±	31.1
	15IA03-12	0.54	0.0563	±	0.0047	0.0509	±	0.0013	0.395	±	0.035	320.1	±	8.0	338.0	±	29.6
1	15IA03-13	0.20	0.0679	±	0.0027	0.0202	±	0.0004	0.189	±	0.008	129.1	±	2.4	176.2	±	7.8
1	15IA03-14	0.63	0.0750	±	0.0060	0.0383	±	0.0010	0.396	±	0.034	242.0	±	6.4	338.6	±	28.7
	15IA03-15	0.68	0.0544	±	0.0035	0.0516	±	0.0011	0.387	±	0.026	324.4	±	6.9	332.5	±	22.5
	15IA03-16	0.30	0.0599	±	0.0034	0.0881	±	0.0018	0.727	±	0.044	544.2	±	11.2	555.1	±	33.5
1	15IA03-17	0.70	0.1079	±	0.0047	0.0397	±	0.0009	0.591	±	0.029	251.1	±	5.5	471.5	±	22.8
1	IA12-1	0.32	0.0619	±	0.0045	0.0313	±	0.0008	0.267	±	0.021	198.4	±	4.9	240.2	±	18.5
	IA12-2	0.35	0.0521	±	0.0049	0.0366	±	0.0010	0.263	±	0.026	232.0	±	6.4	237.3	±	23.5
1	IA12-3	0.28	0.0561	±	0.0027	0.0375	±	0.0008	0.290	±	0.015	237.6	±	4.9	258.8	±	13.7
1	IA12-4	0.50	0.0756	±	0.0045	0.0321	±	0.0007	0.334	±	0.021	203.4	±	4.7	292.8	±	18.6
	IA12-5	0.50	0.0553	±	0.0065	0.0335	±	0.0011	0.255	±	0.031	212.4	±	6.8	230.9	±	28.3
1	IA12-6	0.66	0.0602	±	0.0030	0.0432	±	0.0009	0.359	±	0.019	272.9	±	5.8	311.5	±	16.9
1	IA12-7	0.27	0.0607	±	0.0024	0.0366	±	0.0007	0.306	±	0.014	231.6	±	4.6	271.3	±	12.0
	IA12-8	0.43	0.0539	±	0.0056	0.0448	±	0.0013	0.333	±	0.036	282.6	±	8.5	291.9	±	31.5
1	IA12-9	0.24	0.0578	±	0.0040	0.0339	±	0.0008	0.270	±	0.020	214.7	±	5.3	242.7	±	17.6
*	IA12-10	0.32	0.0555	±	0.0027	0.0423	±	0.0009	0.324	±	0.017	267.0	±	5.8	284.7	±	15.1
1	IA12-11	0.81	0.0652	±	0.0057	0.0434	±	0.0012	0.390	±	0.036	274.2	±	7.8	334.6	±	31.0
1	IA12-12	0.18	0.0753	±	0.0036	0.0262	±	0.0006	0.272	±	0.014	166.6	±	3.7	244.2	±	13.0
*	IA12-13	0.33	0.0546	±	0.0028	0.0366	±	0.0008	0.276	±	0.015	231.9	±	5.1	247.4	±	13.6
1	IA12-14	0.45	0.0596	±	0.0031	0.0457	±	0.0010	0.376	±	0.021	288.2	±	6.4	323.9	±	18.1

	Sample Name	Th/U	207Pb/206Pb		Error 2σ	206Pb/238U		Error 2σ	207Pb/235U		Error 2σ	238U-206Pb age (Ma)		Error 2σ	235U-207Pb age (Ma)		Error 2σ
1	IA12-15	0.44	0.0858	±	0.0035	0.0160	±	0.0003	0.189	±	0.009	102.1	±	2.2	175.7	±	8.1
	IA12-16	0.54	0.0505	±	0.0042	0.0507	±	0.0012	0.353	±	0.030	318.7	±	7.3	306.8	±	26.2
*	IA12-17	0.49	0.0550	±	0.0030	0.0406	±	0.0008	0.308	±	0.018	256.6	±	4.9	272.6	±	15.8
1	IA12-18	0.45	0.0562	±	0.0030	0.0337	±	0.0006	0.261	±	0.015	213.4	±	4.0	235.4	±	13.5
1	IA12-19	1.74	0.0613	±	0.0029	0.0445	±	0.0008	0.376	±	0.019	280.6	±	5.1	324.1	±	16.4
1	IA12-20	0.43	0.0649	±	0.0026	0.0325	±	0.0006	0.291	±	0.013	205.9	±	3.6	259.0	±	11.5
	IA12-21	0.26	0.0529	±	0.0036	0.0388	±	0.0008	0.284	±	0.020	245.7	±	5.1	253.5	±	17.9
	IA12-22	0.49	0.0520	±	0.0034	0.0542	±	0.0011	0.388	±	0.026	340.0	±	6.9	332.9	±	22.5
	IA12-23	0.60	0.0550	±	0.0053	0.0480	±	0.0013	0.364	±	0.036	302.1	±	7.9	314.9	±	31.4
	IA68-1	0.70	0.0539	±	0.0024	0.0539	±	0.0011	0.401	±	0.020	338.3	±	6.8	342.2	±	16.7
1	IA68-2	0.46	0.0581	±	0.0030	0.0505	±	0.0011	0.404	±	0.022	317.4	±	6.7	344.7	±	19.1
*	IA68-3	0.59	0.0566	±	0.0031	0.0518	±	0.0011	0.404	±	0.024	325.7	±	7.0	344.8	±	20.2
1	IA68-4	0.33	0.0614	±	0.0042	0.0533	±	0.0013	0.451	±	0.033	335.0	±	8.1	378.3	±	27.7
	IA68-5	0.48	0.0545	±	0.0038	0.0542	±	0.0013	0.407	±	0.030	340.1	±	8.0	346.6	±	25.3
1	IA68-6	0.50	0.0745	±	0.0028	0.0527	±	0.0010	0.541	±	0.023	331.1	±	6.6	439.4	±	18.5
1	IA68-7	0.57	0.0659	±	0.0029	0.0517	±	0.0011	0.470	±	0.022	325.0	±	6.6	391.2	±	18.7
1	IA68-8	0.88	0.0600	±	0.0033	0.0480	±	0.0010	0.396	±	0.024	301.9	±	6.6	339.1	±	20.3
*	IA68-9	0.51	0.0571	±	0.0033	0.0476	±	0.0009	0.375	±	0.023	300.1	±	5.7	323.3	±	19.5
	IA68-10	0.68	0.0507	±	0.0034	0.0509	±	0.0010	0.356	±	0.025	320.2	±	6.4	309.5	±	21.4
*	IA68-11	0.69	0.0556	±	0.0026	0.0494	±	0.0009	0.379	±	0.019	310.7	±	5.4	326.1	±	16.5
	IA68-12	0.52	0.0565	±	0.0050	0.0517	±	0.0013	0.403	±	0.037	324.8	±	8.0	343.7	±	31.9
	IA68-13	0.64	0.0528	±	0.0028	0.0506	±	0.0009	0.368	±	0.020	318.0	±	5.7	318.5	±	17.6
	IA68-14	0.54	0.0535	±	0.0062	0.0526	±	0.0016	0.388	±	0.047	330.3	±	9.8	332.9	±	40.1
1	IA68-15	0.68	0.0858	±	0.0070	0.0457	±	0.0012	0.541	±	0.046	288.2	±	7.6	439.2	±	37.4
	IA68-16	0.24	0.0553	±	0.0040	0.0516	±	0.0011	0.394	±	0.030	324.5	±	7.0	337.1	±	25.5

b) CEF dataset

(1 marks data with probability of concordance < 0.01)

(* For host rocks and basement, probability of concordance < 0.1 and > 0.01, and error > 10.0 % and < 10 % are included in calculation)

	Sample Name	Th/U	207Pb/206Pb		Error 2σ	206Pb/238U		Error 2σ	207Pb/235U		Error 2σ	238U-206Pb age (Ma)		Error 2σ	235U-207Pb age (Ma)		Error 2σ
1	15IA01-1	0.34	0.0642	±	0.0025	0.0536	±	0.0010	0.475	±	0.020	336.9	±	6.2	394.5	±	16.9
*	15IA01-2	0.53	0.0686	±	0.0176	0.0124	±	0.0008	0.118	±	0.031	79.7	±	5.2	112.9	±	30.0
1	15IA01-4	1.15	0.1202	±	0.0126	0.0121	±	0.0005	0.200	±	0.022	77.4	±	2.9	185.4	±	20.7
1	15IA01-5	0.52	0.0733	±	0.0121	0.0128	±	0.0006	0.129	±	0.022	81.8	±	3.7	123.2	±	21.1
1	15IA01-6	0.71	0.0780	±	0.0028	0.0823	±	0.0015	0.884	±	0.036	509.7	±	9.4	643.3	±	25.9
1	15IA01-7	1.25	0.1287	±	0.0243	0.0087	±	0.0006	0.154	±	0.031	55.6	±	3.6	145.2	±	28.9

	Sample Name	Th/U	207Pb/206Pb		Error 2σ	206Pb/238U		Error 2σ	207Pb/235U		Error 2σ	238U-206Pb age (Ma)		Error 2σ	235U-207Pb age (Ma)		Error 2σ
[1]	15IA01-8	0.87	0.1009	±	0.0149	0.0129	±	0.0006	0.179	±	0.028	82.5	±	3.9	167.4	±	25.9
[1]	15IA01-9	0.95	0.1292	±	0.0341	0.0093	±	0.0008	0.166	±	0.046	59.6	±	5.1	155.5	±	43.2
[1]	15IA01-10	1.14	0.0614	±	0.0074	0.0123	±	0.0004	0.104	±	0.013	78.5	±	2.6	100.3	±	12.5
[1]	15IA01-11	0.46	0.5843	±	0.0303	0.0297	±	0.0010	2.393	±	0.148	188.7	±	6.3	1,240.5	±	76.6
*	15IA01-13	0.76	0.0640	±	0.0125	0.0118	±	0.0006	0.104	±	0.021	75.7	±	3.7	100.7	±	20.3
*	15IA01-14	0.75	0.0551	±	0.0086	0.0146	±	0.0006	0.111	±	0.018	93.3	±	3.6	106.7	±	17.2
[1]	15IA01-17	0.46	0.1726	±	0.0240	0.0162	±	0.0009	0.385	±	0.058	103.6	±	5.7	331.0	±	49.4
	15IA01-18	0.70	0.0486	±	0.0104	0.0120	±	0.0006	0.080	±	0.018	76.8	±	3.8	78.4	±	17.2
[1]	15IA01-22	0.95	0.0782	±	0.0086	0.0127	±	0.0004	0.136	±	0.016	81.1	±	2.8	129.8	±	14.9
[1]	15IA01-24	0.50	0.0889	±	0.0157	0.0131	±	0.0007	0.161	±	0.030	83.9	±	4.5	151.2	±	28.0
	IA66-1	0.70	0.0577	±	0.0025	0.0719	±	0.0011	0.572	±	0.027	447.5	±	6.9	459.0	±	21.4
	IA66-2	0.38	0.0562	±	0.0038	0.0969	±	0.0019	0.750	±	0.053	596.2	±	11.6	568.4	±	40.4
[1]	IA66-3	0.50	0.0729	±	0.0132	0.0130	±	0.0006	0.130	±	0.024	83.0	±	4.0	124.3	±	23.2
	IA66-4	0.69	0.0472	±	0.0075	0.0124	±	0.0004	0.081	±	0.013	79.6	±	2.8	79.0	±	12.8
[1]	IA66-5	0.77	0.0900	±	0.0033	0.1405	±	0.0022	1.744	±	0.069	847.5	±	13.0	1,024.9	±	40.3
	IA66-6	0.63	0.0536	±	0.0028	0.0496	±	0.0008	0.366	±	0.020	312.0	±	4.9	317.0	±	17.5
[1]	IA66-7	0.87	0.0999	±	0.0122	0.0138	±	0.0005	0.190	±	0.024	88.1	±	3.4	176.2	±	22.6
	IA66-8	0.90	0.0549	±	0.0040	0.0438	±	0.0009	0.331	±	0.025	276.3	±	5.4	290.5	±	21.9
*	IA66-9	0.64	0.0585	±	0.0109	0.0126	±	0.0006	0.101	±	0.019	80.5	±	3.6	98.0	±	18.8
[1]	IA66-10	0.44	0.0749	±	0.0109	0.0125	±	0.0005	0.129	±	0.019	79.8	±	3.1	122.9	±	18.5
*	IA66-11	0.63	0.0652	±	0.0127	0.0129	±	0.0006	0.116	±	0.023	82.8	±	4.1	111.5	±	22.5
[1]	IA66-12	0.83	0.0901	±	0.0032	0.1944	±	0.0027	2.415	±	0.092	1,144.9	±	16.1	1,247.1	±	47.5
[1]	IA66-13	0.89	0.1140	±	0.0172	0.0140	±	0.0007	0.220	±	0.035	89.8	±	4.4	202.2	±	32.2
	IA66-14	0.65	0.0521	±	0.0054	0.0746	±	0.0025	0.536	±	0.059	464.0	±	15.5	435.6	±	47.6
[1]	IA66-15	0.59	0.2022	±	0.0206	0.0153	±	0.0007	0.428	±	0.048	98.1	±	4.7	361.5	±	40.7
	13IA07-2	0.31	0.0741	±	0.0048	0.1843	±	0.0053	1.883	±	0.135	1,090.2	±	31.5	1,075.1	±	76.9
	13IA07-3	0.68	0.0496	±	0.0162	0.0117	±	0.0009	0.080	±	0.027	75.1	±	5.5	78.3	±	26.2
[1]	13IA07-4	0.16	0.0749	±	0.0030	0.1255	±	0.0032	1.297	±	0.061	762.4	±	19.3	844.4	±	39.8
	13IA07-6	0.69	0.0622	±	0.0042	0.0775	±	0.0022	0.665	±	0.048	481.4	±	13.6	517.7	±	37.6
	13IA07-7	0.45	0.0577	±	0.0035	0.0604	±	0.0016	0.481	±	0.032	378.0	±	10.3	398.5	±	26.5
[1]	13IA07-8	0.14	0.1444	±	0.0047	0.2079	±	0.0053	4.141	±	0.170	1,217.8	±	30.9	1,662.4	±	68.2
	13IA07-9	0.87	0.0815	±	0.0038	0.2035	±	0.0032	2.288	±	0.114	1,194.4	±	18.9	1,208.5	±	60.0
[1]	13IA07-10	0.67	0.0898	±	0.0185	0.0140	±	0.0008	0.173	±	0.037	89.3	±	5.3	161.8	±	34.7
	13IA07-11	0.11	0.0663	±	0.0034	0.1407	±	0.0022	1.285	±	0.069	848.7	±	13.4	839.2	±	45.0
[1]	13IA07-12	0.56	0.0588	±	0.0035	0.0480	±	0.0008	0.390	±	0.024	302.4	±	5.1	334.1	±	20.6
[1]	13IA07-13	0.20	0.0767	±	0.0042	0.1412	±	0.0024	1.493	±	0.085	851.5	±	14.6	927.5	±	52.7
	13IA07-14	2.28	0.0608	±	0.0036	0.0948	±	0.0016	0.795	±	0.050	584.0	±	10.0	594.1	±	37.0

	Sample Name	Th/U	207Pb/206Pb		Error 2σ	206Pb/238U		Error 2σ	207Pb/235U		Error 2σ	238U-206Pb age (Ma)		Error 2σ	235U-207Pb age (Ma)		Error 2σ
[1]	13IA07-15	0.15	0.0683	±	0.0029	0.0930	±	0.0013	0.876	±	0.039	573.4	±	8.1	638.7	±	28.7
[1]	13IA07-16	0.35	0.1043	±	0.0108	0.1001	±	0.0033	1.440	±	0.156	615.1	±	20.3	905.7	±	98.1
*	13IA07-17	0.72	0.0719	±	0.0183	0.0107	±	0.0007	0.106	±	0.028	68.8	±	4.6	102.7	±	27.0
[1]	13IA07-18	0.97	0.1028	±	0.0211	0.0106	±	0.0007	0.151	±	0.032	68.2	±	4.3	142.6	±	30.6
[1]	13IA07-19	0.74	0.2020	±	0.0229	0.0256	±	0.0012	0.712	±	0.088	162.7	±	7.8	545.7	±	67.1
	IA84-1	0.51	0.0532	±	0.0153	0.0116	±	0.0008	0.085	±	0.025	74.3	±	4.8	83.0	±	24.4
[1]	IA84-2	0.63	0.5290	±	0.0587	0.0126	±	0.0008	0.916	±	0.118	80.4	±	5.3	660.2	±	85.0
[1]	IA84-3	0.59	0.2463	±	0.0291	0.0120	±	0.0006	0.407	±	0.053	76.9	±	4.1	347.0	±	45.0
[1]	IA84-4	0.65	0.0822	±	0.0194	0.0116	±	0.0008	0.132	±	0.032	74.6	±	4.9	125.9	±	30.8
	IA84-5	0.54	0.0504	±	0.0122	0.0120	±	0.0006	0.084	±	0.021	77.1	±	4.2	81.5	±	20.2
[1]	IA84-6	0.55	0.1084	±	0.0160	0.0123	±	0.0006	0.185	±	0.029	79.1	±	3.7	172.0	±	26.6
	IA84-7	0.67	0.0489	±	0.0053	0.0114	±	0.0003	0.077	±	0.009	73.3	±	1.9	75.4	±	8.3
[1]	IA84-8	0.66	0.1265	±	0.0204	0.0125	±	0.0007	0.219	±	0.037	80.4	±	4.5	200.8	±	34.3
*	IA84-9	0.60	0.0722	±	0.0204	0.0104	±	0.0008	0.103	±	0.030	66.6	±	5.1	99.8	±	29.2
	IA84-10	0.72	0.0522	±	0.0158	0.0107	±	0.0008	0.077	±	0.024	68.4	±	4.8	75.1	±	23.4
	IA84-12	0.72	0.0506	±	0.0169	0.0107	±	0.0008	0.075	±	0.026	68.8	±	5.2	73.3	±	25.1
*	IA84-13	0.84	0.0627	±	0.0139	0.0122	±	0.0007	0.106	±	0.024	78.3	±	4.4	102.0	±	23.3
	IA84-14	0.87	0.0495	±	0.0051	0.0429	±	0.0012	0.293	±	0.031	270.7	±	7.4	260.6	±	27.8
[1]	IA84-15	0.45	0.1284	±	0.0129	0.0324	±	0.0012	0.573	±	0.061	205.5	±	7.8	460.3	±	49.2
	IA84-16	0.84	0.0511	±	0.0160	0.0144	±	0.0010	0.102	±	0.033	92.3	±	6.7	98.3	±	31.6
[1]	IA84-17	0.69	0.1963	±	0.0332	0.0131	±	0.0009	0.355	±	0.065	84.1	±	6.0	308.8	±	56.7
*	IA84-18	0.57	0.0762	±	0.0222	0.0112	±	0.0009	0.118	±	0.036	72.0	±	5.6	113.3	±	34.3
*	IA84-19	0.80	0.0704	±	0.0166	0.0123	±	0.0008	0.120	±	0.029	79.1	±	5.0	114.8	±	28.0
	IA84-20	0.51	0.0598	±	0.0153	0.0109	±	0.0007	0.090	±	0.024	70.2	±	4.4	87.7	±	23.2
	IA84-21	0.51	0.0441	±	0.0126	0.0105	±	0.0006	0.064	±	0.019	67.5	±	4.1	63.0	±	18.4
	IA84-22	0.85	0.0530	±	0.0139	0.0111	±	0.0007	0.081	±	0.022	71.1	±	4.4	79.0	±	21.3
[1]	IA84-23	0.62	0.1030	±	0.0226	0.0117	±	0.0008	0.166	±	0.038	74.7	±	5.2	155.6	±	35.7
[1]	IA84-24	0.56	0.1385	±	0.0193	0.0120	±	0.0006	0.228	±	0.034	76.6	±	4.1	208.9	±	31.2
	IA84-25	0.56	0.0534	±	0.0197	0.0109	±	0.0009	0.080	±	0.030	69.8	±	5.6	78.3	±	29.6
	IA84-26	0.52	0.0437	±	0.0122	0.0113	±	0.0007	0.068	±	0.019	72.2	±	4.3	66.7	±	19.0
[1]	IA84-27	0.52	0.0883	±	0.0177	0.0123	±	0.0007	0.150	±	0.031	78.8	±	4.7	141.7	±	29.6
[1]	IA84-28	0.87	0.1313	±	0.0137	0.0123	±	0.0005	0.222	±	0.025	78.7	±	3.3	203.8	±	23.0
	IA84-29	0.42	0.0534	±	0.0157	0.0117	±	0.0008	0.086	±	0.026	75.3	±	5.0	84.2	±	25.4
[1]	IA84-30	0.67	0.0699	±	0.0126	0.0125	±	0.0006	0.121	±	0.023	80.1	±	4.0	115.6	±	21.6
	IA84-31	0.46	0.0435	±	0.0151	0.0115	±	0.0008	0.069	±	0.024	73.4	±	5.1	67.5	±	23.8
[1]	IA84-32	0.84	0.1051	±	0.0176	0.0125	±	0.0007	0.182	±	0.032	80.3	±	4.5	169.6	±	30.0
[1]	IA84-33	0.45	0.0796	±	0.0175	0.0117	±	0.0007	0.128	±	0.029	75.0	±	4.7	122.7	±	28.0

	Sample Name	Th/U	207Pb/206Pb		Error 2σ	206Pb/238U		Error 2σ	207Pb/235U		Error 2σ	238U-206Pb age (Ma)		Error 2σ	235U-207Pb age (Ma)		Error 2σ
	IA84-34	0.48	0.0542	±	0.0185	0.0111	±	0.0009	0.083	±	0.029	71.4	±	5.5	81.2	±	28.4
*	IA84-35	0.58	0.0685	±	0.0162	0.0113	±	0.0007	0.107	±	0.026	72.3	±	4.6	102.8	±	25.2
	IA84-36	0.63	0.0490	±	0.0159	0.0118	±	0.0008	0.080	±	0.026	75.8	±	5.4	78.1	±	25.8
*	IA84-37	0.71	0.0649	±	0.0125	0.0118	±	0.0006	0.106	±	0.021	75.8	±	4.0	102.1	±	20.4
	IA84-38	0.78	0.0557	±	0.0108	0.0138	±	0.0007	0.106	±	0.021	88.1	±	4.4	102.0	±	20.4
*	IA84-39	0.92	0.0606	±	0.0129	0.0111	±	0.0006	0.093	±	0.020	71.1	±	4.0	90.1	±	19.8
*	IA84-40	0.58	0.0582	±	0.0052	0.0431	±	0.0014	0.346	±	0.033	272.1	±	8.9	301.8	±	28.8

c) VBX dataset

(1 marks data with probability of concordance < 0.01; 2 marks data with error > 10%)

(* For host rocks and basement, probability of concordance < 0.1 and > 0.01, and error > 10.0 % and < 10 % are included in calculation)

	Sample Name	Th/U	207Pb/206Pb		Error 2σ	206Pb/238U		Error 2σ	207Pb/235U		Error 2σ	238U-206Pb age (Ma)		Error 2σ	235U-207Pb age (Ma)		Error 2σ
1	13IA06-1	0.65	0.1959	±	0.0299	0.0125	±	0.0008	0.338	±	0.056	80.1	±	5.3	295.3	±	49.1
1	13IA06-2	0.66	0.5542	±	0.0568	0.0172	±	0.0011	1.317	±	0.160	110.2	±	7.2	853.3	±	103.6
1	13IA06-3	0.63	0.5364	±	0.0528	0.0120	±	0.0007	0.888	±	0.103	76.9	±	4.8	645.2	±	75.1
2	13IA06-4	0.55	0.0943	±	0.0335	0.0094	±	0.0010	0.122	±	0.045	60.2	±	6.5	116.8	±	43.3
1	13IA06-5	1.17	0.4546	±	0.0633	0.0240	±	0.0020	1.505	±	0.243	153.0	±	12.4	932.4	±	150.4
1	13IA06-6	0.95	0.1146	±	0.0288	0.0091	±	0.0008	0.143	±	0.038	58.1	±	4.9	135.8	±	36.0
	13IA06-7	0.70	0.0467	±	0.0188	0.0087	±	0.0007	0.056	±	0.023	55.8	±	4.7	55.3	±	22.7
	13IA06-9	0.79	0.0600	±	0.0219	0.0092	±	0.0008	0.076	±	0.029	58.9	±	5.1	74.3	±	27.9
	13IA06-10	1.17	0.0448	±	0.0111	0.0084	±	0.0005	0.052	±	0.013	54.0	±	3.1	51.4	±	13.1
*	13IA06-11	0.71	0.0661	±	0.0181	0.0142	±	0.0010	0.130	±	0.037	91.2	±	6.5	124.0	±	35.0
	13IA06-12	0.82	0.0482	±	0.0165	0.0085	±	0.0006	0.057	±	0.020	54.7	±	4.1	56.0	±	19.7
1	13IA06-13	0.60	0.5177	±	0.0551	0.0235	±	0.0016	1.675	±	0.210	149.6	±	9.9	999.2	±	125.2
	13IA06-14	0.80	0.0567	±	0.0179	0.0106	±	0.0008	0.083	±	0.027	67.9	±	5.1	80.6	±	26.2
1	13IA06-15	0.69	0.5638	±	0.0591	0.0171	±	0.0012	1.327	±	0.166	109.1	±	7.4	857.6	±	107.2
1	13IA06-16	1.00	0.5950	±	0.0543	0.0284	±	0.0017	2.331	±	0.256	180.6	±	11.1	1,221.7	±	134.2
	13IA06-18	0.88	0.0654	±	0.0235	0.0101	±	0.0009	0.091	±	0.034	64.5	±	5.9	88.2	±	32.6
1	13IA06-19	1.03	0.0874	±	0.0225	0.0095	±	0.0007	0.115	±	0.031	61.1	±	4.7	110.3	±	29.6
	13IA06-20	0.82	0.0481	±	0.0071	0.0254	±	0.0011	0.169	±	0.026	161.9	±	6.8	158.3	±	24.3
*	13IA06-21	0.85	0.0801	±	0.0215	0.0098	±	0.0008	0.109	±	0.030	63.1	±	4.9	104.7	±	29.3
	13IA06-22	1.01	0.0591	±	0.0202	0.0087	±	0.0007	0.071	±	0.025	56.1	±	4.7	69.8	±	24.6
	IA49-1	0.74	0.0540	±	0.0245	0.0096	±	0.0009	0.072	±	0.033	61.9	±	6.1	70.4	±	32.7
*	IA49-2	0.35	0.0811	±	0.0248	0.0090	±	0.0007	0.100	±	0.032	57.4	±	4.8	96.8	±	30.7
1	IA49-3	0.65	0.4000	±	0.0755	0.0093	±	0.0010	0.516	±	0.111	60.0	±	6.2	422.2	±	91.0
1	IA49-4	0.93	0.1142	±	0.0307	0.0082	±	0.0007	0.129	±	0.037	52.7	±	4.7	123.5	±	35.0

	Sample Name	Th/U	207Pb/206Pb		Error 2σ	206Pb/238U		Error 2σ	207Pb/235U		Error 2σ	238U-206Pb age (Ma)		Error 2σ	235U-207Pb age (Ma)		Error 2σ
1	IA49-5	0.68	0.2533	±	0.0525	0.0108	±	0.0010	0.377	±	0.086	69.3	±	6.7	324.9	±	74.3
	IA49-6	0.44	0.0562	±	0.0215	0.0088	±	0.0008	0.068	±	0.027	56.2	±	5.2	66.6	±	26.2
	IA49-7	1.05	0.0463	±	0.0203	0.0085	±	0.0008	0.054	±	0.024	54.4	±	5.2	53.5	±	24.0
*	IA49-8	0.43	0.0839	±	0.0261	0.0097	±	0.0009	0.112	±	0.036	62.1	±	5.6	107.8	±	34.9
1	IA49-9	1.24	0.3899	±	0.0363	0.0156	±	0.0009	0.838	±	0.090	99.7	±	5.5	618.0	±	66.7
	IA49-10	0.65	0.0407	±	0.0186	0.0090	±	0.0008	0.050	±	0.023	57.5	±	5.4	49.8	±	23.3
	IA49-11	0.72	0.0655	±	0.0242	0.0098	±	0.0009	0.089	±	0.034	63.0	±	5.7	86.3	±	32.8
1	IA49-12	0.94	0.3538	±	0.0291	0.0289	±	0.0014	1.412	±	0.135	183.9	±	8.9	893.9	±	85.4
*	IA49-13	0.43	0.0701	±	0.0241	0.0090	±	0.0008	0.087	±	0.031	57.8	±	5.1	84.8	±	30.1
*	IA49-14	0.68	0.0918	±	0.0328	0.0086	±	0.0009	0.109	±	0.040	55.2	±	5.7	104.9	±	39.0
	IA49-15	0.91	0.0356	±	0.0160	0.0084	±	0.0007	0.041	±	0.019	53.9	±	4.4	41.0	±	18.8
*	IA49-16	0.66	0.0454	±	0.0243	0.0085	±	0.0009	0.053	±	0.029	54.3	±	5.7	52.4	±	28.5
	IA49-17	0.89	0.0373	±	0.0164	0.0093	±	0.0008	0.048	±	0.022	59.8	±	4.9	47.6	±	21.3
1	IA49-18	0.86	0.4763	±	0.0723	0.0172	±	0.0015	1.128	±	0.199	109.8	±	9.8	766.9	±	135.1
1	IA49-19	0.80	0.1475	±	0.0386	0.0088	±	0.0009	0.180	±	0.050	56.6	±	5.6	167.6	±	46.9
*	IA49-20	0.46	0.0575	±	0.0254	0.0097	±	0.0010	0.077	±	0.035	62.1	±	6.4	75.1	±	34.1
1	IA49-21	0.83	0.2488	±	0.0408	0.0107	±	0.0009	0.368	±	0.067	68.7	±	5.5	317.9	±	58.0
	IA49-22	0.71	0.0645	±	0.0258	0.0091	±	0.0009	0.081	±	0.034	58.6	±	5.9	79.3	±	32.7
1	IA49-23	1.09	0.1284	±	0.0255	0.0087	±	0.0007	0.154	±	0.033	56.0	±	4.2	145.8	±	31.0
1	IA49-24	1.06	0.1030	±	0.0299	0.0081	±	0.0008	0.115	±	0.035	51.8	±	4.8	110.2	±	33.6
1	IA49-25	0.86	0.4276	±	0.0606	0.0136	±	0.0011	0.804	±	0.133	87.3	±	7.4	598.9	±	98.8
	IA49-26	0.90	0.0638	±	0.0231	0.0086	±	0.0008	0.076	±	0.028	55.4	±	5.1	74.3	±	27.8
1	IA49-32	0.89	1.0939	±	0.1442	0.0083	±	0.0008	1.257	±	0.205	53.5	±	5.1	826.8	±	134.7
*	IA49-33	0.75	0.0216	±	0.0157	0.0085	±	0.0007	0.025	±	0.018	54.6	±	4.6	25.4	±	18.5
	IA49-34	0.78	0.0495	±	0.0219	0.0086	±	0.0008	0.059	±	0.027	55.4	±	4.8	58.1	±	26.2
1	IA49-35	0.81	0.3278	±	0.0523	0.0094	±	0.0008	0.426	±	0.076	60.5	±	4.9	360.6	±	64.5
	IA49-36	0.63	0.0560	±	0.0137	0.0106	±	0.0006	0.082	±	0.020	67.8	±	3.9	79.6	±	20.0

d) PTN dataset

(1 marks data with probability of concordance < 0.1; 2 marks data with error > 10.0 %)

	Sample Name	Th/U	207Pb/206Pb		Error 2σ	206Pb/238U		Error 2σ	207Pb/235U		Error 2σ	238U-206Pb age (Ma)		Error 2σ	235U-207Pb age (Ma)		Error 2σ
1	15IA09-1	1.25	0.1447	±	0.0189	0.0128	±	0.0006	0.256	±	0.036	82.1	±	4.1	231.2	±	32.4
1	15IA09-2	0.68	0.0860	±	0.0269	0.0087	±	0.0008	0.103	±	0.034	55.8	±	4.9	99.7	±	32.4
1	15IA09-3	1.06	0.0664	±	0.0206	0.0090	±	0.0007	0.083	±	0.026	57.9	±	4.5	80.6	±	25.8
1	15IA09-4	0.82	0.1746	±	0.0272	0.0105	±	0.0007	0.252	±	0.042	67.0	±	4.2	227.9	±	38.2
2	15IA09-5	0.64	0.0442	±	0.0321	0.0097	±	0.0013	0.059	±	0.043	62.0	±	8.3	58.2	±	42.9

Sample Name	Th/U	207Pb/206Pb		Error 2σ	206Pb/238U		Error 2σ	207Pb/235U		Error 2σ	238U-206Pb age (Ma)		Error 2σ	235U-207Pb age (Ma)		Error 2σ
[1] 15IA09-6	0.59	0.0996	±	0.0341	0.0097	±	0.0010	0.133	±	0.048	62.2	±	6.4	126.9	±	45.4
15IA09-6(2)	1.11	0.0449	±	0.0145	0.0083	±	0.0006	0.051	±	0.017	53.3	±	3.7	51.0	±	16.8
15IA09-7	0.92	0.0405	±	0.0135	0.0090	±	0.0006	0.050	±	0.017	57.9	±	3.9	50.0	±	17.0
[1] 15IA09-8	0.79	0.3962	±	0.0512	0.0178	±	0.0013	0.972	±	0.144	113.7	±	8.2	689.6	±	102.2
[1] 15IA09-9	0.50	0.2274	±	0.0282	0.0137	±	0.0008	0.429	±	0.059	87.7	±	5.4	362.8	±	50.2
[1] 15IA09-10	0.59	0.4431	±	0.0550	0.0146	±	0.0011	0.894	±	0.130	93.6	±	7.2	648.4	±	94.6
[1] 15IA09-11	0.73	0.0992	±	0.0279	0.0105	±	0.0010	0.144	±	0.043	67.6	±	6.5	136.8	±	40.6
[2] 15IA09-12	0.82	0.0739	±	0.0323	0.0090	±	0.0012	0.091	±	0.042	57.5	±	7.6	88.7	±	40.5
[1] 15IA09-13	1.18	0.1341	±	0.0325	0.0094	±	0.0009	0.174	±	0.045	60.5	±	5.7	163.2	±	42.4
[1] 15IA09-14	1.13	0.1234	±	0.0278	0.0093	±	0.0008	0.158	±	0.038	59.7	±	5.0	149.1	±	35.9
[2] 15IA09-15	0.68	0.0660	±	0.0265	0.0088	±	0.0010	0.080	±	0.033	56.3	±	6.3	78.0	±	32.5
[2] 15IA09-16	0.91	0.0723	±	0.0357	0.0088	±	0.0013	0.087	±	0.045	56.3	±	8.4	85.0	±	43.9
[1] 15IA09-17	0.54	0.0982	±	0.0331	0.0102	±	0.0011	0.139	±	0.049	65.7	±	6.8	131.8	±	46.4
[1] 15IA09-18	0.70	0.1488	±	0.0363	0.0095	±	0.0009	0.194	±	0.050	60.7	±	5.5	180.1	±	46.8
[1] 15IA09-19	1.11	0.1342	±	0.0564	0.0092	±	0.0013	0.170	±	0.076	58.9	±	8.7	159.4	±	70.9
[1] 15IA09-20	0.67	0.2110	±	0.0528	0.0103	±	0.0011	0.299	±	0.081	65.9	±	7.0	265.7	±	72.3
15IA09-21	0.89	0.0474	±	0.0129	0.0091	±	0.0006	0.059	±	0.017	58.4	±	3.6	58.7	±	16.3
[1] 15IA09-22	0.95	0.0803	±	0.0239	0.0086	±	0.0007	0.095	±	0.030	55.3	±	4.6	92.5	±	28.6
15IA09-23	0.43	0.0539	±	0.0101	0.0084	±	0.0004	0.062	±	0.012	53.8	±	2.5	61.4	±	11.9
[1] 15IA09-24	0.69	0.1066	±	0.0386	0.0075	±	0.0009	0.110	±	0.042	48.1	±	5.5	106.1	±	40.3
[1] 15IA09-25	0.61	0.0933	±	0.0382	0.0078	±	0.0009	0.101	±	0.043	50.2	±	5.8	97.4	±	41.4
15IA09-26	1.27	0.0468	±	0.0130	0.0080	±	0.0005	0.052	±	0.015	51.3	±	3.2	51.0	±	14.5
[1] 15IA09-27	0.62	0.0985	±	0.0370	0.0089	±	0.0010	0.121	±	0.048	57.3	±	6.3	116.1	±	45.5
[1] 15IA09-28	0.78	0.1177	±	0.0426	0.0081	±	0.0009	0.132	±	0.050	52.3	±	6.0	126.0	±	47.9
[1] 15IA09-29	1.07	0.1167	±	0.0277	0.0090	±	0.0007	0.145	±	0.036	57.9	±	4.6	137.6	±	34.4
[2] 15IA09-30	0.58	0.0644	±	0.0395	0.0077	±	0.0010	0.068	±	0.043	49.3	±	6.7	66.9	±	42.0
IA29-1	0.79	0.0633	±	0.0195	0.0084	±	0.0007	0.073	±	0.023	54.0	±	4.3	71.9	±	22.9
[1] IA29-2	0.71	0.4250	±	0.0498	0.0157	±	0.0011	0.922	±	0.125	100.7	±	6.8	663.5	±	89.9
IA29-3	0.91	0.0425	±	0.0125	0.0119	±	0.0008	0.070	±	0.021	76.1	±	4.9	68.3	±	20.6
IA29-4	0.80	0.0402	±	0.0162	0.0081	±	0.0007	0.045	±	0.018	51.9	±	4.3	44.6	±	18.3
[1] IA29-5	0.81	0.1139	±	0.0230	0.0088	±	0.0006	0.138	±	0.029	56.3	±	3.9	131.1	±	28.0
IA29-6	0.87	0.0579	±	0.0143	0.0080	±	0.0005	0.064	±	0.016	51.2	±	3.2	62.7	±	15.9
[1] IA29-7	0.86	0.1096	±	0.0228	0.0092	±	0.0006	0.139	±	0.030	59.0	±	4.1	132.0	±	28.9
IA29-8	0.99	0.0585	±	0.0152	0.0088	±	0.0006	0.071	±	0.019	56.3	±	3.7	69.4	±	18.6
[1] IA29-9	0.84	0.1710	±	0.0302	0.0095	±	0.0007	0.225	±	0.043	61.2	±	4.2	206.0	±	39.1
[1] IA29-10	0.71	0.4888	±	0.0540	0.0161	±	0.0011	1.086	±	0.139	103.1	±	6.7	746.6	±	95.8
IA29-11	0.94	0.0420	±	0.0157	0.0081	±	0.0006	0.047	±	0.018	51.9	±	3.7	46.4	±	17.7

	Sample Name	Th/U	207Pb/206Pb		Error 2σ	206Pb/238U		Error 2σ	207Pb/235U		Error 2σ	238U-206Pb age (Ma)		Error 2σ	235U-207Pb age (Ma)		Error 2σ
[1]	IA29-12	1.10	0.0830	±	0.0213	0.0097	±	0.0007	0.110	±	0.029	61.9	±	4.4	106.4	±	28.4
	IA29-13	0.91	0.0484	±	0.0162	0.0086	±	0.0006	0.058	±	0.020	55.3	±	3.8	56.8	±	19.3
[1]	IA29-14	0.79	0.2118	±	0.0355	0.0094	±	0.0007	0.276	±	0.050	60.6	±	4.3	247.3	±	45.0
	IA29-15	0.89	0.0383	±	0.0153	0.0079	±	0.0006	0.041	±	0.017	50.4	±	3.6	41.2	±	16.8
	IA29-16	0.72	0.0438	±	0.0183	0.0085	±	0.0007	0.051	±	0.022	54.3	±	4.3	50.6	±	21.5
[1]	IA29-17	0.41	0.0634	±	0.0040	0.0565	±	0.0014	0.494	±	0.034	354.2	±	8.8	407.5	±	27.6
[1]	IA29-18	0.91	0.1789	±	0.0311	0.0095	±	0.0007	0.233	±	0.044	60.7	±	4.3	212.8	±	39.8
[1]	IA29-19	0.78	0.1348	±	0.0320	0.0089	±	0.0007	0.166	±	0.042	57.3	±	4.8	155.9	±	39.2
[1]	IA29-21	0.83	0.1586	±	0.0319	0.0111	±	0.0008	0.242	±	0.052	71.1	±	5.4	220.3	±	47.5
[1]	IA29-22	0.69	0.1088	±	0.0251	0.0089	±	0.0007	0.134	±	0.032	57.3	±	4.3	127.7	±	30.9
[1]	IA29-23	0.97	0.0841	±	0.0193	0.0085	±	0.0006	0.099	±	0.024	54.6	±	3.6	95.5	±	22.8
	IA29-24	0.72	0.0620	±	0.0181	0.0082	±	0.0006	0.070	±	0.021	52.9	±	3.8	69.2	±	20.8
	IA80-1	0.79	0.0558	±	0.0185	0.0083	±	0.0006	0.064	±	0.022	53.3	±	4.0	62.9	±	21.4
	IA80-2	0.82	0.0529	±	0.0096	0.0081	±	0.0004	0.059	±	0.011	52.0	±	2.3	58.2	±	10.9
[1]	IA80-3	0.80	0.0702	±	0.0183	0.0086	±	0.0006	0.083	±	0.022	55.1	±	3.7	81.1	±	21.9
[1]	IA80-4	0.77	0.1168	±	0.0316	0.0095	±	0.0008	0.153	±	0.043	60.8	±	5.3	144.2	±	40.9
	IA80-5	0.94	0.0583	±	0.0199	0.0088	±	0.0007	0.071	±	0.025	56.7	±	4.4	69.6	±	24.4
	IA80-6	0.91	0.0373	±	0.0132	0.0086	±	0.0006	0.044	±	0.016	55.2	±	3.6	43.9	±	15.8
[1]	IA80-7	0.84	0.1253	±	0.0261	0.0089	±	0.0006	0.153	±	0.034	57.0	±	4.0	144.9	±	31.9
	IA80-8	0.60	0.0570	±	0.0206	0.0083	±	0.0007	0.065	±	0.024	53.2	±	4.3	64.1	±	23.7
[2]	IA80-9	0.83	0.0431	±	0.0311	0.0104	±	0.0013	0.062	±	0.045	66.7	±	8.3	60.9	±	44.6
	IA80-10	0.21	0.0522	±	0.0035	0.0302	±	0.0006	0.217	±	0.015	191.6	±	3.9	199.5	±	14.0
[1]	IA80-11	0.03	0.0618	±	0.0037	0.0092	±	0.0002	0.078	±	0.005	58.7	±	1.2	76.2	±	4.8
	IA80-12	0.97	0.0517	±	0.0138	0.0088	±	0.0005	0.063	±	0.017	56.3	±	3.4	61.6	±	16.9
[1]	IA80-13	0.95	0.8778	±	0.1055	0.0083	±	0.0007	1.003	±	0.147	53.2	±	4.4	705.5	±	103.2
[1]	IA80-14	0.68	0.3072	±	0.0618	0.0101	±	0.0010	0.426	±	0.096	64.6	±	6.4	360.6	±	80.8
[1]	IA80-15	0.87	0.0877	±	0.0263	0.0072	±	0.0006	0.087	±	0.027	46.2	±	3.9	84.6	±	26.4
	IA80-16	0.67	0.0478	±	0.0181	0.0085	±	0.0007	0.056	±	0.022	54.3	±	4.2	55.1	±	21.3
[1]	IA80-17	0.42	0.0618	±	0.0087	0.0361	±	0.0012	0.307	±	0.044	228.4	±	7.5	272.2	±	39.3
[1]	IA80-18	0.64	0.1483	±	0.0615	0.0086	±	0.0006	0.175	±	0.074	54.9	±	4.1	163.7	±	69.0
[1]	IA80-19	0.70	0.1089	±	0.0606	0.0091	±	0.0007	0.137	±	0.077	58.5	±	4.4	130.3	±	73.2
	IA80-20	1.18	0.0426	±	0.0309	0.0078	±	0.0004	0.046	±	0.033	49.8	±	2.8	45.3	±	32.9
[1]	IA80-21	0.84	0.0895	±	0.0351	0.0086	±	0.0005	0.106	±	0.042	55.2	±	3.2	102.4	±	40.6
[1]	IA80-23	0.83	0.0938	±	0.0287	0.0091	±	0.0005	0.118	±	0.037	58.6	±	3.1	113.4	±	35.2
[1]	IA80-24	1.04	0.2069	±	0.0319	0.0088	±	0.0004	0.252	±	0.041	56.7	±	2.9	228.1	±	37.1
[1]	IA81-1	0.44	0.2223	±	0.0374	0.0118	±	0.0009	0.362	±	0.067	75.7	±	5.7	313.6	±	57.9
	IA81-1(2)	0.85	0.0496	±	0.0094	0.0089	±	0.0004	0.061	±	0.012	57.3	±	2.7	60.2	±	11.7

	Sample Name	Th/U	207Pb/206Pb		Error 2σ	206Pb/238U		Error 2σ	207Pb/235U		Error 2σ	238U-206Pb age (Ma)		Error 2σ	235U-207Pb age (Ma)		Error 2σ
[1]	IA81-2	1.28	0.1511	±	0.0287	0.0090	±	0.0007	0.187	±	0.038	57.7	±	4.2	174.4	±	35.5
[1]	IA81-2(2)	0.31	0.0550	±	0.0068	0.0080	±	0.0003	0.061	±	0.008	51.6	±	1.9	60.1	±	7.8
[1]	IA81-3	1.12	0.0851	±	0.0306	0.0090	±	0.0009	0.106	±	0.040	58.0	±	5.6	102.4	±	38.1
[1]	IA81-4	0.92	0.1933	±	0.0354	0.0115	±	0.0009	0.307	±	0.061	73.9	±	5.5	272.1	±	53.7
[1]	IA81-5	0.86	0.1419	±	0.0488	0.0119	±	0.0014	0.233	±	0.085	76.2	±	8.9	212.5	±	77.2
[1]	IA81-6	1.18	0.0737	±	0.0204	0.0092	±	0.0007	0.094	±	0.027	59.3	±	4.3	91.1	±	26.0
[1]	IA81-7	0.74	0.2209	±	0.0574	0.0158	±	0.0017	0.483	±	0.136	101.3	±	11.1	399.9	±	112.8
[1]	IA81-8	0.72	0.0989	±	0.0369	0.0089	±	0.0010	0.122	±	0.047	57.4	±	6.1	116.9	±	45.3
	IA81-9	0.82	0.0503	±	0.0065	0.0088	±	0.0003	0.061	±	0.008	56.5	±	1.8	60.1	±	7.9
[1]	IA81-10	0.77	0.0918	±	0.0180	0.0091	±	0.0005	0.115	±	0.024	58.3	±	3.4	110.6	±	22.7
[1]	IA81-11	0.81	0.2223	±	0.0425	0.0098	±	0.0008	0.300	±	0.063	62.9	±	5.1	266.7	±	55.5
[1]	IA81-12	0.93	0.6834	±	0.0986	0.0183	±	0.0017	1.725	±	0.296	117.0	±	10.9	1,018.0	±	174.7
[1]	IA81-13	1.04	0.4532	±	0.0703	0.0188	±	0.0017	1.177	±	0.210	120.3	±	10.5	789.7	±	140.7
[1]	IA81-14	0.38	0.1254	±	0.0381	0.0090	±	0.0009	0.156	±	0.050	57.8	±	5.7	146.9	±	46.9
[1]	IA81-15	0.58	0.0710	±	0.0047	0.0465	±	0.0011	0.455	±	0.032	292.9	±	6.9	380.8	±	27.0
[1]	IA81-16	0.86	0.1969	±	0.0448	0.0122	±	0.0011	0.331	±	0.081	78.1	±	7.2	290.4	±	71.3
[1]	IA81-17	0.71	0.3740	±	0.0670	0.0114	±	0.0011	0.588	±	0.119	73.1	±	6.9	469.4	±	94.9
[1]	IA81-18	0.86	0.1544	±	0.0202	0.0092	±	0.0005	0.196	±	0.027	59.2	±	3.0	182.0	±	25.4
[1]	IA81-19	0.98	0.2030	±	0.0289	0.0087	±	0.0006	0.244	±	0.038	55.9	±	3.6	221.7	±	34.6
	IA81-20	0.60	0.0589	±	0.0167	0.0082	±	0.0006	0.067	±	0.020	52.9	±	3.8	65.7	±	19.3
[1]	IA81-21	1.23	0.2591	±	0.0508	0.0096	±	0.0009	0.342	±	0.074	61.5	±	5.7	299.0	±	64.8
[1]	IA81-22	0.66	0.3806	±	0.0570	0.0156	±	0.0013	0.819	±	0.140	99.8	±	8.2	607.3	±	103.9
[1]	IA81-23	0.83	0.5818	±	0.0732	0.0218	±	0.0017	1.745	±	0.260	138.8	±	11.1	1,025.4	±	152.9
[1]	IA81-24	0.89	0.3862	±	0.0465	0.0188	±	0.0013	1.004	±	0.139	120.4	±	8.2	705.6	±	97.5
[1]	IA81-25	0.92	0.5140	±	0.1369	0.0093	±	0.0015	0.663	±	0.205	60.0	±	9.5	516.2	±	160.1
[1]	IA81-26	1.20	0.1105	±	0.0489	0.0087	±	0.0012	0.132	±	0.062	55.7	±	8.0	126.0	±	58.7
[1]	IA81-27	0.76	0.0919	±	0.0217	0.0081	±	0.0006	0.103	±	0.026	52.3	±	3.8	99.8	±	24.7
[1]	IA81-28	0.89	0.1108	±	0.0355	0.0081	±	0.0008	0.123	±	0.041	51.8	±	5.1	117.9	±	39.5
[1]	IA81-29	0.89	0.5902	±	0.1502	0.0135	±	0.0021	1.098	±	0.327	86.4	±	13.3	752.1	±	223.8
[1]	IA81-30	0.91	0.1828	±	0.0521	0.0087	±	0.0010	0.219	±	0.067	55.7	±	6.1	200.8	±	61.4
[1]	IA81-31	1.01	0.1007	±	0.0337	0.0093	±	0.0009	0.129	±	0.045	59.7	±	5.8	123.3	±	43.0
	IA81-32	0.65	0.0580	±	0.0142	0.0084	±	0.0005	0.067	±	0.017	54.0	±	3.4	66.1	±	16.8
[1]	IA81-33	0.75	0.1976	±	0.0685	0.0107	±	0.0014	0.293	±	0.109	68.9	±	9.2	260.8	±	96.9
[1]	IA81-34	0.88	0.1974	±	0.0357	0.0131	±	0.0010	0.358	±	0.070	84.2	±	6.6	310.4	±	61.2
	1006-1	0.62	0.0518	±	0.0122	0.0085	±	0.0005	0.061	±	0.015	54.4	±	3.2	59.7	±	14.5
[1]	1006-2	0.47	0.0340	±	0.0136	0.0087	±	0.0006	0.041	±	0.017	55.7	±	4.2	40.5	±	16.5
[1]	1006-4	0.49	0.1143	±	0.0449	0.0081	±	0.0010	0.128	±	0.053	52.1	±	6.5	122.2	±	50.4

	Sample Name	Th/U	207Pb/206Pb		Error 2σ	206Pb/238U		Error 2σ	207Pb/235U		Error 2σ	238U-206Pb age (Ma)		Error 2σ	235U-207Pb age (Ma)		Error 2σ
2	1006-5	1.09	0.0394	±	0.0278	0.0083	±	0.0010	0.045	±	0.032	53.3	±	6.5	44.8	±	32.1
	1006-7	0.97	0.0515	±	0.0112	0.0080	±	0.0004	0.057	±	0.013	51.4	±	2.9	56.1	±	12.6
1	1006-8	0.78	0.1978	±	0.0694	0.0090	±	0.0013	0.245	±	0.093	57.5	±	8.2	222.1	±	84.1
1	1006-9	0.57	0.4011	±	0.1247	0.0081	±	0.0015	0.448	±	0.161	52.1	±	9.5	376.1	±	135.4
1	1006-10	0.92	0.0817	±	0.0038	0.2351	±	0.0060	2.647	±	0.141	1,361.1	±	34.6	1,313.8	±	69.8
1	1006-11	0.24	0.0914	±	0.0303	0.0135	±	0.0013	0.170	±	0.059	86.5	±	8.6	159.7	±	55.3
2	1006-12	0.61	0.0392	±	0.0438	0.0082	±	0.0016	0.044	±	0.050	52.7	±	10.1	44.1	±	50.0
	1006-13	0.82	0.0455	±	0.0113	0.0091	±	0.0005	0.057	±	0.015	58.7	±	3.3	56.6	±	14.4
1	1006-14	0.63	0.0903	±	0.0378	0.0096	±	0.0012	0.120	±	0.052	61.8	±	7.7	115.1	±	50.2
2	1006-15	0.71	0.0887	±	0.0548	0.0080	±	0.0014	0.098	±	0.063	51.4	±	9.3	94.8	±	61.0
	1006-16	0.51	0.0452	±	0.0155	0.0081	±	0.0006	0.051	±	0.018	52.2	±	3.8	50.2	±	17.5
2	1006-22	0.49	0.0447	±	0.0156	0.0080	±	0.0013	0.050	±	0.019	51.7	±	8.4	49.2	±	18.9
	1006-29	0.66	0.0395	±	0.0136	0.0088	±	0.0006	0.048	±	0.017	56.3	±	3.7	47.4	±	16.6
2	1006-34	0.72	0.0684	±	0.0470	0.0101	±	0.0017	0.095	±	0.067	64.7	±	10.9	92.2	±	65.3
2	1006-35	1.15	0.0589	±	0.0403	0.0095	±	0.0015	0.077	±	0.054	61.0	±	9.5	75.5	±	53.0
	1006-36	0.57	0.0440	±	0.0122	0.0082	±	0.0005	0.050	±	0.014	52.7	±	3.1	49.4	±	13.9
1	1006-37	0.66	0.1384	±	0.0761	0.0116	±	0.0022	0.221	±	0.129	74.3	±	14.1	202.8	±	118.0
1	1006-38	1.10	0.1657	±	0.0455	0.0119	±	0.0012	0.271	±	0.080	76.0	±	8.0	243.5	±	71.6
	1006-39	0.46	0.0492	±	0.0156	0.0084	±	0.0006	0.057	±	0.018	54.1	±	3.8	56.4	±	18.3
2	1006-40	0.62	0.0390	±	0.0281	0.0105	±	0.0014	0.057	±	0.042	67.6	±	9.0	56.0	±	41.0

e) PMN dataset

(1 marks data with probability of concordance < 0.1; 2 marks data with error > 10.0 %)

	Sample Name	Th/U	207Pb/206Pb		Error 2σ	206Pb/238U		Error 2σ	207Pb/235U		Error 2σ	238U-206Pb age (Ma)		Error 2σ	235U-207Pb age (Ma)		Error 2σ
	13IA02-1	0.71	0.0624	±	0.0214	0.0076	±	0.0006	0.066	±	0.023	49.0	±	3.8	64.6	±	22.7
	13IA02-2	0.58	0.0488	±	0.0186	0.0079	±	0.0006	0.053	±	0.021	50.7	±	3.8	52.5	±	20.4
	13IA02-3	0.57	0.0440	±	0.0090	0.0077	±	0.0004	0.047	±	0.010	49.5	±	2.5	46.4	±	9.7
1	13IA02-4	0.53	0.2635	±	0.0442	0.0078	±	0.0006	0.285	±	0.053	50.3	±	4.1	254.4	±	47.3
	13IA02-5	0.82	0.0414	±	0.0263	0.0100	±	0.0010	0.057	±	0.037	64.4	±	6.1	56.6	±	36.4
	13IA02-6	0.37	0.0440	±	0.0150	0.0074	±	0.0005	0.045	±	0.016	47.6	±	3.2	44.7	±	15.5
	13IA02-7	0.91	0.0549	±	0.0171	0.0082	±	0.0006	0.062	±	0.020	52.9	±	3.7	61.4	±	19.6
	13IA02-8	0.68	0.0513	±	0.0202	0.0080	±	0.0006	0.056	±	0.023	51.1	±	4.0	55.6	±	22.4
1	13IA02-9	0.51	0.1521	±	0.0458	0.0094	±	0.0009	0.198	±	0.063	60.5	±	6.1	183.1	±	58.1
1	13IA02-10	0.67	0.2440	±	0.0306	0.0078	±	0.0005	0.261	±	0.037	49.9	±	3.3	235.7	±	33.4
	13IA02-11	0.77	0.0510	±	0.0192	0.0076	±	0.0006	0.053	±	0.020	48.8	±	3.7	52.8	±	20.2
2	13IA02-12	0.84	0.0417	±	0.0335	0.0084	±	0.0009	0.048	±	0.039	53.9	±	5.5	47.9	±	38.7

	Sample Name	Th/U	207Pb/206Pb		Error 2σ	206Pb/238U		Error 2σ	207Pb/235U		Error 2σ	238U-206Pb age (Ma)		Error 2σ	235U-207Pb age (Ma)		Error 2σ
	13IA02-13	1.22	0.0473	±	0.0139	0.0072	±	0.0005	0.047	±	0.014	46.1	±	3.0	46.5	±	14.0
	13IA02-14	0.41	0.0534	±	0.0177	0.0077	±	0.0006	0.057	±	0.019	49.5	±	3.6	56.1	±	19.1
	13IA02-15	0.79	0.0494	±	0.0096	0.0080	±	0.0004	0.054	±	0.011	51.1	±	2.8	53.6	±	10.8
1	13IA02-16	0.54	0.0712	±	0.0109	0.0081	±	0.0004	0.079	±	0.013	52.0	±	2.8	77.6	±	12.7
1	13IA02-17	0.51	0.0807	±	0.0162	0.0086	±	0.0005	0.096	±	0.020	55.4	±	3.1	93.1	±	19.5
1	13IA02-18	0.52	0.0710	±	0.0183	0.0076	±	0.0005	0.074	±	0.020	48.6	±	3.2	72.6	±	19.3
	13IA02-19	0.75	0.0646	±	0.0242	0.0097	±	0.0009	0.086	±	0.033	62.0	±	5.5	83.8	±	32.3
1	13IA02-20	0.10	0.0612	±	0.0020	0.0345	±	0.0006	0.291	±	0.011	218.8	±	3.9	259.5	±	9.8
	13IA02-21	0.46	0.0466	±	0.0138	0.0080	±	0.0005	0.051	±	0.015	51.1	±	3.1	50.6	±	15.3
1	13IA02-22	0.39	0.0662	±	0.0172	0.0074	±	0.0005	0.067	±	0.018	47.5	±	3.1	66.3	±	17.8
	13IA04-1	0.42	0.0629	±	0.0220	0.0091	±	0.0007	0.079	±	0.028	58.6	±	4.8	77.4	±	27.8
	13IA04-2	0.65	0.0528	±	0.0030	0.0507	±	0.0009	0.369	±	0.022	319.0	±	5.9	319.1	±	19.3
	13IA04-3	0.46	0.0571	±	0.0184	0.0090	±	0.0007	0.071	±	0.024	58.1	±	4.2	69.9	±	23.1
	13IA04-4	0.63	0.0613	±	0.0227	0.0087	±	0.0007	0.074	±	0.028	56.0	±	4.7	72.2	±	27.4
1	13IA04-5	0.72	0.0702	±	0.0165	0.0077	±	0.0005	0.074	±	0.018	49.4	±	3.0	72.9	±	17.6
	13IA04-6	0.32	0.0514	±	0.0097	0.0097	±	0.0004	0.069	±	0.013	62.4	±	2.7	67.8	±	13.1
	13IA04-7	0.83	0.0433	±	0.0108	0.0120	±	0.0006	0.072	±	0.018	77.1	±	3.9	70.4	±	17.9
	13IA04-8	0.61	0.0522	±	0.0238	0.0081	±	0.0008	0.058	±	0.027	51.9	±	4.9	57.4	±	26.7
	13IA04-9	0.51	0.0484	±	0.0273	0.0077	±	0.0008	0.052	±	0.030	49.5	±	5.0	51.0	±	29.2
1	13IA04-10	0.65	0.0284	±	0.0214	0.0084	±	0.0008	0.033	±	0.025	53.7	±	5.1	32.7	±	24.9
	13IA04-11	0.52	0.0602	±	0.0248	0.0078	±	0.0007	0.065	±	0.027	50.3	±	4.4	63.9	±	26.9
1	13IA04-12	0.58	0.2797	±	0.0668	0.0076	±	0.0008	0.292	±	0.077	48.6	±	5.3	260.2	±	68.3
	13IA04-13	0.61	0.0469	±	0.0273	0.0078	±	0.0008	0.051	±	0.030	50.4	±	5.1	50.2	±	29.7
	13IA04-14	0.69	0.0531	±	0.0231	0.0082	±	0.0007	0.060	±	0.027	52.6	±	4.6	59.1	±	26.2
1	13IA04-15	1.11	0.0206	±	0.0275	0.0084	±	0.0010	0.024	±	0.032	53.8	±	6.2	23.8	±	32.0
2	13IA04-16	0.75	0.0487	±	0.0334	0.0086	±	0.0010	0.058	±	0.040	55.4	±	6.4	57.2	±	39.8
2	13IA04-17	0.39	0.0575	±	0.0220	0.0084	±	0.0018	0.066	±	0.029	53.6	±	11.5	65.2	±	28.5
	13IA04-18	1.06	0.0595	±	0.0180	0.0077	±	0.0006	0.063	±	0.020	49.3	±	3.6	62.1	±	19.4
	13IA11-1	0.70	0.0520	±	0.0114	0.0123	±	0.0006	0.088	±	0.020	79.0	±	4.1	86.0	±	19.3
	13IA11-2	0.41	0.0491	±	0.0230	0.0091	±	0.0009	0.062	±	0.029	58.3	±	5.8	60.6	±	29.0
1	13IA11-3	0.55	0.0653	±	0.0125	0.0120	±	0.0006	0.108	±	0.021	76.8	±	3.9	104.1	±	20.5
	13IA11-4	0.60	0.0477	±	0.0088	0.0113	±	0.0005	0.074	±	0.014	72.3	±	3.1	72.6	±	13.8
	13IA11-5	0.43	0.0556	±	0.0142	0.0088	±	0.0005	0.067	±	0.018	56.3	±	3.4	66.1	±	17.4
	13IA11-6	0.64	0.0478	±	0.0071	0.0112	±	0.0004	0.074	±	0.011	71.9	±	2.6	72.4	±	11.1
1	13IA11-7	0.59	0.0426	±	0.0059	0.0116	±	0.0004	0.068	±	0.010	74.4	±	2.5	66.9	±	9.5
	13IA11-8	0.47	0.0481	±	0.0055	0.0114	±	0.0004	0.076	±	0.009	73.0	±	2.3	73.9	±	8.8
	13IA11-17	0.48	0.0462	±	0.0079	0.0095	±	0.0004	0.061	±	0.011	61.1	±	2.4	59.8	±	10.5

	Sample Name	Th/U	207Pb/206Pb		Error 2σ	206Pb/238U		Error 2σ	207Pb/235U		Error 2σ	238U-206Pb age (Ma)		Error 2σ	235U-207Pb age (Ma)		Error 2σ
[1]	13IA11-18	0.74	0.0312	±	0.0174	0.0084	±	0.0008	0.036	±	0.020	53.7	±	5.0	35.9	±	20.3
	13IA11-19	0.93	0.0592	±	0.0171	0.0090	±	0.0006	0.073	±	0.022	57.6	±	4.1	71.8	±	21.4
	13IA11-20	0.97	0.0407	±	0.0156	0.0093	±	0.0007	0.052	±	0.020	59.4	±	4.5	51.5	±	20.1
	13IA11-21	1.04	0.0406	±	0.0141	0.0095	±	0.0007	0.053	±	0.019	60.7	±	4.2	52.4	±	18.6
	13IA11-22	0.61	0.0563	±	0.0141	0.0094	±	0.0006	0.073	±	0.019	60.0	±	3.6	71.1	±	18.3
	13IA11-23	0.92	0.0406	±	0.0130	0.0086	±	0.0006	0.048	±	0.016	55.4	±	3.6	47.9	±	15.6
[1]	13IA11-24	0.47	0.0611	±	0.0085	0.0523	±	0.0020	0.441	±	0.064	328.8	±	12.5	370.9	±	53.4
	13IA11-25	0.16	0.0544	±	0.0044	0.0428	±	0.0011	0.321	±	0.027	270.2	±	6.7	282.7	±	23.8
	13IA11-26	0.53	0.0443	±	0.0098	0.0127	±	0.0006	0.078	±	0.017	81.4	±	3.6	76.0	±	17.1
	13IA11-27	0.86	0.0402	±	0.0335	0.0081	±	0.0008	0.045	±	0.037	51.7	±	5.1	44.3	±	37.2
	13IA11-28	0.70	0.0377	±	0.0218	0.0091	±	0.0007	0.047	±	0.028	58.2	±	4.5	46.8	±	27.3
[1]	13IA11-29	0.26	0.0673	±	0.0134	0.0084	±	0.0004	0.078	±	0.016	53.9	±	2.6	76.2	±	15.6
	13IA11-30	0.75	0.0419	±	0.0200	0.0091	±	0.0007	0.052	±	0.025	58.1	±	4.2	51.8	±	25.0
	13IA11-32	0.77	0.0577	±	0.0196	0.0079	±	0.0005	0.063	±	0.022	50.6	±	3.4	61.8	±	21.4
	13IA11-33	0.56	0.0458	±	0.0144	0.0083	±	0.0006	0.052	±	0.017	53.1	±	3.6	51.7	±	16.6
[1]	13IA11-34	0.81	0.0703	±	0.0213	0.0075	±	0.0006	0.073	±	0.023	48.4	±	3.8	71.6	±	22.5
[2]	13IA11-35	0.87	0.0663	±	0.0294	0.0078	±	0.0008	0.071	±	0.032	50.0	±	5.3	69.8	±	31.8
	13IA11-36	0.81	0.0396	±	0.0170	0.0078	±	0.0006	0.043	±	0.019	50.1	±	4.1	42.4	±	18.5
	13IA11-37	1.05	0.0498	±	0.0184	0.0080	±	0.0006	0.055	±	0.021	51.4	±	4.1	54.3	±	20.6
	13IA11-38	0.73	0.0433	±	0.0157	0.0076	±	0.0006	0.046	±	0.017	49.0	±	3.7	45.3	±	16.8
	13IA11-39	1.30	0.0485	±	0.0130	0.0076	±	0.0005	0.051	±	0.014	48.6	±	3.0	50.1	±	13.8
[1]	13IA11-40	0.80	0.3932	±	0.0441	0.0154	±	0.0010	0.836	±	0.108	98.6	±	6.3	616.8	±	79.7
	13IA11-41	1.01	0.0474	±	0.0165	0.0071	±	0.0005	0.046	±	0.017	45.7	±	3.3	46.1	±	16.4
	IA97-1	0.70	0.0469	±	0.0032	0.0098	±	0.0003	0.063	±	0.005	62.8	±	1.7	62.3	±	4.5
[1]	IA97-2	0.81	0.0710	±	0.0155	0.0082	±	0.0005	0.080	±	0.018	52.4	±	3.1	78.0	±	17.6
[1]	IA97-3	1.10	0.0546	±	0.0023	0.0411	±	0.0010	0.309	±	0.015	259.6	±	6.3	273.5	±	13.4
	IA97-4	0.49	0.0492	±	0.0083	0.0108	±	0.0005	0.074	±	0.013	69.5	±	3.0	72.0	±	12.6
	IA97-5	0.45	0.0490	±	0.0079	0.0077	±	0.0003	0.052	±	0.009	49.5	±	2.1	51.6	±	8.6
[1]	IA97-6	0.67	0.0634	±	0.0096	0.0120	±	0.0005	0.104	±	0.017	76.6	±	3.3	100.9	±	16.0
	IA97-7	1.33	0.0540	±	0.0135	0.0083	±	0.0005	0.062	±	0.016	53.3	±	3.2	60.9	±	15.7
[1]	IA97-8	0.46	0.0914	±	0.0178	0.0099	±	0.0006	0.125	±	0.025	63.4	±	3.9	119.2	±	24.3
	IA97-9	0.54	0.0398	±	0.0105	0.0120	±	0.0006	0.066	±	0.018	77.0	±	4.0	64.9	±	17.5
	IA97-10	0.55	0.0518	±	0.0108	0.0123	±	0.0006	0.087	±	0.019	78.5	±	3.7	85.1	±	18.2
[1]	IA97-11	0.71	0.1555	±	0.0173	0.0144	±	0.0006	0.308	±	0.037	91.9	±	3.9	272.7	±	32.4
	IA97-12	0.86	0.0513	±	0.0146	0.0078	±	0.0005	0.055	±	0.016	50.2	±	3.1	54.7	±	15.9
	IA97-13	0.94	0.0487	±	0.0204	0.0091	±	0.0008	0.061	±	0.026	58.2	±	4.9	59.9	±	25.6
[2]	IA97-14	0.61	0.0710	±	0.0501	0.0080	±	0.0012	0.078	±	0.056	51.4	±	7.7	76.6	±	55.2

	Sample Name	Th/U	207Pb/206Pb		Error 2σ	206Pb/238U		Error 2σ	207Pb/235U		Error 2σ	238U-206Pb age (Ma)		Error 2σ	235U-207Pb age (Ma)		Error 2σ
1	IA97-15	0.36	0.0653	±	0.0037	0.0603	±	0.0011	0.543	±	0.032	377.3	±	6.9	440.5	±	26.2
	IA97-16	1.07	0.0524	±	0.0215	0.0092	±	0.0008	0.067	±	0.028	59.2	±	5.1	65.6	±	27.5
1	IA97-17	0.71	0.0585	±	0.0085	0.0096	±	0.0004	0.078	±	0.012	61.8	±	2.3	75.9	±	11.4
	IA97-18	0.87	0.0510	±	0.0133	0.0084	±	0.0005	0.059	±	0.016	54.1	±	3.2	58.4	±	15.6
1	IA97-19	0.84	0.0792	±	0.0201	0.0102	±	0.0007	0.111	±	0.029	65.3	±	4.5	107.1	±	28.2
	IA97-21	0.50	0.0630	±	0.0237	0.0078	±	0.0007	0.068	±	0.026	50.1	±	4.4	66.7	±	25.7
	IA97-22	0.82	0.0590	±	0.0142	0.0083	±	0.0005	0.067	±	0.017	53.0	±	3.1	65.9	±	16.4
	IA97-23	0.30	0.0494	±	0.0068	0.0087	±	0.0003	0.059	±	0.008	55.8	±	1.9	58.4	±	8.3
1	IA97-24	0.60	0.0300	±	0.0167	0.0079	±	0.0007	0.033	±	0.018	50.8	±	4.4	32.7	±	18.4

f) LQP dataset

(1 marks data with probability of concordance < 0.1; 2 marks data with error > 10.0 %)

	Sample Name	Th/U	207Pb/206Pb		Error 2σ	206Pb/238U		Error 2σ	207Pb/235U		Error 2σ	238U-206Pb age (Ma)		Error 2σ	235U-207Pb age (Ma)		Error 2σ
	13IA05-1	0.95	0.0470	±	0.0191	0.0075	±	0.0006	0.048	±	0.020	47.9	±	3.9	48.0	±	19.9
	13IA05-2	0.77	0.0522	±	0.0147	0.0077	±	0.0005	0.056	±	0.016	49.7	±	3.1	55.0	±	15.9
1	13IA05-3	1.60	0.6327	±	0.0280	0.0299	±	0.0011	2.609	±	0.149	189.9	±	6.9	1,303.1	±	74.7
	13IA05-4	0.63	0.0518	±	0.0105	0.0115	±	0.0006	0.082	±	0.017	73.9	±	3.7	80.4	±	16.8
1	13IA05-5	0.72	0.0895	±	0.0252	0.0103	±	0.0008	0.127	±	0.037	65.9	±	5.2	121.1	±	35.4
	13IA05-6	0.65	0.0478	±	0.0070	0.0118	±	0.0005	0.078	±	0.012	75.6	±	3.0	76.0	±	11.5
2	13IA05-7	0.68	0.0460	±	0.0332	0.0075	±	0.0008	0.047	±	0.035	47.9	±	5.4	46.9	±	34.2
	13IA05-8	1.16	0.0556	±	0.0146	0.0082	±	0.0005	0.063	±	0.017	52.8	±	3.2	62.2	±	16.7
1	13IA05-9	0.60	0.1018	±	0.0276	0.0083	±	0.0007	0.117	±	0.033	53.5	±	4.3	112.4	±	31.8
	13IA05-10	0.68	0.0559	±	0.0173	0.0078	±	0.0005	0.060	±	0.019	50.1	±	3.4	59.3	±	18.8
	13IA05-11	0.59	0.0500	±	0.0087	0.0118	±	0.0005	0.082	±	0.015	75.9	±	2.9	79.7	±	14.2
	13IA05-12	0.45	0.0430	±	0.0109	0.0120	±	0.0006	0.071	±	0.018	76.7	±	3.8	69.6	±	18.0
1	13IA05-13	0.53	0.0630	±	0.0111	0.0123	±	0.0005	0.107	±	0.019	79.0	±	3.4	103.2	±	18.8
	13IA05-14	1.26	0.0440	±	0.0116	0.0084	±	0.0004	0.051	±	0.014	54.1	±	2.7	50.6	±	13.5
1	13IA05-15	0.77	0.2341	±	0.0347	0.0080	±	0.0005	0.257	±	0.042	51.1	±	3.3	232.0	±	37.6
	13IA05-16	0.47	0.0501	±	0.0057	0.0144	±	0.0004	0.100	±	0.012	92.4	±	2.6	96.6	±	11.4
	13IA05-17	0.88	0.0512	±	0.0172	0.0095	±	0.0006	0.067	±	0.023	60.8	±	4.0	65.8	±	22.5
1	13IA05-18	0.49	0.0809	±	0.0123	0.0108	±	0.0005	0.120	±	0.019	69.2	±	3.0	115.4	±	18.3
	13IA05-19	1.47	0.0414	±	0.0128	0.0080	±	0.0004	0.046	±	0.014	51.6	±	2.8	45.6	±	14.3
1	13IA05-20	0.96	0.0534	±	0.0066	0.0118	±	0.0004	0.087	±	0.011	75.5	±	2.3	84.4	±	10.7
	13IA05-21	0.47	0.0481	±	0.0111	0.0134	±	0.0006	0.089	±	0.021	85.6	±	4.0	86.3	±	20.3
1	13IA05-22	0.40	0.0652	±	0.0133	0.0084	±	0.0004	0.076	±	0.016	54.0	±	2.6	74.0	±	15.5
	13IA05-23	0.93	0.0599	±	0.0218	0.0085	±	0.0006	0.070	±	0.026	54.7	±	3.9	69.1	±	25.6

Sample Name	Th/U	207Pb/206Pb		Error 2σ	206Pb/238U		Error 2σ	207Pb/235U		Error 2σ	238U-206Pb age (Ma)		Error 2σ	235U-207Pb age (Ma)		Error 2σ
13IA05-24	0.44	0.0507	±	0.0041	0.0117	±	0.0003	0.082	±	0.007	74.9	±	1.8	79.7	±	6.6
13IA05-25	0.85	0.0474	±	0.0208	0.0086	±	0.0006	0.056	±	0.025	55.5	±	4.1	55.8	±	24.8
13IA05-26	0.82	0.0492	±	0.0195	0.0082	±	0.0006	0.056	±	0.022	52.6	±	3.7	55.0	±	22.1
[1] 13IA05-27	0.74	0.0150	±	0.0066	0.0455	±	0.0022	0.094	±	0.041	287.0	±	13.7	91.5	±	40.2
13IA05-29	0.82	0.0498	±	0.0122	0.0086	±	0.0005	0.059	±	0.015	55.4	±	2.9	58.4	±	14.6
13IA05-30	1.16	0.0399	±	0.0125	0.0080	±	0.0005	0.044	±	0.014	51.6	±	3.0	43.9	±	14.0
13IA05-31	0.66	0.0541	±	0.0106	0.0080	±	0.0004	0.060	±	0.012	51.6	±	2.4	59.1	±	11.9
[1] 13IA05-32	0.78	0.0597	±	0.0115	0.0078	±	0.0004	0.064	±	0.013	50.0	±	2.4	63.0	±	12.6
13IA05-33	0.51	0.0488	±	0.0122	0.0104	±	0.0006	0.070	±	0.018	66.7	±	3.6	68.7	±	17.6
13IA05-34	0.52	0.0509	±	0.0094	0.0115	±	0.0005	0.080	±	0.015	73.5	±	3.2	78.6	±	14.9
13IA05-43	1.12	0.0611	±	0.0185	0.0082	±	0.0006	0.069	±	0.021	52.6	±	3.8	67.8	±	21.0
[1] 13IA05-44	0.94	0.0694	±	0.0261	0.0080	±	0.0007	0.076	±	0.030	51.2	±	4.6	74.6	±	28.9
[1] 13IA05-45	1.05	0.1570	±	0.0128	0.0081	±	0.0003	0.176	±	0.016	52.3	±	2.1	164.9	±	15.0
[1] 13IA05-47	0.59	0.1781	±	0.0292	0.0113	±	0.0008	0.278	±	0.049	72.6	±	4.9	249.2	±	44.3
13IA05-48	0.51	0.0412	±	0.0084	0.0117	±	0.0005	0.066	±	0.014	74.8	±	3.5	65.2	±	13.6
[1] 13IA05-49	0.66	0.0954	±	0.0263	0.0086	±	0.0007	0.114	±	0.033	55.4	±	4.5	109.2	±	31.3
[1] 13IA05-50	0.76	0.0709	±	0.0145	0.0078	±	0.0004	0.076	±	0.016	49.8	±	2.8	74.2	±	15.8
[1] 13IA10-1	0.43	0.0281	±	0.0121	0.0077	±	0.0005	0.030	±	0.013	49.6	±	3.4	29.9	±	13.1
13IA10-2	0.47	0.0441	±	0.0180	0.0078	±	0.0006	0.047	±	0.020	49.9	±	4.0	46.9	±	19.4
13IA10-3	0.55	0.0535	±	0.0219	0.0076	±	0.0007	0.056	±	0.024	49.0	±	4.3	55.5	±	23.2
[2] 13IA10-4	0.72	0.0695	±	0.0365	0.0090	±	0.0011	0.086	±	0.046	57.5	±	7.0	83.6	±	45.1
13IA10-5	0.69	0.0434	±	0.0162	0.0082	±	0.0006	0.049	±	0.019	52.9	±	3.9	48.9	±	18.6
[1] 13IA10-6	0.50	0.0660	±	0.0141	0.0077	±	0.0004	0.070	±	0.016	49.6	±	2.8	68.9	±	15.2
13IA10-7	0.62	0.0401	±	0.0152	0.0087	±	0.0006	0.048	±	0.018	55.7	±	4.0	47.6	±	18.3
[1] 13IA10-8	0.59	0.0692	±	0.0209	0.0081	±	0.0006	0.078	±	0.024	52.2	±	4.0	75.9	±	23.6
13IA10-9	0.89	0.0385	±	0.0160	0.0084	±	0.0005	0.045	±	0.019	54.0	±	3.4	44.3	±	18.7
13IA10-10	0.76	0.0531	±	0.0157	0.0094	±	0.0006	0.069	±	0.021	60.6	±	3.6	67.9	±	20.5
13IA10-11	0.63	0.0455	±	0.0164	0.0075	±	0.0005	0.047	±	0.017	48.0	±	3.0	46.5	±	17.1
13IA10-12	0.23	0.0490	±	0.0057	0.0343	±	0.0012	0.232	±	0.028	217.6	±	7.4	211.7	±	25.6
13IA10-13	0.71	0.0414	±	0.0188	0.0075	±	0.0005	0.043	±	0.020	48.4	±	3.3	42.7	±	19.6
[2] 13IA10-14	0.75	0.0588	±	0.0605	0.0092	±	0.0012	0.074	±	0.077	58.9	±	7.6	72.9	±	75.5
[1] 13IA10-15	0.60	0.0712	±	0.0216	0.0074	±	0.0005	0.072	±	0.022	47.4	±	3.2	71.0	±	22.0
13IA10-16	1.78	0.0527	±	0.0084	0.0075	±	0.0003	0.054	±	0.009	48.1	±	2.0	53.8	±	8.8
13IA10-17	0.77	0.0396	±	0.0109	0.0086	±	0.0005	0.047	±	0.013	55.0	±	3.2	46.4	±	13.1
[1] 13IA10-18	0.93	0.0562	±	0.0094	0.0080	±	0.0004	0.062	±	0.011	51.1	±	2.4	60.8	±	10.6
[1] 13IA10-19	0.62	0.1311	±	0.0301	0.0087	±	0.0007	0.158	±	0.038	56.0	±	4.5	148.8	±	36.2
13IA10-20	0.55	0.0610	±	0.0187	0.0080	±	0.0006	0.067	±	0.021	51.3	±	3.8	66.0	±	20.9

	Sample Name	Th/U	207Pb/206Pb		Error 2σ	206Pb/238U		Error 2σ	207Pb/235U		Error 2σ	238U-206Pb age (Ma)		Error 2σ	235U-207Pb age (Ma)		Error 2σ
[1]	13IA10-21	0.72	0.0801	±	0.0240	0.0079	±	0.0006	0.087	±	0.027	50.7	±	4.2	85.0	±	26.4
[1]	Mo6-2	0.95	0.1503	±	0.0311	0.0076	±	0.0006	0.157	±	0.035	48.7	±	3.7	148.3	±	32.7
[1]	Mo6-3	0.72	0.0641	±	0.0136	0.0082	±	0.0004	0.072	±	0.016	52.5	±	2.8	70.9	±	15.5
	Mo6-4	0.46	0.0611	±	0.0179	0.0084	±	0.0006	0.070	±	0.021	53.7	±	3.8	69.1	±	20.9
[1]	Mo6-5	0.72	0.1080	±	0.0240	0.0087	±	0.0006	0.130	±	0.030	56.0	±	3.9	124.0	±	28.9
[1]	Mo6-6	1.25	0.3145	±	0.0279	0.0150	±	0.0007	0.652	±	0.065	96.1	±	4.5	509.4	±	51.0
[1]	Mo6-7	1.33	0.0690	±	0.0127	0.0077	±	0.0004	0.073	±	0.014	49.6	±	2.5	72.0	±	13.7
[1]	Mo6-8	0.53	0.1399	±	0.0307	0.0082	±	0.0006	0.158	±	0.037	52.7	±	4.1	149.3	±	34.8
[1]	Mo6-9	0.74	0.1683	±	0.0230	0.0088	±	0.0005	0.205	±	0.031	56.8	±	3.3	189.6	±	28.2
	Mo6-10	0.51	0.0555	±	0.0122	0.0116	±	0.0007	0.089	±	0.020	74.5	±	4.2	86.5	±	19.7
[1]	Mo6-11	0.79	0.1259	±	0.0123	0.0119	±	0.0005	0.206	±	0.022	76.0	±	3.2	190.0	±	20.3
	Mo6-12	0.64	0.0455	±	0.0101	0.0114	±	0.0006	0.072	±	0.016	73.2	±	3.8	70.2	±	16.0
[1]	Mo6-13	1.01	0.0669	±	0.0192	0.0093	±	0.0007	0.086	±	0.026	59.9	±	4.4	83.8	±	24.9
[1]	Mo6-14	0.79	0.1509	±	0.0254	0.0090	±	0.0006	0.188	±	0.034	57.9	±	3.8	174.8	±	31.6
[1]	Mo6-15	1.45	0.1216	±	0.0199	0.0088	±	0.0005	0.147	±	0.026	56.2	±	3.4	139.2	±	24.3
	Mo6-16	0.70	0.0476	±	0.0081	0.0106	±	0.0005	0.070	±	0.012	68.3	±	3.1	68.6	±	12.1
[1]	Mo6-17	1.46	0.0628	±	0.0087	0.0139	±	0.0006	0.120	±	0.017	88.8	±	3.6	115.1	±	16.7
[1]	Mo6-18	0.47	0.0799	±	0.0027	0.1483	±	0.0035	1.634	±	0.067	891.5	±	21.0	983.2	±	40.5
	Mo6-19	0.52	0.0532	±	0.0145	0.0082	±	0.0005	0.060	±	0.017	52.4	±	3.3	59.0	±	16.5
[1]	Mo6-20	0.96	0.0928	±	0.0241	0.0086	±	0.0007	0.110	±	0.030	55.1	±	4.2	105.8	±	28.6
	Mo6-21	0.84	0.0615	±	0.0200	0.0105	±	0.0008	0.089	±	0.030	67.5	±	5.3	86.9	±	29.1
	Mo6-22	0.77	0.0512	±	0.0102	0.0082	±	0.0004	0.058	±	0.012	52.7	±	2.6	57.2	±	11.7
[1]	Mo6-23	0.56	0.0644	±	0.0084	0.0111	±	0.0004	0.098	±	0.013	70.9	±	2.7	95.0	±	12.9
[1]	Mo6-24	0.63	0.0376	±	0.0078	0.0114	±	0.0005	0.059	±	0.012	73.0	±	3.2	58.2	±	12.3
[1]	Mo6-25	1.01	0.1359	±	0.0207	0.0082	±	0.0005	0.153	±	0.025	52.5	±	3.0	144.7	±	23.5
[2]	Mo6-26	0.79	0.0595	±	0.0268	0.0077	±	0.0009	0.063	±	0.029	49.7	±	5.5	62.5	±	29.0
	Mo6-27	0.99	0.0486	±	0.0133	0.0079	±	0.0005	0.053	±	0.015	50.5	±	3.2	52.1	±	14.6
[1]	Mo6-28	0.28	0.0636	±	0.0040	0.0379	±	0.0010	0.332	±	0.023	239.6	±	6.3	291.4	±	20.0
[1]	Mo6-29	0.25	0.0871	±	0.0072	0.0315	±	0.0010	0.378	±	0.034	200.0	±	6.3	325.8	±	28.9
[1]	Mo6-30	1.22	0.0868	±	0.0144	0.0081	±	0.0004	0.097	±	0.017	52.3	±	2.7	94.4	±	16.4
[1]	Mo6-31	0.57	0.2639	±	0.0295	0.0110	±	0.0006	0.401	±	0.050	70.7	±	3.9	342.4	±	42.7
	IA76-1	0.66	0.0473	±	0.0074	0.0113	±	0.0005	0.074	±	0.012	72.5	±	3.1	72.3	±	11.8
[1]	IA76-2	0.62	0.3764	±	0.0393	0.0136	±	0.0008	0.706	±	0.085	87.1	±	5.3	542.6	±	65.5
[1]	IA76-3	0.55	0.0449	±	0.0085	0.0500	±	0.0024	0.309	±	0.060	314.7	±	15.2	273.8	±	53.3
	IA76-4	0.45	0.0524	±	0.0065	0.0488	±	0.0019	0.352	±	0.046	307.0	±	12.1	306.4	±	39.9
[1]	IA76-5	0.16	0.2605	±	0.0096	0.0154	±	0.0005	0.553	±	0.027	98.4	±	3.0	446.8	±	21.5
[1]	IA76-6	0.87	0.1218	±	0.0505	0.0082	±	0.0011	0.138	±	0.060	52.9	±	7.4	131.5	±	57.5

	Sample Name	Th/U	207Pb/206Pb		Error 2σ	206Pb/238U		Error 2σ	207Pb/235U		Error 2σ	238U-206Pb age (Ma)		Error 2σ	235U-207Pb age (Ma)		Error 2σ
	IA76-7	0.81	0.0504	±	0.0214	0.0108	±	0.0010	0.075	±	0.033	69.2	±	6.6	73.4	±	32.0
2	IA76-8	1.00	0.0455	±	0.0225	0.0096	±	0.0010	0.060	±	0.030	61.4	±	6.3	59.2	±	29.9
	IA76-9	1.16	0.0442	±	0.0151	0.0083	±	0.0006	0.050	±	0.018	53.0	±	3.7	49.8	±	17.4
	IA76-10	2.80	0.0453	±	0.0142	0.0082	±	0.0005	0.051	±	0.016	52.8	±	3.5	50.9	±	16.3
1	IA76-11	0.83	0.0786	±	0.0232	0.0081	±	0.0006	0.088	±	0.027	51.9	±	4.1	85.2	±	26.0
	IA76-12	0.50	0.0553	±	0.0040	0.0462	±	0.0010	0.352	±	0.026	291.2	±	6.0	306.4	±	22.9
1	IA76-13	1.09	0.0625	±	0.0167	0.0082	±	0.0005	0.071	±	0.019	52.6	±	3.4	69.2	±	19.0
	IA76-14	0.68	0.0455	±	0.0177	0.0091	±	0.0007	0.057	±	0.023	58.4	±	4.7	56.4	±	22.4
1	IA76-15	0.84	0.0902	±	0.0352	0.0079	±	0.0009	0.099	±	0.040	50.9	±	5.6	95.5	±	38.7
1	IA76-16	0.95	0.0746	±	0.0179	0.0104	±	0.0007	0.107	±	0.027	66.8	±	4.3	103.4	±	25.7
1	IA76-17	0.53	0.3310	±	0.0399	0.0077	±	0.0005	0.353	±	0.047	49.6	±	3.0	306.7	±	41.3
	IA76-18	0.50	0.0596	±	0.0173	0.0081	±	0.0005	0.067	±	0.020	52.0	±	3.4	65.5	±	19.5
	IA76-19	0.77	0.0533	±	0.0202	0.0096	±	0.0008	0.071	±	0.027	61.9	±	4.8	69.5	±	26.9
1	IA76-20	1.02	0.0418	±	0.0053	0.0116	±	0.0003	0.067	±	0.009	74.5	±	2.1	65.9	±	8.6
	IA76-21	0.56	0.0433	±	0.0079	0.0115	±	0.0004	0.068	±	0.013	73.5	±	2.8	67.1	±	12.5
1	IA76-22	0.62	0.0936	±	0.0178	0.0100	±	0.0006	0.129	±	0.026	64.3	±	3.6	123.5	±	24.5
	IA76-23	0.52	0.0437	±	0.0097	0.0123	±	0.0006	0.074	±	0.017	78.8	±	3.6	72.6	±	16.5
	IA76-24	0.49	0.0546	±	0.0129	0.0120	±	0.0006	0.090	±	0.022	76.8	±	4.1	87.7	±	21.2

g) PGD dataset

(1 marks data with probability of concordance < 0.1; 2 marks data with error > 10.0 %)

	Sample Name	Th/U	207Pb/206Pb		Error 2σ	206Pb/238U		Error 2σ	207Pb/235U		Error 2σ	238U-206Pb age (Ma)		Error 2σ	235U-207Pb age (Ma)		Error 2σ
1	IA37-1	0.57	0.0817	±	0.0307	0.0083	±	0.0009	0.094	±	0.037	53.4	±	5.6	91.0	±	35.5
2	IA37-2	0.77	0.0615	±	0.0493	0.0082	±	0.0015	0.069	±	0.057	52.5	±	9.8	68.1	±	56.0
2	IA37-3	0.60	0.0405	±	0.0512	0.0076	±	0.0017	0.042	±	0.054	48.7	±	11.0	42.2	±	54.1
2	IA37-4	0.63	0.0512	±	0.0443	0.0074	±	0.0013	0.052	±	0.046	47.2	±	8.7	51.4	±	45.5
1	IA37-5	0.44	0.0829	±	0.0240	0.0107	±	0.0009	0.123	±	0.037	68.8	±	5.7	117.4	±	35.4
1	IA37-6	0.69	0.0827	±	0.0322	0.0089	±	0.0010	0.102	±	0.041	57.2	±	6.2	98.4	±	39.8
1	IA37-7	0.79	0.1093	±	0.0330	0.0085	±	0.0008	0.128	±	0.041	54.6	±	5.3	122.5	±	38.9
1	IA37-8	0.84	0.1225	±	0.0358	0.0085	±	0.0008	0.144	±	0.044	54.5	±	5.4	136.2	±	42.0
1	IA37-18	1.32	0.0629	±	0.0166	0.0087	±	0.0006	0.076	±	0.021	56.0	±	3.7	74.1	±	20.1
1	IA37-19	0.36	0.0602	±	0.0044	0.0432	±	0.0011	0.359	±	0.028	272.8	±	6.7	311.5	±	24.2
1	IA37-20	0.64	0.0948	±	0.0338	0.0094	±	0.0010	0.122	±	0.045	60.1	±	6.2	117.3	±	43.5
2	IA37-21	0.66	0.0450	±	0.0251	0.0085	±	0.0009	0.053	±	0.030	54.7	±	5.9	52.3	±	29.7
	IA37-22	0.86	0.0576	±	0.0250	0.0094	±	0.0009	0.075	±	0.033	60.5	±	5.9	73.2	±	32.6
1	IA37-23	0.87	0.0710	±	0.0244	0.0094	±	0.0008	0.092	±	0.032	60.1	±	5.2	89.0	±	31.5

	Sample Name	Th/U	207Pb/206Pb		Error 2σ	206Pb/238U		Error 2σ	207Pb/235U		Error 2σ	238U-206Pb age (Ma)		Error 2σ	235U-207Pb age (Ma)		Error 2σ
1	IA37-24	0.96	0.0734	±	0.0296	0.0082	±	0.0008	0.083	±	0.035	52.8	±	5.4	81.1	±	33.7
	IA37-25	0.92	0.0453	±	0.0208	0.0083	±	0.0007	0.052	±	0.024	53.3	±	4.7	51.4	±	24.0
1	IA37-26	1.08	0.0966	±	0.0285	0.0080	±	0.0007	0.107	±	0.033	51.4	±	4.4	102.8	±	31.6
1	IA37-27	1.04	0.1880	±	0.0443	0.0082	±	0.0008	0.213	±	0.054	52.8	±	4.9	196.3	±	49.8
1	IA37-28	1.23	0.0884	±	0.0227	0.0080	±	0.0006	0.097	±	0.026	51.3	±	3.7	94.3	±	25.1
1	IA37-29	0.74	0.0810	±	0.0332	0.0083	±	0.0009	0.093	±	0.039	53.6	±	5.6	90.5	±	38.3
	IA37-30	1.24	0.0480	±	0.0159	0.0091	±	0.0006	0.060	±	0.020	58.3	±	4.0	59.3	±	20.0
1	IA37-31	0.92	0.0812	±	0.0276	0.0083	±	0.0007	0.092	±	0.032	53.0	±	4.7	89.8	±	31.5
	IA37-32	1.13	0.0599	±	0.0223	0.0078	±	0.0007	0.064	±	0.025	50.0	±	4.2	63.3	±	24.2
	IA47-1	0.90	0.0493	±	0.0165	0.0081	±	0.0007	0.055	±	0.019	52.0	±	4.8	54.3	±	18.9
	IA47-2	0.85	0.0449	±	0.0181	0.0085	±	0.0008	0.053	±	0.022	54.8	±	5.4	52.3	±	21.7
1	IA47-3	1.39	0.1099	±	0.0252	0.0086	±	0.0008	0.130	±	0.032	55.0	±	5.1	124.0	±	30.7
1	IA47-4	0.57	0.0687	±	0.0235	0.0087	±	0.0009	0.082	±	0.029	55.7	±	5.7	80.2	±	28.7
2	IA47-5	0.60	0.0346	±	0.0221	0.0087	±	0.0010	0.041	±	0.027	55.9	±	6.6	41.3	±	26.8
1	IA47-6	0.84	0.0917	±	0.0186	0.0081	±	0.0007	0.102	±	0.022	51.9	±	4.3	98.8	±	21.7
1	IA47-7	1.14	0.0634	±	0.0187	0.0078	±	0.0007	0.068	±	0.021	49.9	±	4.6	66.8	±	20.7
1	IA47-8	0.70	0.0781	±	0.0129	0.0098	±	0.0007	0.106	±	0.019	63.1	±	4.7	102.3	±	18.6
	IA47-9	1.15	0.0591	±	0.0204	0.0073	±	0.0006	0.059	±	0.021	46.9	±	3.9	58.7	±	20.8
1	IA47-10	0.89	0.0651	±	0.0148	0.0075	±	0.0005	0.067	±	0.016	47.9	±	3.2	65.8	±	15.6
1	IA47-11	0.89	0.1062	±	0.0260	0.0085	±	0.0007	0.125	±	0.032	54.6	±	4.5	119.3	±	30.9
1	IA47-12	1.08	0.0702	±	0.0228	0.0080	±	0.0007	0.077	±	0.026	51.3	±	4.4	75.6	±	25.4
	IA47-13	1.23	0.0576	±	0.0168	0.0081	±	0.0006	0.064	±	0.019	52.0	±	3.9	63.3	±	19.0
	IA47-14	0.61	0.0432	±	0.0159	0.0080	±	0.0006	0.048	±	0.018	51.5	±	4.0	47.4	±	17.8
1	IA47-15	1.80	0.1659	±	0.0270	0.0092	±	0.0007	0.210	±	0.038	59.0	±	4.3	193.7	±	34.6
1	IA47-16	1.06	0.2197	±	0.0393	0.0089	±	0.0008	0.268	±	0.053	56.9	±	4.8	241.3	±	47.8
1	IA47-17	0.93	0.1501	±	0.0315	0.0084	±	0.0007	0.173	±	0.039	53.7	±	4.4	162.0	±	36.5
1	IA47-18	0.79	0.1027	±	0.0275	0.0085	±	0.0007	0.121	±	0.034	54.6	±	4.8	115.5	±	32.6
	IA47-20	0.85	0.0634	±	0.0248	0.0090	±	0.0009	0.079	±	0.032	57.7	±	5.6	76.8	±	31.0
2	IA47-21	0.91	0.0664	±	0.0300	0.0073	±	0.0008	0.067	±	0.031	46.9	±	5.2	65.6	±	30.6
1	IA47-22	0.78	0.0728	±	0.0249	0.0084	±	0.0008	0.084	±	0.030	53.9	±	5.0	82.1	±	29.1
1	IA47-23	1.28	0.0777	±	0.0223	0.0077	±	0.0006	0.083	±	0.025	49.4	±	4.1	80.5	±	24.0
1	IA47-24	0.96	0.0716	±	0.0225	0.0080	±	0.0007	0.079	±	0.026	51.2	±	4.4	77.0	±	25.0
	IA47-25	1.04	0.0411	±	0.0203	0.0079	±	0.0007	0.045	±	0.022	50.4	±	4.5	44.2	±	22.2
1	IA47-26	1.02	0.1136	±	0.0237	0.0100	±	0.0007	0.156	±	0.034	63.9	±	4.5	147.2	±	32.4
1	IA47-27	0.87	0.1196	±	0.0335	0.0081	±	0.0007	0.134	±	0.040	52.3	±	4.8	127.9	±	37.8

CEF 800 m weighted mean plot

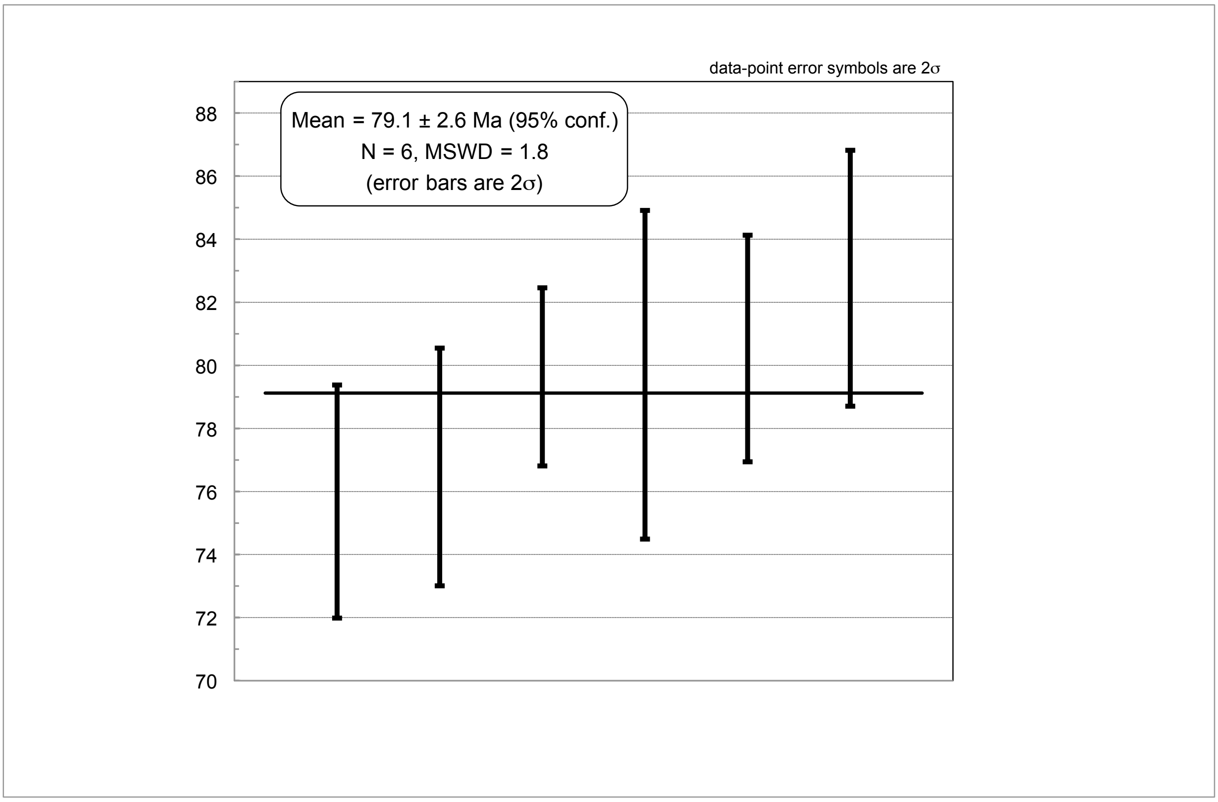

CEF Diorite weighted mean plot

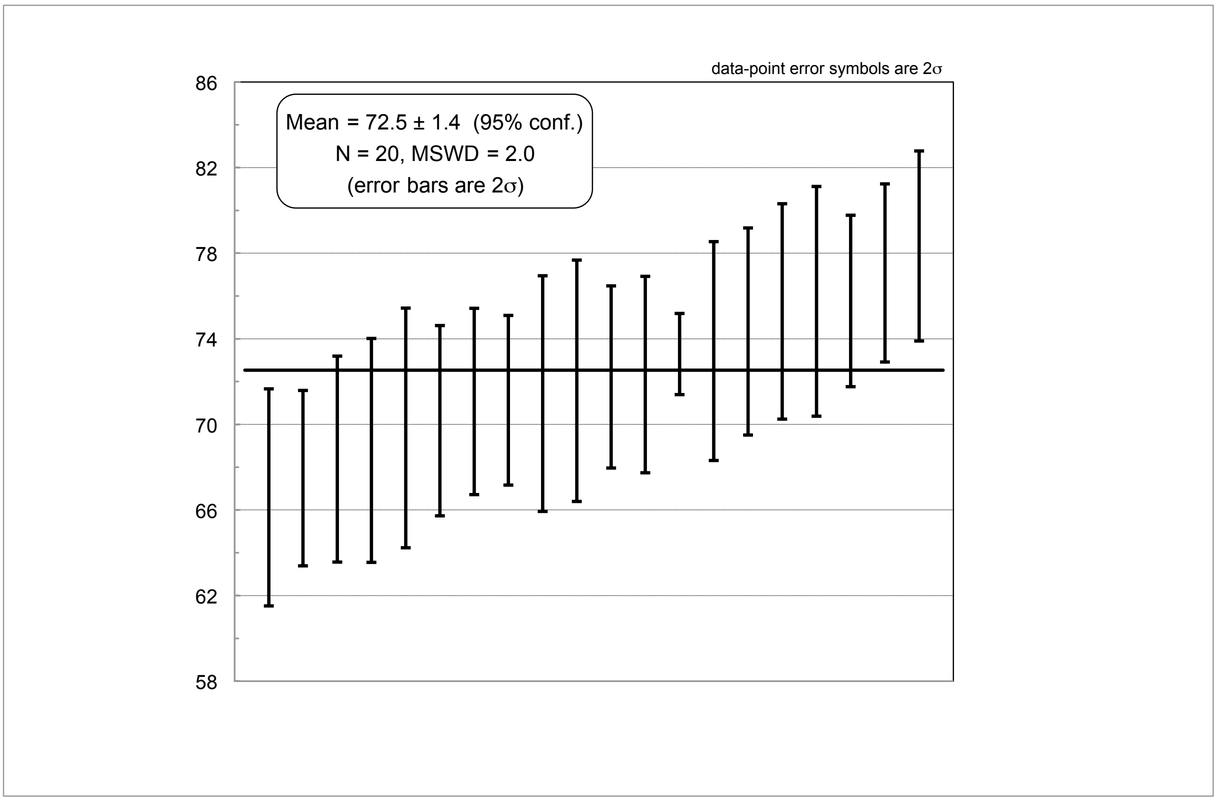

VBX weighted mean plot

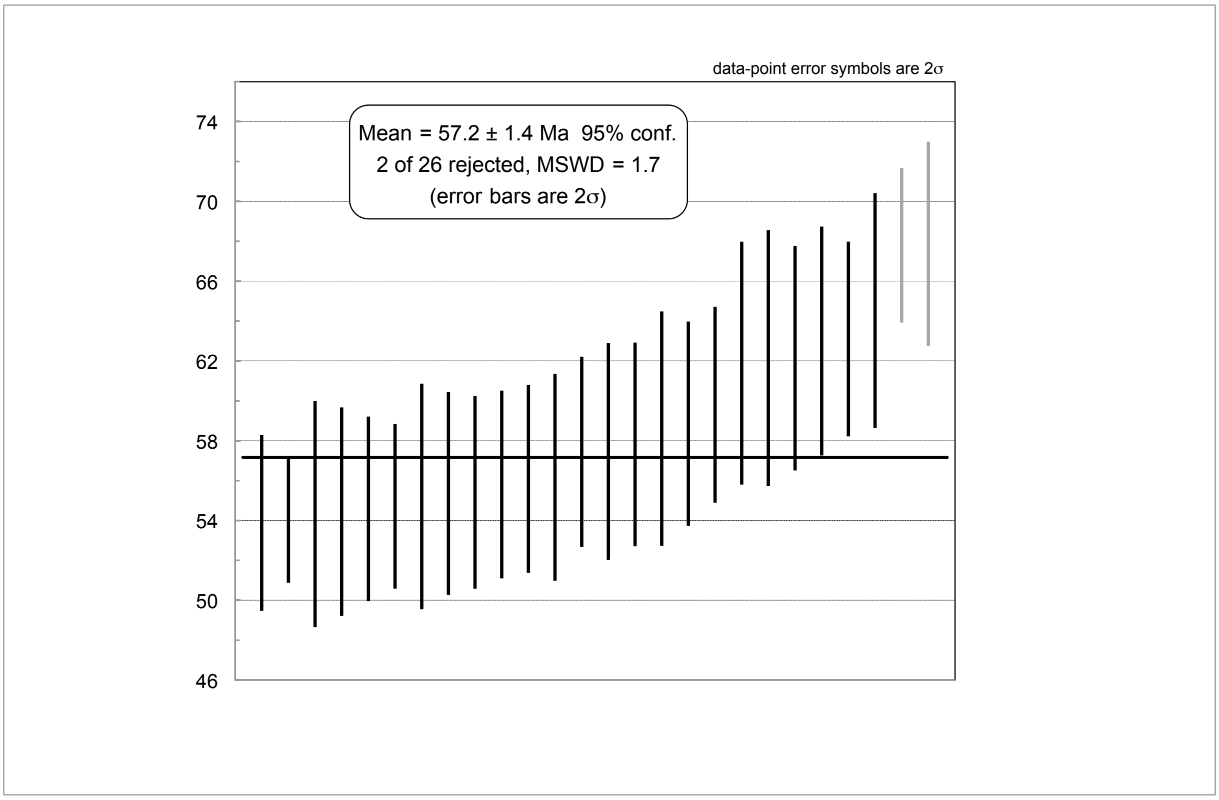

PTN weighted mean plot

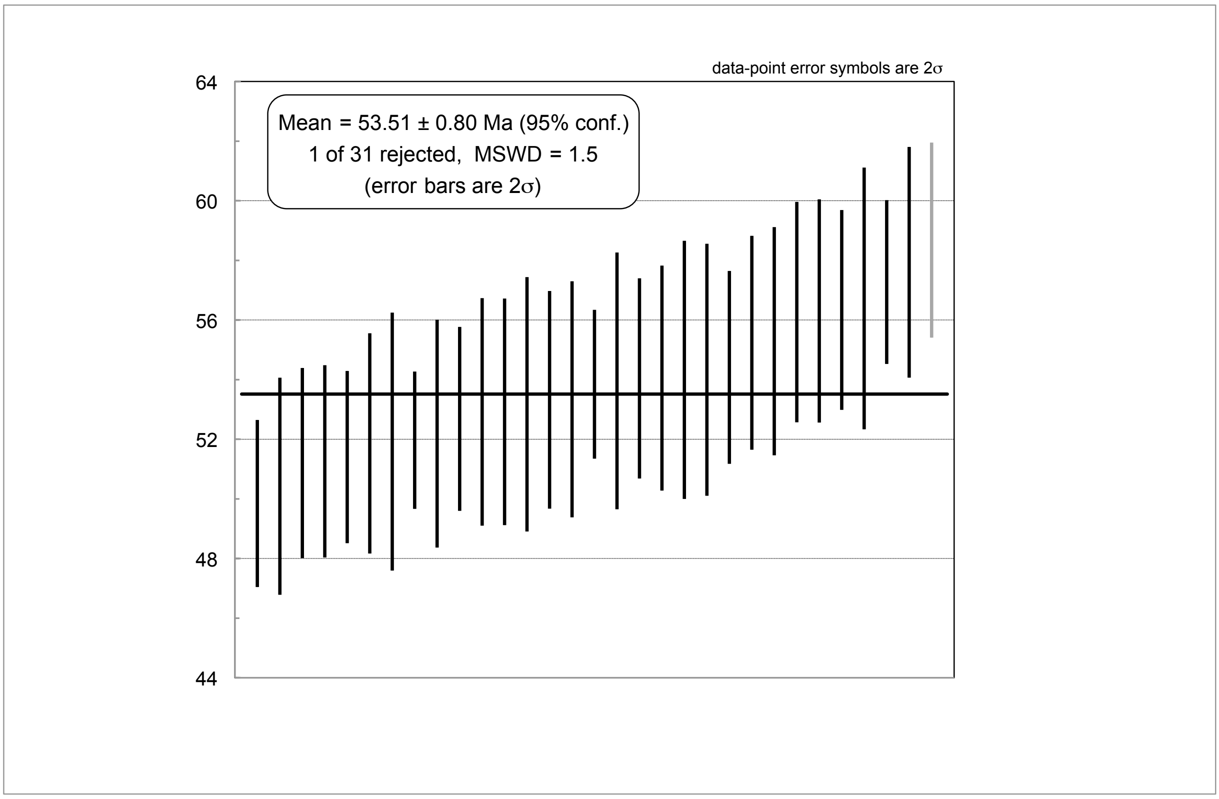

PMN deconvolution ages plot

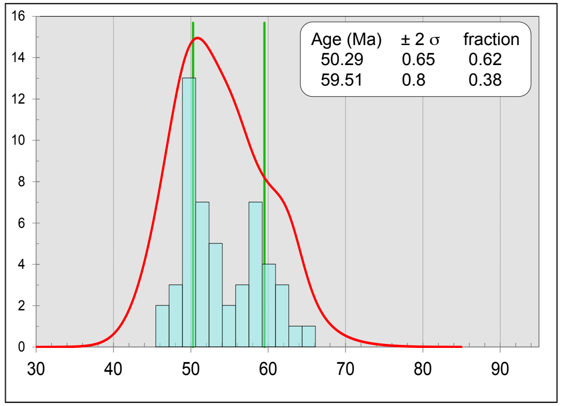

PMN young peak weighted mean plot

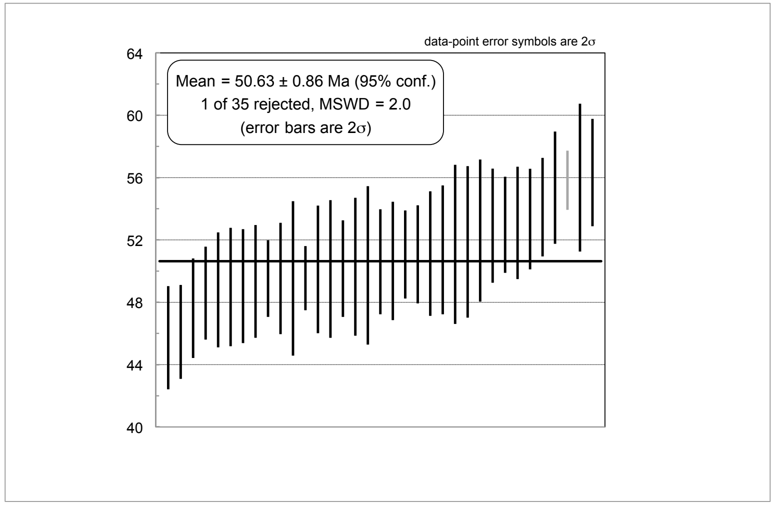

LQP deconvolution ages plot

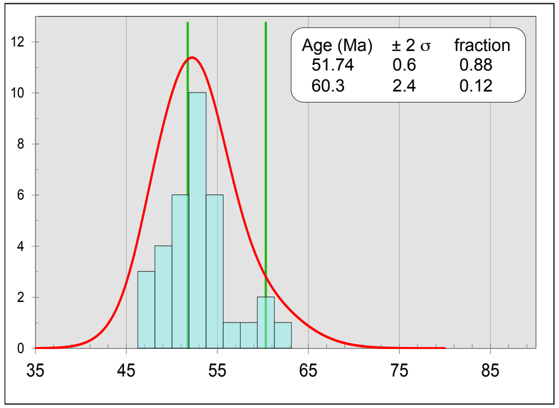

LQP young peak weighted mean plot

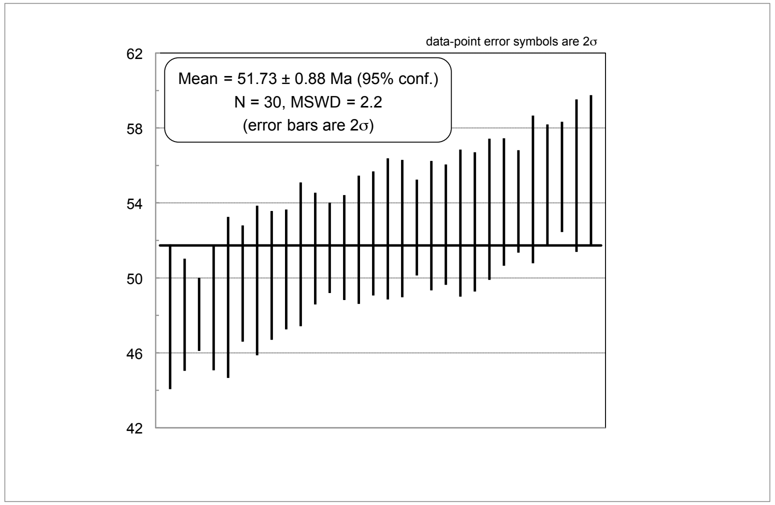

PGD deconvolution ages plot

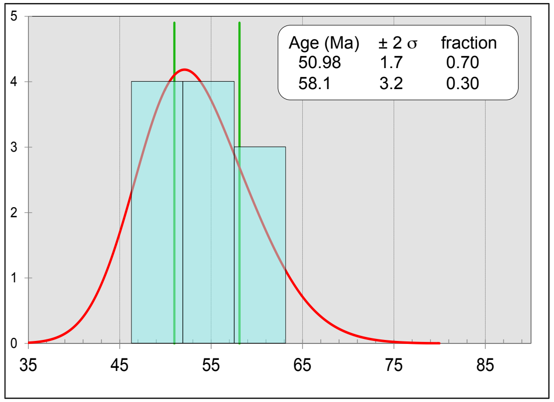

PGD young peak weighted mean plot

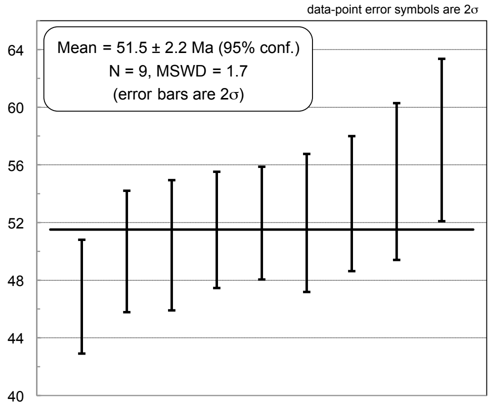

Supplementary sheet 4 Parameters used for lithostatic and hydrostatic pressure range calculations in Fig. 41

	Assumed eroded mass (km)		Approx. sample depth (km)		Density (Mg/m3)		Hydrostatic pressure range (bar)	Lithostatic pressure range (bar)
Scenario 1								
Maksaev & Zentilli (1999)	Max.	5	Max.	0.6	Max.	2.81	549.36	1543.7016
	Min.	3	Min.	0.15	Min.	2.65	309.015	818.88975
	Max.	4	Max.	0.6	Max.	2.81	451.26	1268.0406
	Min.	2.5	Min.	0.15	Min.	2.65	259.965	688.90725
Scenario 2								
Recalculated using Maksaev & Zentilli (1999)	Max.	3.75	Max.	0.6	Max.	2.81	426.735	1199.12535
	Min.	2.25	Min.	0.15	Min.	2.65	235.44	623.916
	Max.	3	Max.	0.6	Max.	2.81	353.16	992.3796
	Min.	1.88	Min.	0.15	Min.	2.65	199.143	527.72895
Scenario 3								
Victor (2004) and Arancibia et al. (2006)	Max.	2.2	Max.	0.6	Max.	2.81	274.68	771.8508
	Min.	1.6	Min.	0.15	Min.	2.65	171.675	454.93875